Technische Universität München

Fakultät für Elektrotechnik und Informationstechnik

Munich School of Bioengineering

Low-Field NMR and the Application on Magnetic Nanoparticles and Multiple-Quantum Coherences

Andreas Wegemann

Vollständiger Abdruck der von der Fakultät für Elektrotechnik und Informationstechnik der Technischen Universität München zur Erlangung des akademischen Grades eines

Doktor-Ingenieurs (Dr.-Ing.)

genehmigten Dissertation.

Vorsitzender:		apl. Prof. Dr.-Ing. habil. Helmut Gräb
Prüfer der Dissertation:	1.	Prof. Dr.-Ing. Werner Hemmert
	2.	Prof. Dr. rer. nat. Axel Haase

Die Dissertation wurde am 17.06.2020 bei der Technischen Universität München eingereicht und durch die Fakultät für Elektrotechnik und Informationstechnik am 12.04.2021 angenommen.

Abstract

Nuclear magnetic resonance (NMR) spectroscopy can be considered as one of the most versatile and powerful tools regarding the investigation of molecular interactions, structures, and dynamics. A rising number of applications rely on low-field permanent magnets due to increased mobility, small outline dimensions and reduced costs. However, NMR spectrometers using permanent magnets suffer from reduced signal-to-noise ratio and resolution as well as temperature-dependent field drifts. Nevertheless, the benefits of permanent magnets dominate in certain circumstances, such that portable NMR spectrometers are used in various scientific fields. In this thesis, two applications of low-field NMR are investigated.
First, low-field NMR spectroscopy is applied for the characterization of magnetic nanoparticles (MNPs). In addition, quality control and reaction monitoring throughout the synthesis process are performed. The rapid characterization regarding NMR relaxation properties right after the synthesis process improves and accelerates the development of functional MNPs. Therefore, an automated system combining the microfluidic synthesis of iron oxide MNPs by coprecipitation with an integrated miniaturized NMR spectrometer is designed and validated. The characterization in terms of transverse and longitudinal relaxation rates is performed with a 0.5 T permanent magnet. Clogging and fouling of the tape-based microreactor are successfully prevented by 3D hydrodynamic flow focusing. MNPs with primary particle sizes of up to 25 nm are synthesized. Finally, the potential use of the system is demonstrated by efficiently optimizing MNPs regarding their transverse relaxivity. Values of 115.5 $mM^{-1}s^{-1}$ are achieved. The compact system shows to be an efficient tool for accelerated optimization and quality control for MNP synthesis as well as subsequent functionalization.
Second, a portable NMR spectrometer, capable of field gradient generation without additional external gradient coils is designed and validated. Various NMR experiments rely on the application of pulsed field gradients. However, the majority of portable low-field NMR systems lacks the ability to generate these due to additional and cumbersome hardware requirements. Therefore, an NMR probe head, incorporating radio frequency (RF)-capabilities with the ability to generate pulsed field gradients in a single center-tapped solenoid is presented. The corresponding circuitry allows to drive direct currents through the center tap without disturbing the RF reception sensitivity. Furthermore, an advanced standalone System-on-Chip-based NMR spectrometer is presented. In combination with the gradient-capable probe head, it represents a very versatile low-cost system. The broadband spectrometer is suitable for proton NMR at magnetic flux densities ranging from 0.5 T to 1 T. A characterization of the probe head is presented regarding quality factor, scatter parameters, and transverse field homogeneity. The external probe head circuitry is discussed and the resulting gradient field is presented by simulation data. Furthermore, the dephasing capabilities and the spatial shape of the gradient are investigated by experimental results. Finally, the potential use of this setup in highly sophisticated two-dimensional NMR experiments is presented by the mapping of J-couplings in 1-butanol via zero-quantum coherences. Prior to a discussion of the results, the pulse sequence is theoretically analyzed for a homonuclear two-spin system using the quantum mechanical approach.

Zusammenfassung

Kernspinresonanzspektroskopie (NMR-Spektroskopie von englisch nuclear magnetic resonance) gilt als eines der vielfältigsten und leistungsstärksten Werkzeuge zur Untersuchung von molekularen Interaktionen, Strukturen sowie deren Dynamiken. Für eine Vielzahl an Anwendungen eignen sich Permanentmagneten auf Grund von erhöhter Mobilität, geringeren Abmessungen und der kostengünstigeren Beschaffung. Niedrige magnetische Flussdichten resultieren allerdings auch in einem reduzierten Signal-Rausch-Verhältnis und einer geringeren Auflösung. Außerdem driftet die Flussdichte mit der Temperatur. Nichtsdestotrotz gibt es einige Anwendungen, bei denen die Vorteile überwiegen. Daher finden tragbare Spektrometer in einigen Wissenschaftsgebieten Anwendung. In dieser Arbeit werden zwei Anwendungsgebiete für Niederfeld-NMR-Spektroskopie vertieft.
Zunächst werden magnetische Nanopartikel mit Hilfe von NMR-Spektroskopie charakterisiert, sowie Reaktions- und Qualitätskontrollen während des Syntheseprozesses durchgeführt. Durch die schnelle Charakterisierung des transversalen und des longitudinalen Relaxationsverhaltens direkt nach der Synthese kann die Entwicklung funktionaler magnetischer Nanopartikel beschleunigt und verbessert werden. Es wird daher ein automatisiertes System entwickelt und validiert, das die mikrofluidische Synthese von Eisenoxid-Nanopartikeln durch Mitfällung mit einem miniaturisiertem Spektrometer kombiniert. Verschmutzungen und Verstopfungen des Mikroreaktors werden durch Einsatz von 3D-Fokussierung verhindert. Die synthetisierten Partikel haben eine primäre Partikelgröße von bis zu 25 nm. Mögliche Anwendungsbereiche werden anhand der Optimierung hinsichtlich der transversalen Relaxivität gezeigt. Dabei werden transversale Relaxivitäten von 115,5 $mM^{-1}s^{-1}$ erreicht. Das kompakte System stellt damit ein effizientes Werkzeug zur beschleunigten Optimierung sowie zur Qualitätskontrolle während der Synthese als auch während der Funktionalisierung von magnetischen Nanopartikeln dar.
Des Weiteren wird im Rahmen dieser Arbeit ein tragbares Spektrometer entwickelt und validiert, das es ermöglicht gepulste Feldgradienten ohne zusätzliche Gradientenspulen zu erzeugen. Diese werden für zahlreiche NMR Experimente benötigt, können allerdings von einem Großteil der miniaturisierten Spektrometer auf Grund des erhöhten Hardwarebedarfs nicht erzeugt werden. Daher wird hier ein Probenkopf, basierend auf einem einzigen Solenoiden mit Mittelanzapfung präsentiert, der neben der Funktionalität im Radiofrequenzbereich Feldgradienten erzeugen kann. Es wird ein Gleichstom durch die Mittelanzapfung getrieben, ohne dabei die Sensitivität im Radiofrequenzbereich zu verringern. In Kombination mit einem breitbandigen Spektrometer, basierend auf einem Ein-Chip-System wird damit ein vielseitig einsetzbares und kostengünstiges System vorgestellt. Die Charakterisierung des Probenkopfes erfolgt anhand des Qualitätsfaktors, der Streuparameter sowie der transversalen Feldhomogenität. Externe Beschaltung und der Feldverlauf des Gradienten werden anhand von Simulationsdaten diskutiert. Experimentelle Ergebnisse zeigen die Auswirkungen des Gradienten bezüglich der Probendephasierung sowie dessen räumliche Verteilung. Zuletzt wird die Eignung des Messgerätes für die komplexe, zwei-dimensionale NMR-Spektroskopie anhand der Detektion von J-Kopplungen an 1-Butanol durch Nullquantenkohärenzen gezeigt. Zusätzlich wird eine ausführliche theoretische quantenmechanische Analyse der Sequenz am Beispiel eines Zwei-Spin Systems präsentiert.

Contents

List of Figures

List of Tables

List of Abbreviations

ADC	Analog-to-Digital Converter
AXI	Advanced eXtensible Interface
CIC	Cascaded-Integrator-Comb
CRAZED	COSY Revamped with Asymmetric Z-gradient Echo Detection
CTP	Coherence Transfer Pathway
CW	Continuous Wave
DAC	Digital-to-Analog Converter
DC	Direct Current
DDS	Direct Digital Synthesizers
DLS	Dynamic Light Scattering
EMIO	Extended Multiplexed I/O
FESEM	Field Emission Scanning Electron Microscopy
FPGA	Field Programmable Gate Array
GIC	Generic Interrupt Controller
GP	General Purpose
HBF	Half-Band Filter
HOMOGENIZED	HOMOGeneity ENhancement by Intermolecular ZEro-quantum Detection
HP	High Performance
HZQC	Homonuclear Zero-Quantum Coherence
ICP-MS	Inductively Coupled Plasma Mass Spectrometry
iMQC	intermolecular Multiple-Quantum Coherence
iZQC	intermolecular Zero-Quantum Coherence
LO	Local Oscillator
lwIP	lightweight IP
µC	microController
MiCSMaP	Microreactor with integrated Characterization for the Synthesis of Magnetic nanoParticles
MIO	Multiplexed I/O
MMCM	Mixed-Mode Clock Manager
MNP	Magnetic NanoParticle
MQC	Multiple-Quantum Coherence
MRI	Magnetic Resonance Imaging
NMR	Nuclear Magnetic Resonance
PL	Programmable Logic
PS	Processing System
QSPI	Quad Serial Peripheral Interface
RF	Radio Frequency
SNR	Signal-to-Noise Ratio

SoC	System-on-Chip
ZQC	Zero-Quantum Coherence

1 Introduction

The advent of nuclear magnetic resonance (NMR) dates back to 1938, when Rabi et al. first discovered and described transitions between nuclear spin states on a beam of molecules [1]. For his work, Rabi was awarded with the Nobel Prize in Physics in 1944. In 1946, Purcell et al. at Harvard University [2] and Bloch et al. at Stanford University [3, 4] first reported NMR in bulk materials. The expansion of NMR observations to liquids and solids was honored with the Nobel Prize in Physics in 1952 [5, 6]. Their experiments relied on the application of variable main magnetic fields and continuous RF-fields (continuous wave, CW-NMR) [2–4]. However, most modern NMR methods are based on a time-dependent series of radio frequency (RF) pulses as well as a constant main magnetic field (pulsed-NMR) [7]. In 1949 and 1950, Hahn presented for the first time the concepts of free induction decay (FID) [8] and spin echo [9], respectively.

Nowadays, NMR spectroscopy can be considered as one of the most versatile and powerful tools regarding the investigation of molecular interactions, structures, and dynamics. Application areas range across a broad spectrum of scientific fields, including chemical reaction monitoring [10, 11], analytical chemistry [12], and medicine [13, 14]. The success of NMR results, amongst other things, from its non-invasive and non-destructive detection capability [15, 16]. As resolution and signal-to-noise ratio (SNR) of NMR are dominated by external field properties like magnitude and homogeneity of the magnetic flux density, highly sophisticated NMR spectrometers are mostly realized by superconducting magnets [17]. These superconducting magnets are usually accompanied by cumbersome electrical current shims [18]. The resulting setups are thus complex, costly and large in their outline dimensions.

However, low-cost desktop systems relying on low-field permanent magnets are used in a rising number of applications [11, 19]. Even though, low-field NMR suffers from drawbacks like limited magnetic flux densities, low homogeneous volumes as well as temperature caused field drifts, the benefits exceed in certain circumstances. Compared to superconductors, no additional cooling architecture is required. This results in reduced cost and maintenance expenditure. Furthermore, compact designs allow for portable devices. Major improvements in the manufacturing of permanent magnets [20, 21], resulted in an increasing number of highly sophisticated and specialized portable NMR spectrometers [19, 22–24]. Digital signal processing is mostly integrated on field programmable gate arrays (FPGAs), whereas some groups even integrated entire NMR transceiver structures on custom-designed integrated circuits [25, 26]. Furthermore, increasingly compact system designs are supported by the miniaturization of NMR probe heads [24, 27].

In this thesis, low-field NMR spectroscopy is applied for the characterization of magnetic nanoparticles (MNPs) as well as for reaction monitoring and quality control throughout the synthesis process. In cooperation with Jonas Bemetz within the IGSSE project 9.06, a Microreactor with integrated Characterization for the Synthesis of Magnetic nanoParticles (MiCSMaP) is developed. Therefore, a microcontroller-(µC) based spectrometer is integrated in a fully automated particle reactor. Furthermore, an advanced System-on-Chip (SoC) based NMR spectrometer, accompanied by a gradient-capable NMR probe head is developed in order to increase the spectrum of low-field applications.

Microreactor with Integrated Characterization for the Synthesis of Magnetic Nanoparticles

MNPs are applied in various scientific fields. This includes environmental pollutant removal [28], targeted drug delivery [29, 30], or analyte preconcentration in analytical chemistry. The interaction of MNPs with their molecular surrounding usually increases for high particle magnetizations. In the context of NMR, the characterization in terms of relaxivities is favorable. The sensitivity of immunoassays based on relaxivity switches [31] improves with rising NMR relaxivities [32]. Furthermore, magnetic resonance imaging (MRI) contrast agents are classified in terms of their transverse (r_2) and longitudinal relaxivity (r_1) [33–35]. Negative contrast agents correspond to a large r_2, whereas positive contrast agents correspond to a large r_1. Particles smaller than 5 nm have shown to be suitable as positive MRI contrast agents [34, 36], whereas negative MRI contrast agents are usually larger than 10 nm [37]. The relaxivity of MNPs is a very sensitive parameter that depends on a variety of particle characteristics. These include saturation magnetization [38], primary particle size, cluster size [39] and coatings [40]. Due to the dependence on a large number of synthesis parameters, an optimization of MNPs towards relaxivities is a cumbersome process. Especially, if the determination of relaxivities is performed by expensive clinical MRIs with limited access, this becomes a resource and time intensive procedure. These difficulties could be strongly reduced by the incorporation of an NMR relaxometer in the synthesis process of MNPs. Moreover, the integration of analytical tools can lead to further advantages including quality control, reaction optimization and process monitoring [41]. However, the availability of miniaturized online measurement tools is limited [41, 42].

The coprecipitation of iron salt precursors with a base [43] represents a fast and cheap synthesis method that leads to hydrophilic MNPs [34]. Compared to synthesis methods like the thermal decomposition of organometallic precursors [44] or microemulsion techniques, coprecipitation exhibits a lower level of control over particle size and size distribution [34]. However, no toxic chemicals are required [45] and the synthesis is possible under standard conditions for temperature and pressure [45]. Reduced control over particle characteristics like primary particle size and size distributions can be compensated by the application of microfluidic reactors. Precise control of the reaction parameters is facilitated by fast heat and mass transfers as well as defined mixing procedures [46, 47]. However, due to the high reactivity of the iron salts, fouling and clogging of microfluidic channels is a challenge [42]. This issue is aggravated by the high surface to volume ratio inherent to microchannels [47]. The formation of particles close to the channel walls and thus fouling of the reactor can be avoided by using 3D hydrodynamic flow focusing [48, 49].

This work discusses the combination of microfluidic synthesis of MNPs by coprecipitation and subsequent surface functionalization with online particle characterization in terms of NMR relaxation properties. A portable system, incorporating the microreactor and a custom-designed low-field NMR relaxometer as well as the required fluidic actuators like pumps and valves is presented. Throughout and right after the synthesis process, the NMR relaxation process is constantly monitored in terms of the transverse and the longitudinal relaxation rate. Furthermore, the integrated spectrometer allows for the determination of the MNP relaxivities in an automated way. NMR relaxation properties strongly depend on particle properties like primary particle and cluster size. Thus, the influence of synthesis parameters on the particle parameters can be investigated indirectly via the relaxation properties of the sample. Finally, synthesis conditions are optimized for maximum transverse relaxivity. The optimized particles are further investigated concerning the influence of alendronate coatings.

SoC-Based NMR Spectrometer and Gradient-Capable Probe Head

In NMR spectroscopy, a large number of pulse sequences rely on the application of pulsed field gradients. Amongst others, this includes the separation of multiple-quantum coherence (MQC) orders [50]. Quantum filters are applied in homonuclear zero-quantum coherence (HZQC) experiments [12, 51, 52], where a single pulsed field gradient (spoiling pulse) is sufficient to isolate zero-quantum coherences (ZQCs) from higher quantum orders. Moreover, correlation pulses are used to manipulate a spin system such that the magnetic isotropy is broken. These field gradients are applied in intermolecular ZQC (iZQC) or intermolecular MQC (iMQC) experiments [53–55]. Furthermore, pulsed field gradients are required for NMR thermometry [56], diffusion NMR [57] or MRI, to name only a few. The need for independently controllable field gradients in each direction requires a complex external gradient coil setup and a high-performance driver circuitry [58]. These cumbersome and space-consuming designs are thus not adequate or realizable for most portable NMR devices, especially under the use of small-outline permanent magnets. Therefore, the majority of portable low-field NMR systems lack the capability of pulsed field gradient generation.

This work discusses the design and the development of a versatile, low-cost low-field NMR system. The system incorporates an NMR probe head design that integrates both, pulsed field gradient generation and RF-capabilities in one single center-tapped solenoid. A probe head circuitry designed to ensure the opportunity for applying direct currents (DC) while providing undisturbed RF reception capabilities is introduced. No additional hardware is required inside the magnet as the gradient field is generated by the RF-coil. Stockmann et al. [59] already introduced the concept of applying DC to RF-coils. However, the aim was to achieve electrical current shims instead of a gradient. Still, it shows the possibility of maintaining the reception sensitivity of the RF-coils. Moreover, an advanced SoC-based NMR spectrometer is presented. The SoC integrates an ARM-based processing system with the parallelizability and versatility of a programmable logic (PL). Versatile square wave pulse sequences, including the capability of switching pulsed field gradients can be designed.

Simulation data of the gradient field is analyzed in order to improve predictions on the sequence outcomes. Furthermore, modulations on the spin system caused by the field gradient are investigated in terms of NMR signal acquisition. Finally, the potential use of the setup is demonstrated by mapping the intramolecular coupling network of 1-butanol via ZQCs. The resolution enhancement of ZQCs is shown by the successful application of a highly inhomogeneous low-field permanent magnet.

2 NMR Theory

This chapter covers the NMR theory required to understand the measurements and sequences presented in chapter 4, 6 and 5 as well as the underlying concepts required for the NMR spectrometer designs presented in chapter 3. Special focus is on the excitation of MQCs as well as internal magnetic interactions like direct or indirect dipole-dipole couplings. The well established theoretical framework of NMR allows for a very detailed deduction of the NMR signal formation [60]. In general, spectrometers or experimental setups need to be adjusted if they do not match the theoretical results [61]. NMR experiments are described either by the classical approach, using the Bloch equations [3, 62] or the quantum mechanical approach. Both approaches show advantages and disadvantages. For instance, the more intuitive classical picture simplifies the inclusion of effects like radiation damping, relaxation and diffusion. Conversely, the quantum mechanical picture allows for an easier access to pulse sequence prediction and the evolution of the spin system [60]. In many cases, a combination of both leads to an enhancement of the results [63]. Throughout this work, the quantum mechanical treatment is mostly preferred. The corresponding theory, combining a summery of the relevant textbook knowledge [64, 65, 69] with recent scientific insights [55, 60, 61] is covered in the following.

2.1 Spin Angular Momentum and Nuclear Magnetic Moment

In quantum mechanical theory, the angular momentum operator $\hat{\boldsymbol{I}}$ given as

$$\hat{\boldsymbol{I}} = \hat{I}_x \boldsymbol{e}_x + \hat{I}_y \boldsymbol{e}_y + \hat{I}_z \boldsymbol{e}_z \tag{2.1}$$

is of highest importance to describe rotating particles. The operator is represented by the three components $\hat{I}_x$, $\hat{I}_y$ and $\hat{I}_z$ corresponding to the three Cartesian axes with the unit vectors $\boldsymbol{e}_x$, $\boldsymbol{e}_y$ and $\boldsymbol{e}_z$. The angular momentum eigenstates and eigenvalues of the z-component $\hat{I}_z$ are defined by two quantum numbers: the nuclear spin quantum number I and the azimuthal quantum number M.
For the following, only spins with spin quantum number $I = \frac{1}{2}$ are considered. The resulting angular momentum can not be explained by rotational motion and is thus just considered as being intrinsic. The azimuthal quantum number of spin-$\frac{1}{2}$ nuclei can take $2I + 1 = 2$ values, denoted as $M_\alpha = +\frac{1}{2}$ and $M_\beta = -\frac{1}{2}$. These two eigenvalues correspond to the Zeeman eigenstates $|\alpha\rangle$ and $|\beta\rangle$ which obey the following eigenequations

$$\begin{aligned} \hat{I}_z |\alpha\rangle &= M_\alpha |\alpha\rangle \\ \hat{I}_z |\beta\rangle &= M_\beta |\beta\rangle , \end{aligned} \tag{2.2}$$

where the angular momentum operators are given in natural units. The spin state $|\psi\rangle(t)$ of a single spin-$\frac{1}{2}$ nucleus can be represented as a time-dependent superposition of the Zeeman eigenstates $|\alpha\rangle$ and $|\beta\rangle$, called the Zeeman basis, such that

$$|\psi\rangle(t) = c_\alpha(t) |\alpha\rangle + c_\beta(t) |\beta\rangle \tag{2.3}$$

The superposition coefficients are denoted as $c_\alpha(t)$ and $c_\beta(t)$. Furthermore, a pair of coupled spin-$\frac{1}{2}$ nuclei, I_i and I_k, can be described by a single quantum system. The total z-angular momentum operator $\hat{I}_z$ of this system is given as $\hat{I}_z = \hat{I}_{iz} + \hat{I}_{kz}$. The state $|\psi\rangle(t)$ is given as a superposition of four Zeeman product states $|\alpha\alpha\rangle$, $|\alpha\beta\rangle$,$|\beta\alpha\rangle$ and $|\beta\beta\rangle$. These eigenstates obey the following eigenequations given as

$$\begin{aligned} \hat{I}_z|\alpha\alpha\rangle &= M_{\alpha\alpha}|\alpha\alpha\rangle \qquad \hat{I}_z|\alpha\beta\rangle \quad = M_{\beta\alpha}|\alpha\beta\rangle \\ \hat{I}_z|\beta\alpha\rangle &= M_{\alpha\beta}|\beta\alpha\rangle \qquad \hat{I}_z|\beta\beta\rangle \quad = M_{\beta\beta}|\beta\beta\rangle\,, \end{aligned} \tag{2.4}$$

where $M_{\alpha\alpha} = +1$, $M_{\beta\alpha} = 0$, $M_{\alpha\beta} = 0$ and $M_{\beta\beta} = -1$ are the corresponding eigenvalues. The time-dependent superposition state $|\psi\rangle(t)$ of this system is given as

$$|\psi\rangle(t) = c_{\alpha\alpha}(t)|\alpha\alpha\rangle + c_{\alpha\beta}(t)|\alpha\beta\rangle + c_{\beta\alpha}(t)|\beta\alpha\rangle + c_{\beta\beta}(t)|\beta\beta\rangle\,, \tag{2.5}$$

where $c_{\alpha\alpha}(t)$, $c_{\alpha\beta}(t)$, $c_{\beta\alpha}(t)$ and $c_{\beta\beta}(t)$ are the corresponding superposition coefficients. Higher order spin systems are treated in an analogous manner but the complexity raises exponentially.

2.2 Spin Dynamics

Spin dynamics or the evolution of $|\psi\rangle(t)$ over time are described by the time-dependent Schrödinger equation given as

$$\frac{d}{dt}|\psi\rangle(t) = -j\hat{\mathcal{H}}|\psi\rangle(t)\,, \tag{2.6}$$

where $\hat{\mathcal{H}}$ is the Hamiltonian operator in natural units ($\hat{\mathcal{H}} = \hbar^{-1}\hat{H}$), valid for the time interval under investigation. A solution for the time-dependent Schrödinger equation is given as

$$|\psi\rangle(t_2) = \hat{U}(\tau)|\psi\rangle(t_1)\,, \tag{2.7}$$

where the linear propagator $\hat{U}(\tau)$ is given as

$$\hat{U}(\tau) = \exp\left(-j\hat{\mathcal{H}}\tau\right) \tag{2.8}$$

and $\tau = t_2 - t_1$.

2.3 Hamiltonians

The Hamiltonian operator describes the interaction energy between the nuclei and their environment. In general, a nucleus can interact with the environment due to an electric charge or a magnetic moment. There are no electrical interaction due to varying nuclear orientations for spin-$\frac{1}{2}$ nuclei because they behave like electric point charges [64]. Therefore, only magnetic interactions need to be considered. The nuclear magnetic moment $\boldsymbol{\mu}_i$ of spin I_i is directly proportional to the intrinsic spin angular momentum $\hat{\boldsymbol{I}}_i$ (see equation 2.1) such that

$$\boldsymbol{\mu}_i = \gamma_i\hat{\boldsymbol{I}}_i = \gamma_i\left(\hat{I}_{ix}\boldsymbol{e}_x + \hat{I}_{iy}\boldsymbol{e}_y + \hat{I}_{iz}\boldsymbol{e}_z\right), \tag{2.9}$$

where the constant of proportionality γ_i is the gyromagnetic ratio. Both, the magnetic moment $\boldsymbol{\mu}_i$ and the angular momentum $\hat{\boldsymbol{I}}_i$ are considered to be in natural units. In general, the Hamiltonian (in natural

units) for magnetic interactions of spin I_i is given as

$$\hat{\mathcal{H}}_i = -\boldsymbol{\mu}_i \cdot \boldsymbol{B} = -\gamma_i \left(B_x \hat{I}_{ix} + B_y \hat{I}_{iy} + B_z \hat{I}_{iz} \right), \tag{2.10}$$

where the magnetic field is defined as $\boldsymbol{B} = B_x \boldsymbol{e}_x + B_y \boldsymbol{e}_y + B_z \boldsymbol{e}_z$. The magnetic field $\boldsymbol{B}$ origins either from sources outside the sample or from internal sources. This leads to a separation of external magnetic interactions and internal magnetic interactions, respectively.

2.3.1 External Magnetic Interactions

External magnetic interactions include interactions with the static magnetic field B_0, the RF-field B_1 or the gradient field B_{grad}.

Static Magnetic Field

Throughout this work the external static magnetic field B_0 is always assumed to point in z-direction such that $\boldsymbol{B}_0 = B_0 \boldsymbol{e}_z$, where $\boldsymbol{e}_z$ is the unit vector in z-direction. For a spatially and temporarily homogeneous magnetic field, using equation 2.10 results in the static or Zeeman Hamiltonian $\hat{\mathcal{H}}_i^{stat}$ for spin I_i given as

$$\hat{\mathcal{H}}_i^{stat} = -\gamma_i B_0 \hat{I}_{iz} \tag{2.11}$$

The static Hamiltonian for the whole sample is given as

$$\hat{\mathcal{H}}^{stat} = \sum_{i=1}^{N} \hat{\mathcal{H}}_i^{stat}, \tag{2.12}$$

where N is the number of spins in the sample.

Radio Frequency Field

The time-varying RF-field $\boldsymbol{B}_1(t)$ is applied perpendicular to the static field B_0. It is assumed to have a rectangular envelope with an amplitude B_1. For the sake of simplicity, the linearly polarized field is separated in two counter-rotating components, one in resonance with the precessing spins and one rotating in the opposite sense. Only the resonant component influences the spins and is given as

$$\boldsymbol{B}_1(t) = \frac{1}{2} B_1 \left(\cos\left(\omega_{RF} t + \Phi_p\right) \boldsymbol{e}_x + \sin\left(\omega_{RF} t + \Phi_p\right) \boldsymbol{e}_y \right), \tag{2.13}$$

where ω_{RF} is the frequency of the RF-pulse and Φ_p the corresponding phase at $t = 0$. Using equation 2.10, this results in an RF Hamiltonian $\hat{\mathcal{H}}_i^{RF}(t)$ for spin I_i given as

$$\hat{\mathcal{H}}_i^{RF}(t) = -\omega_{nut}^i \left(\cos\left(\omega_{RF} t + \Phi_p\right) \hat{I}_{ix} + \sin\left(\omega_{RF} t + \Phi_p\right) \hat{I}_{iy} \right), \tag{2.14}$$

where the nutation frequency $\omega_{nut}^i = |\frac{1}{2} \gamma_i B_{RF}|$. The RF Hamiltonian for the whole sample is given as

$$\hat{\mathcal{H}}^{RF}(t) = \sum_{i=1}^{N} \hat{\mathcal{H}}_i^{RF}(t) \tag{2.15}$$

Gradient Field

In general, the magnetic field $\boldsymbol{B}_{grad}(\boldsymbol{s})$ of the gradient is assumed to be temporarily constant during the on- and the off-periods. Here, a rectangular, switchable gradient field is assumed. The resulting Hamiltonian is given as

$$\hat{\mathcal{H}}_i^{grad}(\boldsymbol{s}_i) = -\gamma_i \boldsymbol{B}_{grad}(\boldsymbol{s}_i)\hat{\boldsymbol{I}}_i \approx -\gamma_i B_{grad,z}(\boldsymbol{s}_i)\hat{I}_{iz}\,, \tag{2.16}$$

where the secular approximation is used for the second transformation. The magnetic flux density of a constant gradient $\boldsymbol{B}_{grad,z}^{const}(\boldsymbol{s})$ is given as

$$\boldsymbol{B}_{grad,z}^{const}(\boldsymbol{s}) = G_x x\boldsymbol{e}_z + G_y y\boldsymbol{e}_z + G_z z\boldsymbol{e}_z\,, \tag{2.17}$$

where $\boldsymbol{s} = \{x, y, z\}$ is the spatial position and G_x, G_y and G_z are the gradient strengths in the corresponding direction. Throughout this work, only z-gradients are used such that the constant gradient Hamiltonian $\hat{\mathcal{H}}_{grad,iz}^{const}(z_i)$ for spin I_i is given as

$$\hat{\mathcal{H}}_{grad,iz}^{const}(z_i) = -\gamma_i G_z z_i \hat{I}_{iz} \tag{2.18}$$

For the whole sample, the gradient Hamiltonian is given as

$$\hat{\mathcal{H}}_{grad,z}^{const}(z) = \sum_{i=1}^{N} \hat{\mathcal{H}}_{grad,iz}^{const}(z_i) \tag{2.19}$$

2.3.2 Internal Magnetic Interactions

Internal magnetic interactions describe the effects of magnetic fields internally generated in the sample. For spin-$\frac{1}{2}$ nuclei in isotropic liquids, this includes three types of interactions: chemical shift, direct dipole-dipole coupling and indirect dipole-dipole coupling (J-coupling). Since strong external interactions with $\boldsymbol{B}_0$ mask rather weak internal ones, a simplification of the internal Hamiltonians by motional averaging and secular approximation is valid in most cases.

Chemical Shift

The external field $\boldsymbol{B}_0$ induces electrical currents in the electron clouds surrounding the spins. These electrical currents in turn lead to a local induced magnetic field $\boldsymbol{B}_{ind}(\boldsymbol{B}_0)$ depending on the electrical environment of the particular spin. Two spins in one molecule might thus experience slightly different magnetic fields $\boldsymbol{B}_{loc} = \boldsymbol{B}_0 + \boldsymbol{B}_{ind}(\boldsymbol{B}_0)$. The corresponding frequency shift is the chemical shift. Throughout this work, the chemical shift is assumed to be a strictly intramolecular phenomenon. For isotropic liquids, the local field $\boldsymbol{B}_{loc}$ is given as

$$\boldsymbol{B}_{loc} = \boldsymbol{B}_0 + \delta_i^{iso}\boldsymbol{B}_0\,, \tag{2.20}$$

where δ_i^{iso} represents the isotropic chemical shift constant. The corresponding Hamiltonian $\hat{\mathcal{H}}_i^{CS}$ is a sum of the static Hamiltonian $\hat{\mathcal{H}}_i^{stat}$ and the chemical shift Hamiltonian.

$$\hat{\mathcal{H}}_i^{CS} = -\gamma_i B_0 \left(1 + \delta_i^{iso}\right)\hat{I}_{iz} = \omega_{i0}\hat{I}_{iz} \tag{2.21}$$

Direct Dipole-Dipole Coupling

The interactions between the magnetic fields generated by each individual spin with all the other spins are called direct dipole-dipole couplings. Figure 2.1a illustrates how the magnetic dipole field $\boldsymbol{B}^i_{dip}(\boldsymbol{r}_{ik})$ generated by the magnetic moment $\boldsymbol{\mu}_i$ of spin I_i interacts with the magnetic moment $\boldsymbol{\mu}_k$ of spin I_k. The interaction between spin I_i and spin I_k is mutual. Therefore, the field $\boldsymbol{B}^k_{dip}(\boldsymbol{r}_{ki})$ generated by the magnetic moment $\boldsymbol{\mu}_k$ of spin I_k also affects spin I_i. This is illustrated in figure 2.1b.

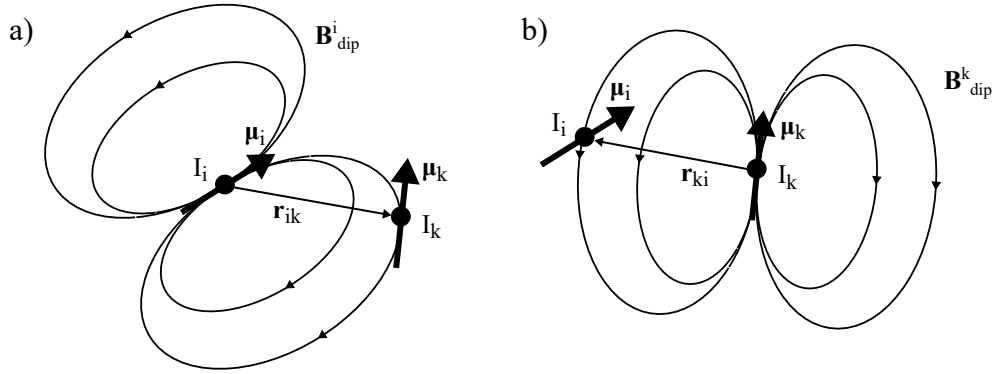

Figure 2.1: Direct intermolecular dipole-dipole couplings between spin I_i and spin I_k. a) The magnetic moment $\boldsymbol{\mu}_i$ of spin I_i generates a dipole field $\boldsymbol{B}^i_{dip}$ that interacts with spin I_k. b) The interaction between spin I_i and spin I_k is mutual. Therefore, the magnetic moment $\boldsymbol{\mu}_k$ of spin I_k also generates a dipole field $\boldsymbol{B}^k_{dip}$ that interacts with spin I_i.

The magnetic field $\boldsymbol{B}^i_{dip}(\boldsymbol{r}_{ik})$ originating from spin I_i, experienced by spin I_k is given as

$$\boldsymbol{B}^i_{dip}(\boldsymbol{r}_{ik}) = \frac{\mu_0}{4\pi|\boldsymbol{r}_{ik}|^3}\left(3\left(\boldsymbol{\mu}_i\cdot\boldsymbol{e}_{ik}\right)\boldsymbol{e}_{ik}-\boldsymbol{\mu}_i\right), \tag{2.22}$$

where $\boldsymbol{e}_{ik} = \frac{\boldsymbol{r}_{ik}}{|\boldsymbol{r}_{ik}|}$ and $\boldsymbol{r}_{ik}$ represents the vector connecting both spins. $\boldsymbol{B}^i_{dip}(\boldsymbol{r}_{ik})$ strongly depends on the orientation of the magnetic moment as well as the orientation of the spins to each other. Moreover, it strongly decays with the distance $|\boldsymbol{r}_{ik}|$ between the involved spins. Using equation 2.10, this results in the full direct dipole-dipole Hamiltonian $\hat{\mathcal{H}}^{DD,full}_{ik}$ between spin I_i and I_k given as

$$\begin{aligned}\hat{\mathcal{H}}^{DD,full}_{ik} &= -\frac{\boldsymbol{\mu}_k}{\hbar}\frac{\mu_0}{4\pi|\boldsymbol{r}_{ik}|^3}\left(3\left(\boldsymbol{\mu}_i\cdot\boldsymbol{e}_{ik}\right)\boldsymbol{e}_{ik}-\boldsymbol{\mu}_i\right)\\ &= -\frac{\mu_0}{4\pi}\frac{\gamma_i\gamma_k\hbar}{|\boldsymbol{r}_{ik}|^3}\left(3\left(\boldsymbol{I}_i\cdot\boldsymbol{e}_{ik}\right)\left(\boldsymbol{I}_k\cdot\boldsymbol{e}_{ik}\right)-\boldsymbol{I}_i\boldsymbol{I}_k\right)\end{aligned} \tag{2.23}$$

Under the assumption of a concurrent Zeeman interaction in z-direction, the secular approximation allows for a truncation of the full direct dipole-dipole Hamiltonian. In general, each element, where $\hat{\mathcal{H}}^{DD,full}_{ik,mn} << \Delta E = |\hat{\mathcal{H}}^{stat}_{mm} - \hat{\mathcal{H}}^{stat}_{nn}|$ holds true can be dropped. In case of a heteronuclear interaction, where ΔE is much higher than in case of homonuclear interactions, this simplifies to

$$\begin{aligned}\hat{\mathcal{H}}^{DD}_{ik,hetero} &= -\frac{\mu_0}{4\pi}\frac{\gamma_i\gamma_k\hbar}{|\boldsymbol{r}_{ik}|^3}\frac{1}{2}\left(3\cos^2(\Theta_{ik})-1\right)2\hat{I}_{iz}\hat{I}_{kz}\\ &= 2\pi D^{hetero}_{ik}\hat{I}_{iz}\hat{I}_{kz}\end{aligned} \tag{2.24}$$

In case of a homonuclear interaction, where ΔE is much smaller, the secular approximation leads to

$$\begin{aligned}\hat{\mathcal{H}}^{DD}_{ik,homo} &= -\frac{\mu_0}{4\pi}\frac{\gamma_i\gamma_k\hbar}{|\boldsymbol{r}_{ik}|^3}\frac{1}{2}\left(3\cos^2(\Theta_{ik})-1\right)\left(3\hat{I}_{iz}\hat{I}_{kz}-\boldsymbol{I}_i\boldsymbol{I}_k\right)\\ &= -\frac{\mu_0}{4\pi}\frac{\gamma_i\gamma_k\hbar}{|\boldsymbol{r}_{ik}|^3}\frac{1}{2}\left(3\cos^2(\Theta_{ik})-1\right)3\hat{I}_{iz}\hat{I}_{kz}\\ &= 2\pi D^{homo}_{ik}\hat{I}_{iz}\hat{I}_{kz}\end{aligned} \tag{2.25}$$

The term $\boldsymbol{I}_i\boldsymbol{I}_k$ can be neglected as evolution due to these operators does not lead to an observable signal throughout the HOMOGENIZED sequence [61]. This sequence is applied for the detection of intermolecular couplings in section 6.2. The secular dipole-dipole coupling constants are given as

$$D^{hetero}_{ik} = -\frac{\mu_0}{8\pi^2}\frac{\gamma_i\gamma_k\hbar}{|\boldsymbol{r}_{ik}|^3}\left(3\cos^2(\Theta_{ik})-1\right) \qquad D^{homo}_{ik} = -\frac{3\mu_0}{16\pi^2}\frac{\gamma_i\gamma_k\hbar}{|\boldsymbol{r}_{ik}|^3}\left(3\cos^2(\Theta_{ik})-1\right), \tag{2.26}$$

where $\Theta_{ik} = \arccos(\boldsymbol{e}_{ik}\cdot\boldsymbol{e}_z)$ is the solid angle between the vector connecting the two involved spins and the direction of the external field $\boldsymbol{B}_0$. The secular direct dipole-dipole Hamiltonians for the whole sample is given as

$$\hat{\mathcal{H}}^{DD}_{hetero} = \sum_{i,k}^{N,M}\hat{\mathcal{H}}^{DD}_{ik,hetero} \qquad \hat{\mathcal{H}}^{DD}_{homo} = \sum_{i<k}^{N}\hat{\mathcal{H}}^{DD}_{ik,homo} \tag{2.27}$$

Direct Dipole-Dipole Couplings in Isotropic Liquids The secular direct dipole-dipole constants D^{hetero}_{ik} and D^{homo}_{ik} strongly depend on the solid angle Θ_{ik}, where the strength of the coupling is determined by the factor $(3\cos^2(\Theta_{ik})-1)$. This angular dependence is illustrated graphically in figure 2.2, where spin I_i is located in the center.

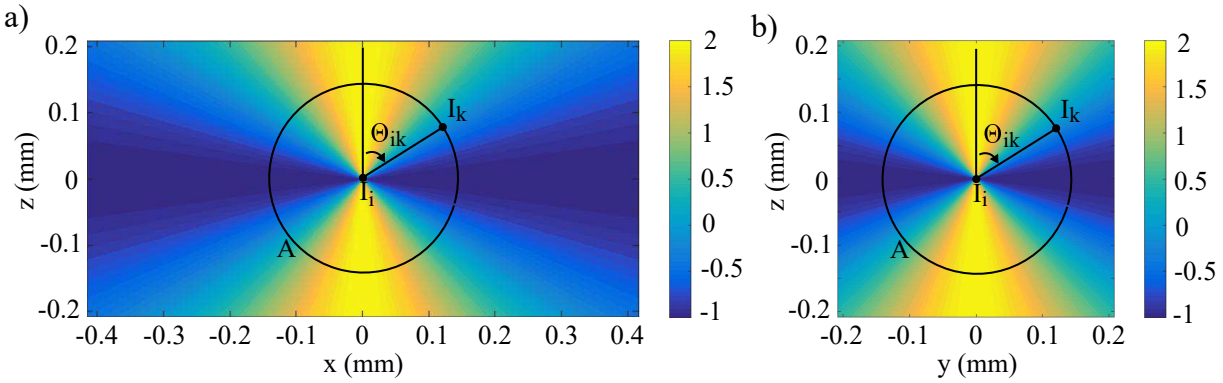

Figure 2.2: Angular dependence of the secular dipole-dipole constant $(3\cos^2(\Theta_{ik})-1)$. The spin $\hat{I}_i$ is located in the center of the sample. Spatial averaging is shown by integrating over the sphere A. a) A cut through the xz-plane of the sample at $y=0$. b) A cut through the yz-plane of the sample $x=0$.

Figure 2.2a shows a cut through the xz-plane at $y=0$ and figure 2.2b shows a cut through the yz-plane at $x=0$. The factor $(3\cos^2(\Theta_{ik})-1)$ behaves equivalent in both planes as the solid angle Θ_{ik} covers the same values. $3\cos^2(\Theta_{ik})-1$ has a maximum of two at $\Theta_{ik}=0$ or $\Theta_{ik}=\pi$ and a minimum of minus one at $\Theta_{ik}=\frac{\pi}{2}$ (xy-plane). At the so-called magic angle, $\Theta_{ik}=\arctan(2)$, the secular dipole-dipole constant becomes zero. The coupling strength is axially symmetric about the z-axis and plane-symmetric to the xy-plane. As all spins in the sample interact with spin I_i, these individual contributions need to be

summed up. In the following, all spins located on a spherical shell A with a unity radius around I_i are summed up. Assuming an infinite amount of spins on the shell, the sum can be expressed in integrative form such that

$$\int_A \left(3\cos^2(\Theta) - 1\right) dA = \int_0^{\pi} \left(3\cos^2(\Theta) - 1\right) \sin(\Theta) d\Theta = 0 \tag{2.28}$$

Hence, the net contribution to spin I_i averages to zero in isotropic liquids. Furthermore, molecular translation needs to be taken into account. Here, only diffusion is considered. The intermolecular vector $\boldsymbol{r}_{ik}(t)$ and therefore the angle $\Theta_{ik}(t)$ become time-dependent. Depending on the diffusion constant D and on the NMR time-scale denoted as t_{NMR} for the specific measurement, a diffusion sphere with a radius $r_0 = \sqrt{2Dt_{NMR}}$ ($\approx 10\,\mu m$ for small molecules [53]) is introduced. During an experiment spins are assumed to take every position inside this sphere. All couplings with a coupling distance $|\boldsymbol{r}_{ik}| < r_0$ are considered as short-range couplings. Couplings with a coupling distance $|\boldsymbol{r}_{ik}| > r_0$ are considered as long-range couplings.

Short-Range Couplings As the dipole field $\boldsymbol{B}_{dip}(\boldsymbol{r}_{ik})$ is proportional to $|\boldsymbol{r}_{ik}|^{-3}$, short-range couplings are very strong. However, as the spins I_i and I_k and thus the vector $\boldsymbol{r}_{ik}(t)$ take every possible orientation, the angle Θ_{ik} covers all values. Therefore, short range dipolar couplings always average to zero (see equation 2.28) even if the individual couplings are strong. This is called temporal averaging and can not be avoided. Hence, direct dipole-dipole coupling is considered to be a strictly intermolecular phenomenon.

Long-Range Couplings Individual long-range dipolar couplings are considered to be very weak due to the proportionality to $|\boldsymbol{r}_{ik}|^{-3}$. As the coupling distance $|\boldsymbol{r}_{ik}| > r_0$, there is no temporal averaging and therefore no inherent averaging to zero. Still, these couplings average to zero due to spatial averaging (see equation 2.28). However, spatial averaging can be canceled by breaking the magnetic isotropy, for instance by using pulsed field gradients. Furthermore, spatial averaging can be reduced by using non-spherical samples. Still, long-range dipolar couplings are often neglected as the individual dipolar couplings decrease with $|\boldsymbol{r}_{ik}|^{-3}$ and are therefore very weak. On the other hand, the number of couplings at a certain coupling distance increases with r^2. Hence, the net coupling with spin I_i decreases only proportional to r.

J-Coupling

J-Coupling or indirect dipole-dipole coupling describes the effect of the dipolar magnetic field through a cloud of bonding electrons. Therefore, J-coupling is here considered to be a strictly intramolecular phenomenon. These electron clouds alter the orientation dependence of the direct dipole-dipole coupling described previously. This leads to an isotropic remainder that is not averaged to zero by motional averaging. After secular approximation, the direct dipole-dipole Hamiltonian is given as

$$\hat{\mathcal{H}}^J_{ik,hetero} = 2\pi J_{ik} \hat{I}_{iz} \hat{I}_{kz} \tag{2.29}$$

for a heteronulear spin pair and

$$\hat{\mathcal{H}}^J_{ik,homo} = 2\pi J_{ik} \boldsymbol{I}_i \boldsymbol{I}_j \approx 2\pi J_{ik} \hat{I}_{iz} \hat{I}_{kz}, \tag{2.30}$$

for a homonuclear spin. The isotropic J-coupling constant J_{ik} is independent of the molecular orientation and the static magnetic field $\boldsymbol{B}_0$. Simplification of equation 2.30 applies as long as weak coupling is assumed.

2.4 Zeeman Energy Levels

The spin interactions with the external static magnetic field $\boldsymbol{B}_0$ are described by the Zeeman Hamiltonian $\hat{\mathcal{H}}_0 = \hat{\mathcal{H}}^{stat}$ (see equation 2.12). The eigenstates of $\hat{\mathcal{H}}_0$ and $\hat{I}_z$ are equal as $\hat{\mathcal{H}}_0$ is directly proportional to $\hat{I}_z$. The corresponding eigenequations (see equation 2.2) for an uncoupled spin-$\frac{1}{2}$ system are thus given as

$$\begin{aligned} \hat{\mathcal{H}}_0 \left|\alpha\right\rangle &= \omega_\alpha \left|\alpha\right\rangle \\ \hat{\mathcal{H}}_0 \left|\beta\right\rangle &= \omega_\beta \left|\beta\right\rangle , \end{aligned} \tag{2.31}$$

where the eigenvalues $\omega_\alpha = +\frac{1}{2}\omega_0$ and $\omega_\beta = -\frac{1}{2}\omega_0$ correspond to the energy levels of the states $\left|\alpha\right\rangle$ and $\left|\beta\right\rangle$ in frequency units. The Zeeman splitting of this system is equal to the Larmor frequency ω_0 given as

$$\omega_0 = -\gamma B_0 \tag{2.32}$$

An illustration of the energy levels of the uncoupled spin-$\frac{1}{2}$ system is given by figure 2.3a, where the eigenstates are connected by the corresponding coherences.

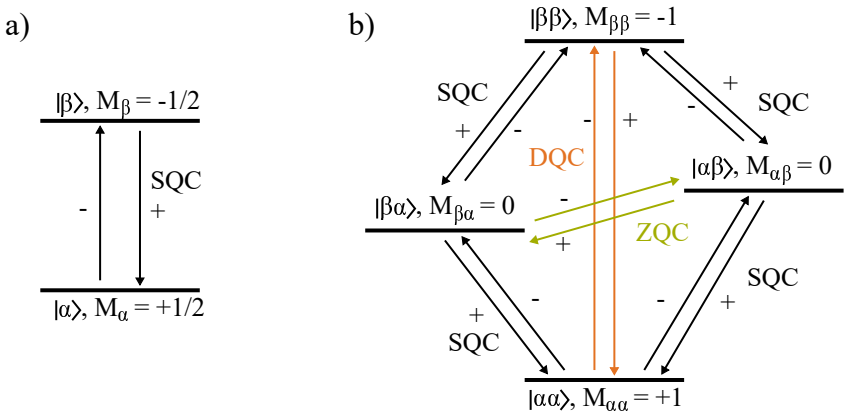

Figure 2.3: Energy levels of the spin systems. a) Energy levels of a single spin-$\frac{1}{2}$ system. b) Energy levels of coupled spin-$\frac{1}{2}$ pair. The single spin-$\frac{1}{2}$ system has two energy levels separated by the Larmor frequency ω_0. The coupled spin-$\frac{1}{2}$ pair has four energy levels.

For a spin-$\frac{1}{2}$ pair, coupled by an arbitrary coupling mechanism G_{ik} the Hamiltonian $\hat{\mathcal{H}}_0$ is given by the sum of the Zeeman Hamiltonian (equation 2.12) and the Hamiltonian resulting from the coupling mechanism. $\hat{\mathcal{H}}_0$ is given as $\hat{\mathcal{H}}_0 = \omega_{i0}\hat{I}_{iz} + \omega_{k0}\hat{I}_{kz} + 2\pi G_{ik}\hat{I}_{iz}\hat{I}_{kz}$. The eigenstates of this Hamiltonian are the Zeeman product states, which obey the following eigenequations given as

$$\begin{aligned} \hat{\mathcal{H}}_0 \left|\alpha\alpha\right\rangle &= \omega_{\alpha\alpha} \left|\alpha\alpha\right\rangle \qquad & \hat{\mathcal{H}}_0 \left|\alpha\beta\right\rangle &= \omega_{\alpha\beta} \left|\alpha\beta\right\rangle \\ \hat{\mathcal{H}}_0 \left|\beta\alpha\right\rangle &= \omega_{\beta\alpha} \left|\beta\alpha\right\rangle \qquad & \hat{\mathcal{H}}_0 \left|\beta\beta\right\rangle &= \omega_{\beta\beta} \left|\beta\beta\right\rangle , \end{aligned} \tag{2.33}$$

where the eigenvalues correspond to the energy levels of the eigenstates in frequency units such that

$$\begin{aligned} \omega_{\alpha\alpha} &= +\frac{1}{2}\omega_{i0} + \frac{1}{2}\omega_{k0} + \frac{1}{2}\pi G_{ik} \qquad & \omega_{\alpha\beta} &= +\frac{1}{2}\omega_{i0} - \frac{1}{2}\omega_{k0} - \frac{1}{2}\pi G_{ik} \\ \omega_{\beta\alpha} &= -\frac{1}{2}\omega_{i0} + \frac{1}{2}\omega_{k0} - \frac{1}{2}\pi G_{ik} \qquad & \omega_{\beta\beta} &= -\frac{1}{2}\omega_{i0} - \frac{1}{2}\omega_{k0} + \frac{1}{2}\pi G_{ik} \end{aligned} \tag{2.34}$$

Figure 2.3b illustrates the observable energy levels and the corresponding coherences.

2.5 Influence of RF-Pulses and the Rotating Frame

For the sake of computational simplicity in the presence of RF-pulses, a rotating frame with a reference frequency $\omega_{ref} = \omega_{RF}$ is introduced. The frequency ω_{RF} is the frequency of the external RF-field B_1 (see equation 2.13). In the rotating frame, the spins precess with the offset frequency Ω given as

$$\Omega = \omega - \omega_{ref} \tag{2.35}$$

The rotating frame Zeeman Hamiltonian is then given as $\hat{\tilde{\mathcal{H}}}_0 = \Omega_0 \hat{I}_z$. Furthermore, the RF-Hamiltonian $\hat{\mathcal{H}}^{RF}(t)$ (equation 2.14) describing the interaction of spin I_i with the external RF-field simplifies to

$$\hat{\tilde{\mathcal{H}}}_i^{RF} = -\omega_{nut}^i \left(\cos(\phi_p)\hat{I}_{ix} + \sin(\phi_p)\hat{I}_{iy}\right) \tag{2.36}$$

The Hamiltonian is no longer time-dependent. The pulse propagator $\hat{U}$ (see equation 2.7) used to solve the rotating-frame time-dependent Schrödinger equation (see equation 2.6) with $\hat{\mathcal{H}} = \hat{\tilde{\mathcal{H}}}_{RF}$ is given as

$$\hat{U}(\tau_p) = \exp\left(-j\beta_p \left(\cos(\phi_p)\hat{I}_x + \sin(\phi_p)\hat{I}_y\right)\right), \tag{2.37}$$

where the Hamiltonian is applied for a duration τ_p and the flip angle $\beta_p = \omega_{nut}\tau_p$.

2.6 Matrix Representation of the Angular Momentum Operators

The Zeeman eigenstates form the basis for the matrix representation of the spin angular operators. The dimension M of the matrices is equal to the number of eigenstates required to represent the spin state. For a single spin-$\frac{1}{2}$ system, the matrix representation in the Zeeman basis $\{|\alpha\rangle, |\beta\rangle\}$ of the four operators $\frac{1}{2}\hat{1}$, $\hat{I}_x$, $\hat{I}_y$ and $\hat{I}_z$ in natural units (divided by $\hbar$) is given as

$$\begin{aligned} \frac{1}{2}\hat{1} &= \frac{1}{2}\begin{pmatrix} 1 & 0 \\ 0 & 1 \end{pmatrix} \qquad & \hat{I}_x &= \frac{1}{2}\begin{pmatrix} 0 & 1 \\ 1 & 0 \end{pmatrix} \\ \hat{I}_y &= \frac{1}{2j}\begin{pmatrix} 0 & 1 \\ -1 & 0 \end{pmatrix} \qquad & \hat{I}_z &= \frac{1}{2}\begin{pmatrix} 1 & 0 \\ 0 & -1 \end{pmatrix} \end{aligned} \tag{2.38}$$

Furthermore, the shift operators $\hat{I}_+$ and $\hat{I}_-$ are given as

$$\hat{I}_+ = \begin{pmatrix} 0 & 1 \\ 0 & 0 \end{pmatrix} \qquad \hat{I}_- = \begin{pmatrix} 0 & 0 \\ 1 & 0 \end{pmatrix} \tag{2.39}$$

For the sake of consistency, the angular momentum operators are given in natural units throughout this work.

2.7 Ensemble of Identical Spin Systems and the Density Operator

In the theory of product operators, all information about the spin system is contained in the density operator. An ensemble of single spin-$\frac{1}{2}$ systems or coupled spin-$\frac{1}{2}$ pairs describes a large number of magnetically equivalent and independent particles. Each particle is described by its individual superposition state. To calculate macroscopic properties of the system, each particle needs to be treated individually. In general, this is not possible for real systems. To overcome this, the quantum state of the whole system can be conveniently described by the density operator $\hat{\rho}$. This method is based on the properties of the expectation value $\langle\hat{Q}\rangle$ of an observable $\hat{Q}$. Even though the result of a single observation is non-committal, the average over many observations can be expressed as

$$\langle\hat{Q}\rangle = \langle\psi|\,\hat{Q}\,|\psi\rangle = \mathrm{Tr}\{|\psi\rangle\langle\psi|\,\hat{Q}\}, \tag{2.40}$$

where $\mathrm{Tr}\{\cdot\}$ indicates the trace of the argument. The same is valid when an ensemble of N spins is observed. Each single observation is still non-committal but the expectation value is given as the sum of all individual expectation values, such that

$$\langle\hat{Q}\rangle_N = \sum_{i=1}^{N}\langle\psi_i|\,\hat{Q}\,|\psi_i\rangle = \mathrm{Tr}\{\sum_{i=1}^{N}(|\psi_i\rangle\langle\psi_i|)\hat{Q}\} = N\,\mathrm{Tr}\{\hat{\rho}\hat{Q}\}\,, \tag{2.41}$$

where the density operator $\hat{\rho}$ is given as

$$\hat{\rho} = N^{-1}\sum_{i=1}^{N}|\psi_i\rangle\langle\psi_i| = \overline{|\psi\rangle\langle\psi|} \tag{2.42}$$

For the single spin-$\frac{1}{2}$ ensemble the matrix representation of the density operator is given as

$$\hat{\rho} = \begin{pmatrix} \overline{c_\alpha c_\alpha^*} & \overline{c_\alpha c_\beta^*} \\ \overline{c_\beta c_\alpha^*} & \overline{c_\beta c_\beta^*} \end{pmatrix} = \begin{pmatrix} \rho_\alpha & \rho_+ \\ \rho_- & \rho_\beta \end{pmatrix}, \tag{2.43}$$

where ρ_α and ρ_β are the populations of the α and the β state. The difference between the populations indicates the longitudinal spin polarization. Off-diagonal elements (ρ_+ and ρ_-) are the $(+1)$ and (-1) coherences, which always come in conjugate pairs. The density operator for the ensemble spin-$\frac{1}{2}$ pairs is given as

$$\hat{\rho} = \begin{pmatrix} \rho_{\alpha\alpha} & \rho_{\alpha+} & \rho_{+\alpha} & \rho_{++} \\ \rho_{\alpha-} & \rho_{\alpha\beta} & \rho_{+-} & \rho_{+\beta} \\ \rho_{-\alpha} & \rho_{-+} & \rho_{\beta\alpha} & \rho_{\beta+} \\ \rho_{--} & \rho_{-\beta} & \rho_{\beta-} & \rho_{\beta\beta} \end{pmatrix} \tag{2.44}$$

The diagonal elements are again the populations of the eigenstates, whereas the off-diagonal elements state the coherences. There are ten independent matrix entries, as upper and lower triangular matrices are conjungate complex to each other. The order of coherence depends on the difference in the z-angular momentum quantum number ΔM between the two states, connected by the corresponding coherence. As all information about the observables of a spin system is contained in the density operator, it is sufficient to know how the density operator evolves over time. The evolution of the density operator is given as

$$\hat{\rho}(t_2) = \hat{U}(\tau)\hat{\rho}(t_1)\hat{U}(-\tau)\,, \tag{2.45}$$

where $\hat{U}(\tau)$ is the linear operator given in equation 2.8, using the Hamiltonian valid during the interval $\tau = t_2 - t_1$. Furthermore, the density operator can be expressed as a linear combination of operators or product operators. For the single spin-$\frac{1}{2}$ ensemble, the three spin angular momentum operators and the unity operator are required. For more complex systems, product operators are introduced. In the case of the spin-$\frac{1}{2}$ pair, 16 product operators are required.

2.8 Equilibrium Density Operator

A spin system reaches a state of thermal equilibrium with the surrounding after not being disturbed for a certain period of time. In the state of thermal equilibrium all coherences are zero. Only populations are different from zero. The equilibrium density matrix $\hat{\rho}_{eq}$ is given as

$$\hat{\rho}_{eq} = \frac{\exp(-\hat{\mathcal{H}}/kT)}{\mathrm{Tr}\{\exp(-\hat{\mathcal{H}}/kT)\}} = \frac{\exp\left(-\sum_i^N \omega_{i0}\hat{I}_{iz}/kT\right)}{\mathrm{Tr}\{\exp(-\hat{\mathcal{H}}/kT)\}} = \frac{\prod_i^N \exp(-\omega_{i0}\hat{I}_{iz}/kT)}{\mathrm{Tr}\{\exp(-\hat{\mathcal{H}}/kT)\}}, \tag{2.46}$$

where the Hamiltonian $\hat{\mathcal{H}}$ is the chemical shift Hamiltonian (see equation 2.21). Therefore, $\omega_{i0} = -\gamma_i B_0 \left(1 + \delta_i^{iso}\right)$. Rewriting equation 2.46 leads to

$$\hat{\rho}_{eq} = 2^{-N} \prod_{i=1}^{N} (\hat{1} - \zeta_i \hat{I}_{iz}), \tag{2.47}$$

where $\zeta_i = 2\tanh\left(\frac{\hbar\omega_{i0}}{2kT}\right) \approx \frac{\hbar\omega_{i0}}{kT}$ [61]. Terms that are proportional to ζ^n always correspond to an n-spin operator. Power series approximation of equation 2.47 leads to

$$\hat{\rho}_{eq} = 2^{-N}\left(\hat{1} - \zeta\sum_{i=1}^{N}\hat{I}_{iz} + \frac{1}{2}\zeta^2\sum_{i,j=1}^{N}{}'\hat{I}_{iz}\hat{I}_{jz} - \frac{1}{6}\zeta^3\sum_{i,j,k=1}^{N}{}'\hat{I}_{iz}\hat{I}_{jz}\hat{I}_{kz} + ...\right), \tag{2.48}$$

where the prime indicates that the sums do not include multiple indices that are equal. For most NMR experiments it is sufficient to use first order truncation. Considering that $kT >> \hbar\omega_{i0}$, terms containing ζ^n, where $n > 1$ can be neglected. The high temperature approximation, where only terms proportional to ζ^1 are considered leads to a reduced equilibrium density operator

$$\hat{\rho}_{eq}^{HT} = 2^{-N}(\hat{1} - \zeta\sum_{i=1}^{N}\hat{I}_{iz}) \tag{2.49}$$

However, it is not as trivial to argue for the first order truncation, even if the prefactor ζ^n becomes very small. In fact, some experiments show that the two-spin operator terms ($n = 2$) can not be dropped in all cases. Even if the factor ζ^2 is very small, there is an enormous amount of couplings $\hat{I}_{iz}\hat{I}_{kz}$ such that these terms can become comparable in size to $\hat{I}_{iz}$ [53]. On the other hand, higher order terms ($n \geq 3$) are neglected for this discussion as n-spin operators, modulated by the very small factor ζ^n, require to evolve under $n-1$ dipolar interactions in order to become observable again. As the dipolar coupling constant D_{ik}^{n-1} also becomes very small, these terms can surely be neglected for the discussion of iZQC. The second order approximation ($n = 2$) of the equilibrium density matrix $\hat{\rho}_{eq}$ is given as

$$\hat{\rho}_{eq} = 2^{-N}\left(\hat{1} - \zeta\sum_{i=1}^{N}\hat{I}_{iz} + \frac{1}{2}\zeta^2\sum_{i,k=1}^{N}{}'\hat{I}_{iz}\hat{I}_{kz}\right) \tag{2.50}$$

Equilibrium Magnetization

The equilibrium magnetization M_0 can be extracted from the equilibrium density matrix $\hat{\rho}_{eq}$. In case of an N spin-$\frac{1}{2}$ ensemble, M_0 in SI units can be calculated as

$$\begin{aligned} M_0 &= Tr\left[\hat{\rho}_{eq}\gamma\hbar\sum_{i=1}^{N}\hat{I}_{iz}/V\right] = 2^{-N}\frac{\gamma\hbar}{V}Tr\left[\left(\hat{1} - \zeta\sum_{i=1}^{N}\hat{I}_{iz} + \frac{1}{2}\zeta^2\sum_{i,k=1}^{N}{}'\hat{I}_{iz}\hat{I}_{kz}\right)\sum_{i=1}^{N}\hat{I}_{iz}\right] \\ &= 2^{-N}\frac{\gamma\hbar}{V}Tr\left[\sum_{i=1}^{N}\hat{I}_{iz} - \zeta\sum_{i=1}^{N}\hat{I}_{iz}\sum_{i=1}^{N}\hat{I}_{iz} + \frac{1}{2}\zeta^2\sum_{i,k=1}^{N}{}'\hat{I}_{iz}\hat{I}_{kz}\sum_{i=1}^{N}\hat{I}_{iz}\right] \\ &= 2^{-N}\frac{\gamma\hbar}{V}Tr\left[-\zeta\sum_{i,k=1}^{N}\hat{I}_{iz}\hat{I}_{kz}\right] = -2^{-N}\frac{\gamma\hbar}{V}\zeta Tr\left[\sum_{i=1}^{N}\hat{I}_{iz}\hat{I}_{iz}\right] \\ &= -2^{-N}\frac{\gamma\hbar}{V}\zeta\frac{N2^N}{4} = -\frac{N}{V}\frac{\gamma\hbar}{4}\zeta\,, \end{aligned} \tag{2.51}$$

where $\zeta = \frac{\gamma\hbar B_0}{k_B T}$ in case of high temperature approximation. Hence, M_0 depends linearly on B_0. $\hat{I}_z$ and $\hat{\rho}_{eq}$ are given in natural units and V is the sample volume containing N spins. The transformation from line two to line three is valid because the trace of the one- and the three-spin operators here is zero. The second transformation in line three is valid because only two-spin operators of the form $\hat{I}_{iz}\hat{I}_{iz}$ lead to a trace different from zero.

Observable Magnetization

The observable magnetizations $M^+(t)$, corresponding to the $+1$ coherence and $M^-(t)$, corresponding to the -1 coherence can be extracted from the density operator matrix $\hat{\rho}(t)$ in a similar way as shown for the equilibrium magnetization.

$$\begin{aligned} M^+(t) &= Tr\left[\hat{\rho}(t)\gamma\hbar\sum_{i=1}^{N}\left(\hat{I}_{ix} + j\hat{I}_{iy}\right)/V\right] \\ M^-(t) &= Tr\left[\hat{\rho}(t)\gamma\hbar\sum_{i=1}^{N}\left(\hat{I}_{ix} - j\hat{I}_{iy}\right)/V\right] \end{aligned} \tag{2.52}$$

2.9 Coherence Order Classified by Rising and Lowering Operators

Product operators composed of N spins can represent a number of coherences with a coherence order ranging from $p = -N$ to $p = +N$ in integer steps. The coherence order $p \in \mathbb{Z}$ of a particular operator or product operator is defined as how it is affected by a z-rotation of an angle Φ. If an operator or product operator has the coherence order p, the following is valid:

$$\hat{\rho} \xrightarrow{\Phi\hat{I}_z} \hat{\rho}\exp(-jp\Phi)\,, \tag{2.53}$$

where $\hat{\rho}$ is the density operator representation of the corresponding operator or product operator. Operators with coherence order $p = 0$ are defined to be either zero-quantum or populations. It is useful to represent operators or product operators by the lowering operator $\hat{I}_{i-}$ and the raising operator $\hat{I}_{i+}$ given as

$$\begin{aligned}\hat{I}_{i+} &= \hat{I}_{ix} + j\hat{I}_{iy} \xrightarrow{\Omega_{Ii}t\hat{I}_{iz}} \exp(-\Omega_{Ii}t)\hat{I}_{i+} \\ \hat{I}_{i-} &= \hat{I}_{ix} - j\hat{I}_{iy} \xrightarrow{\Omega_{Ii}t\hat{I}_{iz}} \exp(+\Omega_{Ii}t)\hat{I}_{i-},\end{aligned} \tag{2.54}$$

where $\hat{I}_{ix}$ and $\hat{I}_{iy}$ are the in-phase single-quantum operators of spin I_i. $\hat{I}_{i-}$ has only coherence order $p = -1$ and $\hat{I}_{i+}$ has only coherence order $p = +1$. Rearranging equation 2.54 shows that the operators $\hat{I}_{ix}$ and $\hat{I}_{iy}$ consist of an equal mixture of coherence orders $p = \pm 1$. For this work two-spin operators of the form $2\hat{I}_{ix}\hat{I}_{kx}$, $2\hat{I}_{iy}\hat{I}_{ky}$, $2\hat{I}_{ix}\hat{I}_{ky}$ and $2\hat{I}_{iy}\hat{I}_{kx}$ are of high importance. They consist of both, zero- ($p = \pm 0$) and double-quantum coherences ($p = \pm 2$).

$$\begin{aligned}2\hat{I}_{ix}\hat{I}_{kx} &= \frac{1}{2}\left(\underbrace{\hat{I}_{i+}\hat{I}_{k+}}_{p=+2} + \underbrace{\hat{I}_{i-}\hat{I}_{k-}}_{p=-2} + \underbrace{\hat{I}_{i+}\hat{I}_{k-}}_{p=+0} + \underbrace{\hat{I}_{i-}\hat{I}_{k+}}_{p=-0}\right) = \frac{1}{2}\left(\hat{DQ}_x^{IiIk} + \hat{ZQ}_x^{IiIk}\right) \\ 2\hat{I}_{iy}\hat{I}_{ky} &= \frac{1}{2}\left(-\hat{I}_{i+}\hat{I}_{k+} - \hat{I}_{i-}\hat{I}_{k-} + \hat{I}_{i+}\hat{I}_{k-} + \hat{I}_{i-}\hat{I}_{k+}\right) = \frac{1}{2}\left(-\hat{DQ}_x^{IiIk} + \hat{ZQ}_x^{IiIk}\right) \\ 2\hat{I}_{ix}\hat{I}_{ky} &= \frac{1}{2j}\left(\hat{I}_{i+}\hat{I}_{k+} - \hat{I}_{i-}\hat{I}_{k-} - \hat{I}_{i+}\hat{I}_{k-} + \hat{I}_{i-}\hat{I}_{k+}\right) = \frac{1}{2}\left(\hat{DQ}_y^{IiIk} - \hat{ZQ}_y^{IiIk}\right) \\ 2\hat{I}_{iy}\hat{I}_{kx} &= \frac{1}{2j}\left(\hat{I}_{i+}\hat{I}_{k+} - \hat{I}_{i-}\hat{I}_{k-} + \hat{I}_{i+}\hat{I}_{k-} - \hat{I}_{i-}\hat{I}_{k+}\right) = \frac{1}{2}\left(\hat{DQ}_y^{IiIk} + \hat{ZQ}_y^{IiIk}\right)\end{aligned} \tag{2.55}$$

The distinction between positive and negative coherence orders is important. If $p > 0$, it is called a P-type coherence and if $p < 0$ it is called an N-type coherence. Free evolution of the purely zero- and double-quantum operators under the Zeeman Hamiltonian $\hat{H} = \Omega_{Ii}\hat{I}_{iz} + \Omega_{Ik}\hat{I}_{kz}$ leads to

$$\begin{aligned}\hat{I}_{i+}\hat{I}_{k+} &\xrightarrow{\Omega_{Ii}t\hat{I}_{iz}+\Omega_{Ik}t\hat{I}_{kz}} \exp(-j[+\Omega_{Ii}+\Omega_{Ik}]t)\hat{I}_{i+}\hat{I}_{k+} = \exp\left(-j\Omega_{IiIk}^{DQ,P}t\right)\hat{I}_{i+}\hat{I}_{k+} \\ \hat{I}_{i-}\hat{I}_{k-} &\xrightarrow{\Omega_{Ii}t\hat{I}_{iz}+\Omega_{Ik}t\hat{I}_{kz}} \exp(-j[-\Omega_{Ii}-\Omega_{Ik}]t)\hat{I}_{i-}\hat{I}_{k-} = \exp\left(-j\Omega_{IiIk}^{DQ,N}t\right)\hat{I}_{i-}\hat{I}_{k-} \\ \hat{I}_{i+}\hat{I}_{k-} &\xrightarrow{\Omega_{Ii}t\hat{I}_{iz}+\Omega_{Ik}t\hat{I}_{kz}} \exp(-j[+\Omega_{Ii}-\Omega_{Ik}]t)\hat{I}_{i+}\hat{I}_{k-} = \exp\left(-j\Omega_{IiIk}^{ZQ,P}t\right)\hat{I}_{i+}\hat{I}_{k-} \\ \hat{I}_{i-}\hat{I}_{k+} &\xrightarrow{\Omega_{Ii}t\hat{I}_{iz}+\Omega_{Ik}t\hat{I}_{kz}} \exp(-j[-\Omega_{Ii}+\Omega_{Ik}]t)\hat{I}_{i-}\hat{I}_{k+} = \exp\left(-j\Omega_{IiIk}^{ZQ,N}t\right)\hat{I}_{i-}\hat{I}_{k+},\end{aligned} \tag{2.56}$$

where $\Omega_{IiIk}^{DQ,P} = \Omega_{Ii} + \Omega_{Ik} = -\Omega_{IiIk}^{DQ,N}$ and $\Omega_{IiIk}^{ZQ,P} = \Omega_{Ii} - \Omega_{Ik} = -\Omega_{IiIk}^{ZQ,N}$. Therefore, also the distinction between $p = +0$ and $p = -0$ is important when discussing systems where $\Omega_{Ii} \neq \Omega_{Ik}$. For instance, this has to be taken into account in case of heteronuclear spin systems ($\Omega_{Ii} \neq \Omega_{Sk}$) or systems, where the external magnetic field $\boldsymbol{B}_0$ is spatially or temporarily not constant. In these cases, P-type and N-type zero-quantum precession frequencies are not equal such that $\Omega_{IiIk}^{ZQ,P} \neq \Omega_{IiIk}^{ZQ,N}$. The pure double- ($\hat{DQ}_x$, $\hat{DQ}_y$) and zero-quantum operators ($\hat{ZQ}_x$, $\hat{ZQ}_y$) are defined as

$$
\begin{aligned}
\hat{DQ}_x^{IiIk} &= 2\hat{I}_{ix}\hat{I}_{kx} - 2\hat{I}_{iy}\hat{I}_{ky} = \hat{I}_{i+}\hat{I}_{k+} + \hat{I}_{i-}\hat{I}_{k-} \\
\hat{DQ}_y^{IiIk} &= 2\hat{I}_{ix}\hat{I}_{ky} + 2\hat{I}_{iy}\hat{I}_{kx} = -j\left(\hat{I}_{i+}\hat{I}_{k+} - \hat{I}_{i-}\hat{I}_{k-}\right) \\
\hat{ZQ}_x^{IiIk} &= 2\hat{I}_{ix}\hat{I}_{kx} + 2\hat{I}_{iy}\hat{I}_{ky} = \hat{I}_{i+}\hat{I}_{k-} + \hat{I}_{i-}\hat{I}_{k+} \\
\hat{ZQ}_y^{IiIk} &= 2\hat{I}_{iy}\hat{I}_{kx} - 2\hat{I}_{ix}\hat{I}_{ky} = -j\left(\hat{I}_{i+}\hat{I}_{k-} - \hat{I}_{i-}\hat{I}_{k+}\right)
\end{aligned}
\tag{2.57}
$$

Evolution of these multiple-quantum operators under the Zeeman Hamiltonian always leads to precession with N-type and P-type precession frequencies in equal parts. Internal interaction Hamiltonians do never cause the coherence order to change. The coherence order can only be changed by applying external RF-pulses to the spin system. The resulting coherences depend on the current state of the spin system as well as the kind of applied RF-pulse. The only observables of spin I_i are transverse magnetizations, represented by the operators $\hat{I}_{ix}$ and $\hat{I}_{iy}$. These operators contain the observable coherences $p = \pm 1$. Depending on how the complex baseband signal is reconstructed by the receiver, either the coherence order $p = -1$ or $p = +1$ is detected.

2.10 Reduction of Inhomogeneous Broadening in Zero-Quantum Spectra

Inhomogeneous broadening is one of the major limitations for NMR experiments. The spectral line shapes strongly depend on the spatial homogeneity of the external magnetic field B_0, given as

$$
B_0(\boldsymbol{s}) = B_0^{hom} + B_0^{inhom}(\boldsymbol{s})\,, \tag{2.58}
$$

where the homogeneous component B_0^{hom} is constant over the whole sample and the inhomogeneous component $B_0^{inhom}(\boldsymbol{s})$ depends on the spatial position $\boldsymbol{s}$. The corresponding offset frequency $\Omega_x(\boldsymbol{s})$ of spin x is given as

$$
\begin{aligned}
\Omega_x(\boldsymbol{s}) &= \Omega_x^{hom} + \Omega_x^{inhom}(\boldsymbol{s}_x) \\
&= -\gamma_x\left[B_0^{hom} + B_0^{inhom}(\boldsymbol{s}_x)\right]\,,
\end{aligned}
\tag{2.59}
$$

where the chemical shift is included in the gyromagnetic ratio γ_x. As the offset frequency is directly proportional to $B_0^{inhom}(\boldsymbol{s})$, the resulting spectral line broadens. The ZQ frequency $\Omega_{I_iS_j}^{ZQ}(\boldsymbol{s}_{Ii}, \boldsymbol{s}_{Sj})$ between spin I_i at position $\boldsymbol{s}_{I_i}$ and spin S_j at position $\boldsymbol{s}_{S_j}$ is given as

$$
\begin{aligned}
\Omega_{I_iS_j}^{ZQ}(\boldsymbol{s}_{I_i}, \boldsymbol{s}_{S_j}) =& \Omega_I(\boldsymbol{s}_{I_i}) - \Omega_S(\boldsymbol{s}_{S_j}) \\
=& -\gamma_I\left[B_0^{hom} + B_0^{inhom}(\boldsymbol{s}_{I_i})\right] + \gamma_S\left[B_0^{hom} + B_0^{inhom}(\boldsymbol{s}_{S_j})\right] \\
=& B_0^{hom}\left[\gamma_S - \gamma_I\right] + \gamma_S B_0^{inhom}(\boldsymbol{s}_{S_j}) - \gamma_I B_0^{inhom}(\boldsymbol{s}_{I_i}) \\
=& \Omega_I^{hom} - \Omega_S^{hom} + \gamma_S B_0^{inhom}(\boldsymbol{s}_{S_j}) - \gamma_I B_0^{inhom}(\boldsymbol{s}_{I_i}) \\
=& \Omega_{IS}^{ZQ,hom} + \Omega_{I_iS_j}^{ZQ,inhom}(\boldsymbol{s}_{I_i}, \boldsymbol{s}_{S_j})\,,
\end{aligned}
\tag{2.60}
$$

where $\Omega_{I_iS_j}^{ZQ,inhom}(\boldsymbol{s}_{I_i}, \boldsymbol{s}_{S_j})$ is the inhomogeneous component. It depends on the difference between the inhomogeneous field contributions at the positions $\boldsymbol{s}_{I_i}$ and $\boldsymbol{s}_{S_j}$. The smaller the distance between two interacting spins, the smaller the inhomogeneous contribution. Hence, for indirect dipole-dipole couplings, considered a strictly intramolecular phenomenon (see section 2.3.2), the inhomogeneous components are

very small. The higher the distance between two coupled spins, the more likely a higher field deviation. Therefore, ZQCs caused by direct dipole-dipole interactions are expected to show larger inhomogeneous components. In theory interactions might occur between all spin pairs separated more than r_0 (temporal averaging, see section 2.3.2). However, as shown in section 6.2 intermolecular couplings are most efficient at certain distances, adjustable by the pulsed field gradient. Couplings between spins separated by more than the correlation distance d_c do not contribute to the observable signal. Therefore, a strong reduction of the influence of inhomogeneous broadening on ZQCs is also expected for direct dipole-dipole interactions.

2.11 Relaxation

Relaxation is the process of driving the bulk magnetization and hence the individual spins back to equilibrium state. The transverse magnetization decays to zero, whereas the longitudinal magnetization relaxes to a steady state determined by the slight preference of the spins to align with the external field. The energy of interaction with the external field is very small compared to the thermal energy, such that this alignment is highly disrupted due to the thermal motion. As NMR relaxation is usually on a very low time scale, modulation of coherences as well as their detection becomes possible. However, this rather slow process also limits the repetition rate of NMR experiments. Within a natural sample there are various sources of local magnetic fields that add up with the static magnetic field during the period of free precession. These sources are called relaxation mechanisms. For spin$-\frac{1}{2}$ nuclei the dipolar and the chemical shift anisotropy mechanism are most dominant. Furthermore, relaxation due to paramagnetic species can be used for analysis of MNPs (see chapter 5). Dipolar interactions previously explained in section 2.3.2.
It is distinguished between a secular and a non-secular component of relaxation. The non-secular component describes the influence of the transverse component of the local fields, whereas the secular component describes the influence of the longitudinal component.
The non-secular component of the local fields is only effective for the relaxation process if in resonance with the larmor frequency ω_0 of the spins. The required oscillation might be generated due to random thermal motion. As vibrational motions take place at a very fast time scale, only rotational motions need to be considered. In liquid environments, each collision of molecules changes their orientation only slightly. This is called rotational diffusion. The time dependence of this random process is described by the correlation function $G(\tau)$ given as

$$G(\tau) = \frac{1}{N}\sum_{i=i}^{N} B_{loc,i}(t)B_{loc,i}(t+\tau) \approx \overline{B_{loc}^2}\exp(-|\tau|/\tau_c)\,, \tag{2.61}$$

where τ_c, the time constant of this process is called the rotational correlation time. In average, the rotational orientation changes by 1 rad after the period τ_c. The larger the molecules under consideration, the larger τ_c. The corresponding correlation frequency is then given as $\omega_c = 1/\tau_c$. $B_{loc,i}(t)$ is the local field experienced by spin I_i at time t, depending on the correlation time τ_c and the number N of spins in the sample. As $B_{loc,i}(t)$ is a stationary random process, $G(\tau)$ does not depend on t. The exact form of $B_{loc,i}(t)$ and hence $G(\tau)$ strongly depends on the way of interaction between the molecule and the lattice. For spherical molecules and a solvent simply described by a medium with a certain viscosity, $B_{loc,i}(t)$ turns out to be exponential such that the approximation in equation 2.61 becomes valid. $\overline{B_{loc}}$ is the ensemble average at $\tau = 0$. As the absolute value is of no interest here the reduced correlation

function $g(\tau) = G(\tau)/\overline{B_{loc}^2}$ is introduced. The effective amount of motion for relaxation is qualified by the reduced spectral density $j(\omega)$ given as

$$g(\tau) \circ\!\!-\!\!- j(\omega_0) = \frac{2\tau_c}{1+\omega_0^2\tau_c^2} \approx \begin{cases} 2\tau_c & \omega_0\tau_c << 1 \\ \frac{2}{\omega_0^2\tau_c} & \omega_0\tau_c >> 1 \end{cases} \tag{2.62}$$

Random motions, where $\omega_c = \omega_0$ show most spectral contribution at ω_0 and are thus most efficient in terms of relaxation. For $\omega_0\tau_c << 1$, the fast motion regime applies, where as for $\omega_0\tau_c >> 1$, the slow motion regime applies. Regarding transverse relaxation, also the secular contribution of the local fields need to be considered. These arise due to the z-components of the local fields that alter the local larmor frequency. Secular contributions do not depend on the larmor frequency ω_0. In fact, the secular component linearly depends on the correlation time τ_c. Consequently, the larger τ_c, the more effective is the secular part of the transverse relaxation. The effect of longitudinal and transverse relaxation on the longitudinal and transverse magnetization is given as

$$\begin{aligned} M_z(t) &= \left(M_z(0) - M_z^0\right)\exp(-R_1 t) + M_z^0 \\ M_{xy}(t) &= M_{xy}(0)\exp(-R_2 t)\,, \end{aligned} \tag{2.63}$$

where R_1 and R_2 are the longitudinal and transverse relaxation rates. If assumed that a local field, generated by an arbitrary source has equal mean square values in each direction, the relaxation rates are given as

$$\begin{aligned} R_1 &= \gamma^2\overline{B_{loc}^2} j(\omega_0) = \begin{cases} 2\gamma^2\overline{B_{loc}^2}\tau_c & \omega_0\tau_c << 1 \\ \frac{2\gamma^2\overline{B_{loc}^2}}{\omega_0^2\tau_c} & \omega_0\tau_c >> 1 \end{cases} \\ R_2 &= \gamma^2\overline{B_{loc}^2}\tau_c + \frac{1}{2}R_1 = \begin{cases} 2\gamma^2\overline{B_{loc}^2}\tau_c & \omega_0\tau_c << 1 \\ \gamma^2\overline{B_{loc}^2}\tau_c & \omega_0\tau_c >> 1 \end{cases} \end{aligned} \tag{2.64}$$

Hence, in the fast motion regime (small particles) both relaxation processes behave equally. However, in the slow motion regime R_1 decays to zero, whereas R_2 increases. An easy way for a coarse estimation of R_1 and R_2 are the inversion recovery and the CPMG [66] sequence, respectively.

2.12 NMR Signal Shape

In generally, NMR signals are described as very narrow-banded time domain signals with a carrier frequency ω_0. For the sake of simplicity, only external interactions with the field B_0 are considered for this discussion. Furthermore, the bandwidth is only considered phenomenologically by a finite decay rate R in the time domain. The observable magnetization $M^+(t)$ (see equation 2.52) is then given as

$$M^+(t) = M_0 A(t)\exp(j(\omega_0 t + \phi_0))\,, \tag{2.65}$$

where M_0 is the equilibrium magnetization (see equation 2.51), $A(t)$ the envelope and ϕ_0 the phase. In general, the signal envelope $A(t)$ can either take the FID shape $A_{FID}(t)$ or the spin echo shape $A_{ECHO}(t)$. These are given as

$$\begin{aligned} A_{FID}(t) &= \exp(-Rt)u(t) \quad \circ\!\!-\!\!- \quad A_{FID}(\omega) &&= \frac{R}{R^2+\omega^2} - j\frac{\omega}{R^2+\omega^2} \\ A_{ECHO}(t) &= \exp(-R|t|) \quad \circ\!\!-\!\!- \quad A_{ECHO}(\omega) &&= \frac{2R}{R^2+\omega^2}, \end{aligned} \tag{2.66}$$

where $u(t)$ is the unity step function. The given spectra $A_{FID}(\omega)$ and $A_{ECHO}(\omega)$ are valid for $R > 0$ [67]. The spectra of the overall observable magnetizations $M^+_{FID}(t)$ and $M^+_{ECHO}(t)$ are given as

$$\begin{aligned} M^+_{FID}(\omega) &= M_0 \exp(j\phi_0)\left[\frac{R}{R^2+(\omega-\omega_0)^2} + j\frac{-(\omega-\omega_0)}{R^2+(\omega-\omega_0)^2}\right] = \exp(j\phi_0)\left[\mathcal{A}+j\mathcal{D}\right] \\ M^+_{ECHO}(\omega) &= M_0 \exp(j\phi_0)\left[\frac{2R}{R^2+(\omega-\omega_0)^2}\right] = 2\exp(j\phi_0)\mathcal{A} \end{aligned} \tag{2.67}$$

The expression $\mathcal{L}(\omega,\omega_0,R) = \mathcal{A}+j\mathcal{D}$ is called the complex Lorentzian, where $\mathcal{A}$ is the absorption mode Lorentzian lineshape and $\mathcal{D}$ is the dispersion mode Lorentzian lineshape. The shape of the absorption mode peak is preferable in NMR spectroscopy as it is more narrow than the dispersion mode line. Hence, in most cases the receiver is adjusted to maximize the absorption mode line. The linewidth of the absorption mode peak is defined as $\omega_{LW} = \omega(\mathcal{A}^- = \frac{1}{2}) - \omega(\mathcal{A}^+ = \frac{1}{2}) = 2R$.

3 NMR Devices

In this chapter, two low-cost NMR spectrometers are presented. The application focus of the devices varies strongly. On the one hand side, the MiCSMaP spectrometer, presented in section 3.1 is used for the determination of relaxation processes, especially under the influence of MNPs. Integration of the system in the particle synthesis reactor and the results are presented in chapter 5. On the other hand, the SoC-based spectrometer, presented in section 3.2 is a standalone spectrometer designed for more sophisticated and versatile NMR experiments, including two-dimensional zero-quantum measurements presented in chapter 6. Moreover, the SoC-based system allows for the inclusion of the required pulsed field gradients. However, the general architecture of both devices is analog [64, 65, 68, 69]. The common block diagram is shown in figure 3.1.

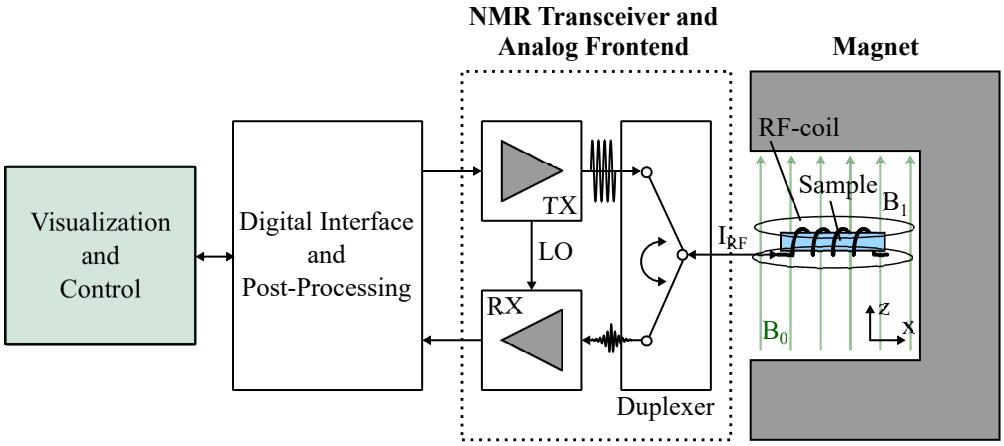

Figure 3.1: General block diagram of an NMR spectrometer.

The NMR probe coil (*RF-coil*), containing the *sample* is located in a static magnetic field $\boldsymbol{B}_0 = B_0 \boldsymbol{e}_z$, where $\boldsymbol{e}_z$ is the unit vector in z-direction. Throughout this work $\boldsymbol{B}_0$ is always assumed to be aligned with the z-axis. The external field is generated by two kinds of permanent magnets (see section 4.1). A palm-size 0.5 T magnet an 1 T magnet, usually used for small-animal MRI. The influence of the external field $\boldsymbol{B}_0$ on the spins is described by the Zeeman Hamiltonian (see section 2.3.1 and section 2.4). The corresponding Zeeman splitting in frequency units for a single spin-$\frac{1}{2}$ is equal to the Larmor frequency ω_0 (see equation 2.32). Macroscopically, this results in a net magnetization vector $\boldsymbol{M}_0 = M_0 \boldsymbol{e}_z$ caused by the sum of the individual nuclear spin moments. The spin system can be manipulated by the application of RF-pulses, transformed into an oscillating magnetic field $\boldsymbol{B}_1$ by the NMR probe head. The efficiency of the RF-pulses on the spin system is maximized if $\boldsymbol{B}_1$ is perpendicular to $\boldsymbol{B}_0$. Therefore, the solenoid probe coils used throughout this work (see chapter 4) are inserted such that the coils central axis (x-axis) is perpendicular to the static field. The Hamiltonian describing the interaction of the square wave RF-pulses and the spin system is given in section 2.3.1. The evolution of the corresponding spin system under the influence of this Hamiltonian is described in the rotating frame in section 2.5. Applying RF-pulses tilts the magnetization depending on the pulse duration as well as the amplitude of $\boldsymbol{B}_1$ (see section 2.5).

As the amplitude of $\boldsymbol{B}_1$ is much smaller than B_0, RF-pulses are required to be in close resonance with the nuclear spin precession frequency ω_0 in order to efficiently flip the magnetization. Here, a single *RF-coil* is used for both, the manipulation of the spin system and the signal acquisition. Therefore, a *duplexer* is required to interconnect either the transmitter (*TX*) or the receiver (*RX*) with the *RF-coil*.
The NMR transmitter generates RF-pulse sequences with a center frequency ω_{RF} close to ω_0 and hence excites the spin system. After excitation, the duplexer interconnects the probe coil with the NMR receiver such that the resulting NMR signal is acquired. The general appearance of an NMR signal is described in section 2.12 as a very weak, narrow-banded, time-domain signal with a center frequency ω_0. Inter-spin couplings as well as inhomogeneous broadening and chemical shifts are not relevant for this discussion. Only a single probe coil is used. Therefore, the received signal at the output of the probe coil is real. Besides a constant factor, which is neglected for the following discussion, the received signal $s(t)$ is given as

$$s(t) = \mathrm{Re}\{M^+(t)\} \approx A(t)\cos(\omega_0 t + \phi_0) \tag{3.1}$$

The amplitude $A(t)$ and the phase ϕ_0 state important NMR parameters that allow for conclusions about molecular structures, dynamics and interactions in the sample. Both are required to be estimated by the receiver. Furthermore, the restoration of the complex component $\mathrm{Im}\{M^+(t)\}$, which is part of the observable magnetization $M^+(t)$ is required in order to allow for frequency discrimination in the direct dimension of the spectrum. This is achieved by synchronous demodulation (see section 3.2.2), where the local oscillator (*LO*) used for frequency conversion in the receiver *RX* is synchronous to the rotating frame (see section 2.5) and hence the transmitter frequency ω_{RF}. ω_{RF} is set to the estimate of the Larmor frequency ω_0 such that $\omega_{LO} \approx \omega_0$. Only a single frequency conversion about ω_{LO} is performed by multiplication of $s(t)$ by $\exp(-j(\omega_{LO}t + \phi_{LO}))$. The phase ϕ_{LO} is adjusted as required (see section 2.12) for optimization of the absorptive spectral component. This results in a complex baseband signal $s_{BB}(t)$ given as

$$s_{BB}(t) = \frac{1}{2}A(t)(1 + \exp(-j(2\omega_0 t + 2\phi_0))) \approx \frac{1}{2}A(t), \tag{3.2}$$

where the approximation of the mixing by-products at the frequency $\omega = 2\omega_0$ is valid due to the frequency response of the subsequent low-pass filter. As real NMR spectra show multiple peaks with multiple carrier frequencies $\omega_{0,i}$, a more accurate description of the baseband frequency is given by the offset frequency $\Omega_i = \omega_{0,i} - \omega_{LO}$.
Implementation of direct, synchronous demodulation can be either performed in the digital or in the analog domain. The SoC-based spectrometer presented in section 3.2 uses a direct sampling receiver architecture, where the complete synchronous demodulation is implemented digitally in the *PL* of the SoC. In the analog domain the signal is only amplified and band-limited at the RF-band. On the other hand, the MiCSMaP spectrometer, presented in section 3.1 performs the direct conversion in the analog domain. Band-limitation as well as amplification are performed at RF and baseband. Little digital processing power is required such that a µC, mostly used for controlling and data forwarding is sufficient.

3.1 MiCSMaP Spectrometer

The application focus of this spectrometer is the investigation of relaxation processes, especially under the influence of MNPs as well as the corresponding reagents during the particle synthesis process. This includes T_1-, T_2- and T_2^*-relaxation. As the spectrometer is integrated into the synthesis reactor (see

chapter 5), a small outline permanent magnet with a magnetic flux density of 0.5 T (see section 4.1) resulting in a Larmor frequency of about 21 MHz is used. The main focus of this design was to develop a small-outline, low-cost spectrometer, integrable into this synthesis reactor. Thereby, the ability of automated sample exchange, required for quasi on-line measurements as well as the automated determination of transversal (r_2) and longitudinal relaxivities (r_1) is particularly important. Furthermore, in-flow measurements were desired. The corresponding NMR *probe head*, fulfilling these requirements is presented in section 4.3. An overview of the system is given in figure 3.2, where figure 3.2a shows a block diagram of the system, figure 3.2b a screenshot of the user interface, figure 3.2c a picture of the device and figure 3.2d a 3D-model of the corresponding NMR *probe head* described in more detail in section 4.3.

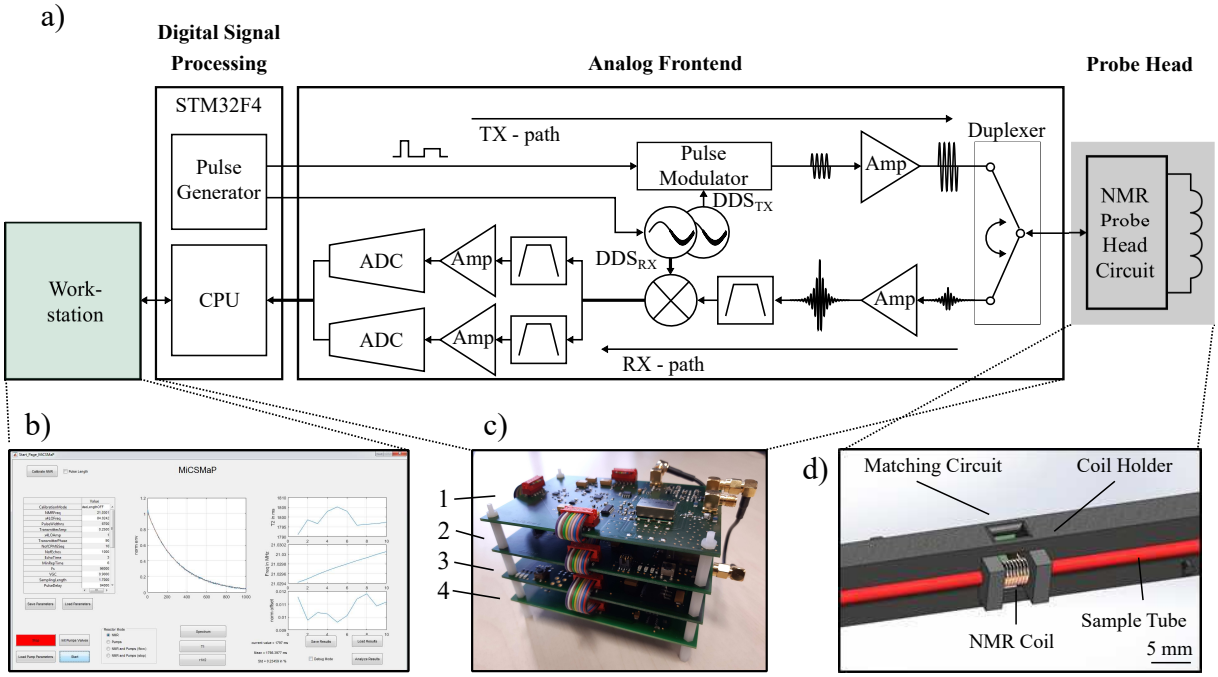

Figure 3.2: Overview of the MiCSMaP spectrometer. a) Block diagram of the MiCSMaP spectrometer. b) The user interface for spectrometer controlling, data visualization and post-processing. c) A picture of the spectrometer. (1) Receiver board, (2) Digital signal processing board including the main µC, (3) Transmitter board and (4) Power supply board. d) 3D-model of the corresponding flow-through probe head.

The basic functionality of the spectrometer is illustrated by the block diagram shown in figure 3.2a. The spectrometer is controlled from the user interface running on a *workstation* via TCP/IP. A screenshot of the corresponding graphical user interface is shown in figure 3.2b. Here, sequence data is generated and the results are visualized and post-processed if required. The spectrometer itself is further functionally divided in two parts - *digital signal processing* and *analog frontend*. Physically, these are separated on four printed circuit boards. A picture of the whole device is shown in figure 3.2c. The *analog frontend* including the NMR transceiver is again separated in a receiver board (1) and a transmitter board (3). Both are controlled from the *digital signal processing* board (2) and supplied by the power board (4). The *digital signal processing* board is further responsible for communication with the user application. Sequence specific user data is forwarded from the user application via the network to the main µC (STM32F429, STMicroelectronics) on the *digital signal processing* unit. The main µC configures the

pulse generator module which in turn controls the transmitter as well as the receiver. Square wave pulse sequences are generated by the concatenation of multiple timer modules integrated in the µC. Furthermore, a dual-channel DDS IC with quadrature outputs, placed on the transmitter board is adjusted by the *pulse generator* on the fly. This allows for arbitrary phase RF-pulse generation. Moreover, the *pulse generator* controls the acquisition window as well as the *duplexer*.
The synchronous direct-conversion transceiver architecture is realized mostly in the analog domain. Core of the analog transceiver circuit is a frequency synthesizer realized by the two-channel quadrature DDS (AD9959, Analog Devices), which is controlled by the *pulse generator*. Thereof, one channel (DDS_{TX}) is connected with the *pulse modulator*, where amplitude modulation of a real sinusoid with a square wave pulse sequence forms the low-power RF-pulses. The second, complex channel (DDS_{RX}) is connected with a quadrature demodulator (see figure 3.2a). Both synthesizer outputs (DDS_{TX} and DDS_{RX}) are synchronized and the phase offsets can be adjusted individually such that the absorptive spectral component is maximized if desired (see section 2.12). Amplitude and phase offset resolution are 14-bit and 10-bit, respectively, whereas the frequency tuning word has 32 bits. With a DDS core frequency of 500 MSPS this results in a frequency resolution of less than 120 mHz. A 5-tap elliptic, equiripple low-pass filter with a 3 dB cutoff frequency of 200 MHz at the outputs of the DDS smooths the signal. Furthermore, the DDS has an analog input for the amplitude modulation with the square wave signal generated by the timer modules of the main µC. The timers are updated via DMA in order to allow for arbitrarily designed pulse sequences.
The resulting low level RF-pulses are amplified by a two-step amplification chain. The output power stage (ADA4870, Analog Devices) achieves about 30 dBm (1 W) at 21 MHz. A pin diode-based duplexer circuit [70] interconnects the transmitter output with the NMR *probe head* (see section 4.3). At 21 MHz the pin diodes provide an attenuation of 48 dB between the receiver and the transmitter. In transmit case, the attenuation between the transmitter and the NMR *probe head* is 0.6 dB. Same is valid for the acquisition period. The corresponding driver circuit floods and empties the intrinsic region of the pin diode with charge carriers, resulting in a switching time of about 40 µs [71].
During signal acquisition, the NMR *probe head* is interconnected with the receiver. The receiver has a preselector with a 3 dB-bandwidth of 4.6 MHz around the center frequency of 21 MHz. Due to the direct-conversion receiver principle, amplification takes place at RF and at baseband. At RF, a variable gain amplifier allows the amplification to range from 7.5 dB to 55 dB (AD8331, Analog Devices). The first amplifier is a low noise amplifier with a noise figure of 4.1 dB in case of actively matching the input to a source impedance of 50 Ω. The signal is then converted to baseband by means of a quadrature demodulator (AD8333, Analog Devices). The differential current outputs are transformed by transimpedance amplifiers with a feedback resistor of 39 kΩ. Finally, a differential amplifier drives the sigma-delta data converter (PCM4202, Texas Instruments) with an oversampling ratio of 384. As the narrow-banded signal is sampled at baseband, an audio converter with sampling frequency of 96 kHz is sufficient. Two synchronous channels allow for quadrature sampling of frequencies ranging from -48 kHz to 48 kHz. Subsequently, the data is transfered, post-processed and visualized by the user application.

3.2 SoC-Based Spectrometer

The standalone, SoC-based spectrometer has a more versatile application focus in terms of pulse sequence design than the MiCSMaP relaxometer presented in section 3.1. Core of the system is the SoC that integrates an ARM-based processing system (*PS*) with the versatility and parallelization of FPGAs. The system allows for arbitrary square wave pulse sequence design including the ability of switching

pulsed field gradients. It is designed for frequencies ranging from 20 MHz up to 50 MHz. Throughout this work, the spectrometer is used in combination with a 1 T permanent magnet (see section 4.1). This results in a Larmor frequency of about 45 MHz. An overview of the system is given in figure 3.3, where figure 3.3a shows a block diagram of the system, figure 3.3b a screenshot of the graphical user application, figure 3.3c a picture of the device and figure 3.3d a 3D-model of the corresponding, gradient-capable NMR probe head described in more detail in section 4.4.

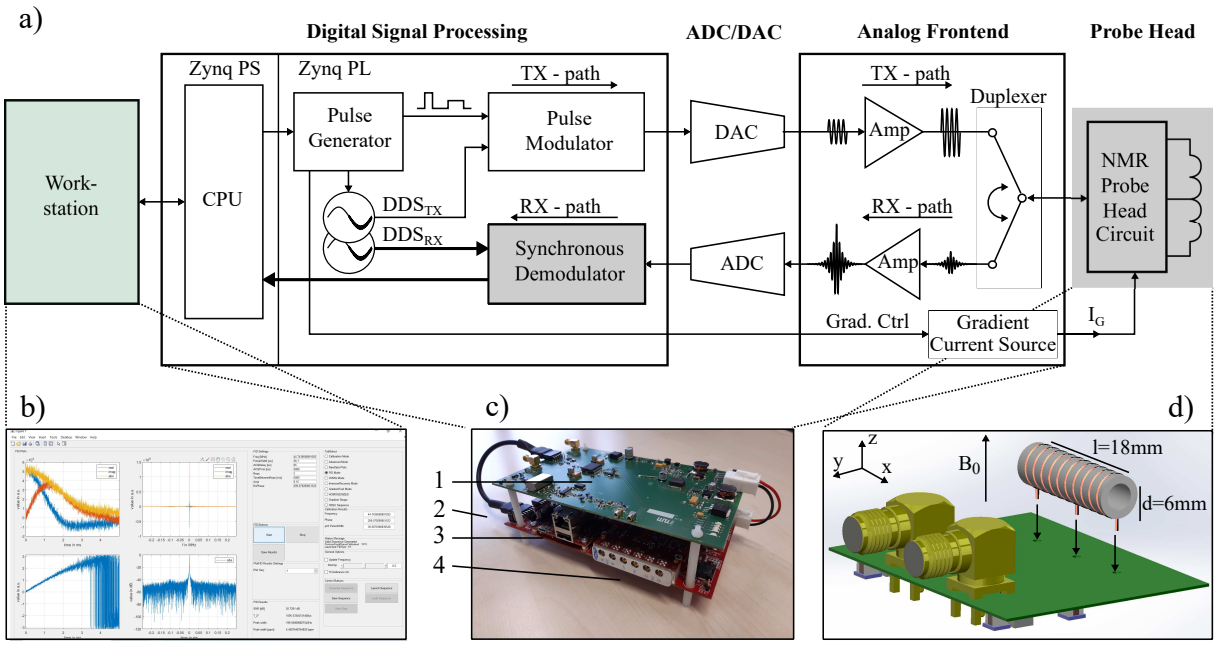

Figure 3.3: Overview of the SoC-based spectrometer. a) Block diagram of the SoC-based spectrometer. b) The user application for spectrometer controlling, data visualization and post-processing. c) A picture of the spectrometer. (1) Analog NMR transceiver, (2) FMC carrier board connecting the MicroZed board and the FMC150, (3) MicroZed board including the SoC and (4) FMC150 data converter board. d) 3D-model of the corresponding gradient-capable probe head.

The basic functionality of the SoC-based NMR spectrometer is illustrated in figure 3.3a. It is controlled by the custom-designed user application (MathWorks, Matlab) running on a *workstation* via TCP/IP. A screenshot of the corresponding graphical user interface is shown in figure 3.3b. After sequence data generation, the results are visualized and post-processed if required. The spectrometer itself is functionally divided in three parts - a *digital signal processing* unit, a data conversion (*ADC/DAC*) unit and an *analog frontend*. These functional groups are physically separated on three circuit boards, shown in figure 3.3c. The *digital signal processing* unit is based on the Zynq SoC (Xilinx, XC7Z010-1CLG400C) mounted on an embeddable system-on-module (Avnet, AES-Z7MB-7Z010-G) (3). The SoC itself comprises an ARM-based *PS* integrated with 28 nm *PL*. The *PL* is equivalent to the Artix-7 series. Physical connection of the *ADC/DAC* board (Abaco Systems, FMC150 FPGA Mezzanine Card) (4) to the *digital signal processing* unit is established by the MicroZed FMC Carrier Card (Avnet, AES-MBCC-FMC-G) (2). The *analog frontend* (1), characterized in detail in section 3.2.3 is directly connected to the *ADC/DAC* board. Furthermore, the *duplexer* circuit on the *analog frontend* interconnects either the *RX-path* or the *TX-path* with the NMR *probe head* (see figure 3.3d). This is discussed in detail in section 4.4.
The *PS* is mainly applied for communication with the *workstation* and data storage throughout this work, whereas digital signal processing and pulse sequence generation is performed on the *PL* (see figure 3.3a).

The *PL* is separated in a *pulse modulator* (*TX-path*), a *synchronous demodulator* (*RX-path*), and two synchronized direct digital synthesizers (DDS) [72], DDS_{TX} for the *TX-path* and DDS_{RX} for the *RX-path*. The *synchronous demodulator* is covered in detail in section 3.2.2. Core of the NMR transceiver is the *pulse generator*, which controls all components according to the desired NMR sequence (see section 3.2.1). Furthermore, a square wave signal depending on the desired pulse durations, delays and amplitudes is generated. The square wave signal modulates the amplitude of a carrier signal generated by DDS_{TX}. This results in a digital RF-pulse sequence at the output of the *pulse modulator*. Frequency and phase settings of DDS_{TX} are updated by the *pulse generator* on the fly after each RF-pulse. Subsequently, the digital RF-pulse sequence is transfered to the analog domain (*DAC* sampling frequency 491.52 MHz) on the *ADC/DAC* board. The RF-pulses are amplified and interconnected with the NMR *probe head* on the *analog frontend* (see section 3.2.3). After sample excitation the *probe head* is interconnected with the *RX-path* of the *analog frontend*. In the analog domain, the NMR signal is only amplified and band-limited prior to high speed digitalization (*ADC* sampling frequency 245.76 MHz). The complex sinusoid of DDS_{RX} is required for frequency conversion performed in the *synchronous demodulator* (see section 3.2.2). The resulting baseband signal is transfered back to the user application.
Figure 3.4 illustrates the spectrometer system with special focus on the *PS*. Furthermore, the clock distribution network originating from the *FMC150* board and the interfaces between the functional units are emphasized.

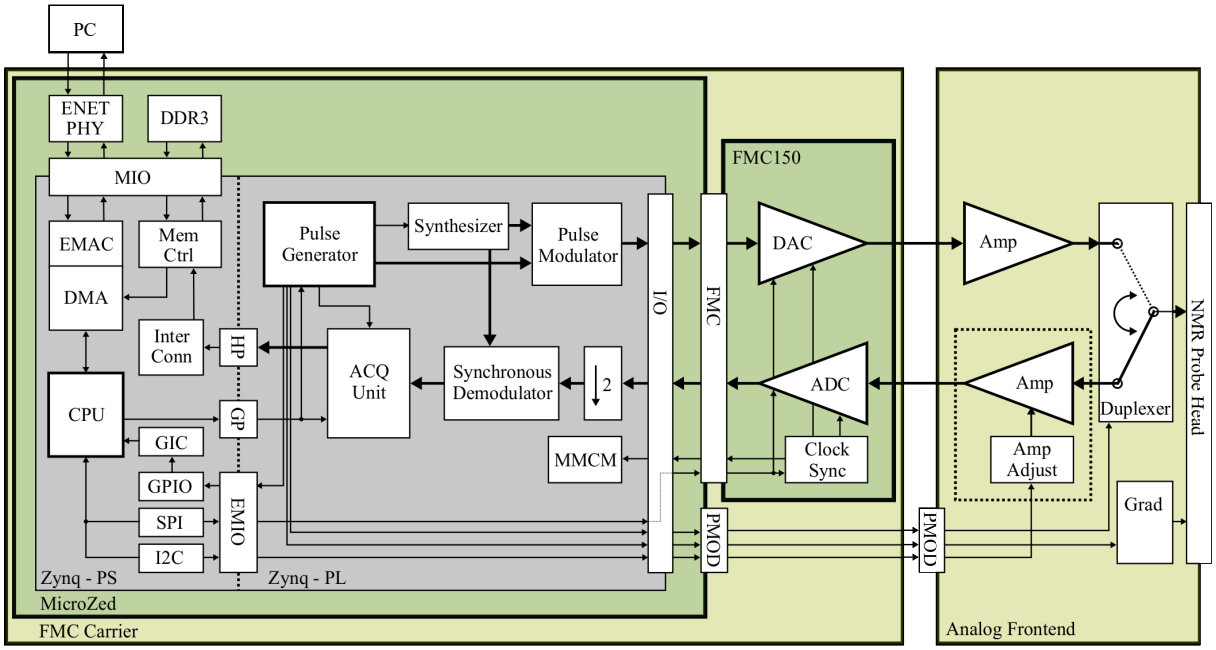

Figure 3.4: Detailed overview of the SoC-based spectrometer. The SoC-based spectrometer is composed of four circuit boards - the MicroZed board, the FMC carrier board, the FMC150 data conversion board and the analog frontend.

The *PS* includes ARMs Dual-Core Cortex A9 *CPUs*, clocked at 866 MHz [73]. L1 and L2 cache as well as a 256kB On-Chip memory and a memory controller (*Mem. Ctrl*) accessing external *DDR3* memory are integrated. Furthermore, the system supports external static memory like QSPI that allows automated system booting after start-up (not included in figure 3.4). Peripherals like *SPI*, *I2C* and *GPIO* enable communication with external chips. Network access is given by an integrated ethernet mac

(*EMAC*) with built-in *DMA* allowing for TCP/IP networking by the LWIP stack. *PS* peripherals can be routed either to the Multiplexed I/Os (*MIOs*) for off-chip communication or to the Extended Multiplexed I/Os (*EMIOs*), which allow for communication with the *PL*. The system runs with the FreeRTOS real time operating system. Only 28k logic cells, 17.6k look-up tables (LUTs), 35.2k flip-flops (FFs) and a total of 2.1 MB of integrated block RAM are integrated in the rather small *PL*. Furthermore, 80 DSP slices, required by the digital NMR transceiver circuit are available. *PS* and *PL* are connected via the AXI high-performance (*HP*) and the AXI general-purpose (*GP*) ports. Both are memory mapped interfaces, where the *HP* port is specifically designed for high data throughput.
The SoC is embedded on the *MicroZed* board. This board includes ICs like QSPI and *DDR3* memory as well as connectors allowing for access to the pin banks of the SoC. Moreover, networking is supported by an ethernet physics *ENET PHY* and a RJ45 connector with integrated magnetics. Debugging is performed via an USB-UART bridge as well as a JTAG configuration port.
The *FMC carrier* provides a connection between the *FMC150* and the *MicroZed* board via a low pin count (LPC) *FMC* interface. Besides the data converters, the *FMC150* also contains a clock synchronizer (*Clock Sync*) (CDCE72010, Texas Instruments), providing the clock tree for the entire system. Synchronous clocks are supplied for the data converters as well as the Mixed-Mode Clock Manager (*MMCM*) module in the *PL*. The *MMCM* in turn generates a clock of 245.76 MHz driving the *I/O* modules as well as the system clock of 122.88 MHz driving the entire *PL*.
The data converters are connected to the *analog frontend* that is characterized in more detail in section 3.2.3. The *analog frontend* realizes the analog NMR transceiver circuit, where amplification of the RF-pulses and the resulting NMR signals takes place. Furthermore, a duplexer circuit interconnects either the transmitter or the receiver with the *NMR probe head*. The gain of the receiver is digitally adjustable via *I2C*. For pulse sequences requiring field gradients, a switchable current source, connected to the center tap of the NMR *probe head* (see section 4.4) is included. All these modules are controlled by the *pulse generator* discussed in detail in section 3.2.1. The *pulse generator* also controls the *ACQ Unit*, the *frequency synthesizer* and *clock sync*.
After start-up, the system is in waiting mode. The desired user sequence commands are transfered via TCP/IP to the *PS*. The *PS* distributes the data via AXI over a *GP* port to the *pulse generator* (see section 3.2.1) and the acquisition unit (*ACQ Unit*). The *pulse generator* triggers the *ACQ Unit* such that only data acquired during the desired acquisitions periods is transfered. The *ACQ Unit* transfers the complex baseband output of the *synchronous demodulator* (see section 3.2.2) via AXI over the *HP* port to the *PS*. The data transfer is performed by an DMA core [74], realized in the *PL*. The *PS* contains a PL/memory interconnect (*InterConn*) such that the data can be routed directly to *Mem. Ctrl* and further to the *DDR3* memory without interfering the *CPU*. When data is available in the *DDR3* memory, the *CPU* is triggered by DMA interrupts to initiate data transfers to the *PC*. The data transfer from memory to the *EMAC* is performed by the built-in *DMA*. Furthermore, the *pulse generator* triggers interrupts if new commands are required. These interrupts are routed to the general interrupt controller (*GIC*) of the *PS* with highest priority (see section 3.2.1).

3.2.1 Digital Signal Processing - Pulse Generator

The *pulse generator* (see figure 3.3 and figure 3.4) is the core of the digital NMR transceiver. It is responsible for the generation of the desired RF-pulse sequences in terms of the number of pulses, pulse durations as well as the delays between the pulses. Furthermore, the individual phases, frequencies and amplitudes of each pulse are adjusted via DDS_{TX}. DDS_{TX} is in turn controlled by the *pulse generator* on

the fly. Frequency and phase of the LO-signal required for downconversion in the *synchronous demodulator* are controlled by the *pulse generator* via DDS_{RX}. Adjustments are individual for each acquisition period. Number and duration of acquisition periods as well as duplexer and gradient switching are also controlled by the *pulse generator*. The whole subsystem runs at the system frequency (122.88 MHz). The corresponding block diagram of the custom-designed IP is shown in figure 3.5.

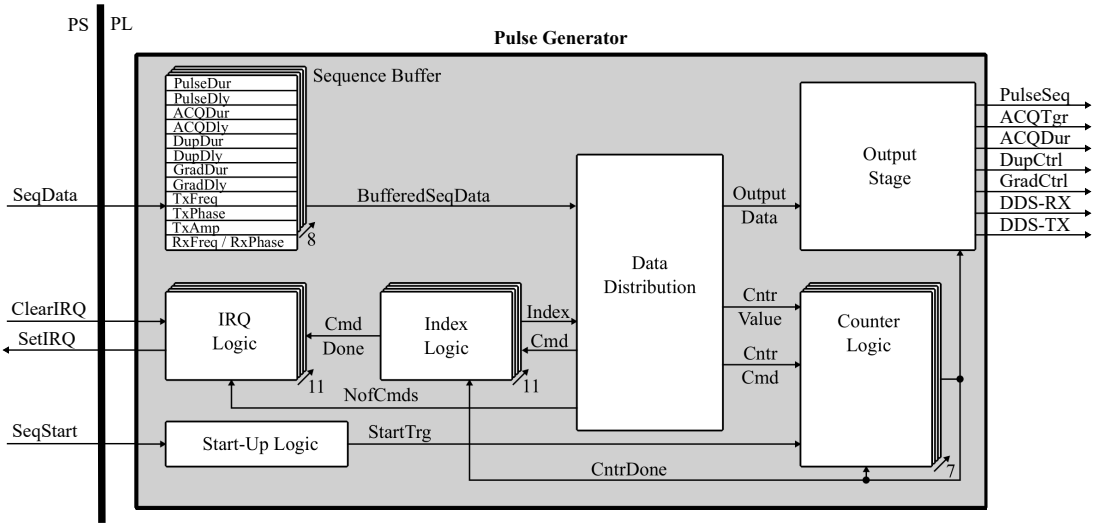

Figure 3.5: Block diagram of the pulse modulator

The *pulse generator* is configured prior to each pulse sequence. Configuration data (*Seq. Data*) is sent via a *GP* port from the *PS* to the integrated *sequence buffer*. Therefore, an AXI lite interface allowing for memory mapped data transfer is implemented. The buffer holds all twelve parameters required to fully describe a pulse sequence.
Timing of the square wave pulse sequence is described by the pulse durations (*PulseDur*) and the delays (*PulseDly*) between the individual pulses. After each pulse an acquisition period starting after an acquisition delay (*ACQDly*) for an acquisition duration (*ACQDur*) can be initialized. Furthermore, duplexer delay (*DupDly*) and duration (*DupDur*) need to be set. If required, gradients can be switched on during the sequence. Timing is adjusted by gradient delay (*GradDly*) and duration (*GradDur*). Pulse frequencies and phases can be set individually by the parameters pulse frequency (*PulseFreq*) and pulse phase (*PulsePhase*). In addition, the pulse amplitude (*PulseAmp*) can be set individually. The receiver parameters including the receiver frequency (*RxFreq*) and receiver phase (*RxPhase*) are valid throughout the whole sequence.
The *sequence buffer* is therefore divided into twelve individual parameter buffers (see figure 3.5). Each parameter buffer again contains eight 64-bit registers, further divided in a 32-bit control word and a 32-bit parameter word. The buffer depth of eight allows one parameter to change eight times during the sequence. If a parameter needs to be changed more than eight times during one pulse sequence, the *IRQ logic* triggers an interrupt such that new configuration data is requested from the *PS*. *IRQ logic* will be discussed later. Pulse sequences like the CPMG sequence that contain repeating patterns, can be configured by a repetition counter value in the control word of each register. The current parameter command is repeated until the repetition counter reaches zero. Therefore, only one command is required for a series of identical pulses. The receiver buffer containing *RxFreq* and *RxPhase* has only one register as these parameters are valid for the entire sequence.

Timing of the *pulse generator* is based on the *counter logic*. The *counter logic* consists of seven individual 32-bit counters, one for each of the following sequence timing parameters: *PulseDur*, *PulseDly*, *ACQDly*, *DupDur*, *DupDly*, *GradDur* and *GradDly*. Each counter contains three inputs, consisting of a *CntrValue* input (32-bit), a trigger input (either *CntrDone* or *StartTrg*) and a *CntrCmd* input as well as one output. The *CntrCmd* input contains information about the timers to be triggered after the corresponding timer expires. Pulse sequence timing is achieved by the way these timers trigger each other. After *SeqStart* rises, the *start-up logic* triggers the *PulseDly*-timer. The *PulseDly*-timer counts from its corresponding *CntrValue* (from the first *PulseDly* register) to zero. After expiration, the *CntrDone* flag triggers the *PulseDur*-timer. The *PulseDur*-timer counts from its corresponding *CntrValue* (from the first *PulseDur* register) to zero. After expiration, the *CntrDone* flag triggers the other timers depending on the *CntrCmd* bits of the first *PulseDur* register. The *CntrDone* flag of the *PulseDur*-timer can trigger the *ACQDly*-timer, the *DupDly*-timer and the *GradDly*-timer, which are all configured with their first register entries. Furthermore, it can retrigger the *PulseDly*-timer, which is configured with the second register value. If a delay counter expires, the corresponding duration timer is always triggered. The acquisition duration (*ACQDur*) is not directly controlled by the *pulse generator*. Instead, the desired acquisition duration is forwarded to the *ACQ unit* (see figure 3.4) along with the corresponding trigger signal (*CntrDone* of the *ACQDur*-timer) to indicate the beginning of the acquisition period.
Furthermore, the *CntrDone* signals trigger the *index logic*. The *index logic* consists of eleven individual index modules corresponding to the sequence parameters with a buffer depth of eight. Each *CntrDone* flag triggers one or more index modules. For instance, after expiration of the *PulseDly*-timer the index module corresponding to the *PulseDly* parameter is triggered. Each time an index module is triggered the corresponding repetition value is lowered by one. If the repetition counter of the corresponding parameter reaches zero, the *index logic* increases the *index* of the corresponding parameter by one. The current command is considered to be done. The *data distribution* unit, in turn forwards the second register of this parameter to the corresponding modules.
Frequency and phase of the RF-pulses and the LO are also set by the *pulse generator*. Two AXI-stream master interfaces, *DDS-TX* for DDS_{TX} and *DDS-RX* for DDS_{RX} transfer a frequency word concatenated with a phase word to the corresponding DDS. These values are taken from the corresponding registers of the *sequence buffer*. The index module controls which register is chosen. As DDS_{RX} is only configured once prior to the first pulse, no index module is required. The index values required for DDS_{TX} are controlled by two index modules. These index modules are triggered by the *CntrDone* of the *PulseDur*-timer, because after one RF-pulse is done DDS_{TX} can be configured for the next pulse. Same is valid for the RF-pulse amplitude. The *PulseAmp* index module is also triggered by the *CntrDone* flag of the *PulseDur*-timer.
Every time the index for a certain parameter increases, the *IRQ logic* is triggered by the *CmdDone* flag. Each index module triggers the corresponding IRQ module such that each IRQ module corresponds to exactly one parameter. The particular IRQ module decides depending on the overall number of commands (*NofCmds*, also in the command word of the corresponding register) whether a new command is required for that parameter. If a new command is required, an interrupt (*SetIRQ*) is initiated. The *PS* initiates a data transfer to *sequence buffer* and clears the interrupt (*ClearIRQ*), if successful.
Finally, the *output stage* states the interface from the *pulse generator* core to the *PL*. The *PulseSeq* signal is a binary square wave pulse train generated depending on the *CntrDone* signals of the *PulseDur*-timer and the *PulseDly*-timer. The amplitudes of each pulse are given by the corresponding *PulseAmp* value at the current *index*. Subsequently, this signal is modulated by the TX carrier signal, generated by DDS_{TX} in the *Pulse Modulator* (see figure 3.4). The *ACQ unit* is triggered by the *ACQTrg* depending on the

CntrDone of the *ACQDly*-timer. Furthermore, the current *ACQDur* is forwarded to the *ACQ unit*. The duplexer control signal *DupCtrl* and the gradient control signal *GradCtrl* are generated by the corresponding *CntrDone* flags of the duplexer and gradient timers.

3.2.2 Digital Signal Processing - Synchronous Demodulator

The *synchronous demodulator* transforms the narrow-band NMR signals described in section 2.12 to baseband and performs a reduction of the sampling frequency. The output data is transfered to the *PS* by the *ACQ unit* (see figure 3.4). An overview of the direct-sampling *synchronous demodulator*, illustrating the decimation stages and the quadrature demodulator is shown in figure 3.6.

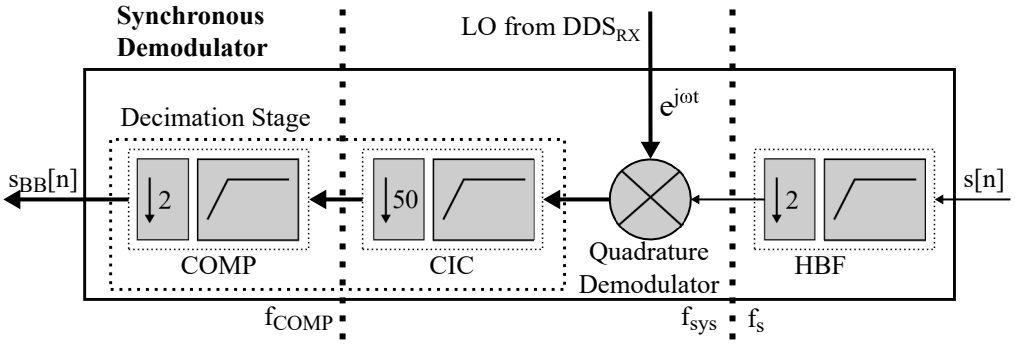

Figure 3.6: Overview of the synchronous demodulator.

The signal $s(t)$ given in equation 3.1 at the output of the *RX-path* of the analog receiver (see figure 3.3a) is sampled at a frequency f_s of 245.76 MHz and a bit width of 14. The resulting discrete signal $s[n]$ is the input signal of the *synchronous demodulator*. A desired downsampling ratio of 200 results in a sampling frequency of 1.2288 MHz at the output. The frequency responses of the filters are configured such that the 3 dB baseband bandwidth is about 400 kHz and the allowable input frequencies range up to 50 MHz.
Decimation is separated in three steps. At first, a decimation of two is performed. The required band limitation is achieved by the half-band filter (*HBF*). The reduced sampling frequency of 122.88 MHz coincidences with the *PL* system frequency, which greatly simplifies the system design. Frequency conversion by the LO-signal generated by *DDS$_{RX}$* to the baseband is followed by another decimation of 100 (*decimation stage*). The *Decimation Stage* is separated in a decimation by 50, band-limited by a cascaded-integrator-comb filter (*CIC*) and a subsequent decimation by two. The corresponding final filter stage (*COMP*) also compensates for the passband characteristics of the *CIC* filter.

Half-Band Filter

The first decimation stage is required to lower the sampling frequency from the ADC sampling frequency (254.76 MHz) to the *PL* system frequency (122.88 MHz). This greatly relaxes the FPGA timing requirements. The (*HBF*) limits the bandwidth prior to downsampling by a factor of two. Passband frequency, normalized to the input sampling frequency f_s is chosen to be 0.2. This results in a frequency of approximately 49.2 MHz. The normalized Nyquist frequency corresponding to a decimation by two is 0.25. This allows for a transition band ranging from 0.2 to 0.3. The corresponding stopband ranges from 0.3 to 0.5. Same considerations are valid for negative frequencies.
The filter taps are designed by use of the Remez-Algorithm [75], which minimizes the maximum error to

the target frequency response. This algorithm designs a linear phase (h_{HBF} is symmetric, see figure 3.7a), equiripple FIR filter. Figure 3.7a shows the impulse response h_{HBF} with 47-taps.

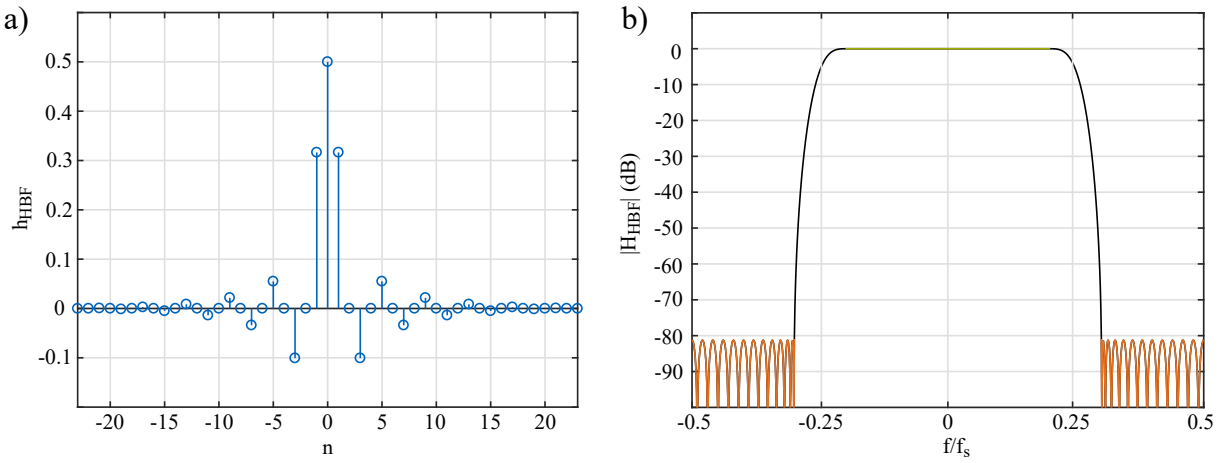

Figure 3.7: Characteristics of the half-band filter (HBF). a) Impulse response of HBF. b) Frequency response of HBF.

The frequency response is shown in figure 3.7b. Due to the strictly real coefficients (see figure 3.7a), the frequency response of the low-pass filter is symmetric about zero. The passband is highlighted in green, the stopband in red and the transition band in black. Furthermore, the frequency is symmetric about the Nyquist frequency (0.25). Thus, passband and stopband frequencies are inherently equidistant. Moreover, passband (0.0015 dB) and stopband ripple are equal in amplitude. The minimum stopband attenuation is slightly greater than 80 dB. Furthermore, FPGA resources are reduced by using a half-band filter topology. This allows for the implementation in polyphase form, because almost every second coefficient is equal to zero. The number of output samples to be calculated is only half the number of input samples. For implementation on the FPGA, the coefficients are truncated to 18 bits. The FIR IP core [76] recognizes the half-band characteristics of the coefficient set and implements the FIR filter using the resource saving half-band filter structure. This way only eight DSP slices are required.

Quadrature Demodulator

Frequency conversion to baseband is performed by a *quadrature demodulator* (see figure 3.6). The corresponding LO-signal (*LO*) is generated by DDS_{RX} (see figure 3.3). The spectrum of the RF-signal with a center frequency ω_0 (see equation 3.1) is shifted to ≈ 0 Hz by use of a complex multiplication. DDS_{RX} runs synchronous to DDS_{TX} such that the demodulation of the NMR signals is synchronous to the RF-pulses. The phase of DDS_{RX} is adjusted to maximize the absorptive component of the spectrum like shown in section 2.12. Using complex multiplication, the irretrievable overlapping of mirrors and noise with the user spectrum is avoided. The bit width of the complex exponential is 18, whereas the input has a bit width of 16. The complex output signal is truncated to a bit width of 16. It shows frequency components at baseband and at $2\omega_0$, whereas the frequency component at $2\omega_0$ needs to be attenuated by the subsequent filter stages (see figure 3.6).

Decimation Stage

In general, high sampling rate changes require very narrow-band filters. These filters show long impulse responses and hence require many fast multipliers. A very resource efficient way to achieve high decimation ratios is to use *CIC* filters [77, 78]. This filter architecture comes with the drawback of a strong droop in the passband region as well as strong sideband lobes, which lead to insufficient stopband attenuation. Compensation of these drawbacks is achieved by the subsequent compensation stage (*COMP*). The main *decimation stage* is therefore split into two cascaded stages. The first with a decimation factor of 50, band-limited by a *CIC* filter and the second with a decimation factor of two, band-limited by the *COMP* filter. Hence, the overall decimation performed at baseband is 100.

CIC Filter

The *CIC* filter is designed for a decimation ratio of 50. The corresponding Nyquist frequency, normalized to the system frequency f_{sys} is 0.01. The normalized passband frequency is desired to be 0.0016, which corresponds to a frequency of 196.6 kHz. Critical frequency bands that fold back in the user spectrum after downsampling range from $0.02k$-0.0016 to $0.02k$+0.0016, where $k \in \mathbb{N}$.
The basic blocks of a CIC decimation filter are integrators and combs. N integrators are cascaded and run at f_{sys}, followed by N combs that run at $f_{sys}/50$. In between both stages is a rate change of 50. The system response $H(z)$ of the CIC low-pass filter is given as

$$H(z) = \frac{(1-z^{-50})^N}{(1-z^{-1})^N} = \left(\sum_{k=0}^{49} z^{-k}\right)^N, \tag{3.3}$$

where the numerator corresponds to the comb section and the denumerator to integrator section. Equation 3.3 shows that CIC filters behaves like N cascaded FIR filters, each with a rectangular impulse response of length 50 even though the integrator itself shows an instable IIR behavior. No multiplications and hence no DSP slices are required because the impulse response only consists of unit-amplitude coefficients. The symmetry of the impulse response leads to a linear-phase and hence a constant group delay. Evaluation of equation 3.3 at $z = \exp\left(j2\pi f/f_{sys}\right)$ results in the magnitude frequency response $|H(f)|$, where

$$|H_{CIC}(f)| = \left[\frac{\sin\left(50\pi f/f_{sys}\right)}{\sin\left(\pi f/f_{sys}\right)}\right]^N \tag{3.4}$$

Equation 3.4 has zeros at $0.02k$, which coincidences with the center frequency of the critical frequency bands folding back to the user band after downsampling. The number N of cascaded *CIC* stages controls the order of the zeros and hence the attenuation of frequency bands in close proximity. Therefore, increasing N also increases the passband droop and is thus narrowing the bandwidth of the filter. The stronger the droop the tighter the requirements for the subsequent compensation filter to flatten the passband. A suitable trade-off for N was found to be 4. The resulting magnitude frequency response is shown in figure 3.8a, whereas figure 3.8b shows a zoom of the frequency band around the first zero. The passband is highlighted in green and the stopband in red.
The slope of the magnitude of the frequency response is very high. Still, as the passband is very narrow (0.0016) the aliasing bands around the zeros are narrow. Therefore, the attenuation of these bands is still strong. Due to the monotonic decay of the local maxima between the zeros, only the first zero ($k = 1$) ranging from 0.0184 to 0.0216 needs to be considered (see figure 3.8b). The area is highlighted in red

and shows an attenuation of larger than 83 dB. At higher order zeros the attenuation is even stronger. Figure 3.8b also shows the droop in the passband, highlighted in green. This droop is to be compensated by the subsequent decimation filter (*COMP*).

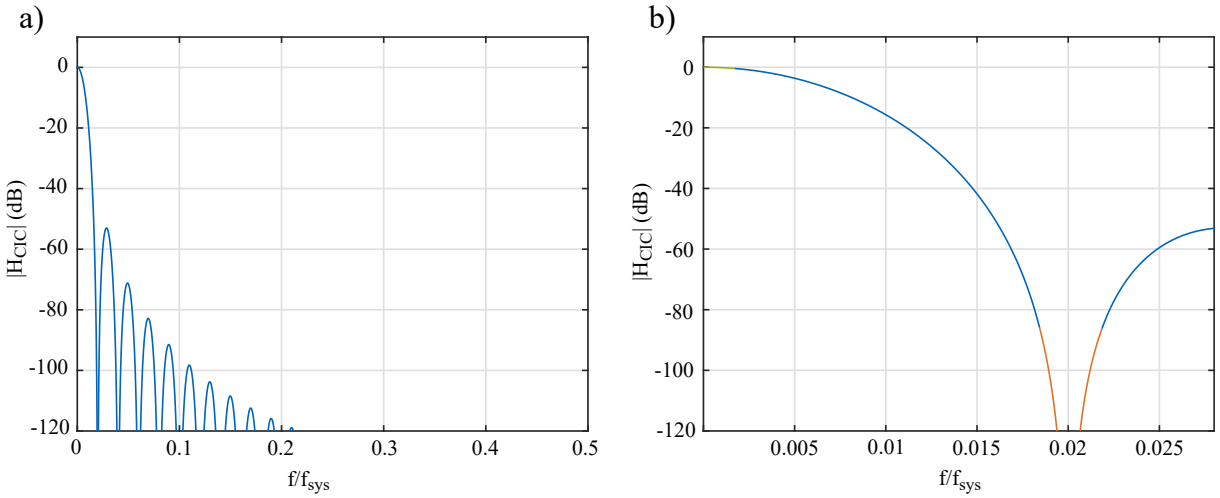

Figure 3.8: Characteristics of the CIC filter. a) Frequency response of the CIC filter. b) Zoom of the frequency response of the CIC filter around the first zero. The passband is highlighted in green and the stopband in red.

Compensation Filter

The passband droop of the *CIC* filter (see figure 3.8) is compensated by the subsequent compensation filter *COMP*. Furthermore, aliasing due to the following rate change of two is prevented. Due to the previous rate change of $R = 50$ the compensation stage runs at a sampling frequency $f_{COMP} = f_{sys}/50$. The corresponding Nyquist frequency, normalized to the input frequency f_{COMP} is 0.25. A normalized passband corner frequency of 0.08 corresponds to a frequency of 196.6 kHz. Hence, the allowed transition band ranges from 0.08 to 0.42.

The frequency response of the ideal compensation filter is desired to result in an ideal frequency response H_{IDEAL} of the concatenated filters that is one in the passband and zero in the stopband (see figure 3.9a, light blue line). The small angle approximation ($\sin(x) \approx x$) simplifies the mathematical description of the passband droop of the *CIC* filter given in equation 3.4 to $[Rsinc(f/f_{COMP})]^N$. Therefore, the desired amplitude response A_d of the *COMP* filter is given as

$$A_d(f) = \begin{cases} 1/|H_{CIC}(f)| = [Rsinc(f/f_{COMP})]^{-N} & 0 < f < 0.08 \\ x & 0.08 \leq f < 0.42 \\ 0 & 0.42 \leq f < 0.5 \end{cases} \tag{3.5}$$

The FIR filter design is based on minimizing the non-weighted, least square error ϵ, where

$$\epsilon = \int_0^{\pi} |A(\omega) - A_d(\omega)|^2 d\omega \tag{3.6}$$

between the amplitude responses $A(\omega) = |H(\omega)|$ and $A_d(\omega)$ [79, 80]. The results are shown in figure 3.9. Figure 3.9a, figure 3.9b and 3.9c each show the amplitude responses $|H_{CIC}|$, $|H_{COMP}|$,

$|H_{ALL}|$ and $|H_{IDEAL}|$, where $|H_{ALL}|$ is the overall amplitude response given as $|H_{CIC}||H_{COMP}|$ for different areas of focus. The amplitude of the *CIC* filter is equivalent to figure 3.8 but is normalized to f_{COMP} for convenience reasons. The red crosses in figure 3.9a show the smallest attenuation in the aliasing bands. The right one corresponds to the *CIC* decimation filter, where lowest attenuation is on the lower end of the band around the first zero. The left one corresponds to the response of the concatenated filter $|H_{ALL}|$ at the lower end of the stopband (0.42). The corresponding attenuation is about 87 dB and 83 dB, respectively.

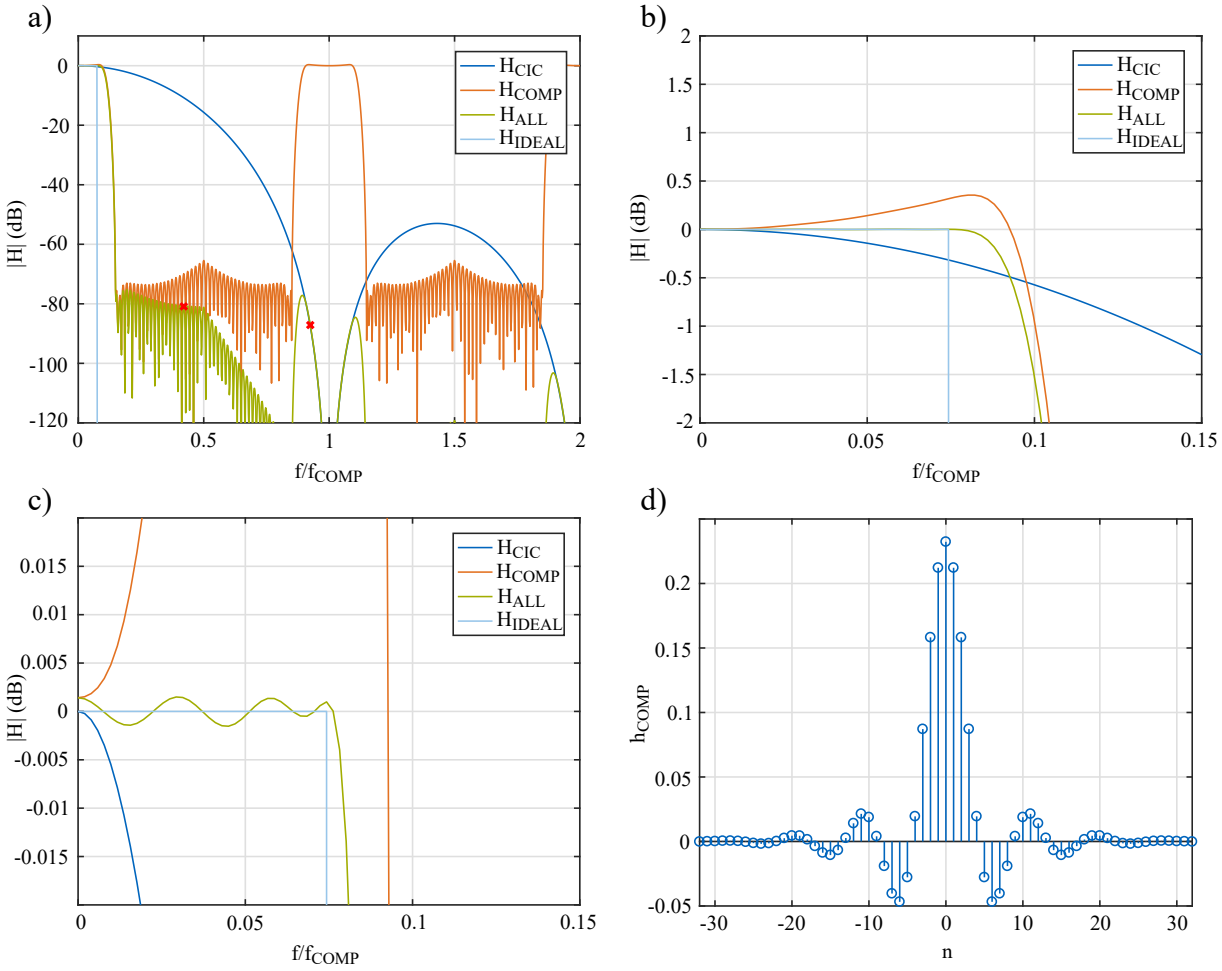

Figure 3.9: Characteristics of the main decimation stage composed of a concatenation of the COMP filter and the CIC filter. H_{ALL} is the frequency response of the concatenated filters, whereas H_{IDEAL} is the desired overall frequency response. a) Frequency response of the main decimation stage. The red crosses indicate the frequencies with lowest attenuation folded back to the user bands after decimation. b) Zoom of the frequency response with focus on the passband droop. c) Zoom of the frequency response with focus on the ripple residue in the passband. d) Impulse response of the COMP filter.

Besides stopband attenuation, this decimation stage also compensates for the passband droop introduced by the *CIC* filter. This is illustrated in figure 3.9b, showing a zoom to the passband. The color coding is equivalent to figure 3.9a. The droop at the passband edge of $|H_{CIC}|$ is already about 0.35 dB. On the other hand, $|H_{COMP}|$ amplifies in the passband such that the amplitude response of $|H_{ALL}|$ of the concatenated filters is very close to 0 dB for frequencies smaller than 0.08. Still, there is a small deviation from zero, illustrated by the zoom shown in figure 3.9c. The residual ripple is less than 0.0015 dB in the

passband. The corresponding 65-taps impulse response h_{COMP} is shown in figure 3.9d.

Evaluation of the Synchronous Demodulator

The amplitude response of the synchronous demodulator is investigated in two steps. A signal generator is directly connected to the *ADC* input (see figure 3.3a). In a first step, the LO frequency and the input frequency of the sinusoid, generated by the signal generator (0.2 V_{RMS}, 1 dBm) are kept equal. This results in a baseband frequency of 0 Hz. The input frequency is swept from 1 MHz up to 80 MHz. This allows for the investigation of the amplitude response of the *HBF* filter (see figure 3.6). Figure 3.10a shows the amplitude response for positive frequencies. The characteristics match well with the theoretical results shown in figure 3.7. The low-pass filter shows a 3 dB cutoff frequency of 58 MHz. In a second step, the input frequency, generated by the signal generator (0.2 V_{RMS}, 1 dBm) is fixed to 30 MHz. The LO frequency is swept from -0.6 MHz to 0.6 MHz. Thus, the amplitude response of the main decimation stage, composed of the *CIC* and *COMP* filter can be investigated. The results shown in figure 3.10b match well with the theoretical amplitude response shown in figure 3.9a. The concatenated decimation stages show bandpass characteristics with a lower 3 dB cutoff frequency of -260 kHz and an upper 3 dB cutoff frequency of 260 kHz. For both measurements, the noise floor is at about -60 dB.

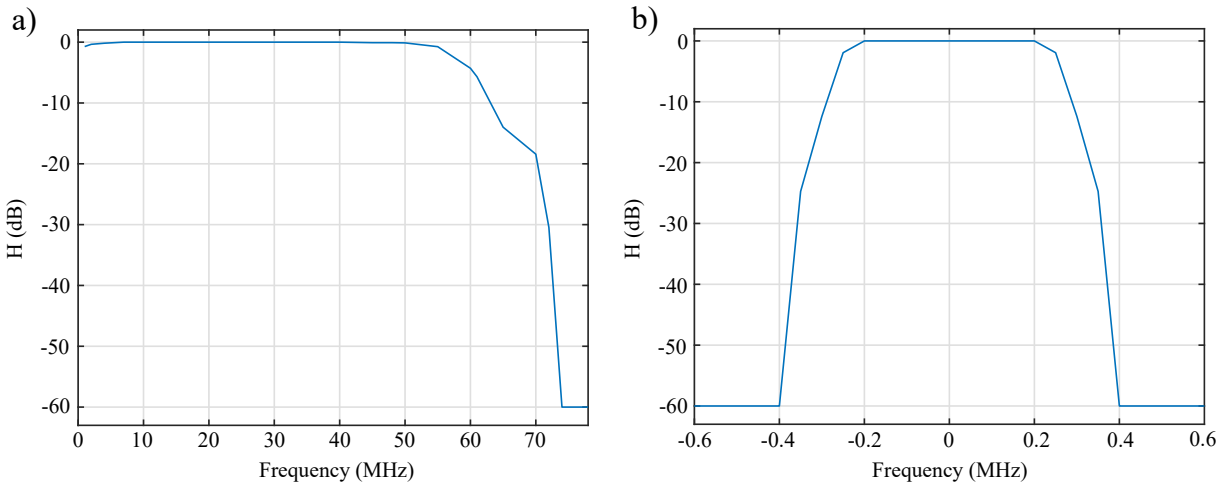

Figure 3.10: Evaluation of the synchronous demodulator. a) Amplitude response of the HBF filter. b) Amplitude response of the main decimation stage composed of the CIC filter and the COMP filter

3.2.3 Analog Frontend

The *analog frontend* (see figure 3.1a) works as an NMR transceiver. Basically, the NMR transceiver consists of an *RX-path*, a *TX-path* and a *duplexer*. Figure 3.11a and figure 3.11b show the amplitude response of the *RX-path* and the *TX-path*, respectively.
The *duplexer* interconnects either the *RX-path* or the *TX-path* with the NMR *probe head*. It is composed of two concatenated single pole, double throw switches, each with an isolation of more than 40 dB between the opened ports. In the reception case, the *TX-path* is isolated from the *RX-path* by more than 80 dB. In the transmit case, the *RX-path* is isolated from the *TX-path* by more than 40 dB. The insertion loss is less than 0.2 dB in both cases.

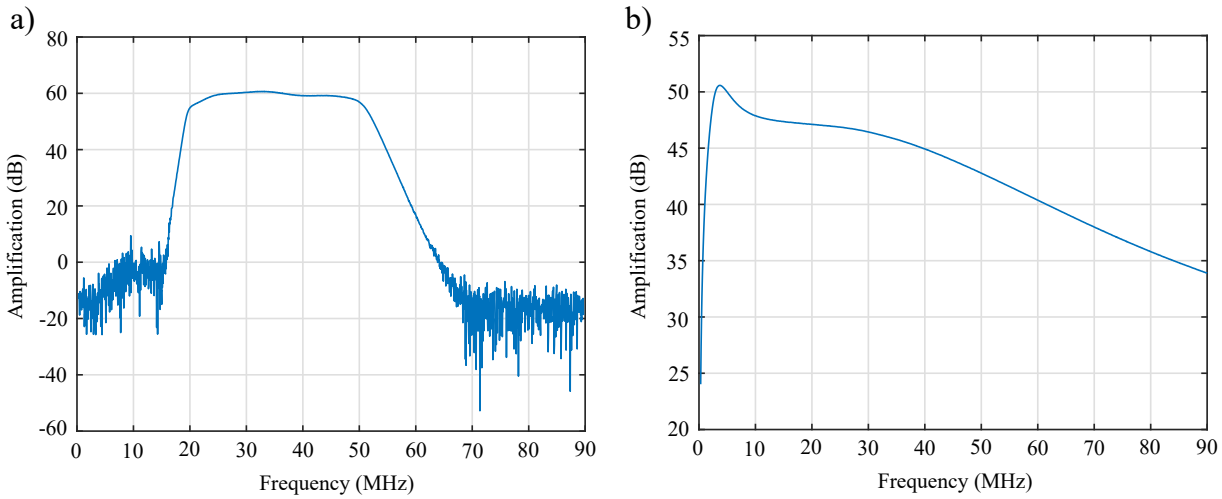

Figure 3.11: Frequency responses of the transceiver board

The NMR receiver has an adjustable gain ranging from 47.5 dB up to 95 dB. For investigating the *RX-path*, the duplexer is held in reception mode. The transmit power of the sweep generator of the network analyzer is set to -30 dBm. Additionally, the transmitter is attenuated by 40 dB such that the receiver input power is -70 dBm. The receiver gain is set to about 60 dB. The results in terms of S_{21} are presented in figure 3.11a. The frequency response shows bandpass characteristics with a lower and an upper 3 dB cutoff frequency of 21 MHz and 50 MHz, respectively. The input amplifier, dominant for the overall noise figure [81] has a noise figure of 2.6 dB (ADL5536, Analog Devices).
For investigating the *TX-path*, the duplexer is held in transmit mode. The transmit power of the sweep generator of the network analyzer is set to -15 dBm. The detector input of the network analyzer is protected by an additional attenuation of 40 dB. Figure 3.11b shows the amplitude response of the transmitter. The total gain of the transmitter is highly frequency dependent. At the desired frequency of 45 MHz, the gain is about 42 dB resulting in a maximum output power of about 27 dBm. As there are no bandpass filter structures in the *TX-path*, the decay with the frequency is rather linear (0.25 dB/MHz). This decay is mainly due to the RF characteristics of the power amplifier (ADA4870, Analog Devices) like the slew rate or the gain bandwidth product. The transmitter is suited for frequencies ranging from 3 MHz up to 50 MHz. Frequencies higher than 50 MHz lead to a decrease in maximum output power if total harmonic distortion is kept constant.

3.3 Spectrometer Discussion

Throughout this work, two NMR spectrometers were designed - the MiCSMaP spectrometer (see section 3.1) and the SoC-based spectrometer (see section 3.2). Due to their different field of focus, the designs differ greatly from each other. The application focus of the MiCSMaP device is on the determination of relaxation processes using a small outline permanent magnet with a magnetic flux density of 0.5 T. T_1-, T_2- and T_2^*-relaxation times require the spectrometer to perform inversion recovery, CPMG [66] and FID measurements, respectively. In comparison, the SoC-based spectrometer (see section 3.2) is more versatile in terms of pulse sequence design. The pulse generator (see section 3.2.1) allows for a completely versatile design of square wave pulse sequences with the option of pulsed field gradients. A graphical user interface (see figure 3.3b) running on top of the user application greatly sim-

plifies and accelerates the sequence design. Furthermore, the system is intended for frequencies ranging from 20 MHz up to 48 MHz, which allows for proton NMR at magnetic flux densities ranging from about 0.5 T to more than 1 T (see section 3.2.3).
Both spectrometers share the concept of a direct-conversion receiver structure. The RF-signal is transformed to baseband using only one frequency conversion. The LO frequency is synchronous with the rotating frame and hence the NMR transmitter frequency. A major advantage of this synchronous demodulation is inherent image rejection if well matched quadrature signals are used. In addition, the filter requirements of the subsequent low-pass, rejecting the spectral component at twice the center frequency are strongly relaxed compared to super heterodyne receivers. Removing the intermediate frequency also greatly reduces circuit complexity and hence hardware requirements.
The way these direct-conversion receivers are implemented greatly differs between the two devices. The SoC-based device uses the direct-sampling approach. Synchronous demodulation is realized digitally in the *PL* of the SoC. On the other hand, the synchronous demodulator of the MiCSMaP device is realized in the analog domain. This has the advantage of strongly reduced requirements on the digital processing power. A cheap µC-based digital control system (see figure 3.2a) is sufficient. Furthermore, digitalization of the baseband signal can be performed by simple audio ADCs. Realization via sigma-delta converters greatly relaxes the anti-aliasing filter requirements [82] due to an oversampling ratio of 384. A simple RC-structure is sufficient. Still, the drawbacks outweigh these advantages. The hardware requirements increase. Additional components like a quadrature demodulator and frequency synthesizers are needed. Furthermore, analog baseband processing requires quadrature amplifiers, filters and two synchronous data converters. The degree of image cancellation is proportional to the quality of quadrature path balancing. In the analog domain, quadrature balancing is rather difficult to realize. In the digital domain, perfect balancing is achieved without any effort. However, the major drawback are DC-offsets caused by analog components like the baseband amplifiers. These offsets overlap irreversibly with the NMR baseband spectrum. LO break through also results in observable DC-components, even though a divide-by-4 circuit generates the internal LO-signal of the quadrature modulator. These DC-components turned out to be dominant. The direct-conversion receiver structure was changed to a low-IF receiver structure, where IF is chosen to be at positive midband (24 kHz). This allows for the attenuation of DC-components prior to a second frequency conversion to baseband, which is performed digitally on the workstation. Due to the finite duration of the corresponding transition band, the maximum achievable signal bandwidth is about 20 kHz. This is much less than the 400 kHz of the SoC-based device (see section 3.2.2). Even though NMR signals usually do not show such high bandwidths, the highly shifting center frequencies caused by temperature induced B_0 shifts of permanent magnets (see section 4.1) require fast frequency follow control.
The direct-sampling, direct-conversion receiver on the other hand requires high speed data converters. For Nyquist sampling, taking into account anti-aliasing transition bands, high sampling frequencies are required (ADC sampling frequency 245.76 MHz). The corresponding anti-aliasing filter is complex. Consequently, high speed digital signal processing is required. This is provided by the PL of the SoC (based on Artix-7 FPGAs) such that the synchronous demodulator can be realized fully digital. As the sampling frequency is much higher than the desired baseband bandwidth, the NMR signal is decimated by a ratio of 200 (see section 3.2.2). This leads to an increase in the theoretical upper limit of the SNR due to a quantization noise reduction of 23 dB, which in turn leads to a bit gain of 3.8.
The transmitter of the SoC-based device generates low-power RF-pulses fully in the digital domain. Conversion to the analog domain also requires high speed data converters (DAC sampling frequency is 491.52 MHz). This data converter is not required by the µC-based system (see figure 3.2a) because the

amplitude modulated carrier is generated by an external DDS IC (AD9959, Analog Devices) with an SFDR of 83 dBc and a frequency resolution of 120 mHz. For the SoC-based device the frequency synthesizer is realized by a DDS IP core [72] driven by the system clock. A phase accumulator bit width of 32 leads to a frequency resolution of 28.6 mHz. A table depth of 16 bits for DDS_{RX} and 14 bits for DDS_{TX} (see figure 3.3a) results in an SFDR of 108 dBc and 96 dBc, respectively. The bit widths of the outputs are set to 18 and 16 bits, respectively, where 18 bits for DDS_{RX} are used to account for the decimation gain of the first decimation stage and the required coefficient bit width (see section 3.2.2).
Both spectrometers generate square wave pulse sequences to excite the nuclear spins. The spectral energy spreads according to a sinc-function about the carrier frequency. In order to avoid artifacts, hard pulses are required. Here, a pulse is considered hard if the magnitude spectrum is larger than 95 % of its maximum for all frequencies contained in the sample. The longer the pulse duration the narrower the spectrum. If the NMR signal bandwidth is assumed to be 2 kHz due to massive inhomogeneous broadening, the pulse duration must not exceed 200 µs. This results in certain power requirements for the RF-transmitter that depend on the probe coil architecture and hence need to be evaluated separately for each coil design. Both spectrometers use the same final power amplifier. The maximum, quasi harmonic-free output power achieved is 1 W (30 dBm) for the MiCSMaP device and only 0.5 W (27 dBm) for the SoC-based device. Due to higher frequencies, the maximal slope of the RF-pulses exceeds the slew rate of the power amplifier at lower power levels. Furthermore, the temporal resolution, important for precise flip angles of the RF-pulses is limited by the clock rate of the timer modules of the µC (see section 3.1) and the pulse generator (see section 3.2.1). These are 168 MHz and 122.88 MHz, respectively, which results in a resolution of 6 ns and 8 ns. This, in turn, is approximately 0.2 % regarding a typical pulse length of about 16 µs for an excitation pulse.
Both analog receivers have a preselector bandpass filter and a low-noise amplifier (not shown explicitly in figure 3.2 and figure 3.3) right after the duplexer circuit. The preselector limits the NMR frequencies for the overall systems. The MiCSMaP device allows for frequencies ranging from 19 MHz to 22 MHz, whereas the SoC-based device allows for frequencies ranging from 20 MHz to 48 MHz. The noise figures and gains of the low-noise amplifiers are 4.1 dB and 20 dB (AD8331, Analog Devices) and 2.6 dB and 20 dB (ADL5536, Analog Devices). According to Friis law [81], these values dominate the overall noise figures of the amplifier chains.
After digitization, the synchronous demodulator of the SoC-based devices allows for frequencies ranging from 0 Hz to 48 MHz (see figure 3.10a), limited by the *HBF* (see figure 3.6). The equiripple filter design is chosen to minimize the transition band for a given ripple and filter order [83]. Passband ripple and minimum stopband attenuation are desired to be less than 0.0015 dB and 80 dB, respectively. The bandwidth of 400 kHz is limited by the concatenation of the *CIC* and the *COMP* filter. The minimum stopband attenuation of the *CIC* and the *COMP* filter is 87 dB and 83 dB, respectively. As both attenuations are in the same range, the use of four *CIC* stages and a 65-taps compensation filter is a reasonable choice concerning resource utilization. The entire synchronous demodulator is designed using only 14 DSP slices. Furthermore, the duration of the impulse response is only 26 µs. This highly advantages the detection of fast decaying FIDs in very inhomogeneous fields.

4 NMR Probe Heads

Throughout this work two kinds of NMR probe heads were designed for permanent magnets with a magnetic flux density B_0 of 0.5 T and 1 T (see section 4.1). Both probe heads generate an RF-field $\boldsymbol{B}_1$ perpendicular to the external field $\boldsymbol{B}_0$. The main design consideration for the flow-through probe head was to allow for automated sample exchange and even in-flow NMR measurements. The resulting probe head is presented in section 4.3. The gradient-capable NMR probe head includes the ability to generate a secular pulsed field gradient $\boldsymbol{B}_{grad}$ using only one center-tapped solenoid and thus avoiding additional and cumbersome hardware. This probe head is presented in section 4.4. Both are tuned and matched by a balanced capacitive matching network presented in section 4.2.

4.1 External Magnetic Field

The external static magnetic flux densities B_0 used throughout this work are generated by low-field permanent magnets. Figure 4.1a shows a 0.5 T magnet used with the flow-through probe head (see section 4.3) and figure 4.1b shows a 1 T magnet used with the gradient-capable probe head (see section 4.4).

a) b)

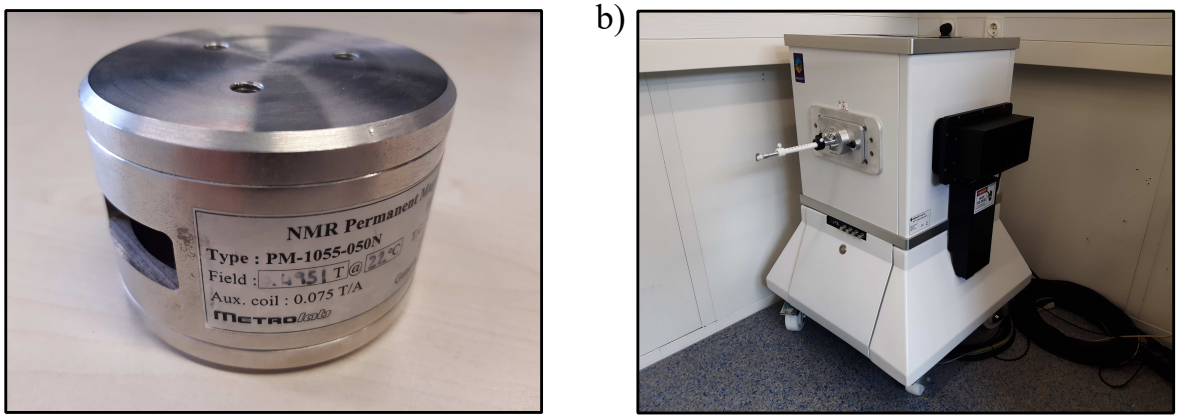

Figure 4.1: NMR permanent magnets. a) 0.5 T permanent magnet. b) 1 T permanent magnet.

The magnetic flux density B_0 of the smaller permanent magnet (Metrolab, PM-1055-050N [84]) is 0.5 T ($\pm 10\,\%$). According to equation 2.32, this results in a Larmor frequency of $\approx$ 21.3 MHz for protons. The magnet has very small outline dimensions, such that the diameter is only 80 mm and the height is only 55 mm. Overall the weight of the magnet is only about 1250 g. The core is made of a composition of neodymium, iron and boron ($NdFeB$) which allows for such high field strengths while still maintaining small outline dimensions [21]. Unfortunately, the temperature dependence of the core material also leads to a significant temperature coefficient [85, 86] of -1200 ppm/K. This identifies to a field drift of -60mT/K or 25 kHz/K in frequency units. Especially for long term two-dimensional experiments (see chapter 6) with a duration of many hours this can cause problems that need to be considered. The field homogeneity is not stated in particular but will be examined later in terms of T_2^* (see section 5) for the

flow-though probe coil architecture. Nevertheless, a quasi homogeneous zone or sweet spot, suitable for NMR experiments is given in the datasheet as 1 cm^3 [84].
The magnetic flux density B_0 of the magnet (Aspect Imaging, M2) [87] used for the gradient-capable probe head is a little higher than 1 T. FID-measurements revealed that the corresponding Larmor frequency is ≈ 44.74 MHz for protons. According to equation 2.32, this results in a magnetic flux density of ≈ 1.05 T. The footprint of the magnetic subsystem is about $1m^2$. As a custom-designed probe head is used for the subsequent experiments, the RF-coils of the imaging system are removed from the magnetic subsystem. The custom-designed NMR probe head is fixed on the sample mounting unit which is then inserted in the magnet. As the magnet is built for small animal imaging, the homogeneous field area is much larger than the one of the 0.5 T magnet. Furthermore, the use of shimming coils allows for a more homogeneous field compared to the smaller magnet. An exact value for the field drift due to the temperature dependence of the core material is not stated in the datasheet but definitly needs to be considered for long term measurements as shown in chapter 6.

4.2 Balanced Series Capacitive Matching Network

Impedance matching is essential to maximize the power transfer between source and load. In case of perfect matching the efficiency rises up to 50 %. Furthermore, matching line and load impedance is important to avoid the wave being partially reflected. Otherwise, destructive addition of the incoming and the reflected wave leads to a loss of power [68]. The system impedance Z_0 is chosen to be equal to the purely resistive standard line impedance of 50 Ω.
The equivalent circuit diagram of the *NMR coil* consists of a purely inductive component L_{NMR} in series with a purely resistive component $r \propto r_0\sqrt{\omega}$, where r_0 is the DC resistance. The impedance of the NMR coil is given as

$$Z_{NMR} = jX_{NMR} + r = j\omega L_{NMR} + r \tag{4.1}$$

The quality factor Q is given as

$$Q = \frac{X_{NMR}}{r} = \frac{\omega L_{NMR}}{r}, \tag{4.2}$$

where X_{NMR} is the inductance. The quality factor describes the ratio of magnetic energy stored in the coil to the energy dissipated in r per cycle. The impedance conversion from Z_{NMR} to Z_0 at the spectrometer frequency ω_0 is performed in terms of a reactive matching network. In case of perfect impedance matching all incident power is dissipated in r. Narrow band matching is achieved by connecting a tuning capacitor C_T in parallel to the *NMR coil* (see figure 4.2). At the resonance frequency ω_{res} the imaginary component of the impedance is zero, whereas the real one shows a maximum. For frequencies much higher and much lower than ω_{res} the real part converges to r, where the rate of change is proportional to Q. The real part of the parallel resonator is exactly 50 Ω for two frequencies in between. Choosing C_T and hence ω_{res} such that $\omega_0 < \omega_{res}$, the residual reactive component is positive and can be compensated by a serial matching capacitor with an impedance $Z_M = -j(\omega C_M)^{-1}$. Capacitive matching is favorable due to difficulties with high quality, variable, non-magnetic inductors [68].
The transversal field $\boldsymbol{B}_1$ is inevitably coupled with an electric field. Electric fields lead to dielectric and radiating losses, where the latter can be neglected as the coil dimensions are much smaller than the wavelength at ω_0. In conducting samples, also magnetic losses due to magnetically induced currents need to be considered. As these currents are proportional to $\boldsymbol{B}_1$ magnetic losses cannot be reduced. However,

the electric field and therefore dielectric loses can be reduced. The approach of using low-inductive coils is mostly limited by the required sample size and the available transmit power. Still, a reduction of the electrical field strength and the dielectric losses can be achieved by balancing the coil. Parasitic, imperfect (lossy dielectrics) capacitive coupling of the coil through the sample increases the resistance r and therefore decreases Q. As the parasitic capacitances C_p are in parallel to the tuning capacitor C_T the resonance frequency ω_{res} decreases. Losses are minimized by minimizing the voltages across the parasitic capacitances. In the symmetrical capacitive matching network shown in figure 4.2 the effective parasitic capacitance is halved and so is the maximum voltage and the lossy current.

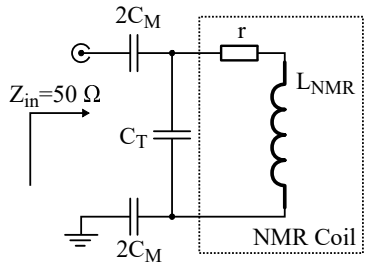

Figure 4.2: Schematic of a balanced capacitive matching network

The matching capacitor with a capacitance C_M is split into two symmetric matching capacitors, each with a capacitance of $2C_M$ [88]. This results in an overall matching capacity C_M. Thus, the network remains well matched. As current and impedance of both matching capacitors are equal, the voltages at the outer taps of the coil, referred to ground (see figure 4.2) are equal in magnitude and phase-shifted by 180°. Furthermore, due to the virtual ground in the center of the coil, the maximum voltage at the coil is halved compared to unbalanced networks. Symmetry and phase shifts are slightly distorted by the resistance r. The higher Q, the better is the symmetry.

4.3 Flow-Through Probe Head

A 3D-model of the flow-through probe head is shown in figure 4.3. The probe head is designed for an external magnetic flux density of 0.5 T (Metrolab, PM-1055-050N [84]).

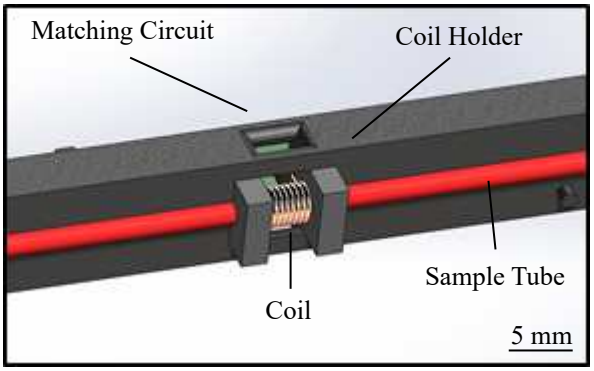

Figure 4.3: 3D-model of the flow-through NMR probe head.

The focus of this NMR probe head design is on automated sample exchange and in-flow NMR measurements. A solenoid is wound around a 3D-printed *coil holder*. The PTFE *sample tube* is inserted in

the *coil holder* such that the sample can flow through the *NMR coil*. The NMR coil, made of enamelled copper wire with a diameter of 0.56 mm has eight windings over a length of 5 mm and a diameter of 4.3 mm. The effective sample volume is about 19 µl depending on the required field homogeneities. The inductance L and the resistance r of the coil, measured with a vector network analyzer at 21 MHz are 187 nH and 715 mΩ, respectively. The custom-designed 3D-printed inset allows to center and fix the NMR coil in the area of highest B_0 homogeneity of the permanent magnet. Impedance matching to 50 Ω is performed by a balanced series capacitive matching network (see section 4.2). The corresponding *matching circuit* is attached on the back of the probe head inset (see figure 4.3). The quality factor Q, determined by S_{11} [89] is approximately 160.

4.4 Gradient-Capable Probe Head

Even though various NMR experiments rely on the application of pulsed field gradients, the majority of portable low-field NMR systems lacks the ability to generate these due to additional and cumbersome hardware requirements. The gradient-capable probe head allows to drive DC through the center tap of an RF coil to generate pulsed field gradients without disturbing the RF reception capabilities. The coil is designed for an external field strength of 1 T (Aspect Imaging, M2 [87]). A 3D-model of the NMR probe head is shown in figure 4.4a.

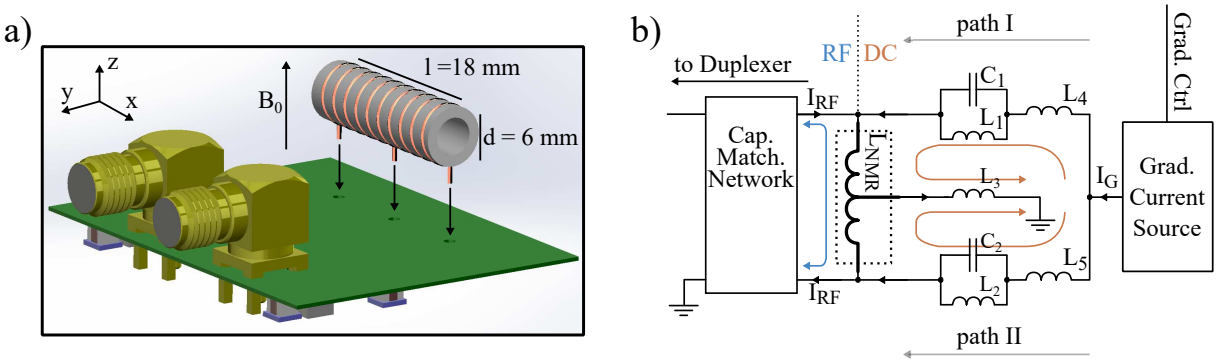

Figure 4.4: Gradient-capable NMR probe head. a) 3D model of the gradient-capable NMR probe head including the probe head circuit board and the center-tapped NMR coil. b) Schematic of the NMR probe head circuit.

There are two SMA-connectors (see figure 4.4a) on the printed circuit board - one for the RF-signal (to duplexer) and one for the DC-signal (to gradient current source). The NMR probe head circuit shown in figure 4.4b interconnects both signals with the center-tapped NMR coil. The coil has a length of 18 mm, a diameter of 6 mm. It is wound around a PTFE coil holder with an inner diameter of 5 mm. Ten windings of enameled copper wire with a diameter of 0.5 mm are used. Glass tubes with PTFE caps (Wilmad-LabGlass) contain the sample inserted in the coil. The inner and outer diameter of the glass tubes is 4 mm and 5 mm, respectively. A schematic of the NMR probe head circuit is shown figure 4.4b. The circuit can be divided into an *RF*- and a *DC*-part, where the *RF*-part interconnects the duplexer via a *capacitive matching network* (see section 4.2) with the NMR coil. At the connection to the duplexer, the NMR coil exhibits a purely resistive impedance of 50 Ω at spectrometer frequency. The *gradient current source* is interconnected via the *DC*-part with the outer taps of the NMR coil. The RF-signal experiences a very high impedance at the tank circuits L_1C_1 and L_2C_2 which are tuned to the spectrometer frequency. Additionally, the serially connected inductors L_4 and L_5 further increase the

impedances such that *path I* and *path II* are no longer observable by the RF-signal. The center tap is DC-coupled to ground with the inductor L_3. No signal loss was detected at spectrometer frequency such that a sufficiently high impedance for RF-signals is assumed. The current I_G on the other hand is driven by the current source from the outer taps through the center tap, to ground. The reactive networks show a neglectable impedance for DC. The duplexer inputs are protected of the gradient current I_G due to the serial capacitive coupling of the matching network.

4.4.1 Field Calculation

For a better understanding the transversal field $\boldsymbol{B}_1$ and the gradient field $\boldsymbol{B}_{grad}$ of the center-tapped coil were simulated (Comsol Inc., Comsol Multiphysics 5.2). The results are shown in figure 4.5 and figure 4.6, respectively. The RF-field $\boldsymbol{B}_1$ is generated by driving a current I_{RF} through the coil like shown in the inset of figure 4.5a. The gradient field $\boldsymbol{B}_{grad}$ is generated by driving a gradient current I_G through the coil like shown in the inset of figure 4.6a. For simulation purposes the current I_{RF} was set to a constant value of 10 mA and I_G was set to 100 mA. The coil dimensions are as described in section 4.4. White arrows in figure 4.5a and figure 4.6a indicate the field direction, whereas the length of the arrows and the color coding indicate the magnitude.

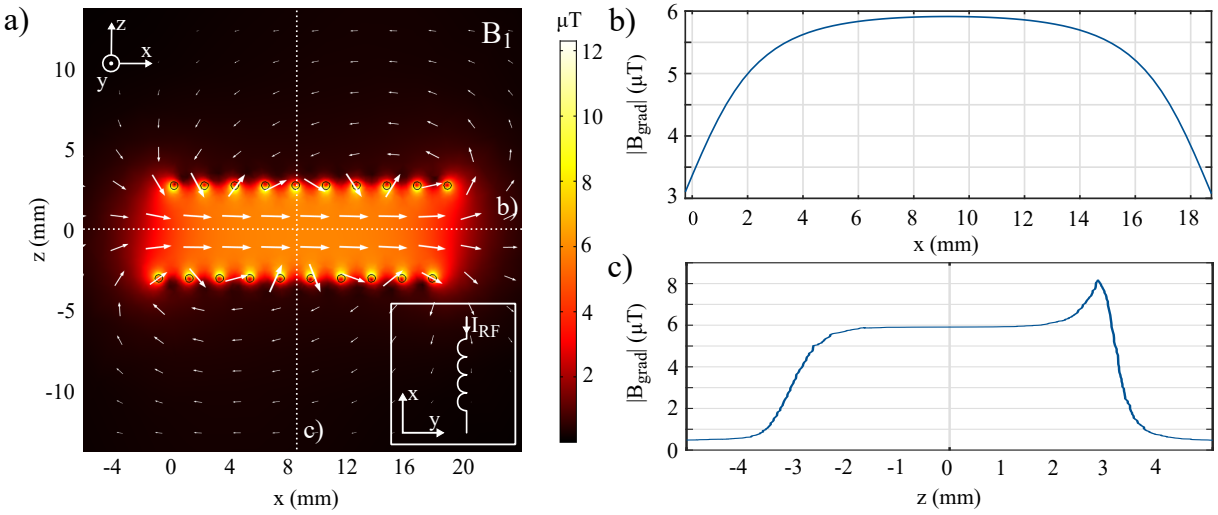

Figure 4.5: Simulation results of the vector field $\boldsymbol{B}_1$ in the xz-plane (a). The field direction is indicated by the white arrows, whereas arrow size and color coding indicate the field magnitude $|\boldsymbol{B}_1|$. The inset indicates the simulation setting. $\boldsymbol{B}_1$ is generated by an RF-current I_{RF} of 10 mA. b), c) Cut through the vector field $\boldsymbol{B}_1$ along the x-axis at $z = 0$ mm and along the z-axis at $x = 8.5$ mm, respectively (see dotted lines).

The simulation result of the magnetic flux density $\boldsymbol{B}_1$ is shown in figure 4.5a. The RF-current I_{RF} is set constant in order to evaluate the maximum field magnitude $|\boldsymbol{B}_1|$ as well as the homogeneity of the RF-field. The RF-characteristics are evaluated in more detail in section 4.4.5. Inside the coil the transversal field is well aligned with the central axis (x-axis) of the NMR coil and hence perpendicular to the external magnetic field $\boldsymbol{B}_0$. The closer to the coil windings, the stronger the field perturbations. The maximum magnitude (neglecting the field close to the coil windings because it is not included in the sample volume) is about 5.91 μT in the center of the coil. The $\boldsymbol{B}_1$ field homogeneity is best observable from the cuts through the center of the coil shown in figure 4.5b in x-direction at $z = 0$ mm and fig-

ure 4.5c in z-direction at $x = 8.5$ mm (see dotted lines). The maximum deviation on the z-axis along the x-direction is 0.029 µT considering a sample length of 4 mm in this direction. The maximum deviation on the x-axis along the z-direction is 0.2 µT considering a sample length of 4 mm in this direction. The resulting field homogeneity is about 16000 ppm. Weighting the field deviations by the number of spins actually experiencing them would result in a higher homogeneity.

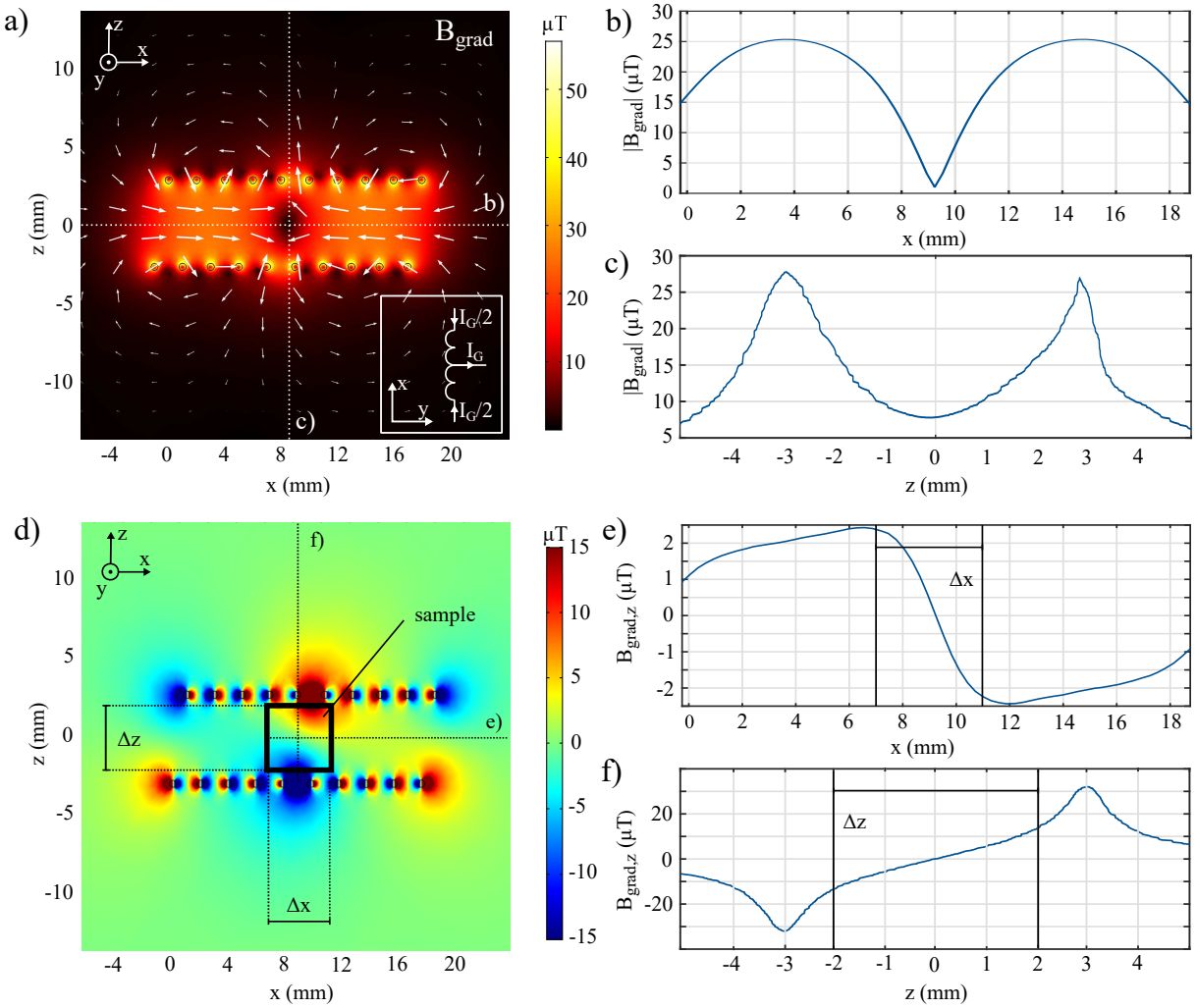

Figure 4.6: Simulation results of the vector field $\boldsymbol{B}_{grad}$ (a) and the secular component $B_{grad,z}$ (d) in the xz-plane. The field is generated by a gradient current I_G of 100 mA. The inset in a) indicates the simulation setting. The sample volume is indicated by the black rectangle in the center. b), c) and e), f) Cuts through $\boldsymbol{B}_{grad}$ and $B_{grad,z}$, respectively. b) and e) show a cut along the x-axis at $z = 0$ mm and c) and f) show a cut along the z-axis at $x = 8.5$ mm (see dotted lines).

Figure 4.6a shows the simulation result of the magnetic flux density $\boldsymbol{B}_{grad}$ generated by the current I_G through the center tap of the coil. The superposition of the vector field generated by the current $I_G/2$ in the upper half running in -x-direction and the vector field generated by the current $I_G/2$ in the lower half running in x-direction results in $\boldsymbol{B}_{grad}$ (see inset figure 4.6a). On the central axis at $x \approx 4$ mm and $x \approx 14$ mm the two vector fields point in exactly the opposite direction because the currents run in opposite directions. At these positions there is almost no interaction between the two individual fields.

The magnitude $|\boldsymbol{B}_{grad}|$ shows a maximum. The closer to the center of the coil the more the interactions increase. The field vectors deviate from the central axis of the coil as field perturbations increase. The field magnitude $|\boldsymbol{B}_{grad}|$ decreases until it reaches a minimum at $x = 0\,\text{mm}$. However, closer to the center, the orthogonal y- and z-components (secular components) increase in magnitude. Cuts through the center of the coil in x-direction at $z = 0\,\text{mm}$ and in z-direction at $x = 8.5\,\text{mm}$ are shown figure 4.6b and figure 4.6c, respectively (see dotted lines). The magnitude $|\boldsymbol{B}_{grad}|$ shows two maxima of about 28 µT on the central axis of the coil. The magnitude is lowest right in the center of the coil.
The secular component $B_{grad,z} = \boldsymbol{B}_{grad}\boldsymbol{e}_z$ is shown in figure 4.6d, where $\boldsymbol{e}_z$ is the unit vector in z-direction. The sample location is indicated by the black rectangle in the center of the coil. The sample location exhibits the highest B_1 homogeneity as well as the strongest gradient over an area of $\Delta x \times \Delta z = 4\,\text{mm} \times 4\,\text{mm}$. An enhanced observability of the field gradients is achieved by limiting the color coding to $\pm 15\,\mu\text{T}$ which coincidences with the absolute maxima inside the sample volume. It is obvious that the gradient is neither unidirectional nor constant inside the sample volume. This is illustrated by the exemplary cuts through $B_{grad,z}$ in x-direction at $z = 0\,\text{mm}$ and in z-direction at $x = 0\,\text{mm}$ shown in figure 4.6e and figure. 4.6f, respectively (see dotted lines). The outlines of the sample volume are indicated by the vertical black lines, labeled Δx and Δz. Obviously, the secular component of the magnetic flux densities shown in the cut plots are not linear. Still, the slope inside the sample area is almost constant and hence allows for an approximation of a quasi constant gradient strength $G_x(y = 0, z = 0) = \Delta B_{grad,z}/\Delta x$ in x-direction of about -1.2 mT/m and $G_z(x = 0, y = 0) = \Delta B_{grad,z}/\Delta z$ in z-direction of about 6.5 mT/m. The y-component is not further discussed as the gradient-capable coil is rotationally symmetric about the central axis and hence y- and the z-direction behave almost identical.

4.4.2 Investigation of the Spatial Gradient Shape

The pulse sequence shown in figure 4.7a allows for the investigation of the spatial shape of the secular field gradient $B_{grad,z}(\boldsymbol{s})$, where $\boldsymbol{s}$ is the spatial position. The corresponding coherence transfer pathway is shown below. In the following the sequence is analyzed using the quantum mechanical approach.

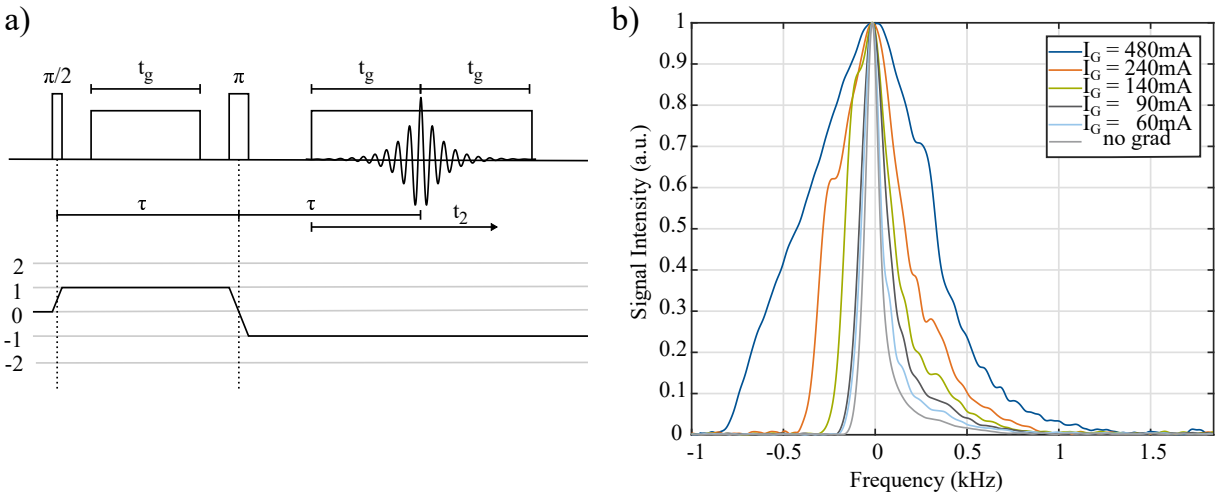

Figure 4.7: Spin echo spectrum modulated by the gradient. a) shows the employed NMR sequence with the corresponding coherence transfer pathway. b) shows the spectra depending on the gradient current I_G for deionized water.

The density operator $\hat{\rho}$ after the first $\pi/2_y$-pulse is given as

$$\hat{\rho}(t=0) = \sum_{i=1}^{N_I} \hat{I}_{ix}, \tag{4.3}$$

for a homogeneous spin system containing N_I spins I_i with an offset frequency Ω_i. Constants are neglected for the sake of simplicity. The excited SQCs dephase in the following period of free precession due to internal spin interactions as well as external interactions like field inhomogeneities and the field gradient $\boldsymbol{B}_{grad}$. The gradient is applied for a duration t_g such that the density operator after the refocusing pulse π_y at $t = \tau$ is given as

$$\begin{aligned}\hat{\rho}(t=\tau) &= \sum_{i=1}^{N_I} \left(-\cos\left(\Omega_i\tau + \gamma \boldsymbol{B}_{grad}(\boldsymbol{s}_i)t_g\right)\hat{I}_{ix} + \sin\left(\Omega_i\tau + \gamma \boldsymbol{B}_{grad}(\boldsymbol{s}_i)t_g\right)\hat{I}_{iy}\right) \\ &\approx \sum_{i=1}^{N_I} \left(-\cos\left(\Omega_i\tau + \gamma B_{grad,z}(\boldsymbol{s}_i)t_g\right)\hat{I}_{ix} + \sin\left(\Omega_i\tau + \gamma B_{grad,z}(\boldsymbol{s}_i)t_g\right)\hat{I}_{iy}\right),\end{aligned} \tag{4.4}$$

where the secular approximation $\boldsymbol{B}_{grad}(\boldsymbol{s_i}) \approx B_{grad,z}(\boldsymbol{s_i})$ is valid as $|\boldsymbol{B}_{grad}(\boldsymbol{s_i})| << B_0$ for all $\boldsymbol{s_i}$. The offsets due to external field inhomogeneities are refocused at $t = 2\tau$. Offsets due to the gradient field are only refocused at $t = 2\tau$ by applying an equivalent gradient in the second period of free precession at $t = 2\tau - t_g$. For simplicity it is assumed that the acquisition period and the gradient start simultaneously at $t_2 = 0$. This way, the gradient can be assumed as constant during the first period of free precession ($B_{grad,z} = 0$) and during the acquisition period where the gradient is switched on. The density operator during the acquisition period ($t_2 < 2t_g$) is given as

$$\hat{\rho}(t_2) = \sum_{i=1}^{N_I} \left(-\cos\left((\Omega_i + \gamma B_{grad,z}(\boldsymbol{s}_i))(t_g - t_2)\right)\hat{I}_{ix} + \sin\left((\Omega_i + \gamma B_{grad,z}(\boldsymbol{s}_i))(t_g - t_2)\right)\hat{I}_{iy}\right). \tag{4.5}$$

Dephasing caused by the first gradient is reversed for $t < 2\tau$. For $t > 2\tau$ the magnetization dephases again due to internal spin interactions as well as external interactions like field inhomogeneities and again the pulsed gradient field $B_{grad,z}$. According to equation 2.52 the observable signal $s(t_2)$ (observing the coherence $p = -1$) is given as

$$\begin{aligned}s(t_2) &= -\sum_{i=1}^{N_I} \exp\left(-j\left(\Omega_i(t_g - t_2) + \gamma B_{grad,z}(\boldsymbol{s}_i)(t_g - t_2)\right)\right) \\ &= -\sum_{i=1}^{N_I} \exp\left(-j\Omega_i(t_g - t_2)\right)\exp\left(-j\gamma B_{grad,z}(\boldsymbol{s}_i)(t_g - t_2)\right) = \sum_{i=1}^{N_I} s_{noGrad,i}(t_2)s_{Grad,i}(t_2)\end{aligned} \tag{4.6}$$

where $s_{noGrad,i}(t_2) = -\exp\left(-j\Omega_i(t_g - t_2)\right)$ is the regular spin echo signal originating from spin I_i if $\boldsymbol{B}_{grad}(\boldsymbol{s}_i) = 0$. If $\boldsymbol{B}_{grad}(\boldsymbol{s}_i) \neq 0$ the spin echo is amplitude modulated by the gradient induced signal $s_{Grad,i}(t_2) = \exp\left(-j\gamma B_{grad,z}(\boldsymbol{s}_i)(t_g - t_2)\right)$. A multiplication in the time domain leads to convolution in the frequency domain such that $S(\omega)$ is given as

$$
\begin{aligned}
S(\omega) &= \frac{1}{2\pi}\sum_{i=1}^{N_I} S_{noGrad,i}(\omega) * S_{Grad,i}(\omega) = \frac{1}{2\pi}\sum_{i=1}^{N_I} S_{noGrad,i}(\omega) * c_i\delta(\omega - \gamma B_{grad,z}(\boldsymbol{s}_i)) \\
&= \frac{1}{2\pi}\sum_{i=1}^{N_I} c_i S_{noGrad,i}(\omega - \gamma B_{grad,z}(\boldsymbol{s}_i)),
\end{aligned} \tag{4.7}
$$

where $c_i = \exp\left(-j\gamma B_{grad,z}(\boldsymbol{s}_i)t_g\right)$. The spatial shape of the gradient influences the spectral shape of the resulting signal in terms of a frequency shift $B_{grad,z}(\boldsymbol{s}_i)\gamma$ and an amplitude modulation of c_i. In theory, the gradient caused modulation signal and hence the spatial shape can be expressed analytically by a time domain division. Due to finite noise the time domain deconvolution is not valid.
Figure 4.7b shows the resulting spectra of deionized water. The spectra $S(\omega)$ of are shown for different gradient currents I_G, including $I_G = 0$. The spectrum is narrowest for $I_G = 0$. The stronger the current I_G, the stronger the gradient. This results in a well observable broadening of the spectrum. Results were obtained by the setting τ to 20 ms and the gradient duration t_g to 10 ms. The acquisition time t_2 was set to 39 ms. To reduce FFT windowing artifacts a Dolph-Chebyshev window [90] with a sideband attenuation of 100 dB was applied. For better comparability the spectra are normalized to one.

4.4.3 Dephasing Capabilities of the Gradient

For many applications the dephasing capabilities of the gradient on coherences with coherence order p greater than zero is crucial. The pulse sequence shown in figure 4.8a allows the investigation of the dephasing of SQCs.

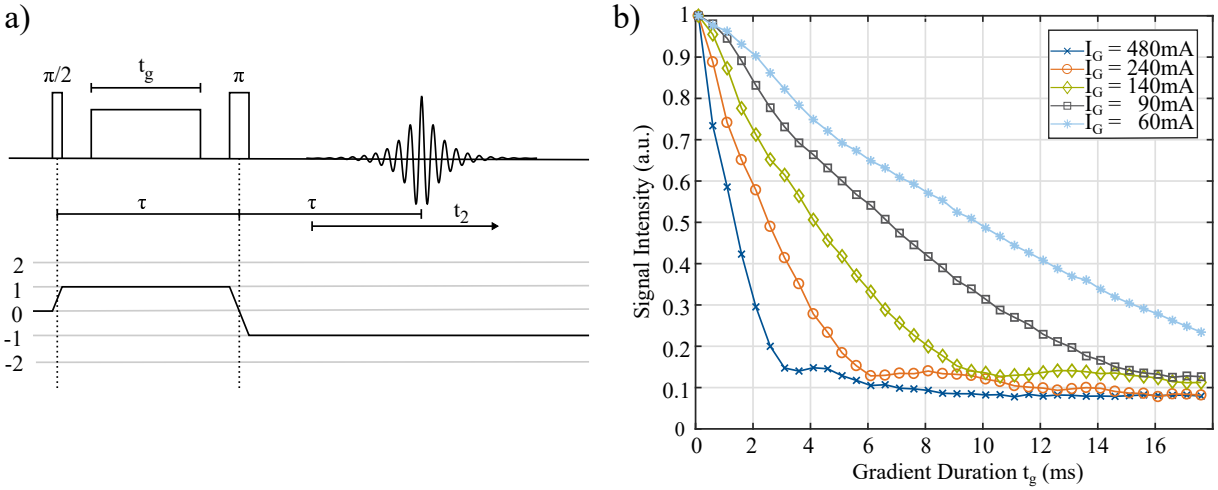

Figure 4.8: Dephasing capabilities of the gradient. a) shows the employed NMR sequence with the corresponding coherence transfer pathway. b) shows the signal intensity of the acquired spin echo depending on the gradient duration t_g for various gradient currents I_G of deionized water.

The $\pi/2$-pulse at $t = \tau$ excites SQCs that dephase during the subsequent period of free precession due to internal spin interactions as well as external interactions like field inhomogeneities and the pulsed field gradient $\boldsymbol{B}_{grad}$. The π-pulse refocuses the offsets caused by inhomogeneous broadening at $t = 2\tau$. Offsets due to the gradient are not refocused. Therefore, the intensity of the acquired spin echo decreases depending on gradient strength and duration. Figure 4.8b shows the signal intensity depending

on the gradient duration t_g for various values of I_G. For a given gradient strength the signal intensity strongly decreases with the gradient duration. Lowering the gradient current leads to a slower signal decay because the smaller the gradient, the slower the gradient-induced dephasing of the magnetization. All graphs are normalized to one for better comparability. The noise floor is different from zero as the absolute part of the spectrum is analyzed. Data was acquired using an acquisition time t_2 of 39 ms and setting τ to 20 ms.

4.4.4 Quality Factor and Scatter Parameters

Figure 4.9 shows the scatter parameters S_{11} and S_{21} measured with a vector network analyzer (Agilent Technologies, E5061A). Results are plotted for an unloaded and a loaded coil (HPLC-grade 1-butanol by Sigma-Aldrich, 34867-1L). Furthermore, the influence of attaching the gradient current source (see figure 4.4b) on S_{11} and S_{21} is shown for both loading conditions.

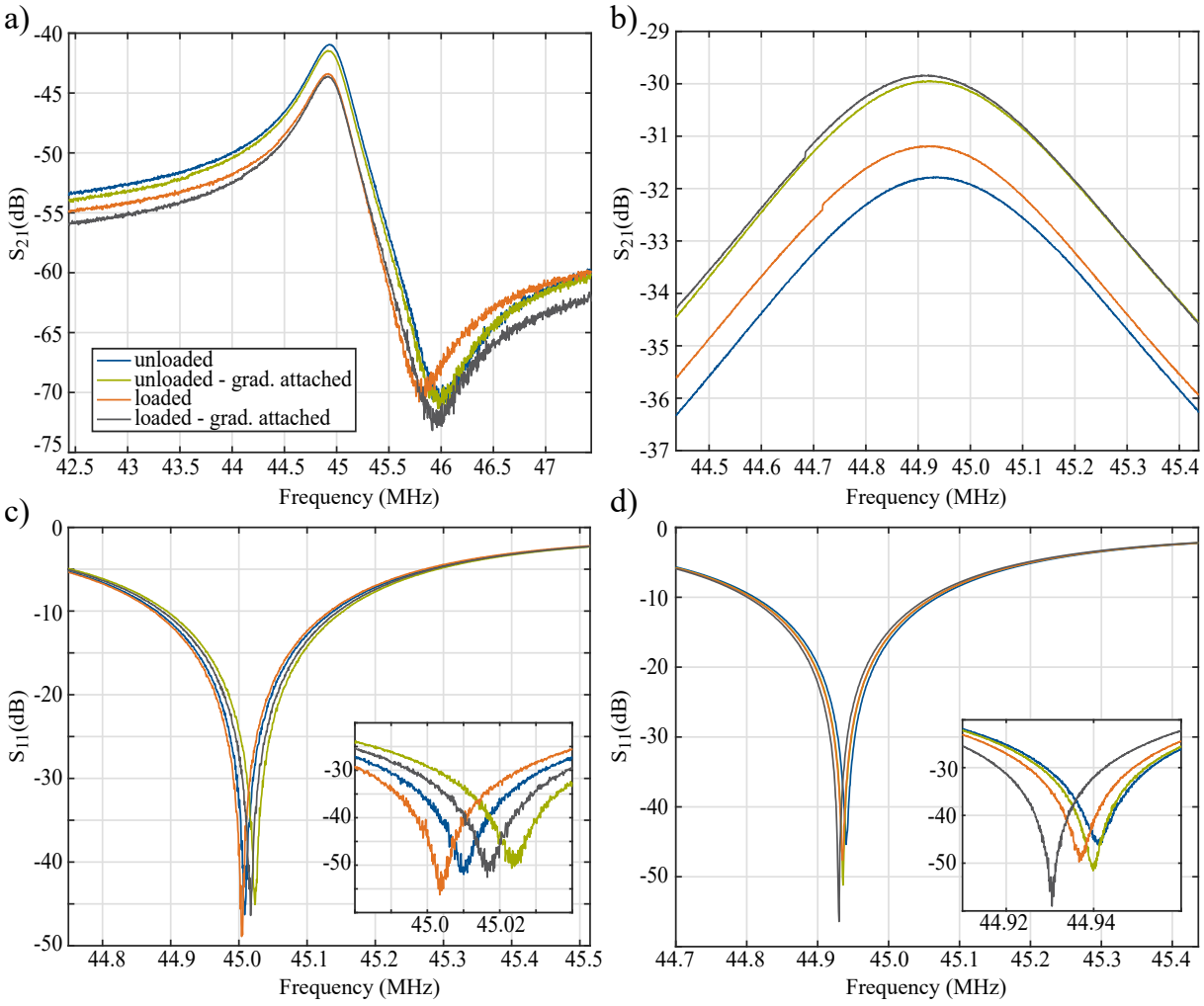

Figure 4.9: Scatter parameters of the gradient-capable probe head. Results are plotted for unloaded and loaded coil (1-butanol) as well as the gradient current source attached or not. a) The scatter parameter S_{21} measured using two pick-up coils. b) The scatter parameter S_{21} using one pick-up coil. c) The scatter parameter S_{11} measured inside the permanent magnet and d) outside the permanent magnet. The insets show a zoom close to the spectrometer frequency.

The scatter parameter S_{21} can be measured either by the use of two pick-up coils (figure 4.9a) or one pick-up coil (figure 4.9b). The diameter of the pick-up coils is about 2 cm. For the tuning procedure using two pick-up coils, a sweep generator excites the tuned circuit via one coil. The excited circuit oscillates such that the resulting emission can be detected by the other pick-up coil. Figure 4.9b shows S_{21} measured using only one pick-up coil to detect the radiation of the NMR coil. The sweep generator is directly connected to the input of the matching network. Figure 4.9c and figure 4.9d show the scatter parameter S_{11}. Sweep generator and detector are multiplexed over one connection. S_{11} is plotted once for the probe head inside the magnet (figure 4.9c) and once for the probe head outside the magnet (figure 4.9d). The insets show zooms close to the spectrometer frequency for better visibility. Frequency shifts due to coil loading or gradient source attachment are best analyzed using S_{11} because the peaks show much narrower characteristics than the peaks of S_{21}. It can be seen from figure 4.9c and figure 4.9d that loading the coil with 1-butanol leads to a slight peak frequency decrease of about 4 kHz, inside and outside the magnet. In case the gradient source is attached, loading the coil inside the magnet also leads to a shift of 4 kHz but the shift outside the magnet is about twice as high (8 kHz). Attaching the gradient current source inside the magnet leads to an increase of the peak frequency of about 15 kHz and 13 kHz for the loaded and the unloaded case, respectively. Outside the magnet there is almost no decrease for the unloaded case. For the loaded case however there is a decrease of about 8 kHz.
Finally, the quality factor Q of the matched probe head is determined (see equation 4.2). The results are shown in table 4.1. At first, Q is determined by the measurement of S_{21} (see figure 4.9a) obtained by loosely coupling the NMR probe coil with two pick-up coils [91]. The quality factor is then calculated as

$$Q = \frac{\omega_0}{\Delta\omega}, \tag{4.8}$$

where ω_0 is the resonance frequency of the circuit and $\Delta\omega$ is the 3 dB-bandwidth. Using this method, the matching network is in open circuit state. Using only one pick-up coil to determine S_{21}, connecting the detector an input of the matching network like shown in figure 4.9b leads to a loading of the matching network by 50 Ω (network analyzer output impedance). The resonator circuit is damped and therefore the determination of the quality factor by equation 4.8 requires a factor of two to compensate for half of the energy dissipated in the load impedance. Furthermore, Q can be obtained by S_{11} [89]. As this connection also adds a load to the network, a factor of two needs to be added to equation 4.8. All methods were evaluated for four cases: unloaded coil with no gradient attached, unloaded coil with gradient attached, loaded coil with pure water sample and no gradient attached and loaded coil with attached gradient. The corresponding Q factors are given in table 4.1.

Q	S_{21} - two pick up coils	S_{21} - one pick up coil	S_{11}	S_{11} in magnet
unloaded - no grad	114.9	121.3	110.7	109.5
unloaded - grad	113.9	122.3	111.0	110.0
loaded - no grad	111.3	123.9	110.7	110.0
loaded - grad	114.0	124.1	111.2	110.4

Table 4.1: Quality factor of the gradient-capable probe head obtained by the scatter parameters S_{21} and S_{11}. S_{21} was measured either by one or by two pick-up coils. The quality factor is shown for loaded and unloaded settings as well as for the gradient current source attached or not.

The quality factor obtained from S_{21} ($\approx$ 112 using two-pick coils and $\approx$ 122 using one pick-up coil)

are slightly higher than the results obtained from S_{11} which are about 110. Loading the coil as well as attaching the gradient does not change the quality factor significantly. Furthermore, the quality factor remains constant if the probe head is inserted in the magnet or not.

4.4.5 Switching Characteristics

The switching characteristics of the gradient are determined by measuring the voltage (V_{L3}) at the center tap of the NMR coil with respect to ground (see figure 4.4b). Figure 4.10 shows V_{L3}, triggered by the gradient current source control signal *Grad. Ctrl* (see figure 4.4b). The purely resistive part of the impedance of L_3 is about 3.1 Ω and allows for direct determination of the temporal behavior of the gradient current measuring the corresponding voltage. About 4 ms after the trigger rises, V_{L3} rises to about 1.3 V. The rise time $t_{10\%-90\%}$ is about 17 µs. With a delay of about 4 ms after *Grad. Ctrl* drops, V_{L3} drops as well with a fall time $t_{90\%-10\%}$ of about 40 µs.

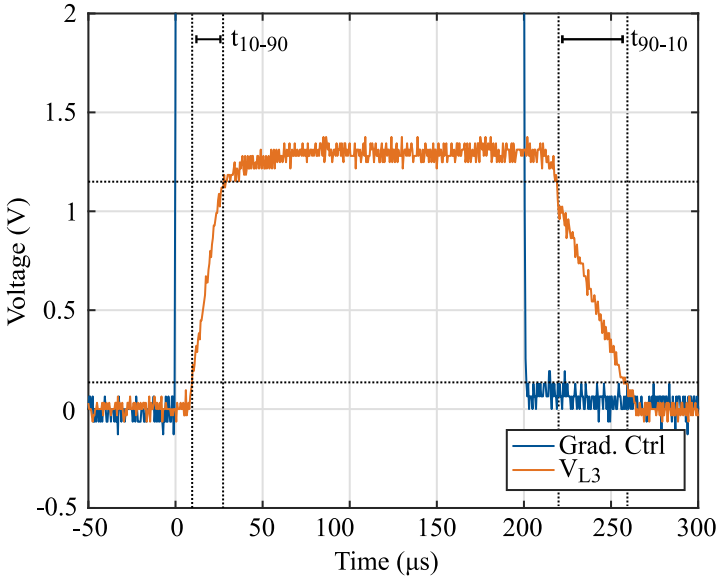

Figure 4.10: Switching characteristics of the gradient. The voltage v_{L_3} at L_3 is triggered by gradient control signal (Grad. Ctrl) to get the rise time $t_{10\%-90\%}$ and the fall time $t_{90\%-10\%}$ of the gradient.

4.5 Probe Head Discussion

Throughout this work two NMR probe heads with a very different application focus were developed. The first step of designing NMR probe heads is to find a suitable NMR coil design. The volume of the coil is defined by the required sample size. If the setup allows for a sample orientation perpendicular to B_0, solenoid NMR coil architectures are often preferable due to their simplicity as well as their ability to generate highly homogeneous B_1-fields. Furthermore, the magnitude $|\boldsymbol{B}_1|$ can be adjusted by the number of windings for a given transmit power. Simulation data (see figure 4.5a, b and c) shows that the center-tapped coil described in section 4.4 generates a maximum field magnitude of 5.9 µT inside the sample volume for an RF-current of 10 mA. The maximum deviation from the mean value in the sample volume is ≈0.1 µT, which results in a B_1-homogeneity of about 16000 ppm. Actually, the deviation is much smaller as the sample does not fill the whole coil and maximum field deviations are located close to

the coil windings. Furthermore, the majority of spins is located in the highly homogeneous center of the sample such that the effective deviation is much less than 0.1 µT. Still, B_1-homogeneity can be further improved by reducing the sample size. This is a trade-off between B_1-homogeneity and the sensitivity of coil, dictated by the filling factor. No field calculation was performed for the flow-through coil but similar results are expected due to the similar coil architectures. Still, if the coil is perfectly matched and hence the entire transmit power is dissipated in the coil resistance ($r = 114\,\mathrm{m}\Omega$), the effective transversal field can be calculated. A transmit power of 0.49 W (see section 3.1) results in an effective current of 2.08 A, which is much higher than the gradient current used for the simulation of the center-tapped coil. This results in a linear polarized magnetic field amplitude $|B_1|$ of 3.16 mT in the center of the solenoid. The amplitude of the effective field B_1^+ is only half of the amplitude of the linear polarized field and equals to 1.58 mT. This result coincides with the value determined by pulse width calibration (see flip angle in section 2.5). The sensitivity of the coil is found to be $2.26\,\mathrm{mT}/\sqrt{W}$ [92].

Dimensioning of a matching network requires knowledge about the impedance of the NMR coil. Even though the inductance and the resistance of the NMR coils were determined by the use of a vector network analyzer, the values calculated for the matching network deviated rather strong. For instance, the flow-through coil showed an reactance X_L of about 25 Ω and a quality factor Q_L of about 35 at 21 MHz. These values are much lower than expected due to insufficient measurement conditions like a bridged matching network. Furthermore, network analyzers are only accurate tools as long the target impedance is close to their characteristic impedance. Same concepts apply for the gradient-capable coil.

The gradient-capable probe head circuit allows to drive DC without disturbing the RF-reception capabilities of the coil. Little additional hardware resources are required for the pulsed field gradient system. The separation of the DC- and the RF-system is demonstrated by the scatter parameters S_{11} and S_{21}. Even though S_{21} is more accurate in many terms, S_{11} has the advantage to be measurable without the use of additional pick-up coils. This allows to measure the influence of small bore hole permanent magnets even though the probe head is inserted and not accessible. The accurate determination of the quality factor however requires a perfectly matched purely capacitive network [89]. Furthermore, narrower peak widths of S_{11} compared to S_{21} allow to observe the differences much easier. Loading the coil with 1-butanol or a saline solution ($NaCl$, molar concentration: 100 mM) leads to parasitic capacitance that corresponds to a frequency shift of ≈ 7 kHz. This demonstrates good coil balancing. Furthermore, the gradient current (DC) barely affects the RF-characteristics of the coil. The tank circuits L_1C_1 and L_2C_2 (see figure 4.4b) strongly reduce the influence of the gradient current source when attached to the outer taps of the coil. Inside the magnet the observed frequency shift is less than 12 kHz for a loaded (1-butanol) and an unloaded coil (see figure 4.9c). This is neglectable as the 20 dB-bandwidth of S_{11} exceeds 12 kHz by far. Pre-measurement adjustments can be used to compensate for the shift as well.

The quality factor obtained from S_{21} is higher (≈ 113 for two pick-up coils and ≈ 122 for one pick-up coil) than the quality factor obtained by S_{11} (≈ 110). Even though the amplitudes of S_{21} strongly depends on the coupling factor of the pick-up coils, shape and position of the peaks are not influenced. However, determination of Q by S_{11} depends on the degree of matching accuracy. Mismatched impedances lead to a decrease [89]. Loading the probe and the attachment of the gradient current source does not alter the quality factor. Furthermore, measurements inside and outside the magnet show equivalent results. This allows for the conclusion that losses due to eddy currents in the magnet are neglectable.

Simulation results of gradient field generated by gradient-capable coil, shown in figure 4.6 demonstrate that the gradient inside the sample area of the coil is neither constant nor independent of the position or the direction. A gradient current of 100 mA leads to a gradient G_x of -1.2 mT/m whereas the gradient G_z is 6.5 mT/m in the center of the sample. Due to the neglectable magnetic susceptibility of biological

samples, the gradient strength can be adjusted linearly with I_G [32]. This is further confirmed by figure 4.8b where the signal decay fits well to the applied current.
The gradient strength is comparable to the spoiling pulse strength used in [51] for HZQC measurements (1 mT/m). Correlation pulses used in iZQC measurements are stronger (60 mT/m, 120 mT/m, 300 mT/m and 200 mT/m) [53–55]. However, as shown in section 4.4.2 and section 4.4.3 the gradient strength can be adjusted by the gradient current. Furthermore, applications relying on correlation pulse depend on the product of gradient strength times gradient duration [55]. The decay rate (see figure 4.8b) is determined by the gradient strength, whereas the overall dephasing depends on the gradient duration.
Usually field gradients strongly prefer one direction [58]. However, the field calculations revealed that the gradient generated by the center-tapped coil is highly direction-dependent. Spoiling (figure 4.8) or correlation pulses for iZQC measurements (see section 6.2) do not rely on unidirectional gradients. However, MRI applications usually rely on three gradients that are independently controllable per direction.
Information about the spatial shape of the gradient is revealed by the results shown in figure 4.7b. The degree of modulation of the spin echo depends on the spatial distribution of the magnetic flux density according to the theoretical results in equation 4.7. The stronger the gradient, the stronger the broadening of the spectrum. A satisfying analytical solution could not be found as the deconvolution is under the presence of noise.
The temporal shape of the gradient is investigated by the switching characteristics of the current I_3 (see schematic in figure 4.4b) through the center tap shown in figure 4.10. The switching characteristics of I_3 are highly proportional to the magnetic flux density that evolves in the center of the coil due to the low magnetic susceptibility of biological samples [32]. Rise and fall time is about 17 µs and 40 µs, respectively. Compared to the typical gradient duration of many ms this is neglectable. Still, rise and fall time needs to be considered during pulse sequence design. Furthermore, there is a fixed delay of 4 ms between the rising and the falling edge of *Grad. Ctrl* and the gradient current which needs to be compensated by the FPGA logic. The current I_G causes a voltage drop of about 1.3 V at the inductor L_3 (see figure 4.4b) which fits well to the set gradient current of 480 mA.
Finally, the temperature evolution of the center-tapped coil and the corresponding DC-path of the gradient current was investigated. The gradient current was set to 480 mA. Gradients were applied for a duration of 200 ms separated by 1 s for 30 minutes. No heating of the corresponding parts above room temperature could be observed by a thermal imaging camera (InfraSight, Optris).

5 MiCSMaP Device and Measurements

The MiCSMaP device integrates the continuous synthesis of MNPs by coprecipitation and subsequent surface functionalization with online MNP characterization in terms of NMR relaxation properties. Incorporation of a miniaturized NMR relaxometer (see section 3.1) with a flow-through NMR probe head (see section 4.3) and a flow-based microreactor allows for particle characterization during and right after the synthesis process in an automated manner. This work focuses on system design, development as well as controlling of the device. Microreactor design and evaluation, as well as the synthesis protocols are exclusively designed by Jonas Bemetz within the IGSSE cooperation 9.06 [11, 93].
Figure 5.1a shows the front view of the MiCSMaP system, whereas the top view (cover opened) is shown in figure 5.1b.

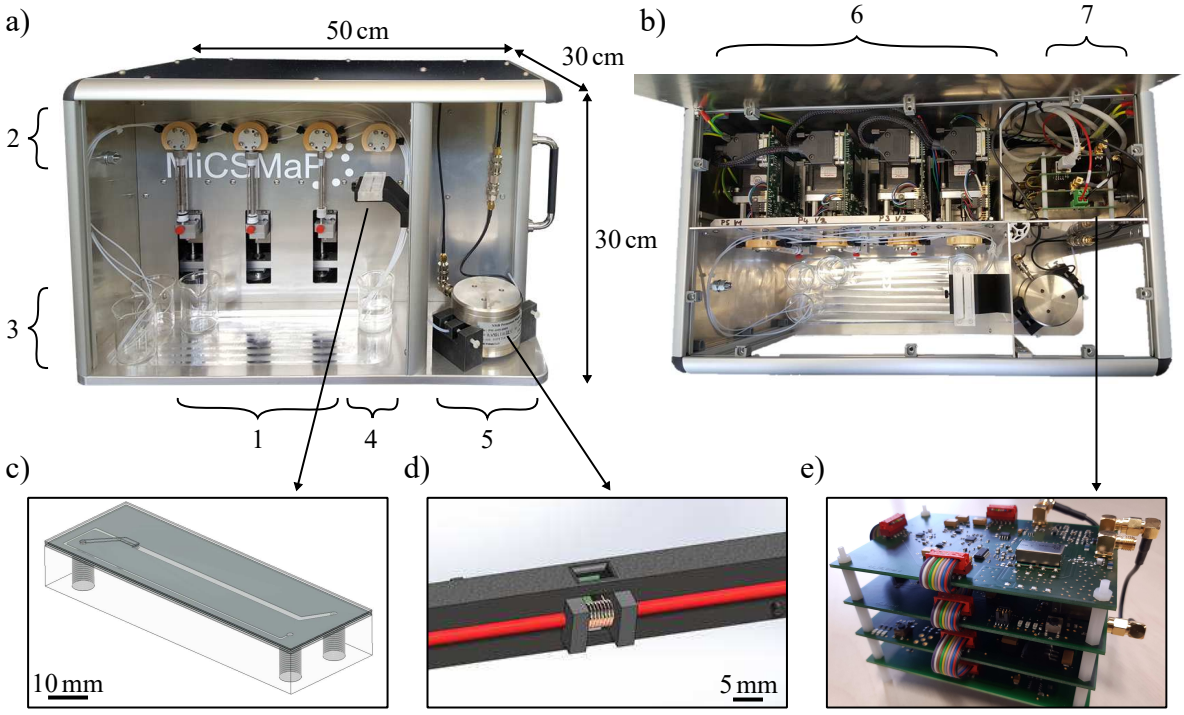

Figure 5.1: MiCSMaP device. a) Front view of the MiCSMaP device. b) Top view of the MiCSMaP device. The reagents are provided by three syringe pumps (1), driven by stepper motors in the back end of the device (6). Reagents are collected from the supply flasks (3) and distributed by four 6-port valves (2) to the microreactor (4). The output of the microreactor is either routed to the NMR magnet (5) and the corresponding NMR spectrometer (7) or is collected directly. c) 3D model of the microreactor. d) 3D model of the NMR probe head located inside the magnet (5). A tube (red) is holding the sample. e) Picture of the NMR spectrometer.

The case is made of aluminum profiles and stainless steel plates. An overall mass of about 30 kg and the small outline dimensions of 50 cm × 30 cm × 30 cm result in convenient portability of the system due to a handle on each side (see figure 5.1a). The reagents are provided by three syringe pumps (1).

A distribution of these reagents from the supply flasks (3) to the microreactor (4) and further from the microrector to the NMR magnet (5) or the collector flask is ensured by four 6-port valves (2). Stepper motors for pumps and valves (6) as well as the NMR spectrometer (7), including the control unit of the overall system and the power supply are located in the back of the device. A 3D model of the flow-based microreactor is shown in figure 5.1c. Furthermore, a 3D model of the flow-through NMR probe head (see section 4.3) and a picture of the NMR spectrometer are shown in figure 5.1d and 5.1e, respectively. The spectrometer works with an external static field generated by a 0.5 T permanent magnet (see section 4.1). Relaxation properties are quantified in terms of transverse (T_2) and longitudinal (T_1) relaxation times.
A schematic overview (see figure 5.2) as well as a detailed description of the device are given in section 5.1. Furthermore, the microreactor, including tape-based design, 3D hydrodynamic flow focusing, as well as the synthesis process is presented in section 5.1.1. The influence of several synthesis parameters on the NMR relaxation process is discussed in section 5.2. Moreover, the effects of alendronate coatings on particles optimized for high transverse relaxivity on the transverse (r_2) and the longitudinal relaxivity (r_1) are investigated in section 5.2.2. Finally, a detailed discussion of the results follows in section 5.3.

5.1 Device Development

A schematic overview of the MiCSMaP device is shown in figure 5.2. Six *flasks* are in the inlet of the front panel (see figure 5.1a). The *supply flasks* (1 to 3) contain the reagents, whereas a cleaning solution is provided by the *cleaning flask* (4). Waste is collected in the *waste flask* (5) and the synthesized particles are collected in the *collector flask* (6).

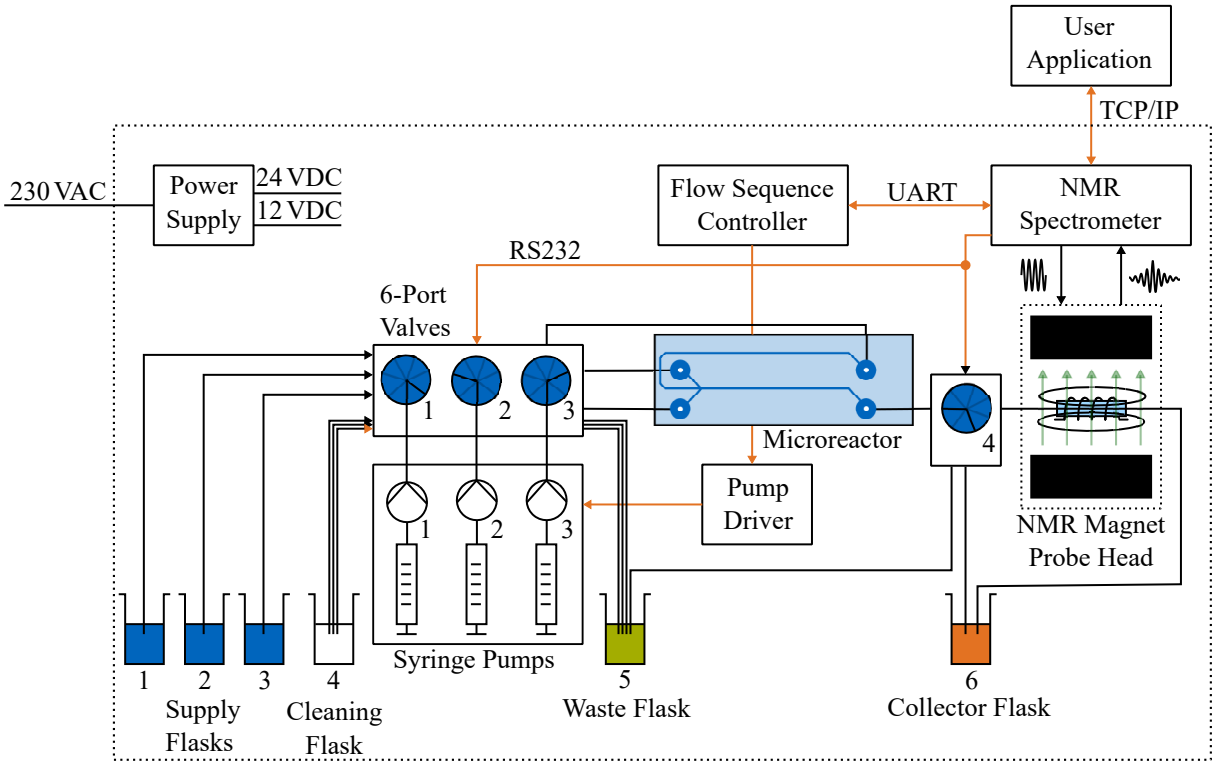

Figure 5.2: Schematic overview of MiCSMaP device.

Reagents are provided to the *microreactor* by three *syringe pumps*, where syringe 1 and 2 hold a volume of 5 ml and syringe 3 holds 1 ml. Each *syringe pump* is directly connected to a *6-port valve*. Moreover, each of these three *6-port valves* is further connected with one of the *supply flasks*, the *cleaning flask*, the *waste flask*, and the *microreactor*. Two additional flasks (not shown here), containing MNPs and water can be connected to allow for the automated determination of transverse and longitudinal relaxivities (see section 5.2.2). To do so, the concentration of the MNPs is reduced by dilution with water. Both are mixed and routed to the *NMR probe head* via valve 4. During the synthesis, valve 4 routes the output of the *microreactor* either to the *NMR probe head* or the *collector flask*. Thereby, the influence of motion during the determination of the relaxation parameters can be avoided. Only a small portion of the sample (19 µl), respecting the limits of B_1-homogeneity is investigated. The remaining stream is directly routed to the *collector flask*. All in all, this tubing allows for a completely automated synthesis process, including cleaning routines and the online determination of NMR relaxation parameters. Furthermore, time consuming determination of relaxivites can be performed in a fully automated manner. Details concerning synthesis, cleaning and relaxivity determination protocols are presented in [93]. Moreover, sequence protocols include the calibration of the NMR spectrometer prior to the synthesis process. After calibration, an automated temperature compensation system tracks the current NMR frequency and updates it in a continuous manner to avoid off-resonance effects caused by B_0 temperature drifts.
The main control unit of the system is the *NMR spectrometer* presented in section 3.1. In addition to the conduction of NMR sequences, the *NMR spectrometer* controls the valves and sets the *flow sequence controller* (ATMEGA2560-15AU, Microchip Technology). The valves (Carvo Smart Valve, Tecan) are adjusted via *RS232*, whereas communication with the *flow sequence controller* is established via *UART*. The *flow sequence controller* sets the pump sequences in terms of speed, direction, and position. Upon reaching the desired positions, feedback is given to the *NMR spectrometer*. Depending on the synthesis sequence, valves are adjusted or NMR experiments are conducted. The *syringe pumps* are driven by bipolar stepper motors (1.4 A, 1.8° step angle). The gear ratio is set such that the 5 ml pumps require 5,689 steps per ml and the 1 ml pump requires 5,000 steps per ml. Each pump has a thread pitch of 1.25 mm. Resolution enhancement can be activated by the microstep mode (1/16). The stepper motors in turn are driven by the *pump driver*, which consists of three microstepping motor drivers (A4988SETTR-T, Allegro Microsystems). A built-in translator as well as five selectable step resolutions, ranging from full- to 1/16-step allow for convenient operation. Switching the step mode is important as cleaning mode and synthesis mode exhibit individual requirements on the plunger speed. In cleaning mode, fast plunger speeds are required, whereas very slow and steady flows are desired in synthesis mode (see section 5.1.1). The drivers are mounted on a breakout board (1182, Pololu). Connectivity between the *flow sequence controller* and the individual motor drivers is established by the carrier card (RAMPS 1.4). To reduce the loss of steps, the plungers are accelerated and decelerated slowly in case of desired speed changes. This is supported by the AccelStepper library.
User data, including the desired sequence parameters are transfered from the user application, running on an external workstation via an ethernet interface (TCP/IP). The device is supplied by mains voltage (230 VAC). 24 VDC and 12 VDC are generated by the *power supply* unit, where the *NMR spectrometer* and the pumps run at 24 V and the valves are supplied with 12 V.

5.1.1 Microreactor and Particle Synthesis

The iron oxide MNPs are synthesized in a tape-based microreactor (see figure 5.2) by coprecipitation of ferric- ($FeCl_3$) and ferrous chloride ($FeCl_2$), and sodium hydroxide ($NaOH$). Furthermore, the iron

precursor solution is acidified by hydrochloric acid (HCl) to reduce the formation of iron hydroxides [94] as well as the oxidation of ferrous ions. The corresponding chemical equation is given as

$$2Fe^{3+} + Fe^{2+} + 8OH^- \rightarrow 2Fe_3O_4 + 4H_2O \tag{5.1}$$

The microfluidic reactor and details concerning 3D flow focusing are shown in figure 5.3.

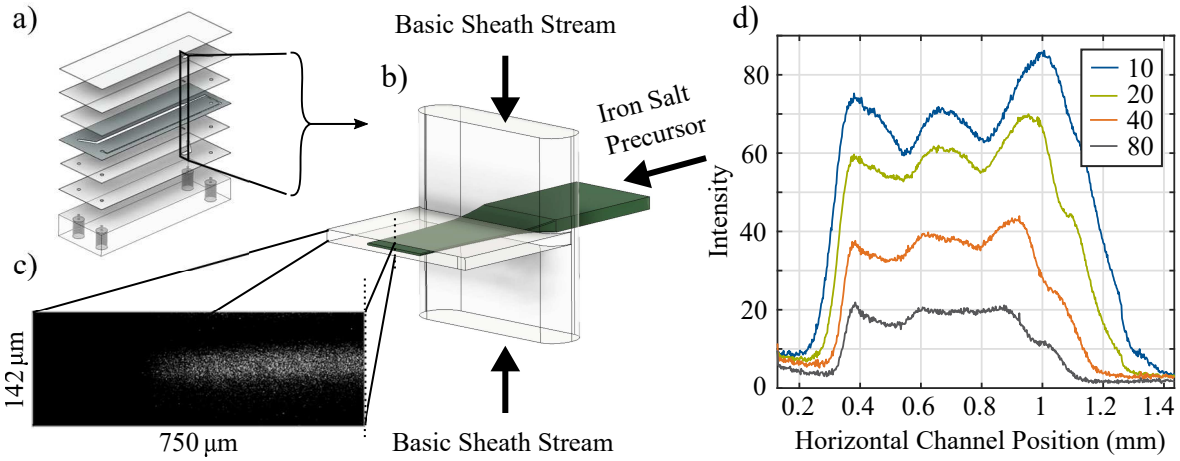

Figure 5.3: Tape-based microreactor and 3D flow focusing. a) The microreactor is designed by the stacking of double-sided pressure sensitive tape and polymer slides. b) Central chamber for 3D flow focusing. c) Characterization of the focused flow profile by confocal microscopy. d) Fluorescence intensity profile of the central reaction channel depending on the flow-rate-ratio between the basic sheath streams and the iron salt precursor.

The microreactor is designed by the stacking of double-sided pressure sensitive tape and polymer slides (Xurography [95]). Formation of the particles takes place in the central reaction channel (see figure 5.3a). This channel is cut into the pressure sensitive tape by a digital cutting plotter. Subsequently, the channel is covered by PMMA slides, applied on both sides of the adhesive tape. The through-hole for 3D focusing (see figure 5.3b) is precisely cut by a laser-cutter. Support channels for the *basic sheath streams* are applied to both sides of the central reaction channel. The microreactor is then covered by two PMMA slides. A thick sheet equipped with four threaded holes is applied to the bottom. Out of this, three holes are for the reagents (two for the *basic sheath streams* and one for the *iron salt precursor*). The fourth one is the outlet for the synthesized particles.
The fast formation of particles synthesized by coprecipitation usually results in depositions inside the microchannels [47, 48, 96]. 3D flow focusing reduces this decomposition as the interface between the *basic sheath streams* and the *iron salt precursor*, where nucleation and growth take place is spatially separated from the channel walls by the *basic sheath stream*. A cross-section view of the central channel is shown in figure 5.3c. The central stream was replaced by fluorescein to display flow focusing via confocal microscopy (LSM 510 Meta, Zeiss). Images were acquired with a 10x/0.3 objective (Plan Neofluor) and a 505 nm to 530 nm bandpass. The pixel exposure time was set to 12.8 µs and the line depth to 1 µm. A separation of the central stream and thus the interface with the base stream from the channel walls is well observable. Figure 5.3d illustrates the influence of the flow-rate-ratio between the outer and the inner stream on the width and the hight of the focused stream. Data was acquired using fluorescence microscopy on a focused stream of a sodium-fluorescein solution. The fluorescence intensity corresponds to the height of the focused stream, which is adjustable by the flow-rate-ratio. Conversely, the width of

the stream is barely affected. Precise control over the interface between the two streams is crucial as this is where particle formation takes place.

5.1.2 Particle Formation and Characterization

Diffusion of the base from the outer sheath in the central sheath leads to the formation of aggregated black precipitates. These are collected at the outlet of the microreactor. The primary particle size is characterized by field emission scanning electron microscopy (FESEM) (see figure 5.4a and figure 5.4b) and dynamic light scattering (DLS) (see figure 5.4c). Furthermore, the composition of the precipitates is characterized by Raman spectroscopy (see figure 5.4d).

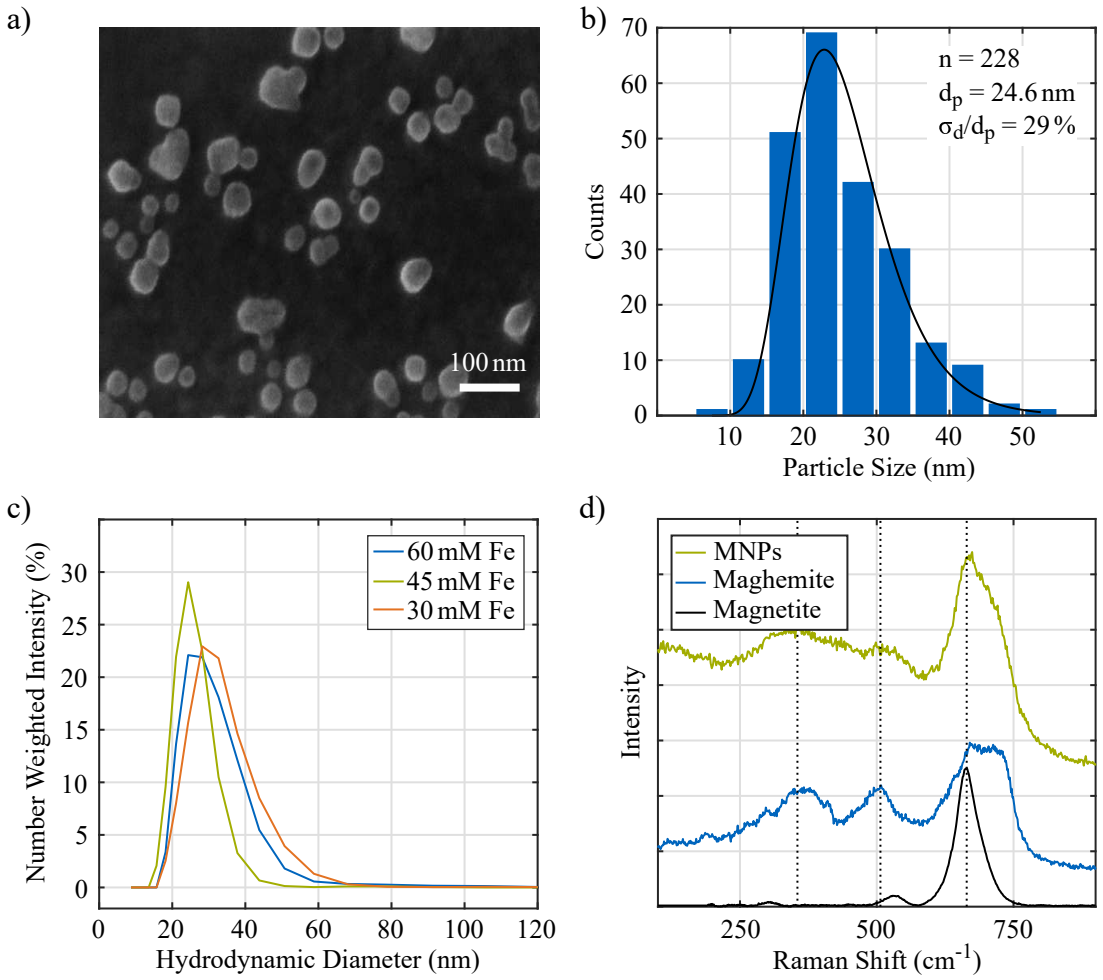

Figure 5.4: Characteristics of peptized particles. a) A FESEM image of peptized particles. b) Evaluation of the FESEM image in terms of primary particle size. Data is fitted with log-normal distribution. c) Peptized particle size distribution determined by DLS. Number weighted intensity as a function of the hydrodynamic diameter depending on the iron precursor concentration. d) Raman spectra of the synthesized particles, maghemite, and magnetite.

The primary particles on the FESEM image (see figure 5.4a) generally show a spherical shape. Particle size is evaluated for 228 particles using ImageJ. The resulting size distribution for an iron precursor

concentration of 60 mM, a sodium hydroxide concentration of 9.8 mM, and a flow-rate-ratio of 20 is shown in figure 5.4b. A log-normal fit reveals an average particle size of 24.6 nm with a relative standard deviation of 29 %. Figure 5.4c shows the number weighted hydrodynamic diameter of peptized particles measured by DLS for various iron precursor concentrations. The results are consistent with the ones obtained by analyzing the FESEM image. Furthermore, synthesizing particles at an increasing sodium hydroxide concentration, corresponding to pH values ranging from 10 to 12 decreases the primary particle size from 24.6 nm to 12.3 nm. The corresponding relative standard deviation σ_d / d_p decreases from 29 % to 23 % for a base concentration increasing from 9.8 mM to 20 mM. For a base concentration of 40 mM, the relative standard deviation is 26 %.
Moreover, the influence of the total iron concentration in the precursor solution on the primary particle size is investigated. An increase of the concentration from 30 mM to 45 mM to 60 mM while keeping the sodium hydroxide concentration at a constant level led to an increase from 15.1 nm to 21.9 nm to 24.6 nm, respectively. For lower precursor concentrations, the relative standard deviation increases to 32 %.
The composition of the synthesized particles is investigated by Raman spectroscopy. Figure 5.4d shows the Raman spectrum of the synthesized MNPs as well as the spectra of magnetite and maghemite as a reference. Typical for magnetite is a strong peak at 664 cm^{-1} and a rather weak one at 532 cm^{-1} [97]. Maghemite exhibits a broad, flat band from 660 cm^{-1} to 710 cm^{-1} and two weaker peaks at 300 cm^{-1} and 530 cm^{-1} [44, 98]. The spectrum of the synthesized MNPs corresponds to a superposition of spectra corresponding to maghemite and magnetite. A strong peak at 664 cm^{-1} indicates the presence of magnetite, whereas the slow decay to 710 cm^{-1} as well as the weak peaks at 300 cm^{-1} and 530 cm^{-1} indicate the presence of maghemite.

5.2 Particle Characterization by NMR Relaxation Properties

In the following, the particle suspension is investigated in terms of transverse (R_2) and longitudinal relaxation rate (R_1) in order to monitor the microfluidic synthesis process. Determination of the relaxation parameters R_2 and R_1 is performed by the CPMG and the inversion recovery sequence, respectively. As both sequences are very sensitive to movements inside the sample, the sample is required to be at rest. To achieve this during a continuous synthesis process, the outlet stream of the microreactor is split into two fluidic lines. An automated valve (valve 4, see figure 5.2) redirects the stream during the measurement directly into the *collector flask* (see figure 5.2). After the measurement, the investigated sample is directed into the *collector flask* as well.

5.2.1 Particle Synthesis

Figure 5.5 shows the results of online measurements of the transverse relaxation rate R_2 for iron precursor concentrations of 60 mM, 45 mM, and 30 mM.
The transverse relaxation rate for an iron precursor concentration of 60 mM ranges from 0.8 s^{-1} to about 1.1 s^{-1}. A concentration of 45 mM results in a rise to about 1.4 s^{-1}, whereas for the lowest iron precursor concentration (30 mM), R_2 exhibits a value of about 1.2 s^{-1}. Conversely, variations of the base concentration do not statistically influence the transverse relaxation rate. Values always ranged between averages of 1.34 s^{-1} and 1.55 s^{-1}, regardless of the base concentrations.
In the following, the synthesized MNPs are analyzed concerning their NMR relaxation properties after peptization and colloidal stabilization by directly adding diluted hydrochloric acid. Figure 5.6d shows

the strong dependence of the iron precursor concentration on the transverse relaxation rate. The higher the concentration, the higher is R_2. The iron concentration was kept constant by dilution after the synthesis in order to enhance the comparability of the results. For lower iron concentrations like 30 mM or 45 mM, the microreactor formed a brown supernatant instead of the black precipitate, found when using an iron precursor concentration of 60 mM. The Raman spectrum of the supernatant exhibits an increasing amount of goethite and hematite with a decreasing iron precursor concentration. For a precursor concentration of 30 mM, goethite and hematite were the main components, whereas at a concentration of 60 mM, no signs of goethite and hematite were present. This is well in line with the results shown in figure 5.6d.

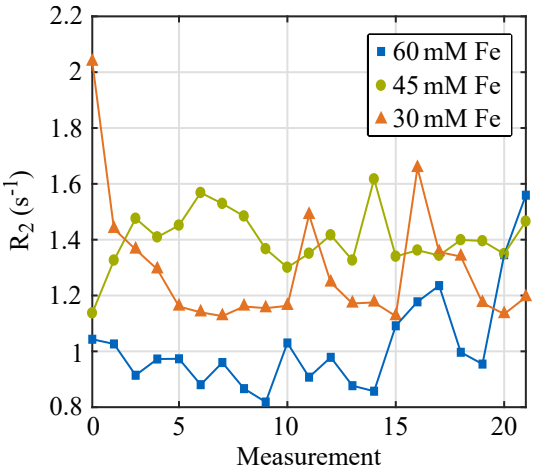

Figure 5.5: Online determination of the transverse relaxation rate during the synthesis process depending on the iron precursor concentration.

Peptization is performed by a hydrochloric acid dispersion with a dispersion pH ranging from 1 to 4. The MNP cluster size can be adjusted by this pH value and thus by the concentration of the hydrochloric acid. This is shown in figure 5.6a, where the intensity averaged hydrodynamic diameter (z-average), measured by DLS right after peptization is given as a function of the peptization pH. The hydrodynamic diameter of the clusters ranges from 38 nm at a pH of 1.08 up to 344 nm at a pH of 3.45. Results do not depend on the pH after synthesis and thus on the sodium hydroxide concentration of the basic sheath stream. For very low pH values (< 1.5), the number weighted size distribution is equal to the size distribution of the primary particles obtained by FESEM (see figure 5.4a and 5.4b). This indicates that clustering is completely avoided by the use of such low peptization pH values.
Right after peptization, the NMR relaxation properties of the sample are investigated in terms of transverse (R_2) and longitudinal (R_1) relaxation rate. For enhanced comparability between different iron precursor concentrations, the sample is diluted such that the total Fe concentration is equal. Figures 5.6b to 5.6d illustrate the dependence of the hydrodynamic cluster diameter on the relaxation rate R_1 and R_2. The transverse relaxation rate R_2 as a function of the z-average is shown in figure 5.6c for various base stream concentrations, whereas figure 5.6d shows R_2 for various iron precursor concentrations. For low diameters, the relaxation rate increases with the hydrodynamic diameter of the particle clusters up to a value of 120 s^{-1}. A maximum is reached at a cluster size of approximately 120 nm. Highest relaxation rates are found for a base concentration resulting in a pH of 10.14 (see figure 5.6c). For even larger particle clusters, the relaxation rate decreases again. Conversely, the longitudinal relaxation rate R_1, shown

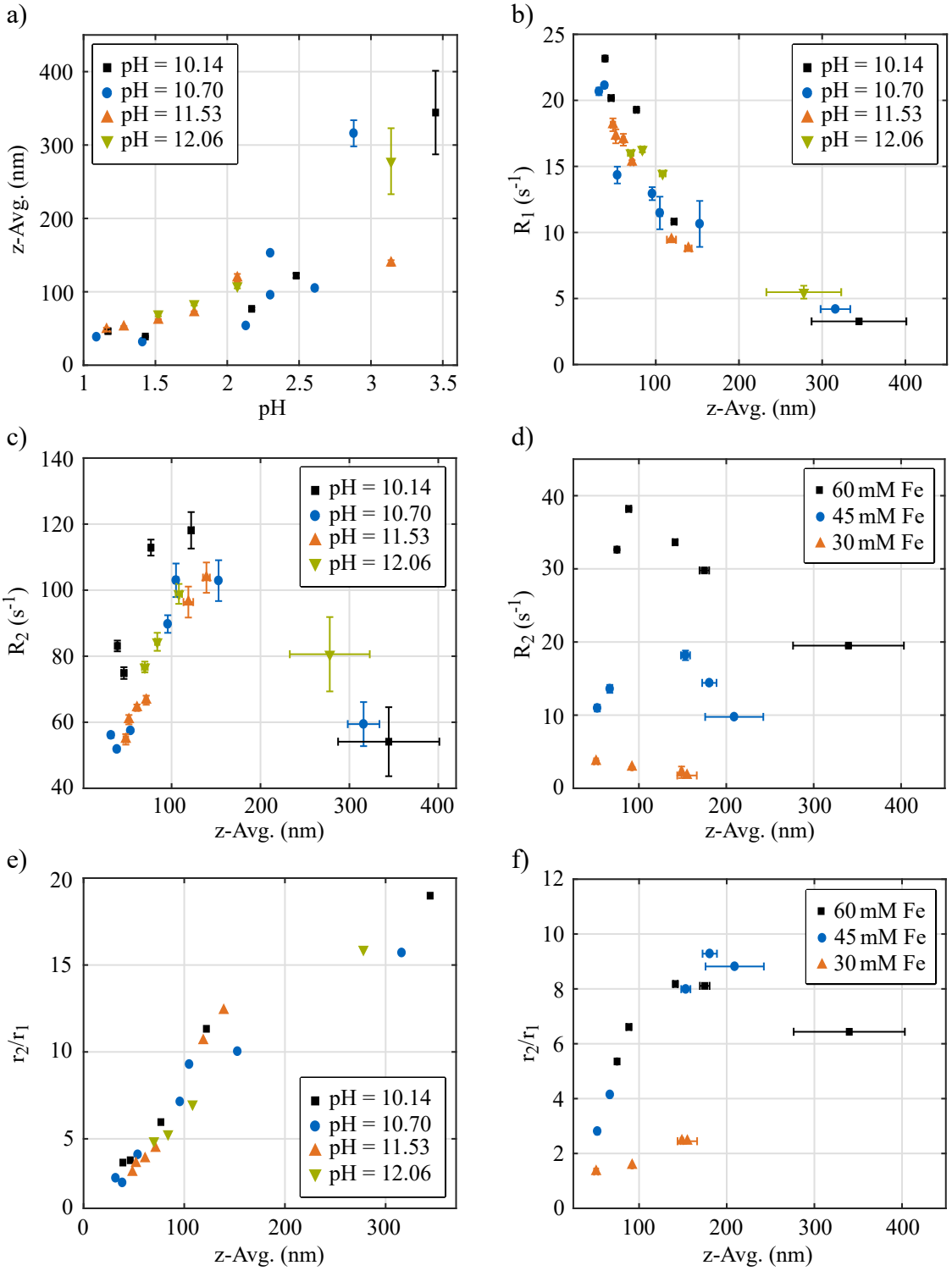

Figure 5.6: Influence of particle synthesis conditions on NMR relaxation parameters. a) Hydrodynamic diameter as a function of the peptization pH value. b) R_1 depending on the base concentration. c) R_2 depending on the base concentration. d) R_2 depending on the iron precursor concentration. e) and f) Relaxivity ratio r_2/r_1 depending on base and iron precursor concentration, respectively.

in figure 5.6b decays continuously with the hydrodynamic diameter.
Figure 5.6e and figure 5.6f show the ratio between the transverse (r_2) and longitudinal relaxivity (r_1) as a function of the hydrodynamic diameter for various base and iron precursor concentrations, respectively. This ratio (see equation 5.2) is a common dimensionless parameter used to classify contrast agents [34, 35]. Small or positive ratios correspond to large longitudinal relaxivities whereas the transverse relaxivity is dominant for large or negative ratios. The determination of relaxivities is a cumbersome and time-consuming process. However, the ratio between transverse and longitudinal relaxivity can be determined by the corresponding relaxation rates without any knowledge about the dispersion concentration c. Assuming that the relaxation rate R_i of the particle dispersion is much higher than the relaxation rate $R_{i,sol}$ of the solvent, the ratio of relaxivities can be expressed by

$$\frac{r_2}{r_1} = \frac{(R_2 - R_{2,sol})/c}{(R_1 - R_{1,sol})/c} = \frac{(R_2 - R_{2,sol})}{(R_1 - R_{1,sol})} \approx \frac{R_2}{R_1} \tag{5.2}$$

The ratio r_2/r_1 shows a maximum of 9 for a cluster size of about 180 nm (see figure 5.6f). Equivalent values are obtained for an iron precursor concentration of 45 mM and 60 mM. However, for 30 mM, values are much lower. According to figure 5.6e, the base concentration does not statistically influence the relaxivity ratio.

5.2.2 Particle Coating

In order to avoid particle aggregation and provide surface functionality in terms of bioconjugation, the synthesized particles are further coated and treated. An efficient way to stabilize MNPs is the application of biocompatible polymers. Since polymer layers lead to a significant increase of the hydrodynamic diameter, NMR relaxation properties are strongly influenced as well [40]. A promising alternative to biocompatible polymers are bifunctional molecules [99] that exhibit a strong affinity to the surface of iron oxides via carboxylate, sulfonate or phosphonate groups [100]. Enhanced hydrophilicity as well as bioconjugation can be achieved by a second amine or carboxylate group. Bisphosphonates like alendronate (bisphosphonate with amine functionality) stand out due to their strong binding capabilities concerning iron oxides [101]. MNPs coated with alendronate find application in various research areas like targeted drug delivery [29, 45] and theranostics [102].
Transverse (r_2) and longitudinal relaxivities (r_1) are investigated by the determination of the corresponding relaxation rates for various iron concentrations. After determination of the relaxation rates, the iron concentration is measured by inductively coupled plasma mass spectrometry (ICP-MS). The relaxivity is defined as the slope of the linear regression over the corresponding relaxation rates. Particle concentrations are set fully automatically by dilution of the synthesized particle dispersion with water. The pump/valve sequence further forwards the sample in the NMR probe head (see figure 5.2).
Prior to the determination of the relaxivity, bare MNPs are stabilized in an acidic medium (see figure 5.7a), whereas the MNPs to be coated are incubated with alendronate. Successful coating is shown by the determination of the isoelectric point [45] that shifts from 7.5 to 3.7. This is consistent with [45, 102]. Due to the reduced isoelectric point of alendronate coated MNPs, the particles tend to flocculate at the applied pH value of 2.5. This allows for magnetic particle separation. Furthermore, coated particle are washed and redispersed prior to the measurements. The influence of alendronate coating on the transverse and the longitudinal relaxivities of particle clusters, optimized in terms of transverse relaxivity are shown in figure 5.7.

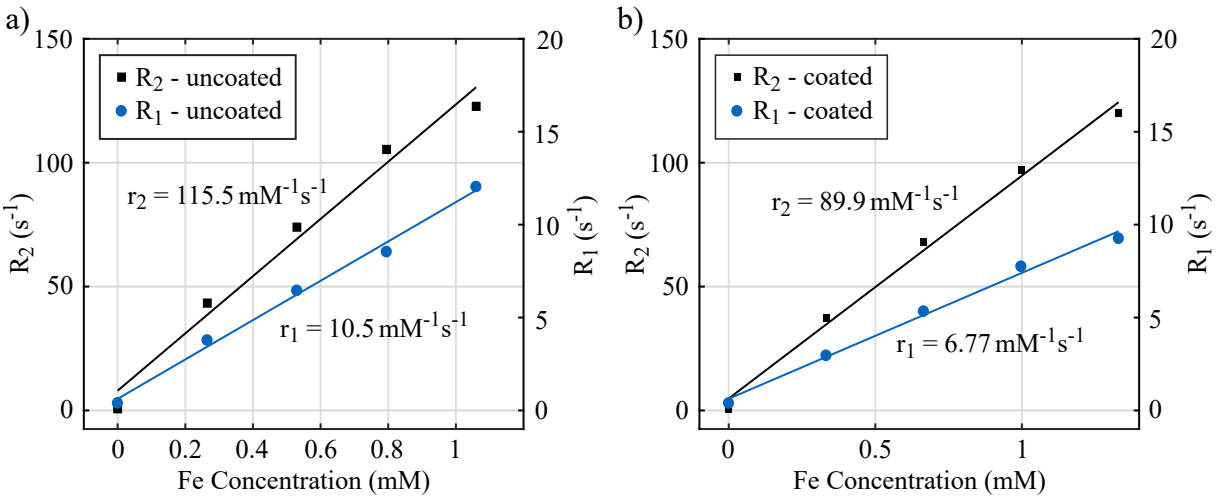

Figure 5.7: Influence of alendronate coating on the transverse and the longitudinal relaxivities of MNPs. Measurement data is obtained by an automated pump sequence. a) Relaxation rates of bare MNPs as a function of the *Fe* concentration. b) Relaxation rates of alendronate coated MNPs as a function of the *Fe* concentration.

Figure 5.7a shows the transverse and the longitudinal relaxation rate as a function of the *Fe* concentration for bare MNPs, whereas figure 5.7b shows the results for alendronate coated MNPs. The transverse relaxivity decreases from 115.5 $mM^{-1}s^{-1}$ to 89.9 $mM^{-1}s^{-1}$ and the longitudinal relaxivity from 10.5 $mM^{-1}s^{-1}$ to 6.77 $mM^{-1}s^{-1}$.

5.3 Discussion

The MiCSMaP reactor presented throughout this chapter integrates the flow-based synthesis and the subsequent functionalization of MNPs with characterization in terms of NMR relaxation parameters in one device. The construction method of the microreactor is called Xurography. Double-sided pressure sensitive tape is stacked with polymer foils [95]. Even though the minimum achievable channel width of about 200 µm is rather large compared to lithographic methods (ranging from tens to several hundreds of microns [103]), Xurography can be favourable due to practicality. The assembly is fast and no clean room facilities are required compared to lithography. New designs can be evaluated by simply modifying the cutting pattern of the cutting plotter. This flexibility states one of the most outstanding advantages. Furthermore, the construction process is simplified by the use of pressure sensitive tape, which avoids cumbersome bonding processes. Channel clogging caused by the fast formation of particles using coprecipitation [47, 48, 96] could be strongly reduced by the application of 3D hydrodynamic flow focusing. Limiting the number of sheath streams to two is important in order to keep the number of pumps and thus the complexity of the system at a minimum (see figure 5.2 and 5.1).
The FESEM image shown in figure 5.4a reveals a generally spherical appearance of the primary particles. Numerical size analysis via ImageJ indicates an average particle size of 24.6 ± 7.1 nm. This is consistent with the size distribution obtained by DLS. Moreover, both methods exhibit a log-normal behavior. However, the hydrodynamic diameter obtained from DLS measurements is slightly larger because of solvation layers around the particles.
The primary particle size strongly depends on the sodium hydroxide concentration. Increasing the pH

value from 10 to 12 led to a decrease of the primary particle size from 24.6 nm to 12.3 nm. Especially for lower pH values, the primary particle size was larger than the most common value of 15 nm reported for bulk syntheses [104–106]. As low pH values after the addition of the iron salt precursor can lead to the formation of non-magnetic materials, bulk syntheses are usually performed at a high pH value. Yet, the pH value is a crucial parameter in terms of primary particle size determination during coprecipitation. Increasing the pH value usually leads to a decrease of the primary particle size [107]. In general, larger primary particles are preferable due to a higher saturation magnetization. This, in turn results in a higher transverse relaxivity. Precise control of these low alcalic pH values throughout the synthesis is realizable using microreactors. The relative standard deviation σ_d / d_p of the primary particle size decreases from 29 % to 23 % when increasing the base concentration from 9.8 mM to 20 mM. Still, the relative standard deviation is small compared to most benchtop batch syntheses of MNPs by coprecipitation [106, 108]. These range between 30 % [105, 109] and 35 % [48]. Furthermore, it was shown that the primary particle size decreases with a decreasing iron precursor concentration. While keeping the sodium hydroxide concentration at a constant level, a decrease from 24.6 nm to 15.1 nm for concentrations from 60 mM to 30 mM was observed.

The Raman spectra shown in figure 5.4d confirm the presence of both, magnetite and traces of maghemite. As Raman spectroscopy has a very limited penetration depth, the spectra mostly represent the surface composition, where the sample tends to be highly oxidized [98].

Furthermore, the influence of the synthesis conditions on the NMR relaxation properties of the sample was investigated. Redirection of the sample flow allows for measurements at rest without interrupting the synthesis process. For iron precursor concentrations ranging from 30 mM to 60 mM, the transverse relaxation rate is between $0.8\,\mathrm{s}^{-1}$ and $1.6\,\mathrm{s}^{-1}$ (see figure 5.5). The consumption of ferric precursors is indicated as each of these values is lower than the relaxation rate expected for the pure iron precursor. No statistical effect on R_2 was observed by variations of the base concentration. Most likely, this is a result of highly aggregated particles during the synthesis process. The size of the clusters was determined to be several hundred nanometers at the outlet of the reactor. This dominates the effects caused by primary particle size variations such that for large clusters, the influence of size variations on T_2 can be neglected [39, 108].

Cluster sizes strongly depend on the peptization pH value. In contrast, the pH value of the base streams did not alter the results (see figure 5.6a). For very low pH values (< 1.5), the size distribution is equal to the size distribution obtained by FESEM measurements. Therefore, it is assumed that the particles are not clustered anymore.

Figure 5.6d shows a strong decay of the transverse relaxation rate with the iron precursor concentration. This decay is due to an increasing amount of non-magnetic goethite and hematite, indicated by Raman spectroscopy for lower concentrations. A fast condensation process, supported by a high iron precursor concentration, turned out the be important for the formation of magnetite. Fast condensation reduces the oxidation of ferrous species at alkaline pH as well as the formation of non-magnetic iron oxides and iron hydroxides [94].

Figure 5.6c and 5.6d show the transverse relaxation rate R_2 as a function of the z-average. The rate distribution matches the three predicted regimes of relaxation rates [39, 108, 110]. In the motional averaging regime, R_2 increases with the hydrodynamic diameter up to values of $120\,\mathrm{s}^{-1}$. The dephasing of proton spins is accelerated by stronger local field inhomogeneities generated by larger particles. Therefore, the refocusing effectiveness of the spin echos decreases [39]. A maximum is reached at a cluster size of approximately 120 nm. The plateau of the static dephasing regime, mostly determined by the saturation magnetization of the particles does not depend on the cluster size anymore. The increasing local field

inhomogeneities are in balance with the reduced mobility due to increased diffusion constants of larger particle clusters (see section 2.11). According to figure 5.6c, a maximum of R_2 is obtained for a pH vlaue of 10.14, resulting from the lowest base concentration. According to several reaction optimization studies on magnetite coprecipitation [111, 112], higher magnetite contents are expected for lower synthesis pH values. This in turn leads to higher saturation magnetizations. Furthermore, the primary particle size and thus the saturation magnetization at a given cluster size was observed to increase with a decreasing synthesis pH value. The subsequent decrease of the relaxation rate for very large particle clusters (see figure 5.6c and 5.6d) is caused by decreasing average field gradients of large clusters. Furthermore, the field inhomogeneities tend to be spatially more constant (see section 2.11). These effects increase the efficiency of spin echos and thus decrease the relaxation rate. The results show a strong dependence of the transverse relaxation rate on the hydrodynamic diameter. This highlights the importance of tuning the cluster size throughout the synthesis process in order to optimize relaxivities.
The relaxivity ratio r_2/r_1 is a dimensionless parameter, independent of the *Fe* concentration (see equation 5.2). By comparing the transverse relaxation rates shown in figure 5.6d to the relaxivity ratio shown in figure 5.6f, it is observable that R_2 is much higher for iron precursor concentrations of 60 mM compared to precursor concentrations of 45 mM, whereas r_2/r_1 is equivalent for both precursor concentrations. This indicates that the maximum transverse relaxivities of particles synthesized under both syntheses conditions can be considered equal. Variations in figure 5.6d result from particle concentration deviations. This dependence is avoided by the relaxivity ratio due to the independence on the concentration. Furthermore, this is in line with the similar primary particle sizes obtained by a synthesis with iron precursor concentration of 45 mM and 60 mM. Thus, a significant analytical value for the optimization of relaxivities is in the determination of relaxation rates.
Transverse (r_2) and longitudinal relaxivities (r_1) were investigated by the determination of the corresponding relaxation rates for various *Fe* concentrations. The actually time-consuming and cumbersome determination of relaxivities is facilitated to a fully automatic process by the MiCSMaP device. This leads to tremendous time savings as no user interventions are required. The decrease of the transverse relaxivity from 115.5 $mM^{-1}s^{-1}$ to 89.9 $mM^{-1}s^{-1}$ and of the longitudinal relaxivity from 10.5 $mM^{-1}s^{-1}$ to 6.77 $mM^{-1}s^{-1}$ for uncoated and alendronate coated particles can be explained by variations in the hydrodynamic diameters [39]. Particle cluster sizes increased from 230 ± 9 nm to 267 ± 4 nm by the coating procedure, according to DLS. Yet, alendronate coating increased the relaxivity ratio r_2/r_1 from 11.0 to 13.27 as the longitudinal relaxivity decreased. These results were benchmarked with [35], a summarization of relaxivities and relaxivity ratios collected from several publications. Depending on the coating of iron oxide MNPs, transverse relaxivities range between 17.5 $mM^{-1}s^{-1}$ and 92.0 $mM^{-1}s^{-1}$, whereas longitudinal relaxivities range between 2.4 $mM^{-1}s^{-1}$ and 9.5 $mM^{-1}s^{-1}$. The corresponding relaxivity ratios r_2/r_1 range between 2.97 and 24.5. Concerning the optimization towards high transverse relaxivity, the synthesized particles are on the upper end.
The maximal production throughput of magnetite is calculated as 40 $\mu mol\,h^{-1}$ under the given synthesis conditions (60 mM iron precursor, 9.8 mM sodium hydroxide, flow rate ratio 20). As an injection of iron oxide based contrast agents for MRI typically requires about 15 µmol *Fe* per kg of bodyweight [113] a throughout of 40 $\mu mol\,h^{-1}$ seems very little on the first sight. However, due to the low production costs, the throughput can be increased by the parallelization of multiple microreactors. Besides product development, the reactor can be applied for the synthesis of individual point-of-use applications.

6 Detection of Direct and Indirect Dipole-Dipole Couplings via Zero-Quantum Coherences

Individual nuclear spins are coupled with each other by various magnetic coupling mechanisms (see section 2.3.2). These include direct and indirect dipole-dipole couplings. While indirect dipolar couplings are observable in the one-dimensional SQ spectra, intermolecular direct dipolar couplings are exclusively observable by multi-dimensional spectroscopy. The coupling of spins results in the formation of MQCs. A subgroup of these are ZQCs, which show outstanding advantages like a reduction of inhomogeneous line broadening (see section 2.10) and thus an enhanced resolution in the indirect dimension. Spins in close proximity to each other show the lowest dependence on field inhomogeneities [114]. Furthermore, the spectral window in the indirect dimension is consistent [115]. MQCs cannot be observed directly. Indirect detection by two- or multi-dimensional experiments is required. The detection of ZQCs allows for the determination of J-coupling networks to investigate intramolecular structures [12], even in very inhomogeneous fields [51]. Moreover, the detection of iZQCs even allows for resolving subvoxel intermolecular structures [13, 14].
In this chapter, the SoC-based NMR spectrometer (see section 3.2) and the gradient-capable NMR probe head (see section 4.4) are applied for the detection of intra- (see section 6.1) and intermolecular (see section 6.2) dipolar couplings. ZQCs caused by intramolecular couplings are detected by the HZQC sequence (see figure 6.1), whereas iZQCs caused by intermolecular couplings are detected by the HOMOGeneity ENhancement by Intermolecular ZEro-quantum Detection (HOMOGENIZED) sequence (see figure 6.7). Both sequences require the application of pulsed field gradients. A single spoiling pulse is sufficient to isolate ZQCs in HZQC experiments [12, 51, 52]. Furthermore, for iZQC experiments, pulsed field gradients are used as correlation pulses. Breaking the magnetic isotropy of a spin system can lead to strong signal enhancements [53–55]. The applicability of the gradient-capable probe head for these applications is determined.

6.1 Detection of Indirect Dipole-Dipole Coupling Networks via ZQCs

In the following, the SoC-based NMR spectrometer (see section 3.2) and the gradient-capable NMR probe head (see section 4.4) are applied on the mapping of J-couplings in 1-butanol via the detection of ZQCs. At first, the pulse sequence for HZQC measurements [12, 51, 52] is presented. A detailed analysis using the quantum mechanical approach is given in section 6.1.1 for an AX-spin system. The spectral analysis of the theoretically observable magnetization and the expected spectral pattern for an AX-spin system follow in section 6.1.2. To ensure that only the desired ZQCs contribute to the final spectrum, a 4-step phase cycling scheme [12, 52], presented in section 6.1.3 is applied. NMR specific characteristics of 1-butanol like coupling constants and chemical shift values [116–118] as well as their influence on the two-dimensional HZQC spectrum are given in section 6.1.4. Limitations due to relaxation processes, FFT window consideration and temperature induced frequency shifts are discussed thereafter. Finally, the resulting measurement data is presented depending on shimming conditions and sequence parameters.

6.1.1 HZQC Pulse Sequence and the Quantum Mechanical Treatment of an AX-Spin System

As ZQCs are not directly detectable via single-excitation experiments, indirect detection in terms of a two-dimensional experiment is required [114]. An NMR pulse sequence, suitable for HZQC measurements is illustrated in figure 6.1 [12, 51, 52]. The corresponding coherence transfer pathway (CTP) is shown below.

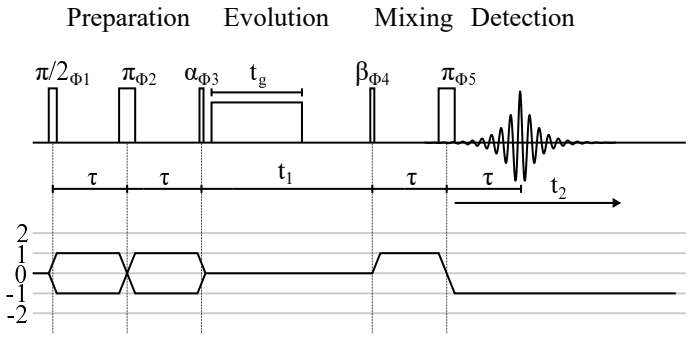

Figure 6.1: HZQC pulse sequence and the corresponding coherence transfer pathway.

In the following, this sequence is analyzed theoretically for an AX-spin ensemble (weak coupling assumed) consisting of N_I I-spins and N_S S-spins, coupled with the constant J_{IS}. The corresponding offset frequencies are denoted as Ω_I and Ω_S, respectively. Typically for two-dimensional multiple-quantum experiments, the sequence is functionally separated in four periods [64, 65]. During the *perparation* period ZQCs are excited. These coherences evolve throughout the *evolution* period prior to the *mixing* period, where ZQCs are transfered back into observable SQCs. These are acquired during the *detection* period. The following calculations are performed for the first phase cycle (see table 6.1b).

Equilibrium Density Operator

The equilibrium density operator (see section 2.8) for this spin system (only first-order terms of equation 2.48) is given as

$$\begin{aligned}\hat{\rho}_{eq} &= 2^{-N_I}\left(\hat{1}-\zeta\sum_{i=1}^{N_I}\hat{I}_{iz}\right)2^{-N_S}\left(\hat{1}-\zeta\sum_{k=1}^{N_S}\hat{S}_{kz}\right)\\ &\approx 2^{-(N_I+N_S)}\left(\hat{1}-\zeta\left(\sum_{i=1}^{N_I}\hat{I}_{iz}+\sum_{k=1}^{N_S}\hat{S}_{kz}\right)\right)\\ &\approx -N\zeta\left(\hat{I}_z+\hat{S}_z\right),\end{aligned} \tag{6.1}$$

where the temperature approximation is applied. The first transformation is valid as two-term product operators of the form $\hat{I}_i\hat{S}_k$ are neglectable due to the prefactor ζ^2, where $\zeta << 1$. All spins I_i and all spins S_k behave equivalent as an ensemble of individual AX-spin systems is assumed. This leads to the second transformation. The result is equivalent to the equilibrium density operator of a single AX-spin system, multiplied by the number of spins $N = N_I + N_S$ in the ensemble. The dimension of the density operator is reduced from $2^{(N_I+N_S)} \times 2^{(N_I+N_S)}$ to 4×4.

Preparation Period

During the *preparation* period, ZQCs are excited [119]. The first RF-pulse transforms longitudinal magnetization into in-phase SQCs. Throughout the subsequent period of free precession, the in-phase SQCs $\hat{I}_y$ and $\hat{S}_y$ evolve under the influence of J-coupling (see section 2.3.2) into anti-phase SQCs of the form $\hat{I}_x\hat{S}_z$ and $\hat{S}_x\hat{I}_z$. These anti-phase SQCs are subsequently transformed into the desired ZQCs as well as undesired double-quantum coherences by a third RF-pulse. The coupling rate J_{IS} is rather small (approximately 7 Hz for aliphatic compounds like 1-butanol [117]) compared to the transversal relaxation rate R_2^*. To avoid a signal reduction due to inhomogeneous line broadening (ranging from 22 Hz to 300 Hz depending on shim settings) during the build-up time, a refocusing pulse is inserted [120]. Thereby, anti-phase SQCs as well as the corresponding ZQCs exclusively depend on the echo time τ. The density operator $\hat{\rho}(2\tau)$ is given as

$$\begin{aligned}\hat{\rho}(2\tau) &= N\zeta\left(\cos(2\pi J_{IS}\tau)\hat{I}_y - \sin(2\pi J_{IS}\tau)2\hat{I}_x\hat{S}_z + \cos(2\pi J_{IS}\tau)\hat{S}_y - \sin(2\pi J_{IS}\tau)2\hat{S}_x\hat{I}_z\right)\\ &\approx -N\zeta\sin(2\pi J_{IS}\tau)\left(2\hat{I}_x\hat{S}_z + 2\hat{S}_x\hat{I}_z\right),\end{aligned} \tag{6.2}$$

where the approximation to line two is valid because in-phase SQCs of the form $\hat{I}_y$ and $\hat{S}_y$ are not affected by the subsequent RF-pulse in y-direction. Therefore, these operators are dephased by the spoiling pulse during the *evolution* period and thus do not contribute to the observable signal. Anti-phase SQCs are transfered to ZQCs by the final preparation pulse with a flip angle α_{Φ_3}. The density operator $\hat{\rho}(t_g = 0)$ at the end of the *preparation* period is given as

$$\begin{aligned}\hat{\rho}(t_g = 0) = -N\zeta\sin(2\pi J_{IS}\tau)\Big(&\cos^2(\alpha)2\hat{I}_x\hat{S}_z - \sin^2(\alpha)2\hat{I}_z\hat{S}_x + \sin(\alpha)\cos(\alpha)(2\hat{I}_x\hat{S}_x - 2\hat{I}_z\hat{S}_z)\\ &+\cos^2(\alpha)2\hat{I}_z\hat{S}_x - \sin^2(\alpha)2\hat{I}_x\hat{S}_z + \sin(\alpha)\cos(\alpha)(2\hat{I}_x\hat{S}_x - 2\hat{I}_z\hat{S}_z)\Big)\\ &\approx -2N\zeta\sin(2\pi J_{IS}\tau)\sin(\alpha)\cos(\alpha)2\hat{I}_x\hat{S}_x\\ &\approx -N\zeta\sin(2\pi J_{IS}\tau)\sin(\alpha)\cos(\alpha)\hat{ZQ}_x^{IS}\\ &= -\frac{N}{2}\zeta\sin(2\pi J_{IS}\tau)(\hat{I}_+\hat{S}_- + \hat{I}_-\hat{S}_+)\\ &= A(\hat{I}_+\hat{S}_- + \hat{I}_-\hat{S}_+),\end{aligned} \tag{6.3}$$

where $A = -\frac{N}{2}\zeta\sin(2\pi J_{IS}\tau)$. All coherences with a coherence order greater than zero are dropped due to dephasing of the subsequent spoiling pulse. The polarization operators $2\hat{I}_z\hat{S}_z$ can be dropped as well as they do not lead to observable magnetization during the *detection* period. ZQCs are exclusively contained in the operator $\hat{I}_x\hat{S}_x$ (see section 2.9) that depends on the factor $\sin(\alpha)\cos(\alpha)$. This term is maximized for $\alpha = \pi/4$ to 0.5. The ZQ operator $\hat{ZQ}_x^{IS}$ is further expressed by the product operators $\hat{I}_+\hat{S}_-$ and $\hat{I}_-\hat{S}_+$ (see section 2.9), where $\hat{I}_+\hat{S}_-$ corresponds to the p-type ZQC and $\hat{I}_-\hat{S}_+$ to the n-type ZQC with respect to spin I. Conversely, the same with respect to S, as the coherences are conjugate complex to each other.

Evolution Period

During the *evolution* period, the excited ZQCs evolve for a duration t_1 with the corresponding ZQ frequency $\pm\Omega_{ZQ}^{IS} = \pm(\Omega_I - \Omega_S)$, where p-type coherences (with respect to I) evolve with $+\Omega_{ZQ}^{IS} = \Omega_I - \Omega_S$ and n-type coherences evolve with $-\Omega_{ZQ}^{IS} = \Omega_S - \Omega_I$. ZQCs are only affected by Zeeman interactions. In contrast, interactions due to indirect dipole-dipole couplings do not affect ZQCs [64, 65]. As $\hat{I}_+\hat{S}_-$ and $\hat{I}_-\hat{S}_+$ precess in opposite directions, both need to be considered separately. P- and n-type ZQCs are expressed by cartesian operators as

$$\begin{aligned}\hat{I}_+\hat{S}_- &= \frac{1}{2}(\hat{ZQ}_x + j\hat{ZQ}_y) = \hat{I}_x\hat{S}_x + \hat{I}_y\hat{S}_y + j\hat{I}_y\hat{S}_x - j\hat{I}_x\hat{S}_y \\ \hat{I}_-\hat{S}_+ &= \frac{1}{2}(\hat{ZQ}_x - j\hat{ZQ}_y) = \hat{I}_x\hat{S}_x + \hat{I}_y\hat{S}_y - j\hat{I}_y\hat{S}_x + j\hat{I}_x\hat{S}_y\end{aligned} \tag{6.4}$$

For the following discussion, the density operator $\hat{\rho}$ is split such that $\hat{\rho} = \hat{\rho}^{(+)} + \hat{\rho}^{(-)}$, where $\hat{\rho}^{(+)}$ corresponds to $\hat{I}_+\hat{S}_-$ and $\rho^{(-)}$ corresponds to $\hat{I}_-\hat{S}_+$. At $t_1 = 0$, the spoiling pulse (see section 4.4) is applied for a duration t_g. Coherences with a coherence order greater than zero dephase (see figure 4.8), which leads to a simplification of the phase cycling scheme shown in table 6.1b by a factor of four [12, 52]. ZQCs evolve in a sinusoidal way such that the density operators at the end of the *evolution* period are given as

$$\begin{aligned}\hat{\rho}^{(+)}(t_1) &= A\frac{1}{2}\left((\cos(\Omega_{ZQ}t_1) - j\sin(\Omega_{ZQ}t_1))\,\hat{ZQ}_x + j\,(\cos(\Omega_{ZQ}t_1) - j\sin(\Omega_{ZQ}t_1))\,\hat{ZQ}_y\right) \\ &= A\frac{1}{2}\left((\cos(\Omega_{ZQ}t_1) - j\sin(\Omega_{ZQ}t_1))\left(\hat{ZQ}_x + j\hat{ZQ}_y\right)\right) \\ &= A\exp(-j\Omega_{ZQ}t_1)\hat{I}_+\hat{S}_-\end{aligned} \tag{6.5}$$

and

$$\begin{aligned}\hat{\rho}^{(-)}(t_1) &= A\frac{1}{2}\left((\cos(\Omega_{ZQ}t_1) + j\sin(\Omega_{ZQ}t_1))\,\hat{ZQ}_x - j\,(\cos(\Omega_{ZQ}t_1) + j\sin(\Omega_{ZQ}t_1))\,\hat{ZQ}_y\right) \\ &= A\frac{1}{2}\left((\cos(\Omega_{ZQ}t_1) + j\sin(\Omega_{ZQ}t_1))\left(\hat{ZQ}_x - j\hat{ZQ}_y\right)\right) \\ &= A\exp(+j\Omega_{ZQ}t_1)\hat{I}_-\hat{S}_+\end{aligned} \tag{6.6}$$

Mixing Period

During the *mixing* period, unobservable ZQCs are transformed back to observable in-phase SQCs by the mixing pulse β_y. The resulting density operators are given as

$$\hat{\rho}^{(+)}(t_2 = 0) = A\exp(-j\Omega_{ZQ}t_1)\left(-\frac{\sin(2\beta)}{2}(\hat{I}_x\hat{S}_z + \hat{I}_z\hat{S}_x) + j\sin(\beta)(\hat{I}_z\hat{S}_y - \hat{I}_y\hat{S}_z)\right) \tag{6.7}$$

and

$$\hat{\rho}^{(-)}(t_2 = 0) = A\exp(+j\Omega_{ZQ}t_1)\left(-\frac{\sin(2\beta)}{2}(\hat{I}_x\hat{S}_z + \hat{I}_z\hat{S}_x) - j\sin(\beta)(\hat{I}_z\hat{S}_y - \hat{I}_y\hat{S}_z)\right) \tag{6.8}$$

The effect of the flip angle β on the two-dimensional spectral pattern is discussed in detail in section 6.1.2. The unobservable anti-phase SQCs evolve to observable in-phase SQCs throughout the subsequent period of free precession. This process is equivalent to the *preparation* period. A spin echo is included to reduce losses caused by field inhomogeneities during the build-up time. The resulting density operators $\hat{\rho}^{(+)}$ and $\hat{\rho}^{(-)}$ at $t_2 = 2\tau$ are given as

$$\begin{aligned}\hat{\rho}^{(+)}(t_2 = 2\tau) &= A\exp(-j\Omega_{ZQ}t_1)\left(-\frac{\sin(2\beta)}{2}\left(\cos(2\pi J_{IS}\tau)(\hat{I}_x\hat{S}_z + \hat{I}_z\hat{S}_x) + \frac{1}{2}\sin(2\pi J_{IS}\tau)(\hat{I}_y + \hat{S}_y)\right)\right.\\ &\quad \left. + j\sin(2\beta)\left(\cos(2\pi J_{IS}\tau)(\hat{I}_y\hat{S}_z - \hat{I}_z\hat{S}_y) + \frac{1}{2}\sin(2\pi J_{IS}\tau)(\hat{I}_x - \hat{S}_x)\right)\right)\\ &= C^+\left(\frac{\sin(2\beta)}{2}\left(\hat{I}_y + \hat{S}_y\right) - j\sin(2\beta)\left(\hat{I}_x - \hat{S}_x\right)\right)\end{aligned} \tag{6.9}$$

and

$$\begin{aligned}\hat{\rho}^{(-)}(t_2 = 2\tau) &= A\exp(+j\Omega_{ZQ}t_1)\left(-\frac{\sin(2\beta)}{2}\left(\cos(2\pi J_{IS}\tau)(\hat{I}_x\hat{S}_z + \hat{I}_z\hat{S}_x) + \frac{1}{2}\sin(2\pi J_{IS}\tau)(\hat{I}_y + \hat{S}_y)\right)\right.\\ &\quad \left. - j\sin(2\beta)\left(\cos(2\pi J_{IS}\tau)(\hat{I}_y\hat{S}_z - \hat{I}_z\hat{S}_y) + \frac{1}{2}\sin(2\pi J_{IS}\tau)(\hat{I}_x - \hat{S}_x)\right)\right)\\ &= C^-\left(\frac{\sin(2\beta)}{2}\left(\hat{I}_y + \hat{S}_y\right) + j\sin(2\beta)\left(\hat{I}_x - \hat{S}_x\right)\right),\end{aligned} \tag{6.10}$$

where $C^+ = \frac{N}{4}\zeta\sin(2\pi J_{IS}\tau)^2\exp(-j\Omega_{ZQ}t_1)$ and $C^- = \frac{N}{4}\zeta\sin(2\pi J_{IS}\tau)^2\exp(+j\Omega_{ZQ}t_1)$. The build-up time manifests in the term $\sin(\pi J_{IS}t_2)$ in C^+ and C^-. The anti-phase operators are not observable. Therefore, only the in-phase operators need to be considered in the *detection* period.

Detection Period

During the *detection* period, the NMR signal is acquired. Under the influence of the J-coupling and the Zeeman Hamiltonian, the density operators $\hat{\rho}^{(+)}$ and $\hat{\rho}^{(-)}$ evolve during the acquisition time t_2 as

$$\begin{aligned}\hat{\rho}(t_2)^{(+)} = C^+\cos(\pi J_{IS}t_2)\left(\frac{\sin(2\beta)}{2}\left(\cos(\Omega_I t_2)\hat{I}_y - \sin(\Omega_I t_2)\hat{I}_x + \cos(\Omega_S t_2)\hat{S}_y - \sin(\Omega_S t_2)\hat{S}_x\right)\right.\\ \left. - j\sin(2\beta)\left(\cos(\Omega_I t_2)\hat{I}_x + \sin(\Omega_I t_2)\hat{I}_y - \cos(\Omega_S t_2)\hat{S}_x - \sin(\Omega_S t_2)\hat{S}_y\right)\right)\end{aligned} \tag{6.11}$$

and

$$\hat{\rho}(t_2)^{(-)} = C^- \cos(\pi J_{IS} t_2) \Bigg(\frac{\sin(2\beta)}{2} \left(\cos(\Omega_I t_2)\hat{I}_y - \sin(\Omega_I t_2)\hat{I}_x + \cos(\Omega_S t_2)\hat{S}_y - \sin(\Omega_S t_2)\hat{S}_x \right) + j \sin(2\beta) \left(\cos(\Omega_I t_2)\hat{I}_x + \sin(\Omega_I t_2)\hat{I}_y - \cos(\Omega_S t_2)\hat{S}_x - \sin(\Omega_S t_2)\hat{S}_y \right) \Bigg), \tag{6.12}$$

These operators are valid for t_2 greater than τ. Unobservable anti-phase operators are omitted for the sake of clarity.

6.1.2 Spectral Analysis and Expected Pattern for an AX-Spin System

The density operators $\hat{\rho}(t_2)^{(+)}$ and $\hat{\rho}(t_2)^{(-)}$, given in equation 6.11 and equation 6.12 reveal that peaks in the indirect dimension can be expected at $\omega_1 = \pm\Omega_{ZQ}^{IS} = \pm(\Omega_I - \Omega_S)$ as well as $\omega_2 = \Omega_I$ and $\omega_2 = \Omega_S$. Hence, four peaks are expected. Peaks that origin from the density operator $\hat{\rho}^{(+)}$ are modulated by a negative exponential and arise at $\omega_1 = -\Omega_{ZQ}$, whereas peaks which origin from the density operator $\hat{\rho}^{(-)}$ are modulated by a positive exponential and arise at $\omega_1 = +\Omega_{ZQ}$. Hence, the p-type ZQCs relative to spin I origin from $\hat{\rho}^{(+)}$ $(-\Omega_{ZQ})$, whereas the p-type ZQCs relative to spin S origin from $\hat{\rho}^{(-)}$ $(+\Omega_{ZQ})$. On the other hand, the n-type ZQCs relative to spin I origin from $\hat{\rho}^{(-)}$ $(+\Omega_{ZQ})$, whereas the n-type ZQCs relative to spin S origin from $\hat{\rho}^{(+)}$ $(-\Omega_{ZQ})$.
In the following, the observable magnetization M_+ is calculated according to equation 2.52. M_+ is separated in four observable peaks such that $M_+ = M_+^{PI} + M_+^{NI} + M_+^{PS} + M_+^{NS}$. These are given as

$$\begin{aligned}
M_+^{PI}(t_2) &= C^+ \left(\frac{\sin(2\beta)}{2} - \sin(\beta) \right) \exp(+j\Omega_I t_2) \cos(\pi J_{IS} t_2) \\
M_+^{NI}(t_2) &= C^- \left(\frac{\sin(2\beta)}{2} + \sin(\beta) \right) \exp(+j\Omega_I t_2) \cos(\pi J_{IS} t_2) \\
M_+^{PS}(t_2) &= C^- \left(\frac{\sin(2\beta)}{2} - \sin(\beta) \right) \exp(+j\Omega_S t_2) \cos(\pi J_{IS} t_2) \\
M_+^{NS}(t_2) &= C^+ \left(\frac{\sin(2\beta)}{2} + \sin(\beta) \right) \exp(+j\Omega_S t_2) \cos(\pi J_{IS} t_2),
\end{aligned} \tag{6.13}$$

where M_+^{PI}, arising from the p-type coherence on spin I $(\hat{\rho}^{(+)})$ leads to a peak at $(\omega_1, \omega_2) = (-\Omega_{ZQ}, \Omega_I)$, M_+^{NI}, arising from the n-type coherence on spin I $(\hat{\rho}^{(-)})$ leads to a peak at $(+\Omega_{ZQ}, \Omega_I)$, M_+^{PS}, arising from the p-type coherence on spin S $(\hat{\rho}^{(-)})$ leads to a peak at $(+\Omega_{ZQ}, \Omega_S)$, and M_+^{NS}, arising from the n-type coherence on spin S $(\hat{\rho}^{(+)})$ leads to a peak at $(-\Omega_{ZQ}, \Omega_S)$. For the sake of simplicity, shared constants are neglected. The factors C^+ and C^- are maximized by adjusting the echo time such that $\tau \approx \frac{1}{4J_{IS}}$. Deviations from this value lead to a steep decrease in signal intensity due to the quadratic dependence $(\sin^2(2\pi J_{IS}\tau))$. Furthermore, the flip angle β of the first mixing pulse needs to be evaluated. Therefore, the spectral pattern, illustrated in figure 6.2 show the observable magnetization M_+ for a flip angle of $\beta = \pi/2$ (figure 6.2a and figure 6.2c) and a flip angle of $\beta = \pi/4$ (figure 6.2b and figure 6.2d). Moreover, the effect of strong inhomogeneous broadening on these spectra is illustrated in figure 6.2c and figure 6.2d. For the graphical representations, $\Omega_S > \Omega_I$ is assumed. The spectra are shown in absolute values, normalized to one.

Figure 6.2a illustrates the results for a flip angle $\beta = \pi/2$. The intensity of all four peaks is equal. Moreover, the signals M_+^{PI} and M_+^{PS} are phase-shifted to M_+^{NI} and M_+^{NS} by π (see equation 6.13). The

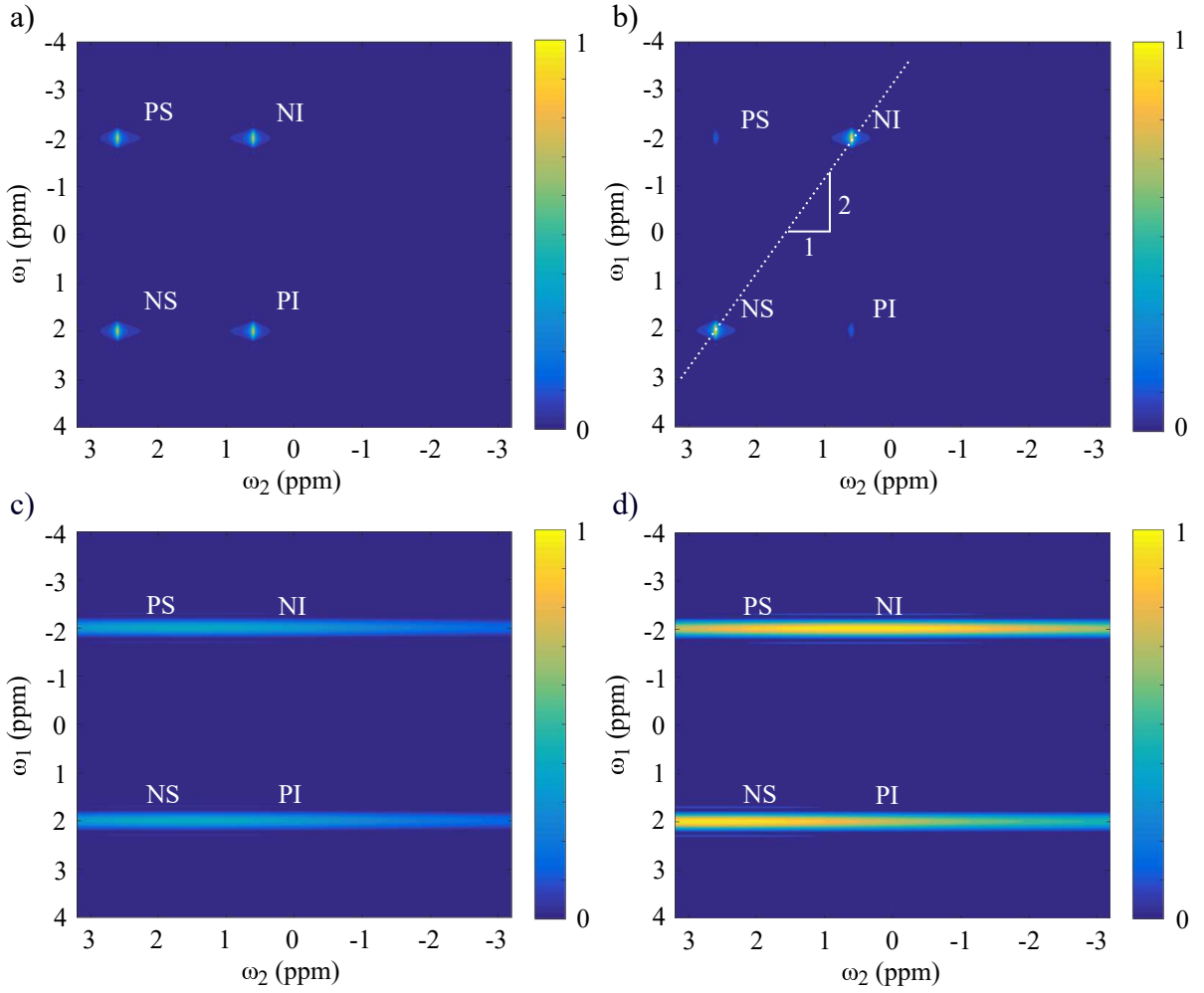

Figure 6.2: Spectral pattern of the HZQC-sequence for an AX-spin system. Absolute data is plotted. Prior to frequency transformation and normalization to one, a sine apodization is applied. a) The flip angle β of the first mixing pulse is set to $\beta = \pi/2$. b) The flip angle β of the first mixing pulse is set to $\beta = \pi/4$. c) The flip angle β of the first mixing pulse is set to $\beta = \pi/2$. The B_0 field homogeneity is reduced. d) The flip angle β of the first mixing pulse is set to $\beta = \pi/4$. The B_0 field homogeneity is reduced.

spectral pattern shown in figure 6.2b is obtained by a mixing pulse with a flip angle $\beta = \pi/4$. As the p-type coherences (see equation 6.13) depend on the difference $\frac{\sin(2\beta)}{2} - \sin(\beta) \approx -0.2$, they are strongly attenuated. For flip angles in between these extrema, the peak magnitude ratio between p- and n-type coherences is given as $\tan^2(\beta/2)$. On the other hand, the n-type coherences depend on the prefactor $\frac{\sin(2\beta)}{2} + \sin(\beta) \approx 1.2$, which leads to an amplification compared to the π-pulse. As half of the spectral components are strongly attenuated, a simplification without a loss of information is achieved. The residual peaks *NS* and *NI* appear at $(\omega_1, \omega_2) = (-\Omega_{ZQ}, \Omega_S)$ and $(\omega_1, \omega_2) = (\Omega_{ZQ}, \Omega_I)$, respectively. Crosspeaks from coupled spins always appear on diagonals with a slope of $\omega_1 = 2\omega_2$. Using a flip angle of $\beta = \pi/4$, the individual peaks, corresponding to one spin are preferably in one quadrant of the spectrum. This allows for quasi quadrature detection and thus for frequency discrimination in the indirect dimension [121, 122]. Moreover, the transfer from ZQCs to passive spins, proportional to $\sin^3(\beta)$ is strongly attenuated [121, 122]. The influence of inhomogeneous broadening is illustrated in

figure 6.2c and figure 6.2d, where figure 6.2c corresponds to $\beta = \pi/2$ and figure 6.2d to $\beta = \pi/4$. Peaks originating from S spins overlap with these originating from I spins destructively due to the phase shift of π. This leads to a decrease in signal amplitude. The peak intensity ratio between figure 6.2c and figure 6.2d is about 0.4. Inhomogeneous broadening is introduced by decreasing the transversal relaxation time T_2^* from 0.2 s to 0.001 s. The spectrum broadens and individual peaks can not be distinguished anymore in the direct dimension ω_2. However, the frequency resolution in the indirect dimension is not affected (see section 2.10).
Prior to the frequency transformation in the indirect dimension, the raw data was multiplied by a sine apodization function [51] in order to reduce spectral leakage (see section 6.1.4). The sampling frequency in the indirect dimension was set to 2 kHz ($\Delta t_1 = 500\,\mu s$), which allows for an aliasing free detection of frequencies up to 1 kHz (22 ppm). 256 samples were acquired in the indirect dimension. This leads to a frequency resolution $1/(N\Delta t_1)$ of about 7.8 Hz (0.173 ppm). The offset frequency Ω_I of the I-spins was set to 27 Hz (0.6 ppm) and the offset frequency Ω_S of the S-spins was set to 117 Hz (2.6 ppm). This results in the ZQ frequencies ± 90 Hz (± 2 ppm), which appear in the indirect dimension (see figure 6.2). The chosen values coincide with the coupling between group three and group four of 1-butanol (see inset figure 6.6a). Thus, the theoretical results can be compared to the measurements presented in section 6.1.4.

6.1.3 Phase Cycling

The desired CTP (see figure 6.1) is achieved by the combination of a pulsed field gradient and the 4-step phase cycling scheme shown in table 6.1. The applied phase cycling scheme is required to cancel undesired coherences occurring due to experimental restrictions like relaxation and RF-pulse imperfections.

	ϕ_1	ϕ_{Rx}	ϕ_2	ϕ_{Rx}	ϕ_3	ϕ_{Rx}
1	$0°(+x)$	$0°(x)$	$+90°(+y)$	$180°(-x)$	$+90°(+y)$	$180°(-x)$
2	$180°(-x)$	$180°(-x)$	$-90°(-y)$	$180°(-x)$	$-90°(-y)$	$0°(+x)$

(a) Individual HZQC phase cycling scheme for pulse one, pulse two and pulse three.

	ϕ_1	ϕ_2	ϕ_3	ϕ_4	ϕ_5	ϕ_{Rx}
1	$0°(+x)$	$+90°(+y)$	$+90°(+y)$	$+90°(+y)$	$0°(+x)$	$0°(+x)$
2	$0°(+x)$	$-90°(-y)$	$+90°(+y)$	$+90°(+y)$	$0°(+x)$	$0°(+x)$
3	$0°(+x)$	$+90°(+y)$	$-90°(-y)$	$+90°(+y)$	$0°(+x)$	$180°(-x)$
4	$0°(+x)$	$-90°(-y)$	$-90°(-y)$	$+90°(+y)$	$0°(+x)$	$180°(-x)$

(b) Overall HZQC phase cycling scheme regarding pulse two and pulse three.

Table 6.1: HZQC phase cycling scheme. a) shows the individual phase cycling schemes for pulse two and pulse three and b) shows the overall phase cycling scheme for the HZQC sequence. Axial peak suppression and hence the phase cycling due to pulse one is not considered in this phase cycling scheme.

Table 6.1a illustrates the required phase cycles for the individual RF-pulses. Focus is on pulse one, pulse two and pulse three with the corresponding phases Φ_1, Φ_2 and Φ_3 (see figure 6.1). Ideally, the first RF-pulse generates only SQCs ($p = \pm 1$). Due to pulse imperfections, also a residual z-magnetization is

generated. This remainder is not modulated during the *evolution* period and thus results in an undesired DC component. Cancellation of the residual z-magnetization can be performed in terms of a two-step axial peak suppression [65]. This method is not applied for the measurements presented in section 6.1.4 for the sake of a measurement time reduction. Both SQCs, generated by the first RF-pulse are desired. The second RF-pulse, a refocusing pulse ideally transforms the SQCs from $p = \pm 1$ to $p = \mp 1$. The desired coherence order change Δp is thus ± 2. This is inherently given for ideal spin echos. However, the behavior of non-ideal spin echos deviates. A two-step phase cycle ($N_{\phi_2} = 2$) for ϕ_2 is introduced (see table 6.1a) to select the coherence change $\Delta p = \pm 2$. As only coherence order changes obeying $+2 + nN_{\phi_2}$, where $n \in \mathbb{Z}$ are allowed, no double-quantum coherence is expected after the pulse. The coherence orders $p = \pm 3$ might occur but their formation is highly unlikely. Moreover, as the first pulse is expected to generate only SQCs as well as z-magnetization, no coherences other than $p = \pm 1$ are expected to be transfered to ∓ 1 by the second pulse. The final pulse of the *preparation* period transfers anti-phase SQCs to ZQCs. Hence, a change in coherence order of $\Delta p = \pm 1$ is desired. As only coherence changes which obey $\Delta p = +1 + nN_{\phi_3}$, where $N_{\phi_3} = 2$ are allowed (see table 6.1a), no double-quantum coherences are transformed to ZQCs. Transformation from coherences with coherence order $p = \pm 3$ are allowed. However, these transfers are again very unlikely. Many coherences with an order different from zero are generated by this pulse. However, these coherences are dephased by the pulsed field gradient [123] (see figure 6.1) such that only ZQCs are assumed to be present at the end of the *evolution* period. The mixing pulse transforms ZQCs back into observable SQCs. Throughout the *detection* period, exclusively $p = +1$ is observed by the receiver. No more phase cycles are applied for the remaining pulses.
The phase cycling scheme does not account for T_1-relaxation. Increasing z-magnetization, mostly during the *evolution* period is transformed to an undesired signal component by the subsequent RF-pulses.

6.1.4 NMR Measurements on 1-Butanol

The butanol (C_4H_9OH) isomer 1-butanol (n-butanol) is used in the following to prove the suitability of the SoC-based spectrometer (see section 3.2) and the gradient-capable probe head (see section 4.4) to determine intramolecular coupling networks via ZQCs in very inhomogeneous fields. 1-butanol is a 4-carbon structure, where the hydroxide group is connected to the first carbon atom [117, 118]. The skeletal formula as well as the direct SQ spectrum of 1-butanol are shown in figure 6.3.
The SQ spectrum was acquired with a 1 T small-animal magnet (see section 4.1) shimmed such that the linewidth of deionized water was about 0.6 ppm. Therefore, not all peaks could be resolved properly. The molecule is divided in five groups, each consisting of one, two or three magnetically equivalent hydrogen atoms. These groups are labeled in the structural formula illustrated in figure 6.3 (inset). The corresponding chemical shifts are given as follows [117, 118]: peak 1 is located at $\omega_1 \approx 0.9\,ppm$, peak 2 at $\omega_2 \approx 1.33\,ppm$, peak 3 at $\omega_3 \approx 1.51 ppm$ and peak 4 at $\omega_4 \approx 3.59\,ppm$. The chemical shift of the hydroxide group is not mentioned in [117, 118] as it strongly depends on sample conditions like the solvent type, the concentration and the purity of the sample, especially whether it is dry or not [124]. Furthermore, strong broadening due to a proton exchange with the solvent is reported [124].
The values from [117, 118] fit well to the acquired spectrum shown in figure 6.3. Due to field inhomogeneities, resulting in a linewidth of 0.6 ppm (for deionized water), peak 2 and 3 are not distinguishable anymore. Furthermore, there is a strong overlapping with group one. Indirect dipole-dipole couplings are reported between group 1 and 2, group 2 and 3, and group 3 and 4 [117, 118]. As 1-butanol belongs to the class of aliphatic compounds, the coupling constants J_{12}, J_{23} and J_{34} between the corresponding

groups are all expected to be approximately 7 Hz [117]. Hydrocarbon 4 couples with hydrocarbon 3 such that peak 4 forms a triplet. The corresponding coupling constant J_{34} is about 6.6 Hz [117]. Furthermore, hydrocarbon 2 couples with hydrocarbon 1 such that peak 1 forms a tripled due to the two hydrogens of hydrocarbon 2. The corresponding coupling constant J_{12} is about 7.2 Hz. Hydrocarbon 2 and hydrocarbon 3 are both coupled with two neighbors. This results in the formation of sextets. The corresponding coupling constant J_{23} is approximately 7.8 Hz. Couplings with the hydroxide group are neglected due to fast proton exchange with the solvent as long as the sample is not absolutely dry. Hence, peak 1 is not split [124]. Due to the low resolution, these multiplets are not observable in figure 6.3.

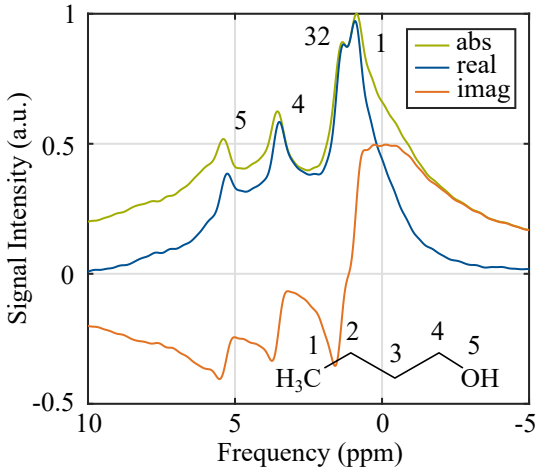

Figure 6.3: One-dimensional single-quantum spectrum of 1-butanol. The inset shows the structural formula. The groups of the molecule are labeled by the numbers 1 to 5, which correspond to the peaks in the spectrum.

The effectiveness of the transformation from in-phase to anti-phase SQCs (see equation 6.2) and vice versa (see equation 6.9 and 6.10) is dominated by the corresponding coupling constants as well as the echo time. As the coupling constants range from 6.6 Hz to 7.8 Hz, the corresponding optimal echo time τ (optimizing $\sin(2\pi J\tau)$) ranges from 32 ms and 37.9 ms. Hence, the transformation is not equal in effectiveness for all couplings and a trade-off needs to be found.
In the indirect dimension of the two-dimensional HZQC spectrum, six peaks are expected at the ZQ frequencies $\omega_{34}^{ZQ} = \pm(\omega_4 - \omega_3) = \pm 2.08\,ppm$, $\omega_{23}^{ZQ} = \pm(\omega_3 - \omega_2) = \pm 0.18\,ppm$ and $\omega_{12}^{ZQ} = \pm(\omega_2 - \omega_1) = \pm 0.43\,ppm$. Nyquist sampling in the indirect dimension requires the sampling intervals Δt_1 to be smaller than $\pi/(\omega_{34}^{ZQ}) = 5.5\,ms$. This corresponds to a sampling frequency of 181 Hz. Furthermore, the frequency resolution, is required to be better than the lowest ZQ frequency ($\omega_{23}^{ZQ} = 0.18\,ppm$). It is adjusted by the maximum duration of the evolution period ($t_{1,max}$) and the spectral shape of the window function applied prior to frequency conversion in the indirect dimension. Due to strong relaxation processes, the duration $t_{1,max}$ of the evolution period (see figure 6.1) is limited. A trade-off between signal intensity and resolution needs to be found.

Relaxation

The major limitation of the frequency resolution origins from the relaxation processes. Coherences relax towards zero according to the time constants T_1 and T_2, corresponding to longitudinal and transversal

relaxation (see section 2.11). The relaxation constants strongly depend on external parameters like temperature as well as setup parameters like the magnetic flux density of the permanent magnet. Therefore, a comparison with values obtained from different setups is difficult. An estimate of T_1 and T_2 of 1-butanol for the given settings is obtained by the inversion recovery and the CPMG sequence [66], respectively. The results are shown in figure 6.4.

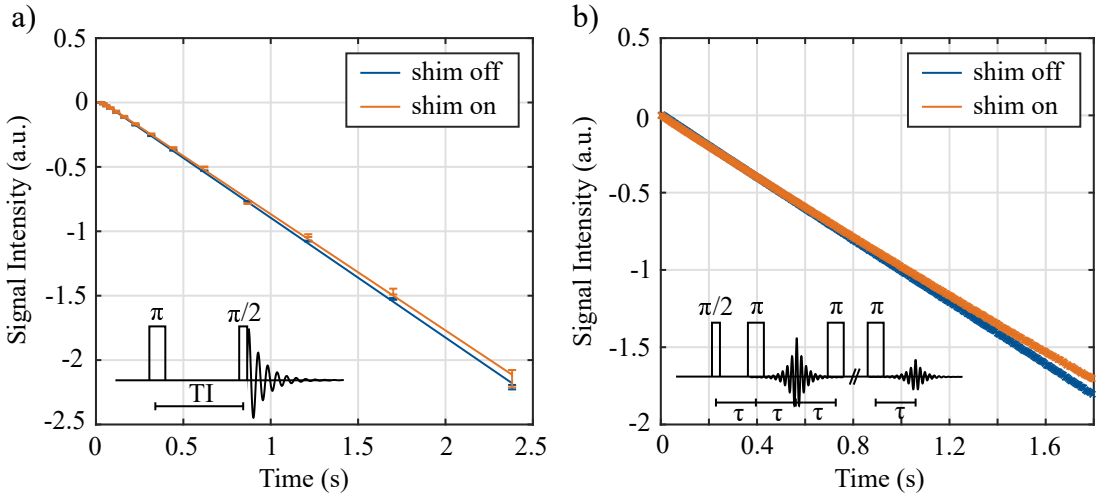

Figure 6.4: Measurement of the relaxation times of 1-butanol with and without an activated current shim. a) Determination of the longitudinal relaxation time T_1 by the inversion recovery sequence (see inset). b) Determination of the transversal relaxation time T_2 by the CPMG sequence (see inset).

Figure 6.4a shows the results of the inversion recovery sequence, where the sequence is illustrated in the inset. The inversion time (TI) was increased 17 times according to $30\,ms * 1.4^x$. Therefore, 17 data samples were gathered, each with an acquisition period of 5 ms. The repetition time was set to $6T_1$ with an initial value of 15 s for the first sequence. Ten repetitions were performed and the corresponding error bars are plotted for each sample. Raw data is normalized to one prior to taking the natural logarithm. The signal intensity plotted in figure 6.4a is expected to be $-R_1 t$, where the longitudinal relaxation rate $R_1 = T_1^{-1}$ is to be estimated. A linear regression leads to a longitudinal relaxation time of 1.08 s ($r^2 = 0.99996$) and 1.11 s ($r^2 = 0.99991$) with the current shim deactivated and activated, respectively.
Figure 6.4b shows the results of the CPMG sequence, where the sequence is illustrated in the inset. 3000 spin echos with an echo time 2τ of 300 µs were recorded with an acquisition time of 300 µs. Ten repetitions were performed. Raw data is normalized to one prior to taking the natural logarithm. The signal intensity plotted in figure 6.4b is expected to be $-R_2 t$, where the transversal relaxation rate $R_2 = T_2^{-1}$ is to be estimated. A linear regression leads to a transversal relaxation time of 0.99 s ($r^2 \approx 1$) and 1.05 s ($r^2 = 0.99997$) with the current shim deactivated and activated, respectively.
Furthermore, throughout studies on the Debye process in monohydroxy alcohols, the longitudinal relaxation time T_1 of 1-butanol was measured over a wide range of temperatures [125]. For low temperatures (150 K to 280 K) the time constant is highly temperature dependent and ranges from 0.1 s to 1 s. For higher temperatures (298 K), the time constant T_1 increases to 2 s, whereas the dependence on the frequency decreases. Data was gathered at 46 MHz and 55.6 MHz. Moreover, in [126] the relaxation time T_1 of 1-butanol was determined at 304 K and 100 MHz for each group of the molecule. The hydrocarbon groups and the hydroxide group (see figure 6.3) show longitudinal relaxation times ranging from 5.6 s to 2.8 s. Similar experiments were conducted by [127] at 298 K and 300 MHz, resulting in T_1 ranging from

3.06 s to 2.4 s depending on the group under consideration. At 310 K and 20 MHz, [128] determined the overall longitudinal (T_1) and transversal relaxation time T_2 to 1.29 s and 1.08 s, respectively.

Window Considerations

Nyquist sampling in the indirect dimension requires the sampling interval Δt_1 to be smaller than 5.5 ms. Furthermore, a frequency resolution better than 0.18 ppm (8.1 Hz) is required to resolve the ZQ transition at Ω_{23}^{ZQ}. In theory, $t_{1,max}$ must be larger than 120 ms, which is much smaller than the estimated relaxation time constants T_1 and T_2. However, spectral leakage due to windowing highly reduces the effective frequency resolution. This effect increases with the dynamic range of the acquired measurement data. Due to experimental imperfections like B_0 and B_1 inhomogeneities or field drifts, the spectra shown in figure 6.6 exhibit a strong DC-component (at $\omega_1 = 0$) and therefore a high dynamic range. Hence, a window with high sidelobe attenuation in close proximity to the axial peaks is required. A strong sidelobe attenuation and therefore a high dynamic range of a window is always linked to reduced resolution.
Mathematically, the finite sampling duration in the indirect dimension is expressed by multiplying the time domain data by a square window. In the frequency domain, this results in a convolution with the spectrum. Consequently, the spectral quality is decreased by spectral leakage and a reduction of the frequency resolution, caused by the sidelobes and the non-zero mainlobe width, respectively. Figure 6.5 shows four window functions (see figure 6.5a) and the corresponding spectral shapes (see figure 6.5b).

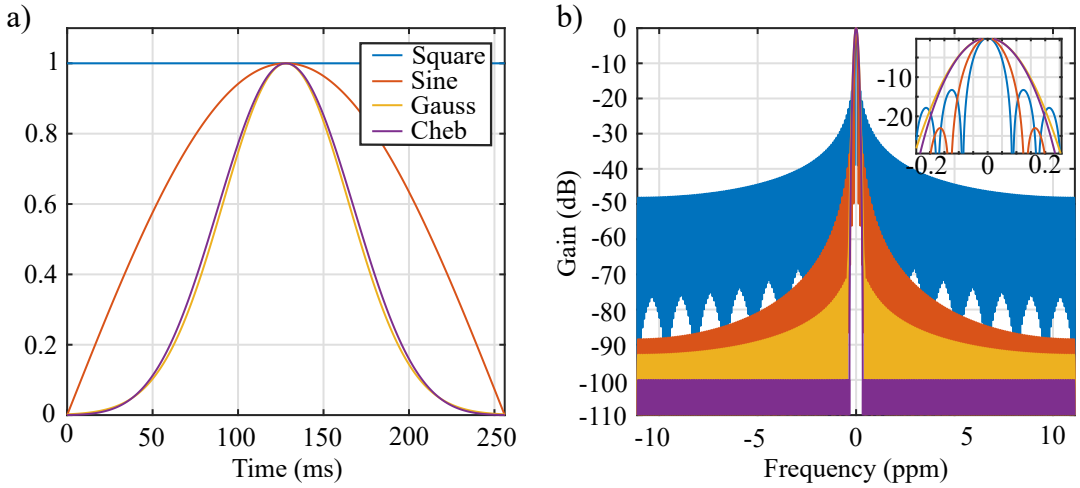

Figure 6.5: Window functions for HZQC measurements with a length of 256 ms (256 samples with a sampling interval of 1 ms). a) A square window, a sine window, a gaussian window ($\alpha = 3.5$) and a Dolph-Chebyshev window (attenuation 100 dB). b) Spectral shape of the corresponding window functions. The inset shows a zoom to the mainlobe.

The sampling duration of the windows shown in figure 6.5 is 256 ms. This is smaller than the estimated relaxation times and corresponds to 256 signals, acquired in the indirect dimension with a sampling interval of 1 ms. The sampling frequency of 1 kHz allows for Nyquist sampling of frequencies up to 500 Hz (11 ppm). Four different window shapes are presented: a square window, a sine window, a gaussian window with a standard deviation of 36 Hz ($\alpha = 3.5$), and a Dolph-Chebyshev window with a sidelobe attenuation of 100 dB [90, 129]. The square window shows the highest selectivity (equivalent noise bandwidth of one). However, the dynamic range of this window is very low. Sidepeaks drop

by approximately $1/f$, such that the first sidelobe is attenuated by only 13 dB. Due to the extensive axial peaks in the HZQC spectra (see figure 6.6) the dynamic range of this window is not sufficient. Sidelobe leakage masks the desired ZQ spectrum. The dynamic range is increased by a sine window. The attenuation of the first peak is already about 23 dB (see inset figure 6.5b). With an equivalent noise bandwidth of 1.2386 the sensitivity of this window is still very high. The gaussian and the Dolph-Chebyshev window posses a very high dynamic range. However, the width of the mainlobe increases (see inset figure 6.6b). The attenuation of the first sidelobe is 71 dB and 100 dB, respectively, where the attenuation of the Dolph-Chebyshev window is a design parameter. However, first sidelobes are at ± 0.49 ppm and ± 0.35 ppm, respectively. This is larger than the smallest expected ZQ frequency of 0.18 ppm. At 0.18 ppm, the attenuation of both windows is only about 17 dB. The sensitivity of both windows is with an equivalent noise bandwidth about 1.9 lower compared to the square and the sine window. For larger frequencies, the first three windows decay to zero, whereas the Dolph-Chebyshev window converges to a constant value corresponding to the allowed minimal attenuation (here: 100 dB). This attenuation can be parametrized at the cost of sensitivity.
Higher dynamic ranges at a given sensitivity can only be achieved by increasing the maximum duration of the evolution period - a parameter that is limited by relaxation processes.

Real Measurements

The HZQC sequence (see figure 6.1) is applied to 1-butanol (sample size: 50 µl, HPLC-grade). The results are shown in figure 6.6, where figure 6.6a-c show spectra acquired from 1-butanol for various sequence settings and figure 6.6d shows a spectrum acquired from purified water, used as a reference. On the right side of each spectra, a one-dimensional spectrum shows the corresponding data accumulated in the direct dimension.
The four spectra were acquired using 256 t_1 increments with a step size Δt_1 of 1 ms. Each t_1 interval was accumulated four times. The delay between the scans or intervals was 8 s. Data was acquired for 15 ms in the direct dimension (t_2) and the echo time 2τ was set to 50 ms. Gradient strength in terms of the gradient current I_G (see section 4.4) and gradient duration t_g were set to 140 mA and 15 ms, respectively. The accumulated data was multiplied by a Dolph-Chebyshev window with a sidelobe attenuation of 100 dB (see figure 6.5), prior to Fourier transformation in the indirect dimension (t_1).
Figure 6.6a shows the acquired HZQC spectrum of 1-butanol. Current shims were adjusted such that the linewidth of deionized water was about 0.6 ppm. The insets illustrate the one-dimensional SQ spectrum of 1-butanol according to figure 6.3 and the structural formula. Hydrocarbons as well as the hydroxide group are labeled by numbers, which are associated to the corresponding SQ transitions. Due to inhomogeneous line broadening, the individual SQ transitions are barely distinguishable. Moreover, the detection of multiplets caused by indirect dipole-dipole coupling between these groups is impossible. The B_0 field homogeneity is not sufficient to resolve these multiplets, separated by about 7 Hz. However, these J-couplings are clearly resolved in the two-dimensional spectrum. As predicted in section 6.1.2, the spectrum exhibits six peaks, two corresponding to each of the three coupled groups (4-3, 2-1 and 3-2). These six peaks appear at the corresponding ZQ frequencies in the indirect dimension of the HZQC spectrum as well as in the accumulated spectrum on the right. To highlight the independence of these measurements from field homogeneities, the same experiment was repeated with deactivated current shims (linewidth of deionized water was about 11 ppm). The results are shown in figure 6.6b. In the direct dimension, peaks resulting from SQ transitions broaden strongly. However, peaks resulting from the ZQ transition in the indirect dimension are not affected by the inhomogeneous broadening. The res-

olution of the accumulated spectra is equivalent.

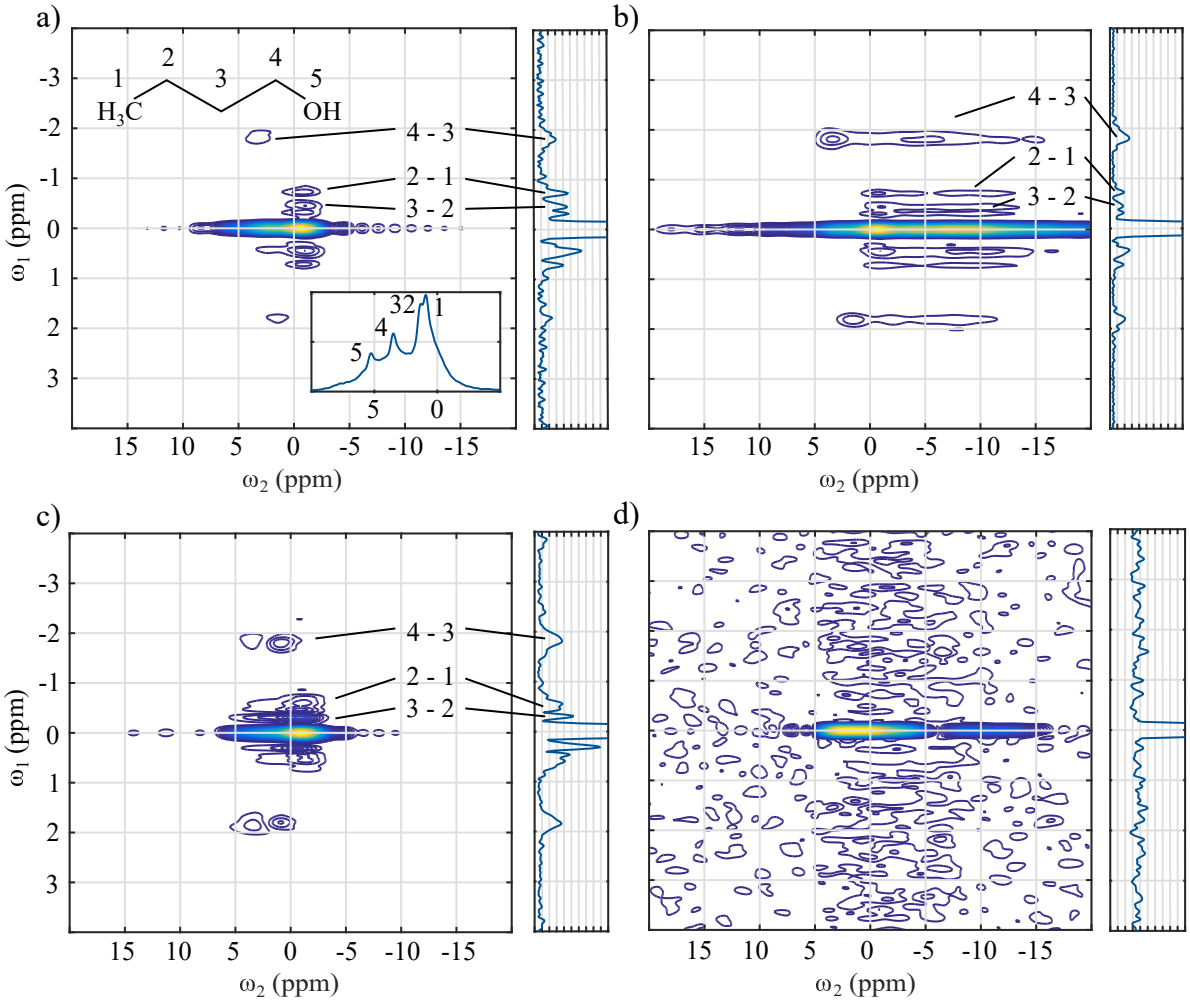

Figure 6.6: HZQC spectra of 1-butanol and water. Projections to the indirect dimension are shown for each spectrum on the right. a) HZQC spectrum of 1-butanol with a shimmed magnet (linewidth of deionized water was about 0.6 ppm). The flip angle of the first mixing is set to $\beta = \pi/4$. The insets show the one-dimensional SQ spectrum of 1-butanol and the corresponding structural formula. b) HZQC spectrum of 1-butanol with a unshimmed magnet (linewidth of deionized water was about 11 ppm). The flip angle of the first mixing is set to $\beta = \pi/4$. c) HZQC spectrum of 1-butanol with a shimmed magnet. The flip angle of the first mixing is set to $\beta = \pi/2$. d) HZQC spectrum of water with a shimmed magnet.

The influence of the flip angle β of the first mixing pulse (see figure 6.1) on the HZQC spectrum, discussed in theory in section 6.1.2 is shown in figure 6.6c. For $\beta = \pi/2$, each J-coupling results in four peaks. Peaks caused by p-type ZQCs are no longer suppressed. The accumulated spectrum still clearly resolves each transition. Finally, the HZQC sequence is applied to pure water. As there are no coupled groups in water, no peaks are expected in the indirect dimension. This is shown in figure 6.6d. Only the axial peak at $\omega_1 = 0$, common to all four spectra is observable. Furthermore, the spectra of 1-butanol exhibit an artifact at $\omega_1 \approx 0.3$ ppm.

6.2 Detection of Direct Dipole-Dipole Coupling Networks via ZQCs

One of the major advantages of NMR is the extensive theoretical framework that allows for extremely detailed predictions concerning the NMR signal formation of most pulse sequences [130, 131]. In general, measurement results deviating from theoretical predictions require adjustments of the NMR spectrometer or of the experiment [61]. An exception were unexpected cross-peaks, appearing apparently from iMQCs [53, 61, 132–134]. These intermolecular cross-peaks were first discovered using the CRAZED (COSY Revamped with Asymmetric Z-gradient Echo Detection) sequence. Two pulsed field gradients with a ratio of $1 : n$ are applied before and after the second RF-pulse of a regular COSY sequence [133]. The resulting two-dimensional spectrum showed cross-peaks between the corresponding molecules with the characteristics of intermolecular n-quantum coherences. These origin from distant direct dipole-dipole interactions (see section 2.3.2). Primarily, low-order iMQCs, including iZQCs, iSQCs and iDQCs find application as they form the strongest observable signal. Especially, iZQCs ($n = 0$) are useful due to outstanding features like the ability to produce high resolution spectra in inhomogeneous fields [54] (see section 2.10). To account for the phenomenon of iMQCs, the existing NMR theories were extended. For the classical approach, a distant dipolar field is added to the Bloch equations [135]. The quantum mechanical approach is extended by direct dipole-dipole interactions (see section 2.3.2). Moreover, the high temperature approximation (see section 2.8) needs to be removed. Predictions of both approaches were shown to be equivalent if diffusion and relaxation are neglected [133, 135]. Even though the classical approach is more suitable for the intuitive inclusion of relaxation or diffusion effects, the quantum mechanical theory shows advantages in sequence design and prediction. Therefore, the quantum mechanical approach is used in the following. In some cases even a combination of both approaches can lead to enhanced results in terms of predictive power and computational convenience [136].
In the following, a detailed analysis of the HOMOGENIZED pulse sequence for an I-S spin system is presented in section 6.2.1 using the quantum mechanical approach. This includes the derivation of the full equilibrium density operator of this spin system without thermal approximation (see section 2.8). Subsequently, spatial and temporal averaging of intermolecular direct dipole-dipole couplings as well as the effects of pulsed field gradients and non-spherical sample shapes are discussed qualitatively (see section 6.2.2) and quantitatively (see section 6.2.3). The quantitative analysis is presented for both, an ideal constant coherence selection gradient in z-direction as well as the gradient generated by the gradient-capable NMR coil (see section 4.4). Finally, the expected spectral pattern of an I-S spin system is derived on the example of a homogeneous mixture of acetone and water in section 6.2.4.

6.2.1 HOMOGENIZED Pulse Sequence and the Quantum Mechanical Treatment of an I-S Spin System

The HOMOGENIZED sequence is a detection method for iMQCs [54, 137], where the *mixing* period of the CRAZED sequence is extended by a spin echo. As the rephasing due to distant dipolar fields is a rather slow process, it is important to remove the influence of field inhomogeneities while retaining chemical shift and J-coupling information. Moreover, by applying an appropriate quantum filter ($n = 0$), iZQCs are extracted. This pulse sequence is illustrated in figure 6.7. The corresponding CTP is shown in the lower part.
In the following, this sequence is analyzed theoretically for an I-S $\frac{1}{2}$-spin system (weak coupling assumed) consisting of N_I I-spins and N_S S-spins. Furthermore, an isotropic liquid is assumed. Direct dipole-dipole couplings between spin I_i and spin I_k and spin S_i and spin S_k are described by the homonuclear direct dipole-dipole Hamiltonian $\hat{\mathcal{H}}^{DD}_{ik,homo}$ (see equation 2.25) with the corresponding homonuclear

secular dipole-dipole coupling constant D_{ik}^{homo} (see equation 2.26). Direct dipole-dipole couplings between spin I_i and spin S_k are described by the heteronuclear direct dipole-dipole Hamiltonian $\hat{\mathcal{H}}_{ik,hetero}^{DD}$ (see equation 2.24) with the corresponding heteronuclear secular dipole-dipole coupling constant D_{ik}^{hetero} (see equation 2.26). The offset frequencies corresponding to spin I_i and S_i are denoted as Ω_{I_i} and Ω_{S_i}, respectively. Equivalent to the HZQC sequence (see section 6.1), the two-dimensional HOMGENIZED sequence is functionally separated in four periods [64, 65]. ZQCs are excited during the *preparation* period by only one RF-pulse (see figure 6.7). Throughout the *evolution* period, these coherences evolve by Zeeman interactions. ZQCs are transfered back into observable in-phase SQCs during the *mixing* period by distant dipolar fields. Subsequently, the observable magnetization is acquired during the *detection* period. Relaxation and diffusion are only included phenomenologically.

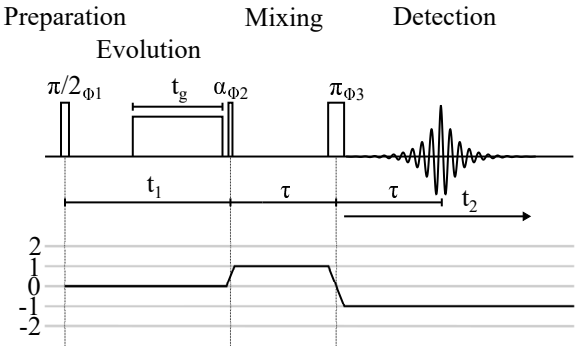

Figure 6.7: HOMOGENIZED pulse sequence and the corresponding coherence transfer pathway.

Equilibrium Density Operator

To account for intermolecular cross-peaks, it transpired that the thermal approximation as given in section 2.8 is not valid anymore. Still, a second order Taylor series truncation of equation 2.47 is performed. Even though higher order spin operators can lead to observable signals, it is very unlikely for two reasons. On the one hand, the term ζ^n of n-spin operators becomes very small as $\zeta << 1$. On the other hand, product operators with an order different from two (this includes one-spin operators) require multiple distant dipolar interactions during the *mixing* period to transform multi-spin anti-phase SQCs to observable in-phase SQCs. Hence, these terms are much smaller compared to observable magnetization originating from two-spin operators. The equilibrium density operator for the I-S spin system is given as

$$\begin{aligned}\hat{\rho}_{eq} &= 2^{-N_I}\left(\hat{1}-\zeta\sum_{i=1}^{N_I}\hat{I}_{iz}+\frac{1}{2}\zeta^2{\sum_{i,j=1}^{N_I}}'\hat{I}_{iz}\hat{I}_{jz}\right)2^{-N_S}\left(\hat{1}-\zeta\sum_{k=1}^{N_S}\hat{S}_{kz}+\frac{1}{2}\zeta^2{\sum_{k,l=1}^{N_S}}'\hat{S}_{kz}\hat{S}_{lz}\right)\\ &\approx 2^{-N_I-N_S}\left(\hat{1}-\zeta\left(\sum_{i=1}^{N_I}\hat{I}_{iz}+\sum_{k=1}^{N_S}\hat{S}_{kz}\right)+\frac{1}{2}\zeta^2\left({\sum_{i,j=1}^{N_I}}'\hat{I}_{iz}\hat{I}_{jz}+{\sum_{k,l=1}^{N_S}}'\hat{S}_{kz}\hat{S}_{lz}+\sum_{i,k=1}^{N_I,N_S}2\hat{I}_{iz}\hat{S}_{kz}\right)\right)\\ &\approx 2^{-(N_I+N_S+1)}\zeta^2\left({\sum_{i,j=1}^{N_I}}'\hat{I}_{iz}\hat{I}_{jz}+{\sum_{k,l=1}^{N_S}}'\hat{S}_{kz}\hat{S}_{lz}+\sum_{i,k=1}^{N_I,N_S}2\hat{I}_{iz}\hat{S}_{kz}\right),\end{aligned} \tag{6.14}$$

where the approximation to line two is valid as three-spin operators are neglected. Furthermore, the

approximation to line three is valid as the signal contribution of one-spin operators is much smaller than the one from two-spin operators. Only the longitudinal two-spin operators $\hat{I}_{iz}\hat{I}_{jz}$, $\hat{S}_{kz}\hat{S}_{lz}$ and $\hat{I}_{iz}\hat{S}_{kz}$ are considered.

Preparation Period

During the *preparation* period, longitudinal two-spin operators are transformed to ZQCs by a single RF-pulse (hard $\frac{\pi}{2}_y$-pulse). The resulting density operator $\hat{\rho}(t_1 = 0)$ is given as

$$\begin{aligned}
&\hat{\rho}(t_1 = 0) = \\
&2^{-N-1}\zeta^2 \left(\sum_{i,j=1}^{N_I}{}' \hat{I}_{ix}\hat{I}_{jx} + \sum_{k,l=1}^{N_S}{}' \hat{S}_{kx}\hat{S}_{lx} + \sum_{i,k=1}^{N_I,N_S} 2\hat{I}_{ix}\hat{S}_{kx} \right) \\
&= 2^{-N-3}\zeta^2 \left(\sum_{i,j=1}^{N_I}{}' \left(Z\hat{Q}_x^{I_iI_j} + D\hat{Q}_x^{I_iI_j} \right) + \sum_{k,l=1}^{N_S}{}' \left(Z\hat{Q}_x^{S_kS_l} + D\hat{Q}_x^{S_kS_l} \right) + 2 \sum_{i,k=1}^{N_I,N_S} \left(Z\hat{Q}_x^{I_iS_k} + D\hat{Q}_x^{I_iS_k} \right) \right) \\
&\approx 2^{-N-3}\zeta^2 \left(\sum_{i,j=1}^{N_I}{}' Z\hat{Q}_x^{I_iI_j} + \sum_{k,l=1}^{N_S}{}' Z\hat{Q}_x^{S_kS_l} + 2 \sum_{i,k=1}^{N_I,N_S} Z\hat{Q}_x^{I_iS_k} \right) \\
&= 2^{-N-2}\zeta^2 \left(\sum_{i,j=1}^{N_I}{}' \left(\hat{I}_{ix}\hat{I}_{jx} + \hat{I}_{iy}\hat{I}_{jy} \right) + \sum_{k,l=1}^{N_S}{}' \left(\hat{S}_{kx}\hat{S}_{lx} + \hat{S}_{ky}\hat{S}_{ly} \right) + 2 \sum_{i,k=1}^{N_I,N_S} \left(\hat{I}_{ix}\hat{S}_{kx} + \hat{I}_{iy}\hat{S}_{ky} \right) \right),
\end{aligned} \tag{6.15}$$

where $N = N_I + N_S$ is the overall number of spins in the system. The product operators $\hat{I}_{ix}\hat{I}_{jx}$, $\hat{S}_{kx}\hat{S}_{lx}$ and $\hat{I}_{ix}\hat{S}_{kx}$ are composed of both, ZQCs and DQCs (see section 2.9). As DQCs are dephased by the pulsed gradient field applied during the subsequent *evolution* period, the approximation to line three is valid. Each coherence is weighted by the factor ζ^2. Even though the individual contributions of these operators is small, the huge number of involved spin couplings results in the formation of observable signals under the influence of long-range dipolar couplings. For the sake of simplicity, in the following, the observable signal is only derived from homonuclear ZQCs between the I-spins ($Z\hat{Q}_x^{I_iI_j}$). In section 6.2.4 the results are transfered to the homonuclear ZQCs between the S-spins as well as the heteronuclear coherences between I- and S-spins.

Evolution Period

During the *evolution* period, the operator $Z\hat{Q}_x^{I_iI_j}$ evolves for a time t_1 exclusively under the Zeeman Hamiltonian (see equation 2.11). Evolution due to spin couplings like indirect or direct dipole-dipole interactions do not influence ZQCs. Subsequently, the correlation gradient is applied for a period t_g. The secular approximation is assumed to be valid, such that only the secular component of the magnetic field $B_{g,z}$ is considered (see equation 2.16). Therefore, during the period t_g, evolution is described by a superposition of the Zeeman and the gradient Hamiltonian. Interactions during t_1 might also lead to three-spin operators of the form $\hat{I}_{ix}\hat{S}_{jx}\hat{I}_{kz}$. However, in this case two interactions are required during t_2 to transform these operators back to observable in-phase SQCs. As operators requiring only one interaction during t_2 are much stronger, three-spin operators do not need to be considered throughout the *evolution*

period. At the end of the *evolution* period, the density operator $\hat{\rho}_{II}^{ZQ}(t_1 + t_g)$ is given as

$$\begin{aligned}
&\hat{\rho}_{II}^{ZQ}(t_1 + t_g) = \\
&2^{-N-2}\zeta^2 \sum_{i,j=1}^{N_I}{}' \Bigg(\cos\Big(\Omega_{I_iI_j}^{ZQ} \cdot (t_1 + t_g) + \gamma B_{g,z}(\boldsymbol{s}_{I_i} - \boldsymbol{s}_{I_j}) t_g\Big) \hat{ZQ}_x^{I_iI_j} \\
&+ \sin\Big(\Omega_{I_iI_j}^{ZQ} \cdot \left(t_1 + t_g\right) + \gamma B_{g,z} \left(\boldsymbol{s}_{I_i} - \boldsymbol{s}_{I_j}\right) t_g\Big) \hat{ZQ}_y^{I_iI_j} \Bigg) \\
&\approx 2^{-N-2}\zeta^2 \sum_{i,j=1}^{N_I}{}' \Bigg(\cos\Big(\gamma B_{g,z}(\boldsymbol{s}_{I_i} - \boldsymbol{s}_{I_j}) t_g\Big) \hat{ZQ}_x^{I_iI_j} + \sin\Big(\gamma B_{g,z} \left(\boldsymbol{s}_{I_i} - \boldsymbol{s}_{I_j}\right) t_g\Big) \hat{ZQ}_y^{I_iI_j} \Bigg) \\
&\approx 2^{-N-2}\zeta^2 \sum_{i,j=1}^{N_I}{}' \Bigg(\cos\Big(\gamma B_{g,z}(\boldsymbol{s}_{I_i} - \boldsymbol{s}_{I_j}) t_g\Big) \hat{ZQ}_x^{I_iI_j} \Bigg),
\end{aligned} \tag{6.16}$$

where the zero-quantum frequency $\Omega_{I_iI_j}^{ZQ} = \Omega_{I_iI_j}^{ZQ,P} = \Omega_{I_iI_j}^{ZQ,N} \approx 0$. This leads to the approximation in line two. No distinction is required between p- and n-type coherence as both follow the same CTP. This is discussed in more detail in section 6.2.4. As the sine function is odd and all interactions between two spins are mutual, the term $\hat{ZQ}_y^{I_iI_j}$ averages to zero.

Mixing Period

During the *mixing* period, unobservable ZQCs are transfered to anti-phase SQCs of the form $\hat{I}_{ix}\hat{I}_{jz}$ and $\hat{I}_{iz}\hat{I}_{jx}$ by a second RF-pulse (hard α_y-pulse). The density operator $\hat{\rho}_{II}^{ZQ}(t_2 = 0)$ after this pulse is given as

$$\begin{aligned}
\hat{\rho}_{II}^{ZQ}(t_2 = 0) = 2^{-N-2}\zeta^2 \sum_{i,j=1}^{N_I}{}' &\cos\Big(\gamma B_{g,z}(\boldsymbol{s}_{I_i} - \boldsymbol{s}_{I_j}) t_g\Big) \\
&\Big(\cos^2(\alpha) 2\hat{I}_{ix}\hat{I}_{jx} + \sin^2(\alpha) 2\hat{I}_{iz}\hat{I}_{jz} - \sin(\alpha)\cos(\alpha)[2\hat{I}_{ix}\hat{I}_{jz} + 2\hat{I}_{iz}\hat{I}_{jx}] + 2\hat{I}_{iy}\hat{I}_{jy}\Big) \\
\approx\ -\sin(2\alpha) 2^{-N-3}\zeta^2 \sum_{i,j=1}^{N_I}{}' &\cos\Big(\gamma B_{g,z}(\boldsymbol{s}_{I_i} - \boldsymbol{s}_{I_j}) t_g\Big) [2\hat{I}_{ix}\hat{I}_{jz} + 2\hat{I}_{iz}\hat{I}_{jx}],
\end{aligned} \tag{6.17}$$

where the approximation to line two is valid as neither ZQCs and DQCs, nor the polarization operators lead to an observable signal. Only the anti-phase SQCs $\hat{I}_{ix}\hat{I}_{jz}$ and $\hat{I}_{iz}\hat{I}_{jx}$ need to be considered. Furthermore, the trigonometric identity $\sin(2\alpha) = 2\cos(\alpha)\sin(\alpha)$ is applied. The signal intensity caused by the homonuclear ZQCs is maximized for $\alpha = \pi/4$. A flip angle of $\alpha = \pi/2$ does not lead to any observable signal caused by homonuclear ZQCs. The influence of the flip angle α, especially on heteronuclear ZQCs is analyzed is more detail in section 6.2.4.

Detection Period

During the *detection* period, the density operator evolves due to Zeeman (see equation 2.11) and distant dipolar interactions (see equation 2.25) simultaneously. The transformation from unobservable anti-phase SQCs to observable in-phase SQCs is caused by direct dipole-dipole couplings, characterized by the secular dipole-dipole coupling constant D^{II} (see equation 2.26). The density operator $\hat{\rho}_{II}^{ZQ}(t_2)$ during the *detection* period is given as

$$\begin{aligned}
\hat{\rho}_{II}^{ZQ}(t_2) = & -\sin(2\alpha)2^{-N-3}\zeta^2 \sum_{i,j=1}^{N_I}{}' \cos\Big(\gamma B_{g,z}(\boldsymbol{s}_{I_i}-\boldsymbol{s}_{I_j})t_g\Big) \\
& \Bigg(\cos\Big(\pi D_{ij}^{II}t_2\Big)\Big[\cos(\Omega_{I_i}t_2)2\hat{I}_{ix}\hat{I}_{jz}+\sin(\Omega_{I_i}t_2)2\hat{I}_{iy}\hat{I}_{jz}+\cos\Big(\Omega_{I_j}t_2\Big)2\hat{I}_{jx}\hat{I}_{iz}+\sin\Big(\Omega_{I_j}t_2\Big)2\hat{I}_{jy}\hat{I}_{iz}\Big] \\
& +\sin\Big(\pi D_{ij}^{II}t_2\Big)\Big[\cos(\Omega_{I_i}t_2)\hat{I}_{iy}-\sin(\Omega_{I_i}t_2)\hat{I}_{ix}+\cos\Big(\Omega_{I_j}t_2\Big)\hat{I}_{jy}-\sin\Big(\Omega_{I_j}t_2\Big)\hat{I}_{jx}\Big]\Bigg) \\
\approx & -\sin(2\alpha)2^{-N-3}\zeta^2 \sum_{i,j=1}^{N_I}{}' \cos\Big(\gamma B_{g,z}(\boldsymbol{s}_{I_i}-\boldsymbol{s}_{I_j})t_g\Big)\pi D_{ij}^{II}t_2 \\
& \Big[\cos(\Omega_{I_i}t_2)\hat{I}_{iy}-\sin(\Omega_{I_i}t_2)\hat{I}_{ix}+\cos\Big(\Omega_{I_j}t_2\Big)\hat{I}_{jy}-\sin\Big(\Omega_{I_j}t_2\Big)\hat{I}_{jx}\Big] \\
= & \sum_{i,j=1}^{N_I}{}' a_{ij}^{II}(t_2)\Big[\cos(\Omega_{I_i}t_2)\hat{I}_{iy}-\sin(\Omega_{I_i}t_2)\hat{I}_{ix}+\cos\Big(\Omega_{I_j}t_2\Big)\hat{I}_{jy}-\sin\Big(\Omega_{I_j}t_2\Big)\hat{I}_{jx}\Big]\,,
\end{aligned} \tag{6.18}$$

where the approximation to line two comes from the small angle approximation $\sin\Big(\pi D_{ij}^{II}t_2\Big) \approx \pi D_{ij}^{II}t_2$. This approximation is valid as the individual distant dipolar interactions, characterized by D_{ij}^{II} are very small (see section 2.3.2). Furthermore, the unobservable anti-phase operators are dropped. For every spin pair I_i-I_j, there are two peaks Ω_{I_i} and Ω_{I_j} in the direct dimension and at the ZQ frequency $\Omega_{I_iI_j}^{ZQ} \approx 0$ in the indirect dimension. These peaks are weighted by the factor $a_{ij}^{II}(t_2)$ given as

$$\begin{aligned}
a_{ij}^{II}(t_2) = & -\sin(2\alpha)2^{-N-3}\zeta^2\pi\cos\Big(\gamma B_{g,z}(\boldsymbol{s}_{I_i}-\boldsymbol{s}_{I_j})t_g\Big)D_{ij}^{II}t_2 \\
= & \sin(2\alpha)2^{-N-3}\zeta^2\pi\gamma_I^2\hbar\frac{3\mu_0}{16\pi^2}\cos\Big(\gamma B_{g,z}(\boldsymbol{s}_{I_i}-\boldsymbol{s}_{I_j})t_g\Big)\frac{3\cos^2(\Theta_{ij})-1}{|\boldsymbol{r}_{ij}|^3}t_2 \\
= & \, c_{II}b_{ij}^{II}t_2\,,
\end{aligned} \tag{6.19}$$

where the weighting factor b_{ij}^{II}, given as

$$b_{ij}^{II} = \cos\Big(\gamma B_{g,z}(\boldsymbol{s}_{I_i}-\boldsymbol{s}_{I_j})t_g\Big)\frac{3\cos^2(\Theta_{ij})-1}{|\boldsymbol{r}_{ij}|^3} \tag{6.20}$$

only depends on the relative position $\boldsymbol{s}_{I_i}-\boldsymbol{s}_{I_j}$ between the corresponding spins as well as on the gradient field $B_{g,z}$ and the gradient duration t_g. It is analyzed qualitatively (see section 6.2.2) and quantitatively for various sample shapes and field gradients (see section 6.2.3). The factor $a_{ij}^{II}(t_2)$ actually

depends on t_2 by $\sin\left(\pi D_{ij}^{II} t_2\right)$. A linear dependence on t_2 is only valid for small arguments. As D_{ij}^{II} is proportional to $|\boldsymbol{r}_{ij}|^3$ (see section 2.3.2), the observable signal shows a rather long build-up time, especially for long distance couplings. To reduce signal losses due to field inhomogeneities during this build-up time, a spin echo is included in the *detection* period (see figure 6.7). Due to the very individual properties of D_{ij}^{II} for each spin pair, no universal optimization approach in terms of the echo time can be given. In the following, the spin echo is only considered qualitatively.

6.2.2 Breaking Magnetic Isotropy

Short-range ($|\boldsymbol{r}_{ij}| < r_0$) intermolecular direct dipole-dipole couplings in isotropic liquid are subject to temporal averaging caused by diffusion (see section 2.3.2). Only long-range ($|\boldsymbol{r}_{ij}| > r_0$) intermolecular direct dipole-dipole couplings are considered unaffected by temporal averaging. However, these couplings underlie spatial averaging (see section 2.3.2), which results in cancellation of the individual couplings. Spatial averaging can be reduced by breaking the magnetic isotropy of the sample such that the spins experience a non-spherical environment. This is either possible by pulsed field gradients or non-spherical sample geometries. For the following discussion the factor b_{ij}^{II} (see equation 6.20), which depends solely on the gradient specific parameters $B_{g,z}$ and t_g as well as on the spatial positions $\boldsymbol{s}_i$ and $\boldsymbol{s}_j$ of the involved spins is analyzed. Figure 6.8a illustrates the exclusively spatial component $(3\cos^2(\Theta_{ij}) - 1)$ (xz-plane) of b_{ij}^{II}, where the term $|\boldsymbol{r}_{ij}|^{-3}$ is not considered here for better visibility. Spin I_i is at the spatial location $\boldsymbol{s}_i = \boldsymbol{0}$. As shown in section 2.3.2, integrating over the sphere A and thus considering all spin couplings with spin I_i is equal to zero (spatial averaging), independent of the inter spin distance $|\boldsymbol{r}_{ij}|$. This assumes magnetic isotropy. However, the application of a field gradient $B_{g,z}$ for a duration t_g can break this isotropy. Figure 6.8b illustrates b_{ij}^{II} in case a constant z-gradient ($B_{g,z}(\boldsymbol{s}_{I_j}) = G_z z_{I_j}$, where z_{I_j} is the z-location of spin I_j and G_z the gradient in z-direction) was applied for a duration t_g. This results in a spatial modulation of b_{ij}^{II} in the direction of the gradient (here z-direction), according to $\cos\left(\gamma G_z z_{I_j} t_g\right)$. For a given inter spin distance $|\boldsymbol{r}_{ij}|$ the integral over the sphere A does not average to zero anymore. Integration over the sphere illustrated in figure 6.8b results in a positive value. However, if the radius is increased (observing couplings at different inter spin distances), integration over the sphere may lead to negative values. The difference between a radius resulting in positive to a radius resulting in negative values is defined by the gradient parameters G_z and t_g according to

$$d_c = \frac{\pi}{\gamma G_z t_g}, \tag{6.21}$$

where d_c is the correlation distance. Usually d_c is much smaller than the sample dimensions. The transversal anti-phase SQCs that are modulated by b_{ij}^{II} (see equation 6.18) and thus transformed to observable in-phase SQCs are dephased by the gradient. They form a helix pointing in the direction of the applied gradient with a half-pitch according to the correlation distance d_c. As intermolecular couplings depend on the individual orientations of the coupled spins, this preference leads to a non-zero remainder. Referring to [53], the effectiveness of constant gradients depending on the gradient direction is given as $\Delta = [3(\boldsymbol{e}_g \boldsymbol{e}_z)^2 - 1]/2$. Hence, gradient induced dephasing is most effectively reversed by dipolar couplings if the dephasing helix points in z-direction. If the gradient direction is towards the magic angle ($\Delta = 0$), the effectiveness is equal to zero.

As not only spins I_k on a sphere A with a certain radius do interact with spin I_i but all spins on shells with the whole range of radii, the individual spherical integrations need to be integrated over the whole range

of radii. This includes inter spin distances that lead to positive values, whereas others lead to negative values. However, the results do not average out due to the strong dependence on the inter spin distance $|\boldsymbol{r}_{ij}|^{-3}$. Therefore, the bulk of the signal comes from spins in the first spatial period greater than the diffusion radius r_0. This is discussed in detail in section 6.2.3.

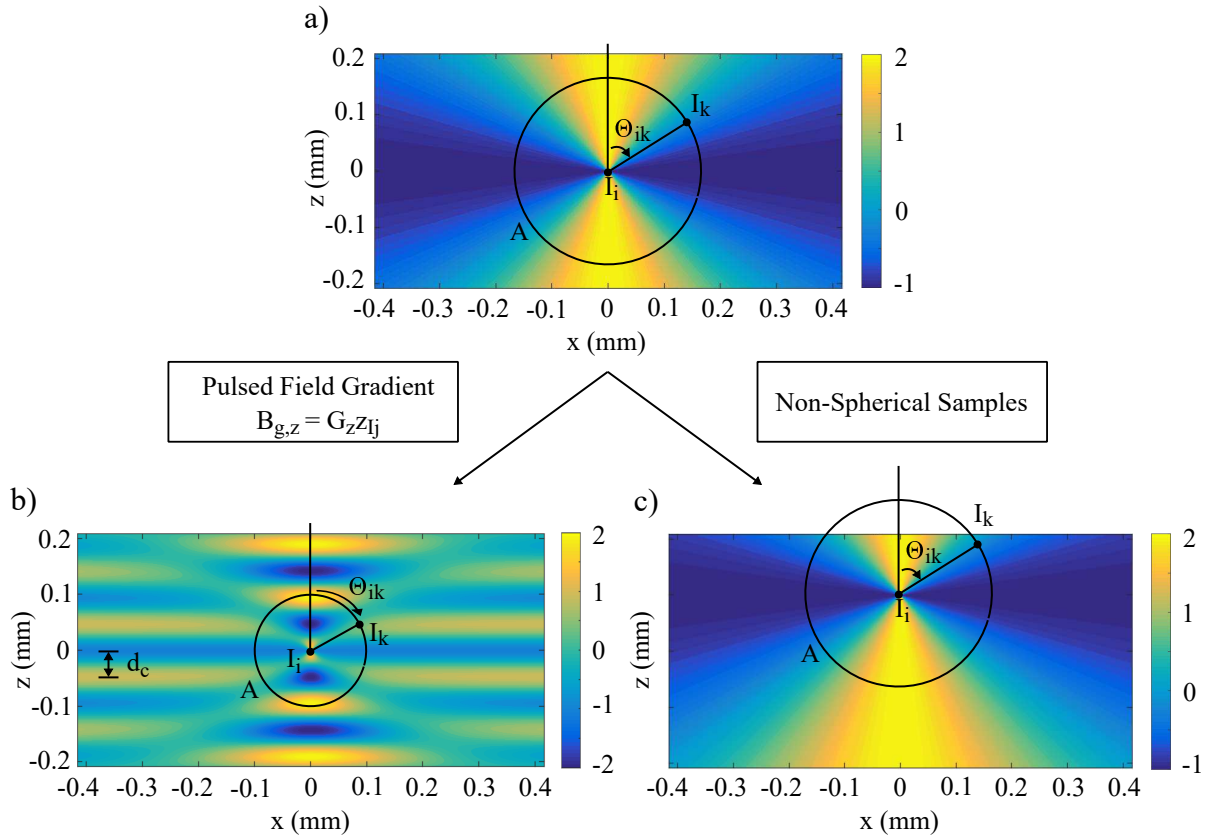

Figure 6.8: Breaking magnetic isotropy. a) Angular dependence of the secular dipole-dipole constant $(3\cos^2(\Theta_{ik}) - 1)$ illustrated on a cut through the xz-plane of the sample at $y = 0$. The spin $\hat{I}_i$ is located in the center of the sample. Spatial averaging is shown by integrating over sphere A. b) Breaking magnetic isotropy by the application of pulsed field gradients, modulating the SQCs. c) Rim effects. Not the entire sphere A contributes to the overall dipolar interactions experienced by spin I_i.

Besides breaking the magnetic isotropy by the application of pulsed field gradients, spatial averaging of distant dipolar couplings can also be reduced by using non-spherical sample geometries. Observing all spins on a shell A with a radius $|\boldsymbol{r}_{ij}|$ such that A is partly out of the sample leads to a residual intermolecular coupling on spin I_i. This is illustrated in figure 6.8c. As intermolecular couplings strongly decrease with the distance, only spins close to the rim of the sample are affected. Spins far away from the rim always experience spherical environments. Therefore, the larger a samples surface, the stronger are the net couplings - even without correlation pulses.

6.2.3 Evaluation of the Signal Magnitude

The signal contribution S of spin I_1, originating from homonuclear ZQCs of the form $\hat{ZQ}_x^{I_1 I_j}$ is proportional to the sum over the contribution of each individual long-range dipole-dipole coupling such that

$$S \propto \begin{cases} \sum_{j=2}^{N_I} b_{1j}^{II} = \sum_{j=2}^{N_I} \cos\left(\gamma B_{g,z}(\boldsymbol{s}_{I_j}) t_g\right) \frac{3\cos^2(\Theta_{1j})-1}{|\boldsymbol{s}_{I_j}|^3} & \text{for} \quad r_0 < |\boldsymbol{r}_{1j}| < r_{sample} \\ 0 & \text{else}, \end{cases} \tag{6.22}$$

where r_0 is the diffusion radius (see section 2.3.2) and r_{sample} is the radius of the spherical sample. For the sake of simplicity, I_1 is assumed to be located at $\boldsymbol{s}_{I_1} = \boldsymbol{0}$ such that $|\boldsymbol{r}_{1j}| = |\boldsymbol{s}_{I_j}|$. Constants are neglected. The results from section 6.2.2 are presented in a quantitative manner. Spatial averaging is reduced either by non-spherical sample geometries or by applying a pulsed field gradient. Both result in the spins experiencing a less spherical environment, in average. Mathematically, this is also implied by equation 6.22 as the signal contribution S firstly depends on the sample geometry in terms of the spatial position $\boldsymbol{s}_{I_j}$ of spin I_j and thus the solid angle Θ_{1j} and secondly on the gradient field $B_{g,z}(\boldsymbol{s}_{I_j})$ as well as the gradient duration t_g.
At first, the influence of a constant gradient on spherical samples is investigated. The overall signal magnitude S is analyzed in dependence of r_0 as well as on gradient strength and duration. Subsequently, a numerical three-dimensional analysis is performed in order to compare the effects of the gradient generated by the gradient-capable probe head (see section 4.4) with an ideal constant gradient in z-direction. Furthermore, the influence of sample geometries, including spherical and cylindrical shapes is investigated.

Evaluation of the Signal Magnitude for Spherical Samples with Constant Field Gradients

In this section, the effect of a constant gradient with a strength G_z in z-direction on the signal intensity S is investigated. S (see equation 6.22) can then be rewritten to

$$S(k_G, r_{1j}, \Theta_{1j}) \propto \sum_{j=2}^{N_I} \cos(k_G z_j) \frac{3\cos^2(\Theta_{1j})-1}{r_{1j}^3} = \sum_{j=2}^{N_I} \cos(k_G \cos(\Theta_{1j}) r_{1j}) \frac{3\cos^2(\Theta_{1j})-1}{r_{1j}^3}, \tag{6.23}$$

where $k_G = \gamma G_z t_g$ (in m^{-1}) is the spatial frequency of the dephasing helix in z-direction and z_j the z-position of spin I_j. The inter spin distance $|r_{1j}|$ is assumed to be greater than r_0. Thus, the signal contribution S solely depends on the spatial position $\boldsymbol{s}_{I_j}$ of spin I_j and the gradient parameter k_G.
Due to the huge amount of spins that couple with spin I_1, a uniform spin distribution is assumed. Therefore, equation 6.23 can be rewritten in integrative form [53] as

$$\begin{aligned} S(k_G) &\propto \int_{V_0<V<V_{sample}} \cos(k_G \cos(\Theta) r) \frac{3\cos^2(\Theta)-1}{r^3} dV \\ &= \int_{r_0}^{r_{sample}} \int_0^{\pi} \int_0^{2\pi} \cos(k_G \cos(\Theta) r) \frac{3\cos^2(\Theta)-1}{r} \sin(\Theta) d\Phi d\Theta dr \\ &= \int_{r_0}^{r_{sample}} S_{shell}(k_G, r) dr, \end{aligned} \tag{6.24}$$

where $dV = r^2 \sin(\theta) dr d\Theta d\Phi$ is the volume element, r, Φ and Θ are the spherical coordinates and $S_{shell}(k_G, r)$ is the contribution of spins located on a spherical shell with a radius r given as

$$S_{shell}(k_G, r) = \int_0^{\pi} 2\pi \cos(k_G \cos(\Theta) r) \frac{3\cos^2(\Theta) - 1}{r} \sin(\Theta) d\Theta \tag{6.25}$$

A numerical solution for the normalized signal intensity $S_{shell}(k_G, r)$ is illustrated in figure 6.9a and figure 6.9b.

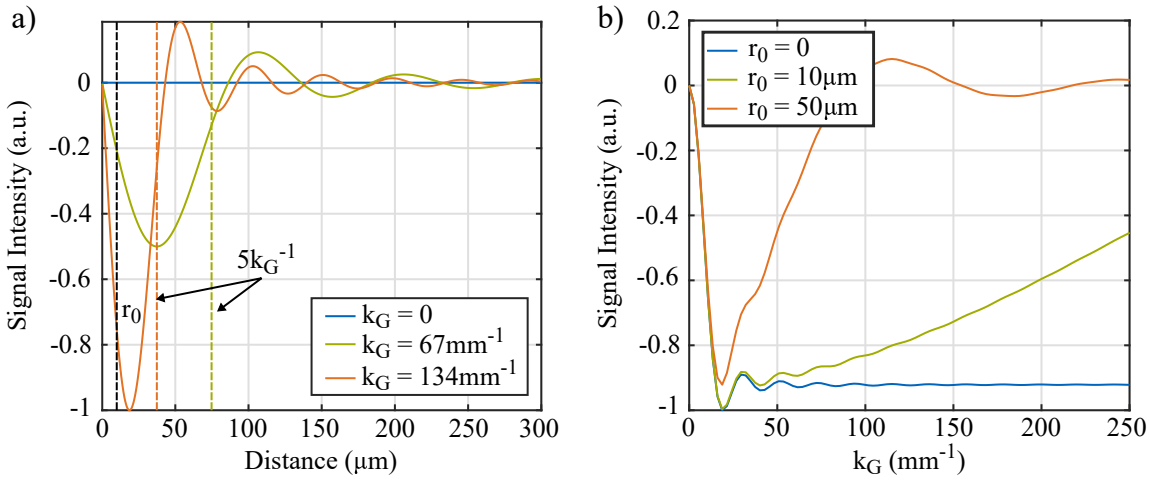

Figure 6.9: Influence of constant field gradients on distant dipolar couplings. a) Signal intensity of spin I_1 depending on the inter spin distance for different values of k_G. b) Overall signal intensity of spin I_1 in a spherical sample depending on k_G for different values of r_0.

Figure 6.9a illustrates the relative signal contribution of spins located on a shell with a radius r around spin I_1. The inter spin distance is plotted on the abscissa. Values are shown for k_G equal to 0 mm^{-1}, 67 mm^{-1} and 134 mm^{-1}. The ordinate is normalized by the maximum value of the magnitude of $S_{shell}(k_g = 134\,mm^{-1})$. In the quantum picture, the signal intensity shown in figure 6.9a is a measure of the efficiency of intermolecular direct dipole-dipole couplings to transform two-spin anti-phase SQ operators to one-spin in-phase SQ operators. If no gradient is applied ($k_G = 0\,mm^{-1}$), the signal intensity is zero, independent of the radius of the shell. This case corresponds to the spatial averaging presented in section 2.3.2. The individual interactions average to zero. Furthermore, signal contributions from spins located on a shell with a radius smaller than the diffusion radius r_0 (diffusion sphere) average to zero due to temporal averaging (see section 2.3.2). This is independent of the applied pulsed field gradient (k_G) and indicated by the black dashed vertical line marked with r_0. In this example, the diffusion length r_0 is set to $r_0 = 10\mu m$, which corresponds to estimations given in [61]. For k_G greater than zero, the magnitude is non-zero for distances greater than r_0. The magnitude rises with the distance up to a maximum, where distant dipolar interactions become most effective. The distance of most effective interactions as well as the maximum value highly depend on k_G. The higher k_G, the smaller the maximum value and the higher the distance of most effective coupling. Further increasing the radius of the shell leads to a decay of the magnitude to a value of zero interaction, prior to a second local maximum with opposite sign. This second maximum is smaller than the first one due to the indirect dependence of individual couplings on the inter spin distance. For even higher distances, the subsequent extrema further decay and alter their sign. The sinusoidal behavior is proportional to the spatial modulation frequency of the gradient illustrated in figure 6.8b. A majority of the signal contributions origin from spins with an inter spin distance ranging from k_G^{-1} to $5k_G^{-1}$. In case of $r_0 > k_G^{-1}$, the majority origins from spins at a distance ranging from r_0 to $5k_G^{-1}$. Shells with $r > 5k_G^{-1}$ contribute little to the overall signal as the integral over

the first halfwave is much bigger than over higher order halfwaves. Still, spins located on the second halfwave slightly decrease the overall signal. As $5/k_G << r_{sample}$, intermolecular direct dipole-dipole couplings are considered a strongly localized effect. Hence, the current discussion is valid for all spins distant more than $5/k_G$ from the sample rim. Due to the strong localization of this effect, inhomogeneous broadening in the indirect dimension can be greatly reduced (see section 2.10). Furthermore, the sensitivity of distant dipolar coupling to the coupling distance can be adjusted by k_G. This allows for a structural analysis of the sample. In case of a homogeneous mixture of interacting spins, k_G needs to be adjusted such that $r_0 < k_G^{-1}$. Otherwise, the most effective coupling distance falls into the regime of temporal averaging caused by diffusion. However, in case of an inhomogeneous spin distribution, where spins are arranged in certain patterns, these spatial patterns can be explored by altering k_G and observing the resultant peak intensities. For instance, this concept is applied for the differentiation of brown and white adipose tissue [13, 14].
The overall relative signal intensity $S(k_G)$ (see equation 6.24) of spin I_1 depending on k_G is illustrated in figure 6.9b for various diffusion radii r_0 (including 0 µm, 10 µm and 50 µm). $S(k_G)$ includes couplings with all spins, where the inter spin distance is smaller than 300 µm. For $k_G = 0\,mm^{-1}$, the overall signal is zero due to spatial averaging. This is independent of diffusion effects. For k_G greater than zero, the signal magnitude increases up to a maximum. As $k_G^{-1} >> r_0$, the behavior is independent of the diffusion radius r_0. However, the maximum slightly decreases with the diffusion radius, as parts of the signal are canceled by temporal averaging. Further increasing k_G leads to a slight ringing effect because higher order halfwaves (see figure 6.9a) appear in the sample. As the magnitude of the subsequent extrema decays with their order, the ringing converges to zero with increasing values of k_G. For $r_0 > 0$, the ringing effect is dominated by an increasing number of effective couplings falling in the region on temporal averaging (see dashed line figure 6.9a). The larger r_0 the faster the signal decay. In the theoretical case of $r_0 = 0\,\mu m$, the signal magnitude stays constant and is not affected by temporal averaging, independent of the k_G.

Evaluation of the Signal Magnitude for Arbitrary Sample Shapes and Field Gradients

In this section, the signal intensity (see equation 6.22) is further analyzed for cylindrical sample geometries as well as the non-ideal gradient generated by the gradient-capable probe head (see section 4.4). Results from the cylindrical sample geometry are compared to the spherical shape. The spherical sample volume is defined by a radius of 300 µm. For enhanced comparability, the sample volumes of the sphere and the cylinder are identical such that both contain the same number of spins. The cylindrical sample is thus parametrized by a radius of 208 µm and a hight of 832 µm. A grid resolution of 2 µm, resulting in approximately $14{\cdot}10^6$ spins allows for aliasing free calculations using spatial frequencies k_G of up to 1570 mm^{-1}. Such high resolutions are required due to the high slopes of the non-ideal gradient in close proximity to the rim areas (see figure 4.6).
Figure 6.10 shows the simulation results for a constant gradient, where results of the spherical sample are shown in figure 6.10a and results of the cylindrical sample are shown in figure 6.10c. Furthermore, the simulation results for the non-ideal gradient presented in section 4.4, are shown in figure 6.10b for the spherical sample and in figure 6.10d for the cylindrical sample. Even though the non-ideal gradient is not constant over the whole sample, the behavior in the very center is quasi-constant in the z-direction (see figure 4.6). The corresponding gradient $G_z^{nonIdeal}$ is defined as $G_z^{nonIdeal} = \frac{dB_{g,z}^{nonIdeal}}{dz}$. The resulting definition of $k_{G-nonIdeal} = \gamma G_z^{nonIdeal} t_g$ allows for a comparison with the ideal constant gradient.

Furthermore, all results are normalized to the maximum of figure 6.10d because it shows the highest intensities of all four simulations.

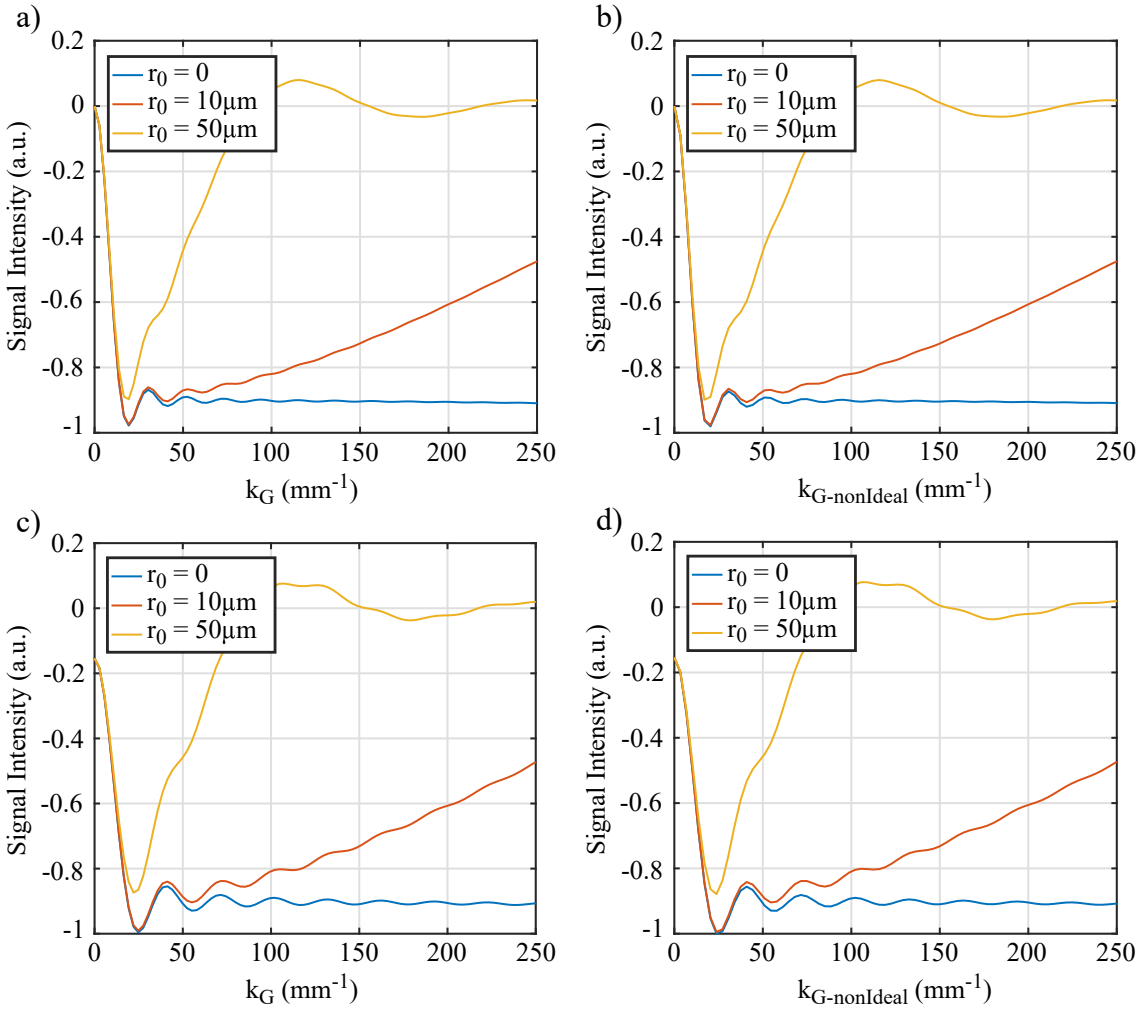

Figure 6.10: Influence of non-ideal field gradients on distant dipolar couplings for various diffusion radii. a) The influence of a constant gradient on a spherical sample. b) The influence of a non-ideal gradient on a spherical sample. c) The influence of a constant gradient on a cylindrical sample. d) The influence of a non-ideal gradient on a cylindrical sample.

Figure 6.10a shows the influence of a constant gradient on a spherical sample. Results are equivalent to the results presented in figure 6.9b. The influence of the non-ideal gradient on the spherical sample is shown in figure 6.10b. As the observed sample volume has only a radius of 300 µm, the non-ideal gradient behaves almost ideal (see figure 4.6). Thus, the influence of the ideal and the non-ideal gradient is almost equivalent. Expanding the simulation volume definitely results in larger deviations. A similar behavior is observed for the influence of the ideal and the non-ideal gradient on the cylindrical sample (see figure 6.10c and figure 6.10d).

Due to spatial averaging, the signal intensity for spherical samples is zero if no gradient is applied ($k_G = 0$ in figure 6.10a and $k_{G-nonIdeal} = 0$ in figure 6.10b). However, cylindrical samples show a significant magnitude of approximately 0.2 at $k_G = 0$ (figure 6.10c and figure 6.10d). Spatial averaging is reduced as the spins do not experience a strictly spherical environment anymore. For stronger gradients,

signal formation is dominated by the gradient. Breaking magnetic isotropy in terms of a pulsed field gradient can lead to signal intensities about six times stronger. For k_G or $k_{G-nonIdeal}$ greater than zero, the signal magnitude follows a similar pattern as described in figure 6.9b for both sample and gradient types.

6.2.4 Spectral Analysis and Expected Pattern for an I-S Spin System

The density operator $\hat{\rho}_{II}^{ZQ}(t_2)$ (see equation 6.18) reveals that peaks resulting from homonuclear ZQCs of the form $\hat{ZQ}_x^{I_iI_j}$ appear in the indirect dimension at $\Omega_{I_iI_j}^{ZQ} = 0$. In the direct dimension, the peaks appear at the offset frequency Ω_I, where n- and p-type coherences overlap. Therefore, no distinction between n- and p-type ZQCs is necessary and only one peak arises. In the following, also observable coherences resulting from homonuclear ZQCs of the form $\hat{ZQ}_x^{S_kS_l}$ of S-spins and from heteronuclear ZQCs of the form $\hat{ZQ}_x^{I_iS_k}$ are investigated. For the sake of simplicity, constants are neglected if these are common to all coherences. Moreover, the influence of the flip angle α of the mixing RF-pulse (see figure 6.7) on the spectral pattern is investigated. To distinguish between n- and p-type coherences, the ZQ operator is separated in terms of lowering and rising operators (see section 2.9). Operators that do not result in observable magnetization throughout the detection period are neglected. Thereby, the homonuclear ZQC $\hat{ZQ}_x^{I_iI_j}$ at the end of the *evolution* period is given as

$$\begin{aligned} \hat{ZQ}_x^{I_iI_j} &= \hat{I}_{i+}\hat{I}_{j-} + \hat{I}_{i-}\hat{I}_{j+} = 2(\hat{I}_{ix}\hat{I}_{jx} + \hat{I}_{iy}\hat{I}_{jy}) \\ \xrightarrow{\alpha\hat{I}_{iy}+\alpha\hat{I}_{jy}} &- \frac{\sin 2\alpha}{2}[2(\hat{I}_{ix}\hat{I}_{jz} + \hat{I}_{iz}\hat{I}_{jx})] \\ \xrightarrow{2\pi D_{ij}^{II} t_2 \hat{I}_{iz}\hat{I}_{jz}} &- \frac{\sin 2\alpha}{2}\sin\left(\pi D_{ij}^{II} t_2\right)[\hat{I}_{iy} + \hat{I}_{jy}] \end{aligned} \tag{6.26}$$

As both operators, $\hat{I}_{i+}\hat{I}_{j-}$ and $\hat{I}_{i-}\hat{I}_{j+}$ evolve with the ZQ frequency $\Omega_{I_iI_j}^{ZQ} = \Omega_{I_i} - \Omega_{I_j} = \Omega_{I_j} - \Omega_{I_i} = 0$, only a single peak is expected at $(\omega_1, \omega_2) = (0, \Omega_I)$. This peak is denoted as I (see figure 6.11a). Equivalent considerations are valid for the homonuclear ZQCs $\hat{ZQ}_x^{S_kS_l}$ resulting from S-spins. The resultant peak is located at $(\omega_1, \omega_2) = (0, \Omega_S)$ and is denoted as II (see figure 6.11a). Observable signals originating from homonuclear ZQCs are maximized for $\alpha = \pi/4$. A total cancellation is expected for $\alpha = \pi/2$. Heteronuclear n- and p-type ZQCs do not evolve at the same frequency. Therefore, n- and p-type coherences need to be evaluated separately. In terms of lowering and raising operators, heteronuclear ZQCs of the form $\hat{ZQ}_x^{I_iS_k}$ are expressed as

$$\hat{ZQ}_x^{I_iS_k} = \hat{I}_{i+}\hat{S}_{k-} + \hat{I}_{i-}\hat{S}_{k+}\,, \tag{6.27}$$

where the operator $\hat{I}_{i+}\hat{S}_{k-}$ evolves with the ZQ frequency $\Omega_I - \Omega_S$ and $\hat{I}_{i-}\hat{S}_{k+}$ with $\Omega_S - \Omega_I$. The operator $\hat{I}_{i+}\hat{S}_{k-}$ results in an observable signal on the I-spins (p-type ZQC with respect to I) and on the S-spins (n-type ZQC with respect to S). The operator $\hat{I}_{i-}\hat{S}_{k+}$ results in an observable signal on the S-spins (p-type ZQC with respect to S) and on the I-spins (n-type ZQC with respect to I). Therefore, four peaks are expected from the heteronuclear distant dipolar coupling between I- and S-spins (see figure 6.11a). p-type coherences are located at $(\omega_1, \omega_2) = (\Omega_I - \Omega_S, \Omega_I)$, denoted as III and $(\omega_1, \omega_2) = (\Omega_S - \Omega_I, \Omega_S)$, denoted as IV. n-type coherence are located at $(\omega_1, \omega_2) = (\Omega_S - \Omega_I, \Omega_I)$, denoted as V and $(\omega_1, \omega_2) = (\Omega_I - \Omega_S, \Omega_S)$, denoted as VI. In the quantum mechanical picture, the evolution of heteronuclear ZQCs is expressed as

$$\begin{aligned}
\hat{I}_{i+}\hat{S}_{k-} &= \frac{1}{2}(\hat{ZQ}_x^{I_iS_k} + j\hat{ZQ}_y^{I_iS_k}) = \hat{I}_{ix}\hat{S}_{kx} + \hat{I}_{iy}\hat{S}_{ky} + j\hat{I}_{iy}\hat{S}_{kx} - j\hat{I}_{ix}\hat{S}_{ky} \\
&\xrightarrow{\alpha\hat{I}_{iy}+\alpha\hat{S}_{ky}} -\frac{\sin 2\alpha}{2}[(\hat{I}_{ix}\hat{S}_{kz} + \hat{I}_{iz}\hat{S}_{kx})] - j\sin(\alpha)[\hat{I}_{iy}\hat{S}_{kz}] + j\sin(\alpha)[\hat{I}_{iz}\hat{S}_{ky}] \\
&\xrightarrow{2\pi D_{ik}^{IS} t_2 \hat{I}_{iz}\hat{S}_{kz}} -\frac{\sin 2\alpha}{4}\sin\left(\pi D_{ik}^{IS} t_2\right)[\hat{I}_{iy} + \hat{S}_{ky}] + j\frac{\sin(\alpha)}{2}\sin \pi D_{ij}^{II} t_2[\hat{I}_{ix} - \hat{S}_{kx}]
\end{aligned} \tag{6.28}$$

and

$$\begin{aligned}
\hat{I}_{i-}\hat{S}_{k+} &= \frac{1}{2}(\hat{ZQ}_x^{I_iS_k} - j\hat{ZQ}_y^{I_iS_k}) = \hat{I}_{ix}\hat{S}_{kx} + \hat{I}_{iy}\hat{S}_{ky} - j\hat{I}_{iy}\hat{S}_{kx} + j\hat{I}_{ix}\hat{S}_{ky} \\
&\xrightarrow{\alpha\hat{I}_{iy}+\alpha\hat{S}_{ky}} -\frac{\sin 2\alpha}{2}[(\hat{I}_{ix}\hat{S}_{kz} + \hat{I}_{iz}\hat{S}_{kx})] + j\sin(\alpha)[\hat{I}_{iy}\hat{S}_{kz}] - j\sin(\alpha)[\hat{I}_{iz}\hat{S}_{ky}] \\
&\xrightarrow{2\pi D_{ik}^{IS} t_2 \hat{I}_{iz}\hat{S}_{kz}} -\frac{\sin 2\alpha}{4}\sin\left(\pi D_{ik}^{IS} t_2\right)[\hat{I}_{iy} + \hat{S}_{ky}] - j\frac{\sin(\alpha)}{2}\sin \pi D_{ij}^{II} t_2[\hat{I}_{ix} - \hat{S}_{kx}]
\end{aligned} \tag{6.29}$$

The expected spectral pattern is illustrated schematically in figure 6.11a.

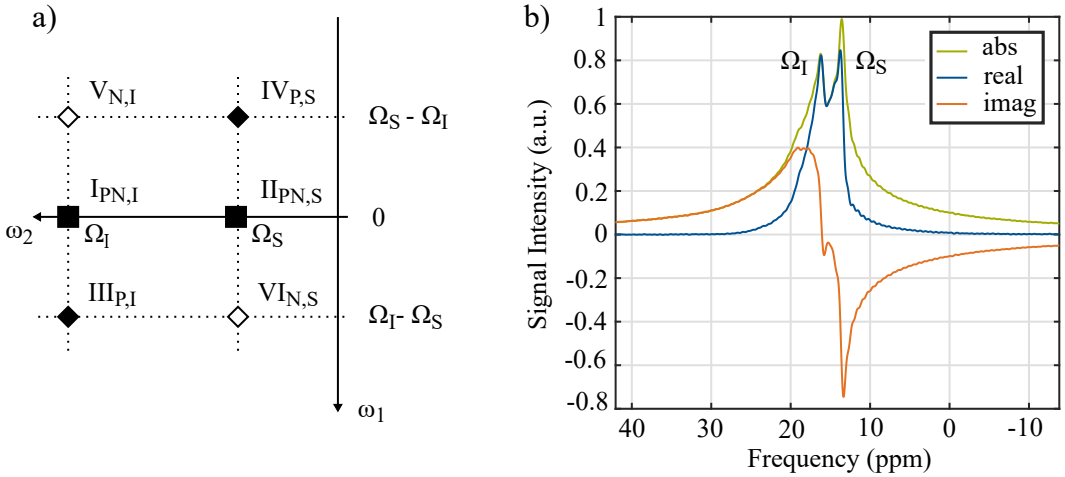

Figure 6.11: Spectral pattern of the HOMOGENIZED-sequence for an I-S spin system. a) Six peaks are expected. In the direct dimension peaks are expected at $\omega_2 = \Omega_I$ and $\omega_2 = \Omega_S$. In the indirect dimension, the peaks due to homonuclear ZQCs are expected at $\omega_1 = 0$. Peaks originating from heteronuclear ZQCs are expected at $\Omega_I - \Omega_S$ and $\Omega_S - \Omega_I$ in the indirect dimension. b) One-dimensional SQ spectrum of an acetone-water mixture.

The homonuclear peaks (I and II) vanish for $\alpha = \pi/2$ and are maximized for $\alpha = \pi/4$. Heteronuclear peaks depend in a more complex way on the flip angle. The observable in-phase SQ operators in equation 6.28 and equation 6.29 show an equivalent dependence to the flip angle as expected from the density operators $\hat{\rho}(t_2)^{(+)}$ and $\hat{\rho}(t_2)^{(-)}$ (see equation 6.11 and equation 6.12) during the detection period of the HZQC-sequence. Therefore, the observable magnetization is not derived explicitly. Detailed derivations of the observable magnetizations are given in [55, 60, 61, 138]. The magnitude ratio of peaks originating from n-type coherences to peaks originating from p-type coherences is given as

$$\left|\frac{M^+_{N,I}}{M^+_{P,I}}\right| = \left|\frac{M^+_{P,S}}{M^+_{N,S}}\right| = \left|\frac{(M_{ix}+jM_{iy})_{N,I}}{(M_{ix}+jM_{iy})_{P,I}}\right| = \left|\frac{-2\sin(\alpha)+\sin(2\alpha)}{+2\sin(\alpha)+\sin(2\alpha)}\right| = \tan^2\left(\frac{\alpha}{2}\right) \tag{6.30}$$

For $\alpha = \pi/2$, p- and n-type coherences are equal in magnitude. For $\alpha = \pi/4$, the magnitude ratio turns out to be approximately 5.8. A more detailed description is given in [138]. A good example for an I-S spin system is the homogeneous mixture of acetone and water. Figure 6.11b shows the corresponding in-phase SQ spectrum for a volume ratio of $1/1$. The chemical shift of the protons bound in acetone (located in the two methyl groups CH_3) is shifted about 2.5 ppm compared to the protons bound in water. The spectrum was acquired by a single $\frac{\pi}{2}_y$-pulse followed by an acquisition period t_{acq} of 35 ms. Attributing the offset frequency Ω_I to the water protons and Ω_S to the acetone protons, the two-dimensional HOMOGENIZED spectrum of acetone and water corresponds the one illustrated in figure 6.11a.

6.3 Discussion

ZQCs Caused by Indirect Dipole-Dipole Couplings The SoC-based NMR spectrometer (see section 3.2) and the gradient-capable NMR probe head (see section 4.4) were applied to the HZQC measurements of 1-butanol. The spectra shown in figure 6.6 exhibit spectral patterns equivalent to the predictions in section 6.1.2. Peaks appear at the ZQ frequencies corresponding to the indirect dipole-dipole couplings between the adjacent groups 4-3, 3-2, and 2-1 (see inset figure 6.6a). The hydroxyl group is not involved in ZQ transitions, as the fast proton exchange with the solution averages J-couplings [124]. Depending on the flip angle β of the first mixing pulse, either six or twelve peaks are observable. Six corresponds to a flip angle of $\pi/4$ (see figure 6.6b) and twelve to a flip angle of $\pi/2$ (see figure 6.6a). As predicted in section 6.1.2, a flip angle of $\pi/4$ leads to an attenuation of the p-type coherences. The observable peaks, located on a diagonal with a slope $\omega_2 = 2\omega_1$ originate exclusively from n-type coherences. The effect of inhomogeneous broadening on ZQCs is illustrated in figure 6.6c. The linewidth of purified water was increased from 0.6 ppm to 11 ppm by deactivating the current shims. As expected (see section 2.10), the resolution in the indirect dimension does not decrease.
Slight frequency shifts of the SQ transitions (see figure 6.3) are observed compared to [116–118]. Exact values cannot be determined due to the low resolution in inhomogeneous fields (0.6 ppm). These slight deviations arise from highly deviant experimental setups (1 T compared to 15 T) and measurement conditions including the employed solvents [117, 118]. As ZQ frequencies appear at the difference between the corresponding offset frequencies, these deviations also reveal in the peak locations in the indirect dimension. Besides the peaks referable to ZQ transitions, all spectra (see figure 6.6) exhibit a strong axial component. The major causes for these peaks are RF-pulse imperfections as well as relaxation processes. Not every RF-pulse, nor the relaxation processes are addressed by phase cycling (see section 6.1.3). Furthermore, the spoiling pulse does not affect residual Zeeman polarizations and bilinear terms. A two step phase cycle on peak one (see table 6.1a) leads to advanced axial peak suppression. This in turn leads to a reduction of the dynamic range of the data, which results in an increased resolution (see section 6.1.4). However, due to the exponential increase in measurement time with the number of phase cycles, this is not performed yet.
ZQCs caused by indirect dipole-dipole couplings are barely affected by inhomogeneous line broadening (see section 2.10). However, the resolution is limited by windowing the data in the indirect dimension (see section 6.1.4). The width of the window depends on a reasonable measurement time as well as

the time constants of the relaxation processes. Due to the high dynamic range of the HZQC spectra, caused by dominant axial peaks, windows with a strong sidelobe attenuation are required. As the lowest expected ZQ frequency origins from group two and group three, the spectral leakage of the window needs to be evaluated at 0.18 ppm. In general, increasing the dynamic range of a window reduces the frequency resolution by an increase of the main lobe width. A suitable trade-off is given by the Dolph-Chebyshev window. With a sidelobe attenuation of 100 dB, the window accounts for very high dynamic ranges. However, the sensitivity decreases compared to the square window (equivalent noise bandwidth increases to 1.9). The main lobe width, defined as the frequency, where the main lobe attenuation is equal to the attenuation of the side lobe is 0.2 ppm. This is higher than the desired resolution of 0.18 ppm. However, a meaningful definition of the main lobe width depends on the dynamic range of the spectra under consideration.

Without decreasing the dynamic range, the frequency resolution can only be increased by increasing the maximal duration of the evolution period to values larger than 256 ms. This is done either by increasing the number of t_1 increments, which maintains the spectral window at the drawback of increased measurement time, or by increasing the step size Δt_1. Increasing Δt_1 lowers the Nyquist frequency. However, increasing the duration of the evolution period is limited by T_1 and T_2 relaxation. A determination of these relaxation constants was performed by the inversion recovery and the CMPG sequence [66], respectively. The longitudinal relaxation time $T_1 = 1.11\,s$ and the transversal relaxation time $T_2 = 1.05\,s$. Activation of current shims did not affect the results appreciably (see figure 6.4). The CPMG sequence states a lower limit for the actual transversal relaxation time T_2 as perfect refocusing is only theoretical for infinitely short echo times. Comparable results at similar external field strengths were obtained by [128]. Other research groups, using setups with much higher external fields mostly described slower relaxation processes for 1-butanol [125–127]. Moreover, each group in the molecule shows a different relaxation behavior. Therefore, some ZQCs disappear faster than others. Besides the influence on ZQCs during the evolution period, relaxation processes also influence SQCs during the preparation and the mixing period. According to equation 6.2 as well as equation 6.9 and 6.10, the optimal value for $\tau_{opt} \approx \frac{1}{4J}$ for the spin echo is 25 ms (assuming an average coupling constant of 7 Hz). However, best results are achieved using approximately 17 ms due to the fast inhomogeneous dephasing of SQCs during these periods.

Equivalent to the frequencies corresponding to SQCs, ZQ frequencies depend on the external field strength. Therefore, low-field NMR requires a higher resolution in the indirect dimension, realizable only by increasing the duration of the evolution period. Especially for magnetic flux densities as low as 1 T, this results in limitations. The resolution in the indirect dimension is further reduced by the strong temperature dependence of permanent magnets. Throughout one HZQC measurement, the center frequency varies from 15 kHz to 80 kHz. To compensate for this, an FID is acquired after the first preparation pulse (see figure 6.1). The estimated frequency is used for the rotating frame of the next t_1 increment. However, the matching network with a 20 dB bandwidth of about 80 kHz (see section 4.4) cannot be adjusted on the fly. This might lead to signal distortions for instance by RF-pulse calibration errors.

Furthermore, artifacts in the direct dimension arise from spectral leakage of the square window (see figure 6.6). These could be suppressed by applying a suitable window in the direct dimension. However, the indirect dimension is not disturbed. The artifact at $\omega_1 \approx 0.3$ ppm is caused by gradient induced effects. A complete dephasing of SQCs (see figure 4.8) and higher order coherences is ensured by a gradient duration of 15 ms and a gradient current of 140 mA (see figure 4.8). The application of this spoiling pulse leads to a reduction of the phase cycling scheme by a factor of four. Accounting for the

HZQC measurement duration of about ten hours, this provides a huge time saving. For the sake of saving time, [50, 51, 139] even suggested to use the sequence without any time consuming phase cycling as they consider the influence of higher order coherences to be small.

ZQCs Caused by Intermolecular Direct Dipole-Dipole Couplings The observable magnetization M^+ (see equation 2.52) resulting from the HOMOGENEIZED sequence applied on an I-S spin system is given in [55, 60, 61, 138]. Solutions are presented for each of the six individual peaks (see figure 6.11a) either from the quantum mechanical approach or the classical approach. The observable magnetization $M^+_{II}(t_2)$ arising due to homonuclear ZQCs of the form $\hat{ZQ}^{II}_x$ is given as

$$M^+_{II}(t_2) \approx -jM^I_0 \frac{\sin(2\alpha)}{4} \frac{t_2}{\tau_{dI}} \exp(j\Omega_I t_2)\,, \tag{6.31}$$

where τ_{dI} is the corresponding time constant given as

$$\tau_d = \frac{1}{\gamma \mu_0 M^I_0} \tag{6.32}$$

Solutions for the magnetization corresponding to the remaining homonuclear ZQCs and for the cross peaks are derived in [55, 60, 61, 138]. The observable magnetization M^+_{II} depends on the square of the equilibrium magnetization M^I_0 (see equation 2.51). The maximum value as well as the rise time τ_{dI} are proportional to M^I_0. As the equilibrium magnetization is directly proportional to the external magnetic flux density B_0 (see equation 2.51), the peak intensity as well as the rise time are directly proportional to B_0. Throughout this work, only low-field permanent magnets with a magnetic flux density of 1 T are used (see section 4.1). The expected magnitude of the observable magnetization is thus very weak. Furthermore, the theoretical upper limit for M^+_{II} is only 0.4 M^I_0 [55]. However, the most critical limitation is the build-up time of the observable magnetization described by the time constant τ_{dI}. Due to the linear dependence of τ_{dI} to B_0, the required echo time (see figure 6.7) to transform anti-phase to in-phase operators rises linearly as well. With an external magnetic flux density B_0 of 17.6 T (750 MHz), [55] estimated a signal maximum for an acetone-water mixture after a transformation period of 150 ms. Experimental results lead to an optimal echo time of 270 ms. Due to the linear dependence of the time constant on B_0, this results in an optimal echo time ranging between 2.6 s and 4.5 s for a permanent magnet with 1 T. This is much higher than the time constants expected for the longitudinal and the transversal relaxation processes (see section 2.11). Hence, prior to completing the transformation from unobservable anti-phase SQCs to observable in-phase SQCs by distant dipolar couplings, the SQCs vanish due to relaxation. The detection of intermolecular direct dipole-dipole couplings via ZQCs is thus barely possible using low field NMR systems with a magnetic flux density of only 1 T.
Moreover, the observable magnetization M^+_{II} given above shows a dependence on the flip angle α that is equivalent to the results presented in section 6.2.4. Diagonal peaks, originating from the homonuclear ZQCs $\hat{ZQ}^{II}_x$ and $\hat{ZQ}^{SS}_x$ completely disappear for a flip angle $\alpha = \pi/2$, whereas a maximum is reached for $\alpha = \pi/4$. However, cross peaks follow a more complex relationship (see section 6.2.4). This relationship is equivalent to the HZQC sequence (see section 6.1.2). The ratio between p- and n-type coherences is given as $\tan^2\left(\frac{\alpha}{2}\right)$. For $\alpha = \pi/2$, p- and n-type coherences are equal in magnitude, whereas a flip angle of $\pi/4$ results in a magnitude ratio of approximately 5.8. This is favorable due to frequency discrimination in the indirect dimension as well as a loss-free simplification of the two-dimensional spectrum. Furthermore, peaks caused by heteronuclear coherences are amplified by a factor of about 1.2 compared to a flip angle of $\pi/2$. For many applications of intermolecular ZQCs like the

distinction of brown and white adipose tissue, the evaluation of cross peaks is required [13, 14]. Thus, mostly a flip angle of $\alpha/4$ is preferable.
The non-ideal gradient (see section 4.4) is suitable for the dephasing of coherences different from zero (see figure 4.8). However, correlation capabilities behave more complex. The simulation results shown in figure 6.10b and 6.10d, for spherical and cylindrical samples, respectively, suggest a correlation effect as efficient as with the ideal constant gradient. Yet, simulation data is only given for a small sample in the center of the coil. Here, the gradient is quasi constant in the z-direction (see figure 4.6). Expanding the sample dimensions certainly leads to deviations. Gradients cannot be considered constant anymore. Moreover, the direction is no longer limited to the z-direction. Still, the z-component is stronger (by a factor of about 6 compared to the x- and y-components, see figure 4.6) and more effective than components in any other direction [54].
The introduction of the factor $k_{G-nonIdeal}$ for non-ideal gradients allows for a comparison with the constant gradient. However, this is only an approximation, not valid for the entire sample. Correlation pulses used in iZQC measurements have gradients of 60 mT/m, 120 mT/m, 300 mT/m and 200 mT/m [53–55] and are therefore much stronger than the gradient strength of 6.5 mT/m generated by a gradient current of 100 mA. With a gradient duration of about 1 ms this results in a maximal value for k_G of about 0.3 mTs/m and a correlation distance of about 50 µm. Equivalent values are achieved with the gradient-capable probe head by increasing the gradient duration by a factor between 10 and 30 or by the use of higher gradient currents. As distant dipolar couplings with an inter spin distance ranging from k_G^{-1} to $5k_G^{-1}$ are most efficient (see figure 6.9a), the exact choice strongly depends on the application. For the simple evidence of these couplings in a homogeneous acetone-water mixture, the choice is not critical as long as k_G^{-1} is greater than the diffusion sphere and $5k_G^{-1}$ is smaller than the sample dimensions. If applying intermolecular ZQCs for the structural analysis of the sample [13, 14], k_G needs to be adjusted to the geometrical patterns of the sample. Moreover, shortening the correlation distance by the pulsed field gradient leads to a reduction of inhomogeneous broadening as intermolecular couplings become more localized. However, an increase in line broadening is caused by temperature dependent field drifts of the permanent magnets, equivalent to the HZQC sequence.
Sampling considerations in the indirect dimension are equivalent to the HZQC sequence (see section 6.1). The step size Δt_1 determines the Nyquist frequency, whereas the maximum duration of the *evolution* period (see figure 6.7) determines the spectral resolution.

7 Conclusion

In this thesis, low-field NMR spectroscopy was applied for the characterization of MNPs as well as for reaction monitoring and quality control throughout the synthesis process. As part of the IGSSE cooperation 9.06, a µC-based NMR spectrometer was developed and integrated in a fully automated particle reactor. Furthermore, an advanced SoC-based NMR spectrometer, accompanied by a gradient-capable NMR probe head was developed.

Microreactor with Integrated Characterization for the Synthesis of Magnetic Nanoparticles

The MiCSMaP device integrates the flow-based synthesis of MNPs and subsequent particle functionalization with a low-field NMR relaxometer. By integrating programmable pumps and valves, a fully automated synthesis and characterization flow was ensured. The synthesis of MNPs by coprecipitation of iron salt precursors and a base, in a foil-based microreactor was supported by 3D hydrodynamic flow focusing. This successfully prevented the reactor from fouling and clogging. In addition, precise diffusion-based mixing in the microchannels resulted in defined primary particle sizes as well as narrow size distributions in terms of standard deviation. For base concentrations increasing from 10 mM to 40 mM $NaOH$, the primary particle size could be adjusted from 24.8 nm to 12.3 nm. The corresponding relative standard deviations ranged from 29 % to 23 %. Moreover, varying the iron salt precursor concentration from 30 mM to 60 mM led to an increase of the primary particle size from 15.1 nm to 24.8 nm, while the standard deviation ranged from 32 % to 29 %, respectively.
The relaxometer allowed for the characterization of relaxation processes in terms of transverse and longitudinal relaxation rates. This was achieved during a continuous synthesis process by splitting the stream and providing only small samples to the NMR probe head. For a more precise process monitoring, the sampling frequency could be increased by expansion to a multi-channel NMR system like proposed in [19]. The acquired relaxation rates allowed for conclusions concerning the MNP characteristics and the synthesis process. Furthermore, the data can be used for optimizations on the peptization process and thus on the cluster size. Finally, the influence of particle coatings on transverse and longitudinal relaxivities could be investigated right after the coating procedure. It was shown that the integrated low-field NMR spectrometer presents a reliable and fast alternative to the rather expensive and time consuming determination using clinical MRIs, spatially separated from the microfluidic reactor. The potential use of the system was demonstrated on the synthesis and optimization of MNPs regarding their transverse relaxivity. Values of 115.5 $mM^{-1}s^{-1}$ for a cluster size of 122 nm were achieved for uncoated particles. Alendronate coating led to a reduction to 89.9 $mM^{-1}s^{-1}$. The obtained relaxivities are comparable to published alternatives [35]. Moreover, the longitudinal relaxivity was determined to 10.5 $mM^{-1}s^{-1}$ for uncoated and 6.8 $mM^{-1}s^{-1}$ for alendronate-coated particles. The corresponding relaxivity ratio resulted in 11.0 and 13.3, respectively. Colloidal stability, evidenced by a negative zeta potential at neutral pH as well as free amino groups of alendronate allow for further functionalization of the particle clusters with biomolecules and thus the application, for instance in analytical bioassays.
Synthesis systems, incorporating analytical tools like the NMR spectrometer presented in this work can

support the fast development of novel synthesis concepts. Furthermore, insights on effects of surface coating and optimization processes of functional MNPs can be gathered. Continuous inline monitoring and thus controlled and defined synthesis processes of MNPs by microfludic reactors may further accelerate applications like NMR-based biosensors [140] or the use of MNPs as contrast agents in clinical MRI applications [34]. The automated synthesis and the immediate determination of the output characteristics can thus reduce the time-to-market. Further expansions of the analytical capabilities, for instance by size or zeta potential determination methods may not only improve the synthsis process of iron oxid particles as shown here but may also lead to improvements of various production processes. Eventually, even decentralized and on-demand production of various nanomaterials might be achieved.

SoC-Based NMR Spectrometer and Gradient-Capable Probe Head

The use of pulsed field gradients is required for a large number of NMR applications. However, most portable low-cost NMR systems lack this feature due to the increased complexity of gradient systems. A solution for this is provided by the SoC-based NMR spectrometer accompanied by the gradient-capable NMR probe head. The spectrometer incorporates a custom designed pulse generator allowing for very versatile square wave pulse sequences in terms of the number of RF-pulses as well as pulse frequencies, phases, durations, and delays. Furthermore, the system allows for an arbitrary number of acquisition intervals with individual receiver settings. The corresponding analog transceiver board was designed for NMR frequencies ranging from 20 MHz to 48 MHz, which thus allows for proton NMR with B_0 ranging from 0.5 T to more than 1 T. The adjustable receiver gain ranges from 47.5 dB up to 95.0 dB with an LNA noise figure of 2.6 dB and an LNA gain of 20 dB. The NMR transmitter achieves an output power of 1 W (30 dBm) at 20 MHz and 0.5 W (27 dBm) at 45 MHz.
Besides the SoC-based spectrometer, a novel gradient-capable NMR probe head design was presented. The probe head incorporates RF-capabilities with the ability of pulsed field gradient generation. Simulation data showed that the gradient is neither constant nor exclusive to one field direction. However, NMR results proved that a gradient with a duration of 10 ms and a gradient current of 140 mA is sufficient to fully dephase the magnetization. The gradient strength is adjustable by the gradient current. Simulation data revealed field gradients of about 6.5 mT/m in the center of the coil for a gradient current of 100 mA. Moreover, the independence of the RF-characteristics of the NMR coil as well as its sensitivity from the field gradient was determined in terms of scatter parameters and NMR acquisition results. Conclusions on the spatial shape of the field gradient were drawn regarding spectral line broadening of the spin echos. The potential use of the system was demonstrated by successfully mapping J-coupling networks at the example of 1-butanol via the investigation of ZQCs. Furthermore, resolution enhancement of ZQCs was proven by the successful application of the HZQC sequence, even in the highly inhomogeneous field of a low-field permanent magnet (linewidth water 11 ppm). Hence, the employment of the gradient-capable NMR probe head extended the spectrum of the SoC-based spectrometer to highly sophisticated multiple-quantum experiments even in very inhomogeneous fields. A graphical user interface running on top of the user application greatly simplifies and accelerates the sequence design. This leads to a fast prototyping and evaluation process of NMR experiments.
Nevertheless, several technical aspects allow for system improvement. The allowable NMR frequency range is currently limited by the data converters, which allow for frequencies of up to 120 MHz. However, the analog transceiver electronics are limited to 48 MHz by now. Even higher frequencies could be achieved by an additional frequency conversion in the analog domain prior to digitization. Furthermore, the system allows for arbitrary sequence design using hard pulses. Arbitrary pulse shapes, including

selective pulses could be achieved by streaming pulse amplitude modulation data from the processing system to the pulse modulator. Similarly, the range of potential applications could be further increased by temporal amplitude modulation of the gradient current. For instance, the formation of gradient echos requires rephasing gradients that rely on reversing the gradient current after the initial dephasing gradient. By integrating multi-channel NMR systems like proposed by [19] and using equivalent samples, the measurement time of two-dimensional NMR experiments could be greatly reduced, depending on the number of applied coils. All these improvements could even further increase the range of potential applications for low-cost low-field NMR measurement systems.

Bibliography

[1] RABI, I. I. ; ZACHARIAS, J. R. ; MILLMAN, S. ; KUSCH, P.: A New Method of Measuring Nuclear Magnetic Moment. In: *Physical Review* 53 (1938), feb, Nr. 4, S. 318. http://dx.doi.org/10.1103/PhysRev.53.318. – DOI 10.1103/PhysRev.53.318. – ISSN 0031899X

[2] PURCELL, E. M. ; TORREY, H. C. ; POUND, R. V.: Resonance absorption by nuclear magnetic moments in a solid. In: *Physical Review* 69 (1946), jan, Nr. 1-2, S. 37–38. http://dx.doi.org/10.1103/PhysRev.69.37. – DOI 10.1103/PhysRev.69.37. – ISSN 0031899X

[3] BLOCH, F.: Nuclear induction. In: *Physical Review* 70 (1946), oct, Nr. 7-8, S. 460–474. http://dx.doi.org/10.1103/PhysRev.70.460. – DOI 10.1103/PhysRev.70.460. – ISSN 0031899X

[4] BLOCH, F. ; HANSEN, W. W. ; PACKARD, M.: The nuclear induction experiment. In: *Physical Review* 70 (1946), oct, Nr. 7-8, S. 474–485. http://dx.doi.org/10.1103/PhysRev.70.474. – DOI 10.1103/PhysRev.70.474. – ISSN 0031899X

[5] BECKER, Edwin D.: A Brief History of Nuclear Magnetic Resonance. In: *Analytical Chemistry* 65 (1993), mar, Nr. 6, S. 295A–302A. http://dx.doi.org/10.1021/ac00054a716. – DOI 10.1021/ac00054a716. – ISSN 0003–2700

[6] FILLER, Aaron: The History, Development and Impact of Computed Imaging in Neurological Diagnosis and Neurosurgery: CT, MRI, and DTI. In: *Nature Precedings* (2009), jun, S. 1–1. http://dx.doi.org/10.1038/npre.2009.3267.3. – DOI 10.1038/npre.2009.3267.3

[7] HAHN, Erwin ; PIPE, Jim: *The Transformative Genius of Erwin Hahn*. http://www.ismrm.org/workshops/MultiSlice15/. Version: 2015

[8] HAHN, Erwin L.: An accurate nuclear magnetic resonance method for measuring spin-lattice relaxation times. In: *Physical Review* 76 (1949), jul, Nr. 1, S. 145–146. http://dx.doi.org/10.1103/PhysRev.76.145. – DOI 10.1103/PhysRev.76.145. – ISSN 0031899X

[9] HAHN, E. L.: Spin echoes. In: *Physical Review* 80 (1950), nov, Nr. 4, S. 580–594. http://dx.doi.org/10.1103/PhysRev.80.580. – DOI 10.1103/PhysRev.80.580. – ISSN 0031899X

[10] GOMEZ, M V. ; HOZ, Antonio de l.: NMR reaction monitoring in flow synthesis. In: *Beilstein Journal of Organic Chemistry* 13 (2017), feb, Nr. 1, 285–300. http://dx.doi.org/10.3762/bjoc.13.31. – DOI 10.3762/bjoc.13.31. – ISSN 1860–5397

[11] BEMETZ, Jonas ; WEGEMANN, Andreas ; SAATCHI, Katayoun ; HAASE, Axel ; HÄFELI, Urs O. ; NIESSNER, Reinhard ; GLEICH, Bernhard ; SEIDEL, Michael: Microfluidic-Based Synthesis of Magnetic Nanoparticles Coupled with Miniaturized NMR for Online Relaxation Studies. In:

Analytical Chemistry 90 (2018), Nr. 16, S. 9975–9982. http://dx.doi.org/10.1021/acs.analchem.8b02374. – DOI 10.1021/acs.analchem.8b02374. – ISSN 15206882

[12] ZEKTZER, Andrew S. ; MARTIN, Gary E.: Proton Zero Quantum Two-Dimensional Nmr Spectroscopy: An Alternative to Proton Double Quantum Inadequate for Mapping Complex Proton Spin Systems of Natural Products. In: *Journal of Natural Products* 50 (1987), Nr. 3, 455–462. https://pubs.acs.org/sharingguidelines

[13] BRANCA, Rosa T. ; ZHANG, Le ; WARREN, Warren S. ; AUERBACH, Edward ; KHANNA, Arjun ; DEGAN, Simone ; UGURBIL, Kamil ; MARONPOT, Robert: In Vivo Noninvasive Detection of Brown Adipose Tissue through Intermolecular Zero-Quantum MRI. In: *PLoS ONE* 8 (2013), sep, Nr. 9, e74206. http://dx.doi.org/10.1371/journal.pone.0074206. – DOI 10.1371/journal.pone.0074206. – ISSN 19326203

[14] BRANCA, Rosa T. ; WARREN, Warren S.: In vivo brown adipose tissue detection and characterization using water-lipid intermolecular zero-quantum coherences. In: *Magnetic Resonance in Medicine* 65 (2011), feb, Nr. 2, 313–319. http://dx.doi.org/10.1002/mrm.22622. – DOI 10.1002/mrm.22622. – ISSN 07403194

[15] LACEY, Michael E. ; SUBRAMANIAN, Raju ; OLSON, Dean L. ; WEBB, Andrew G. ; SWEEDLER, Jonathan V.: High-Resolution NMR Spectroscopy of Sample Volumes from 1 nL to 10 μL. In: *Chemical Reviews* 99 (1999), Nr. 10, S. 3133–3152. http://dx.doi.org/10.1021/cr980140f. – DOI 10.1021/cr980140f. – ISSN 00092665

[16] DEMAS, Vasiliki ; BERNHARDT, Anthony ; MALBA, Vince ; ADAMS, Kristl L. ; EVANS, Lee ; HARVEY, Christopher ; MAXWELL, Robert S. ; HERBERG, Julie L.: Electronic characterization of lithographically patterned microcoils for high sensitivity NMR detection. In: *Journal of Magnetic Resonance* 200 (2009), sep, Nr. 1, 56–63. http://dx.doi.org/10.1016/j.jmr.2009.06.003. – DOI 10.1016/j.jmr.2009.06.003. – ISSN 10907807

[17] FU, R. ; BREY, W. W. ; SHETTY, K. ; GOR'KOV, P. ; SAHA, S. ; LONG, J. R. ; GRANT, S. C. ; CHEKMENEV, E. Y. ; HU, J. ; GAN, Z. ; SHARMA, M. ; ZHANG, F. ; LOGAN, T. M. ; BRÜSCHWELLER, R. ; EDISON, A. ; BLUE, A. ; DIXON, I. R. ; MARKIEWICZ, W. D. ; CROSS, T. A.: Ultra-wide bore 900 MHz high-resolution NMR at the National High Magnetic Field Laboratory. In: *Journal of Magnetic Resonance* 177 (2005), nov, Nr. 1, S. 1–8. http://dx.doi.org/10.1016/j.jmr.2005.07.013. – DOI 10.1016/j.jmr.2005.07.013. – ISSN 10907807

[18] ANDERSON, Weston A.: Electrical current shims for correcting magnetic fields. In: *Review of Scientific Instruments* 32 (1961), mar, Nr. 3, 241–250. http://dx.doi.org/10.1063/1.1717338. – DOI 10.1063/1.1717338. – ISSN 00346748

[19] HUBER, Stephan ; MIN, Changwook ; STAAT, Christoph ; OH, Juhyun ; CASTRO, Cesar M. ; HAASE, Axel ; WEISSLEDER, Ralph ; GLEICH, Bernhard ; LEE, Hakho: Multichannel digital heteronuclear magnetic resonance biosensor. In: *Biosensors and Bioelectronics* 126 (2019), feb, S. 240–248. http://dx.doi.org/10.1016/j.bios.2018.10.052. – DOI 10.1016/j.bios.2018.10.052. – ISSN 18734235

[20] RAICH, H. ; BLÜMLER, P.: Design and construction of a dipolar Halbach array with a homogeneous field from identical bar magnets: NMR Mandhalas. In: *Concepts in Magnetic Resonance Part B: Magnetic Resonance Engineering* 23B (2004), oct, Nr. 1, 16–25. http://dx.doi.org/10.1002/cmr.b.20018. – DOI 10.1002/cmr.b.20018. – ISSN 15525031

[21] DANIELI, Ernesto ; PERLO, Juan ; BLÜMICH, Bernhard ; CASANOVA, Federico: Small magnets for portable NMR spectrometers. In: *Angewandte Chemie - International Edition* 49 (2010), jun, Nr. 24, 4133–4135. http://dx.doi.org/10.1002/anie.201000221. – DOI 10.1002/anie.201000221. – ISSN 14337851

[22] WU, Xiao ; PATTERSON, Donald A. ; BUTLER, Leslie G. ; MILLER, Joel B.: A broadband nuclear magnetic resonance spectrometer: Digital phase shifting and flexible pulse programmer. In: *Review of Scientific Instruments* 64 (1993), may, Nr. 5, 1235–1238. http://dx.doi.org/10.1063/1.1144122. – DOI 10.1063/1.1144122. – ISSN 00346748

[23] TAKEDA, Kazuyuki: A highly integrated FPGA-based nuclear magnetic resonance spectrometer. In: *Review of Scientific Instruments* 78 (2007), Nr. 3. http://dx.doi.org/10.1063/1.2712940. – DOI 10.1063/1.2712940. – ISSN 00346748

[24] ZALESSKIY, Sergey S. ; DANIELI, Ernesto ; BLÜMICH, Bernhard ; ANANIKOV, Valentine P.: Miniaturization of NMR systems: Desktop spectrometers, microcoil spectroscopy, and "nMR on a Chip" for chemistry, biochemistry, and industry. In: *Chemical Reviews* 114 (2014), jun, Nr. 11, S. 5641–5694. http://dx.doi.org/10.1021/cr400063g. – DOI 10.1021/cr400063g. – ISSN 15206890

[25] SUN, Nan ; LIU, Yong ; LEE, Hakho ; WEISSLEDER, Ralph ; HAM, Donhee: CMOS RF biosensor utilizing nuclear magnetic resonance. In: *IEEE Journal of Solid-State Circuits* 44 (2009), may, Nr. 5, S. 1629–1643. http://dx.doi.org/10.1109/JSSC.2009.2017007. – DOI 10.1109/JSSC.2009.2017007. – ISSN 00189200

[26] HA, Dongwan ; PAULSEN, Jeffrey ; SUN, Nan ; SONG, Yi Q. ; HAM, Donhee: Scalable NMR spectroscopy with semiconductor chips. In: *Proceedings of the National Academy of Sciences of the United States of America* 111 (2014), aug, Nr. 33, S. 11955–11960. http://dx.doi.org/10.1073/pnas.1402015111. – DOI 10.1073/pnas.1402015111. – ISSN 10916490

[27] WENSINK, Henk ; BENITO-LOPEZ, Fernando ; HERMES, Dorothee C. ; VERBOOM, Willem ; GARDENIERS, Han J. ; REINHOUDT, David N. ; VAN DEN BERG, Albert: Measuring reaction kinetics in a lab-on-a-chip by microcoil NMR. In: *Lab on a Chip* 5 (2005), Nr. 3, S. 280–284. http://dx.doi.org/10.1039/b414832k. – DOI 10.1039/b414832k. – ISSN 14730197

[28] HARIANI, Poedji L. ; FAIZAL, Muhammad ; RIDWAN, Ridwan ; MARSI, Marsi ; SETIABUDIDAYA, Dedi: Synthesis and Properties of Fe3O4 Nanoparticles by Co-precipitation Method to Removal Procion Dye. In: *International Journal of Environmental Science and Development* (2013), S. 336–340. http://dx.doi.org/10.7763/ijesd.2013.v4.366. – DOI 10.7763/ijesd.2013.v4.366. – ISSN 20100264

[29] SAATCHI, Katayoun ; TOD, Sarah E. ; LEUNG, Donna ; NICHOLSON, Kenton E. ; ANDREU, Irene ; BUCHWALDER, Christian ; SCHMITT, Veronika ; HÄFELI, Urs O. ; GRAY, Sarah L.: Characterization of alendronic- and undecylenic acid coated magnetic nanoparticles for the targeted

delivery of rosiglitazone to subcutaneous adipose tissue. In: *Nanomedicine: Nanotechnology, Biology, and Medicine* 13 (2017), feb, Nr. 2, S. 559–568. http://dx.doi.org/10.1016/j.nano.2016.08.012. – DOI 10.1016/j.nano.2016.08.012. – ISSN 15499642

[30] LAURENT, Sophie ; SAEI, Amir A. ; BEHZADI, Shahed ; PANAHIFAR, Arash ; MAHMOUDI, Morteza: Superparamagnetic iron oxide nanoparticles for delivery of therapeutic agents: Opportunities and challenges. In: *Expert Opinion on Drug Delivery* 11 (2014), Nr. 9, S. 1449–1470. http://dx.doi.org/10.1517/17425247.2014.924501. – DOI 10.1517/17425247.2014.924501. – ISSN 17447593

[31] CHEN, Yiping ; XIE, Mengxia: A magnetic relaxation switching immunosensor for one-step detection of salbutamol based on gold nanoparticle-streptavidin conjugate. In: *RSC Advances* 5 (2015), oct, Nr. 116, S. 95401–95404. http://dx.doi.org/10.1039/c5ra19126b. – DOI 10.1039/c5ra19126b. – ISSN 20462069

[32] LEE, Hakho ; SHIN, Tae H. ; CHEON, Jinwoo ; WEISSLEDER, Ralph: Recent Developments in Magnetic Diagnostic Systems. In: *Chemical Reviews* 115 (2015), Nr. 19, S. 10690–10724. http://dx.doi.org/10.1021/cr500698d. – DOI 10.1021/cr500698d. – ISSN 15206890

[33] RÜMENAPP, Christine ; GLEICH, Bernhard ; HAASE, Axel: Magnetic nanoparticles in magnetic resonance imaging and diagnostics. In: *Pharmaceutical Research* 29 (2012), may, Nr. 5, S. 1165–1179. http://dx.doi.org/10.1007/s11095-012-0711-y. – DOI 10.1007/s11095–012–0711–y. – ISSN 07248741

[34] SHEN, Zheyu ; WU, Aiguo ; CHEN, Xiaoyuan: *Iron Oxide Nanoparticle Based Contrast Agents for Magnetic Resonance Imaging*

[35] SANDIFORD, Lydia ; PHINIKARIDOU, Alkystis ; PROTTI, Andrea ; MESZAROS, Levente K. ; CUI, Xianjin ; YAN, Yong ; FRODSHAM, George ; WILLIAMSON, Peter A. ; GADDUM, Nicholas ; BOTNAR, René M. ; BLOWER, Philip J. ; GREEN, Mark A. ; DE ROSALES, Rafael T.: Bisphosphonate-anchored pegylation and radiolabeling of superparamagnetic iron oxide: Long-circulating nanoparticles for in vivo multimodal (T1 MRI-SPECT) imaging. In: *ACS Nano* 7 (2013), jan, Nr. 1, 500–512. http://dx.doi.org/10.1021/nn3046055. – DOI 10.1021/nn3046055. – ISSN 1936086X

[36] WEI, He ; BRUNS, Oliver T. ; KAUL, Michael G. ; HANSEN, Eric C. ; BARCH, Mariya ; WIŚNIOWSKA, Agata ; CHEN, Ou ; CHEN, Yue ; LI, Nan ; OKADA, Satoshi ; CORDERO, Jose M. ; HEINE, Markus ; FARRAR, Christian T. ; MONTANA, Daniel M. ; ADAM, Gerhard ; ITTRICH, Harald ; JASANOFF, Alan ; NIELSEN, Peter ; BAWENDI, Moungi G.: Exceedingly small iron oxide nanoparticles as positive MRI contrast agents. In: *Proceedings of the National Academy of Sciences of the United States of America* 114 (2017), feb, Nr. 9, S. 2325–2330. http://dx.doi.org/10.1073/pnas.1620145114. – DOI 10.1073/pnas.1620145114. – ISSN 10916490

[37] ESTELRICH, Joan ; SÁNCHEZ-MARTÍN, María Jesús ; BUSQUETS, Maria A.: Nanoparticles in magnetic resonance imaging: From simple to dual contrast agents. In: *International Journal of Nanomedicine* 10 (2015), mar, S. 1727–1741. http://dx.doi.org/10.2147/IJN.S76501. – DOI 10.2147/IJN.S76501. – ISSN 11782013

[38] JUN, Young W. ; HUH, Yong M. ; CHOI, Jin S. ; LEE, Jae H. ; SONG, Ho T. ; KIM, Sungjun ; YOON, Sarah ; KIM, Kyung S. ; SHIN, Jeon S. ; SUH, Jin S. ; CHEON, Jinwoo: Nanoscale Size Effect of Magnetic Nanocrystals and Their Utilization for Cancer Diagnosis via Magnetic Resonance Imaging. In: *Journal of the American Chemical Society* 127 (2005), apr, Nr. 16, S. 5732–5733. http://dx.doi.org/10.1021/ja0422155. – DOI 10.1021/ja0422155. – ISSN 00027863

[39] JOOS, Alexander ; LÖWA, Norbert ; WIEKHORST, Frank ; GLEICH, Bernhard ; HAASE, Axel: Size-dependent MR relaxivities of magnetic nanoparticles. In: *Journal of Magnetism and Magnetic Materials* 427 (2017), apr, S. 122–126. http://dx.doi.org/10.1016/j.jmmm.2016.11.021. – DOI 10.1016/j.jmmm.2016.11.021. – ISSN 03048853

[40] KHALKHALI, Maryam ; ROSTAMIZADEH, Kobra ; SADIGHIAN, Somayeh ; KHOEINI, Farhad ; NAGHIBI, Mehran ; HAMIDI, Mehrdad: The impact of polymer coatings on magnetite nanoparticles performance as MRI contrast agents: A comparative study. In: *DARU, Journal of Pharmaceutical Sciences* 23 (2015), sep, Nr. 1. http://dx.doi.org/10.1186/s40199-015-0124-7. – DOI 10.1186/s40199–015–0124–7. – ISSN 20082231

[41] PHILLIPS, Thomas W. ; LIGNOS, Ioannis G. ; MACEICZYK, Richard M. ; DEMELLO, Andrew J. ; DEMELLO, John C.: Nanocrystal synthesis in microfluidic reactors: Where next? In: *Lab on a Chip* 14 (2014), sep, Nr. 17, S. 3172–3180. http://dx.doi.org/10.1039/c4lc00429a. – DOI 10.1039/c4lc00429a. – ISSN 14730189

[42] JENSEN, Klavs F.: Flow chemistry-Microreaction technology comes of age. In: *AIChE Journal* 63 (2017), mar, Nr. 3, 858–869. http://dx.doi.org/10.1002/aic.15642. – DOI 10.1002/aic.15642. – ISSN 00011541

[43] MASSART, RenÉ: Preparation of Aqueous Magnetic Liquids in Alkaline and Acidic Media. In: *IEEE Transactions on Magnetics* 17 (1981), Nr. 2, S. 1247–1248. http://dx.doi.org/10.1109/TMAG.1981.1061188. – DOI 10.1109/TMAG.1981.1061188. – ISSN 19410069

[44] NISTLER, Angelika ; HARTMANN, Carolin ; RÜMENAPP, Christine ; OPEL, Matthias ; GLEICH, Bernhard ; IVLEVA, Natalia P. ; NIESSNER, Reinhard ; SEIDEL, Michael: Production and characterization of long-term stable superparamagnetic iron oxide-shell silica-core nanocomposites. In: *Journal of Magnetism and Magnetic Materials* 442 (2017), nov, S. 497–503. http://dx.doi.org/10.1016/j.jmmm.2017.07.005. – DOI 10.1016/j.jmmm.2017.07.005. – ISSN 03048853

[45] SCHNEIDER, Thomas ; LÖWA, Anna ; KARAGIOZOV, Stoyan ; SPRENGER, Lisa ; GUTIÉRREZ, Lucía ; ESPOSITO, Tullio ; MARTEN, Gernot ; SAATCHI, Katayoun ; HÄFELI, Urs O.: Facile microwave synthesis of uniform magnetic nanoparticles with minimal sample processing. In: *Journal of Magnetism and Magnetic Materials* 421 (2017), jan, S. 283–291. http://dx.doi.org/10.1016/j.jmmm.2016.07.063. – DOI 10.1016/j.jmmm.2016.07.063. – ISSN 03048853

[46] SALAZAR-ALVAREZ, German ; MUHAMMED, Mamoun ; ZAGORODNI, Andrei A.: Novel flow injection synthesis of iron oxide nanoparticles with narrow size distribution. In: *Chemical Engineering Science* 61 (2006), jul, Nr. 14, S. 4625–4633. http://dx.doi.org/10.1016/j.ces.2006.02.032. – DOI 10.1016/j.ces.2006.02.032. – ISSN 00092509

[47] KUMAR, Kritika ; NIGHTINGALE, Adrian M. ; KRISHNADASAN, Siva H. ; KAMALY, Nazila ; WYLENZINSKA-ARRIDGE, Marzena ; ZEISSLER, Katharina ; BRANFORD, Will R. ; WARE, Ecaterina ; DEMELLO, Andrew J. ; DEMELLO, John C.: Direct synthesis of dextran-coated superparamagnetic iron oxide nanoparticles in a capillary-based droplet reactor. In: *Journal of Materials Chemistry* 22 (2012), mar, Nr. 11, S. 4704–4708. http://dx.doi.org/10.1039/c2jm30257h. – DOI 10.1039/c2jm30257h. – ISSN 09599428

[48] ABOU HASSAN, Ali ; SANDRE, Olivier ; CABUIL, Valérie ; TABELING, Patrick: Synthesis of iron oxide nanoparticles in a microfluidic device: Preliminary results in a coaxial flow millichannel. In: *Chemical Communications* (2008), apr, Nr. 15, S. 1783–1785. http://dx.doi.org/10.1039/b719550h. – DOI 10.1039/b719550h. – ISSN 13597345

[49] LU, Mengqian ; YANG, Shikuan ; HO, Yi P. ; GRIGSBY, Christopher L. ; LEONG, Kam W. ; HUANG, Tony J.: Shape-controlled synthesis of hybrid nanomaterials via three-dimensional hydrodynamic focusing. In: *ACS Nano* 8 (2014), oct, Nr. 10, S. 10026–10034. http://dx.doi.org/10.1021/nn502549v. – DOI 10.1021/nn502549v. – ISSN 1936086X

[50] BAX, A. ; DE JONG, P. G. ; MEHLKOPF, A. F. ; SMIDT, J.: Separation of the different orders of NMR multiple-quantum transitions by the use of pulsed field gradients. In: *Chemical Physics Letters* 69 (1980), feb, Nr. 3, S. 567–570. http://dx.doi.org/10.1016/0009-2614(80)85130-X. – DOI 10.1016/0009–2614(80)85130–X. – ISSN 00092614

[51] HALL, Laurance D. ; NORWOOD, Timothy J.: Use of zero-quantum coherences to measure high resolution n.m.r. spectra in inhomogeneous magnetic fields. In: *Journal of the Chemical Society Chemical Communications* 1 (1986), jan, Nr. 1, S. 44–46. http://dx.doi.org/10.1039/C39860000044. – DOI 10.1039/C39860000044. – ISSN 00224936

[52] MÜLLER, Luciano: Mapping of spin-spin coupling via zero-quantum coherence. In: *Journal of Magnetic Resonance (1969)* 59 (1984), sep, Nr. 2, S. 326–331. http://dx.doi.org/10.1016/0022-2364(84)90177-X. – DOI 10.1016/0022–2364(84)90177–X. – ISSN 00222364

[53] WARREN, Warren S. ; RICHTER, Wolfgang ; ANDREOTTI, Amy H. ; FARMER, Bennett T.: Generation of impossible cross-peaks between bulk water and biomolecules in solution NMR. In: *Science* 262 (1993), dec, Nr. 5142, S. 2005–2009. http://dx.doi.org/10.1126/science.8266096. – DOI 10.1126/science.8266096. – ISSN 00368075

[54] VATHYAM, Sujatha ; LEE, Sanghyuk ; WARREN, Warren S.: Homogeneous NMR spectra in inhomogeneous fields. In: *Science* 272 (1996), apr, Nr. 5258, S. 92–96. http://dx.doi.org/10.1126/science.272.5258.92. – DOI 10.1126/science.272.5258.92. – ISSN 00368075

[55] BALLA, David Z. ; FABER, Cornelius: Localized intermolecular zero-quantum coherence spectroscopy in vivo. In: *Concepts in Magnetic Resonance Part A: Bridging Education and Research* 32 (2008), mar, Nr. 2, 117–133. http://dx.doi.org/10.1002/cmr.a.20104. – DOI 10.1002/cmr.a.20104. – ISSN 15466086

[56] RIEKE, Viola ; PAULY, Kim B.: MR thermometry. In: *Journal of Magnetic Resonance Imaging* 27 (2008), feb, Nr. 2, S. 376–390. http://dx.doi.org/10.1002/jmri.21265. – DOI 10.1002/jmri.21265. – ISSN 10531807

[57] JOHNSON, C. S.: Diffusion ordered nuclear magnetic resonance spectroscopy: Principles and applications. In: *Progress in Nuclear Magnetic Resonance Spectroscopy* 34 (1999), may, Nr. 3-4, S. 203–256. http://dx.doi.org/10.1016/S0079-6565(99)00003-5. – DOI 10.1016/S0079–6565(99)00003–5. – ISSN 00796565

[58] HIDALGO-TOBON, S. S.: Theory of gradient coil design methods for magnetic resonance imaging. In: *Concepts in Magnetic Resonance Part A: Bridging Education and Research* 36 (2010), jul, Nr. 4, 223–242. http://dx.doi.org/10.1002/cmr.a.20163. – DOI 10.1002/cmr.a.20163. – ISSN 15466086

[59] STOCKMANN, Jason P. ; WITZEL, Thomas ; KEIL, Boris ; POLIMENI, Jonathan R. ; MAREYAM, Azma ; LAPIERRE, Cristen ; SETSOMPOP, Kawin ; WALD, Lawrence L.: A 32-channel combined RF and B0 shim array for 3T brain imaging. In: *Magnetic Resonance in Medicine* 75 (2016), jan, Nr. 1, 441–451. http://dx.doi.org/10.1002/mrm.25587. – DOI 10.1002/mrm.25587. – ISSN 15222594

[60] LIN, Yulan ; HUANG, Yuqing ; CAI, Shuhui ; CHEN, Zhong: Intermolecular Zero Quantum Coherence in NMR Spectroscopy. In: *Annual Reports on NMR Spectroscopy* 78 (2013), jan, S. 209–257. http://dx.doi.org/10.1016/B978-0-12-404716-7.00005-5. – DOI 10.1016/B978–0–12–404716–7.00005–5. – ISSN 00664103

[61] LEE, S. ; RICHTER, W. ; VATHYAM, S. ; WARREN, W. S.: Quantum treatment of the effects of dipole-dipole interactions in liquid nuclear magnetic resonance. In: *Journal of Chemical Physics* 105 (1996), jul, Nr. 3, 874–900. http://dx.doi.org/10.1063/1.471968. – DOI 10.1063/1.471968. – ISSN 00219606

[62] TORREY, H. C.: Bloch equations with diffusion terms. In: *Physical Review* 104 (1956), nov, Nr. 3, S. 563–565. http://dx.doi.org/10.1103/PhysRev.104.563. – DOI 10.1103/PhysRev.104.563. – ISSN 0031899X

[63] CAI, Congbo ; CHEN, Zhong ; CAI, Shuhui ; ZHONG, Jianhui: A simulation algorithm based on Bloch equations and product operator matrix: Application to dipolar and scalar couplings. In: *Journal of Magnetic Resonance* 172 (2005), feb, Nr. 2, S. 242–253. http://dx.doi.org/10.1016/j.jmr.2004.11.003. – DOI 10.1016/j.jmr.2004.11.003. – ISSN 10907807

[64] LEVITT, Malcolm H.: *Spin Dynamics*. John Wiley & Sons, Ltd, 2008

[65] KEELER, James: *Understanding NMR Spectroscopy*. John Wiley & Sons, Ltd, 2010

[66] MEIBOOM, S. ; GILL, D.: Modified spin-echo method for measuring nuclear relaxation times. In: *Review of Scientific Instruments* 29 (1958), aug, Nr. 8, 688–691. http://dx.doi.org/10.1063/1.1716296. – DOI 10.1063/1.1716296. – ISSN 00346748

[67] KAMMEYER, Karl-Dirk ; DEKORSY, Armin: *Nachrichtenübertragung*. Springer Fachmedien Wiesbaden GmbH, 2018. – ISBN 9783658170042

[68] MISPELTER, Joel ; LUPO, Mihaela ; BRIGUET, Andre: *NMR Probeheads for Biophysical and Biomedical Experiments*. Imperial College Press, 2006

[69] FUKUSHIMA, Eiichi ; ROEDER, Stephen B. W.: *Experimental Pulse NMR A Nuts and Bolts Approach*. Westview Press, 1981

[70] WHITE, Joseph F.: *Microwave Semiconductor Engineering*. Springer Netherlands, 1982

[71] WEGEMANN, Andreas: *Development of an NMR Device to Detect and Count Magnetic Nanoparticles (at 12.305 MHz)*. 2015

[72] XILINX: *DDS Compiler v6.0 LogiCORE IP Product Guide Vivado Design Suite*. www.xilinx.com

[73] XILINX: *Zynq-7000 SoC Family Product Selection Guide*. 2014

[74] XILINX: *AXI DMA v7.1 LogiCORE IP Product Guide Vivado Design Suite*. www.xilinx.com

[75] RABINER, Lawrence R. ; MCCLELLAN, James H. ; PARKS, Thomas W.: FIR Digital Filter Design Techniques Using Weighted Chebyshev Approximation. In: *Proceedings of the IEEE* 63 (1975), Nr. 4, S. 595–610. http://dx.doi.org/10.1109/PROC.1975.9794. – DOI 10.1109/PROC.1975.9794. – ISSN 15582256

[76] XILINX: *FIR Compiler v7.2 LogiCORE IP Product Guide*. www.xilinx.com

[77] HOGENAUER, Eugene B.: An Economical Class of Digital Filters for Decimation and Interpolation. In: *IEEE Transactions on Acoustics, Speech, and Signal Processing* 29 (1981), Nr. 2, S. 155–162. http://dx.doi.org/10.1109/TASSP.1981.1163535. – DOI 10.1109/TASSP.1981.1163535. – ISSN 00963518

[78] XILINX: *CIC Compiler v4.0 LogiCORE IP Product Guide (PG140)*. www.xilinx.com

[79] BURRUS, C. S. ; SOEWITO, Admadji W. ; GOPINATH, Ramesh A.: Least Squared Error FIR Filter Design with Transition Bands. In: *IEEE Transactions on Signal Processing* 40 (1992), Nr. 6, S. 1327–1340. http://dx.doi.org/10.1109/78.139239. – DOI 10.1109/78.139239. – ISSN 19410476

[80] BURRUS, C. S.: Multiband Least Squares FIR Filter Design. In: *IEEE Transactions on Signal Processing* 43 (1995), Nr. 2, S. 412–421. http://dx.doi.org/10.1109/78.348124. – DOI 10.1109/78.348124. – ISSN 19410476

[81] FRIIS, H. T.: Noise Figures of Radio Receivers. In: *Proceedings of the IRE* 32 (1944), Nr. 7, S. 419–422. http://dx.doi.org/10.1109/JRPROC.1944.232049. – DOI 10.1109/JRPROC.1944.232049. – ISSN 00968390

[82] AZIZ, Pervez M. ; SORENSEN, Henrik V. ; VAN DER SPIEGEL, Jan: An Overview of Sigma-Delta Converters: How a 1-bit ADC achieves more than 16-bit resolution Part of the Signal Processing Commons Recommended Citation. In: *IEEE Signal Processing Magazine* 13 (1996), Nr. 1, 61–84. http://repository.upenn.edu/ese{_}papers. ISBN 10535888/96/54.0

[83] WILLIAMS, Arthur ; TAYLOR, Fred: *Electronic Filter Design Handbook*. The McGraw-Hill Companies, 2006

[84] *PM1055 Permanent Magnets - Metrolab Technology SA*. https://www.metrolab.com/products/pm1055-permanent-magnets/

[85] COEY, J M D.: New permanent magnets; manganese compounds. In: *Journal of physics. Condensed matter : an Institute of Physics journal* 26 (2014), feb, Nr. 6, 064211. http://dx.doi.org/10.1088/0953-8984/26/6/064211. – DOI 10.1088/0953–8984/26/6/064211. – ISSN 1361–648X

[86] DEMAS, Vasiliki ; PRADO, Pablo J.: Compact magnets for magnetic resonance. In: *Concepts in Magnetic Resonance Part A: Bridging Education and Research* 34 (2009), jan, Nr. 1, 48–59. http://dx.doi.org/10.1002/cmr.a.20131. – DOI 10.1002/cmr.a.20131. – ISSN 15466086

[87] *M3™ Compact Low-Cost MRI Scanner for Dedicated Mouse Imaging*. https://www.aspectimaging.com/m3-compact-mri/

[88] MURPHY-BOESCH, Joseph ; KORETSKY, Alan P.: An in Vivo NMR probe circuit for improved sensitivity. In: *Journal of Magnetic Resonance (1969)* 54 (1983), oct, Nr. 3, S. 526–532. http://dx.doi.org/10.1016/0022-2364(83)90333-5. – DOI 10.1016/0022–2364(83)90333–5. – ISSN 00222364

[89] JIANG, Yi J.: A Simple Method for Measuring the Q Value of an NMR Sample Coil. In: *Journal of Magnetic Resonance* 142 (2000), feb, Nr. 2, S. 386–388. http://dx.doi.org/10.1006/jmre.1999.1972. – DOI 10.1006/jmre.1999.1972. – ISSN 10907807

[90] LYNCH, Peter ; LYNCH, Peter: The Dolph–Chebyshev Window: A Simple Optimal Filter. In: *http://dx.doi.org/10.1175/1520-0493(1997)125<0655:TDCWAS>2.0.CO;2* (1997), apr. http://dx.doi.org/10.1175/1520-0493(1997)125<0655:TDCWAS>2.0.CO;2. – DOI 10.1175/1520–0493(1997)125¡0655:TDCWAS¿2.0.CO;2

[91] HOULT, D. I.: The NMR receiver: A description and analysis of design. In: *Progress in Nuclear Magnetic Resonance Spectroscopy* 12 (1978), jan, Nr. 1, S. 41–77. http://dx.doi.org/10.1016/0079-6565(78)80002-8. – DOI 10.1016/0079–6565(78)80002–8. – ISSN 00796565

[92] DARRASSE, Luc ; KASSAB, Ghazi: Quick measurement of NMR-coil sensitivity with a dual-loop probe. In: *Review of Scientific Instruments* 64 (1993), jul, Nr. 7, 1841–1844. http://dx.doi.org/10.1063/1.1144020. – DOI 10.1063/1.1144020. – ISSN 00346748

[93] BEMETZ, Jonas A.: *Folienbasierter Mikroreaktor für die magnetischer Nanopartikel und flussbasierte Mikroarrays*, Technische Universität München, Diss., 2019

[94] GRIBANOV, N. M. ; BIBIK, E. E. ; BUZUNOV, O. V. ; NAUMOV, V. N.: Physico-chemical regularities of obtaining highly dispersed magnetite by the method of chemical condensation. In: *Journal of Magnetism and Magnetic Materials* 85 (1990), apr, Nr. 1-3, S. 7–10. http://dx.doi.org/10.1016/0304-8853(90)90005-B. – DOI 10.1016/0304–8853(90)90005–B. – ISSN 03048853

[95] BARTHOLOMEUSZ, Daniel A. ; BOUTTÉ, Ronald W. ; ANDRADE, Joseph D.: Xurography: Rapid prototyping of microstructures using a cutting plotter. In: *Journal of Microelectromechanical Systems* 14 (2005), dec, Nr. 6, S. 1364–1374. http://dx.doi.org/10.1109/JMEMS.2005.859087. – DOI 10.1109/JMEMS.2005.859087. – ISSN 10577157

[96] SIMMONS, Matthew ; WILES, Charlotte ; ROCHER, Vincent ; FRANCESCONI, M. G. ; WATTS, Paul: The preparation of magnetic iron oxide nanoparticles in microreactors. In: *Journal of Flow Chemistry* 3 (2013), mar, Nr. 1, S. 7–10. http://dx.doi.org/10.1556/JFC-D-12-00024. – DOI 10.1556/JFC–D–12–00024. – ISSN 2062249X

[97] IVLEVA, Natalia P. ; HUCKELE, Susanne ; WEINZIERL, Bernadett ; NIESSNER, Reinhard ; HAISCH, Christoph ; BAUMANN, Thomas: Identification and characterization of individual airborne volcanic ash particles by Raman microspectroscopy. In: *Analytical and Bioanalytical Chemistry* 405 (2013), nov, Nr. 28, S. 9071–9084. http://dx.doi.org/10.1007/s00216-013-7328-9. – DOI 10.1007/s00216–013–7328–9. – ISSN 16182642

[98] SCHWAMINGER, S. P. ; BAUER, D. ; FRAGA-GARCÍA, P. ; WAGNER, F. E. ; BERENSMEIER, S.: Oxidation of magnetite nanoparticles: impact on surface and crystal properties. In: *CrystEngComm* 19 (2017), jan, Nr. 2, S. 246–255. http://dx.doi.org/10.1039/c6ce02421a. – DOI 10.1039/c6ce02421a. – ISSN 14668033

[99] DAS, Manasmita ; MISHRA, Debasish ; DHAK, Prasanta ; GUPTA, Satyajit ; MAITI, Tapas K. ; BASAK, Amit ; PRAMANIK, Panchanan: Biofunctionalized, phosphonate-grafted, ultrasmall iron oxide nanoparticles for combined targeted cancer therapy and multimodal imaging. In: *Small* 5 (2009), dec, Nr. 24, S. 2883–2893. http://dx.doi.org/10.1002/smll.200901219. – DOI 10.1002/smll.200901219. – ISSN 16136810

[100] DAVIS, Kathleen ; COLE, Brian ; GHELARDINI, Melanie ; POWELL, Brian A. ; MEFFORD, O. T.: Quantitative Measurement of Ligand Exchange with Small-Molecule Ligands on Iron Oxide Nanoparticles via Radioanalytical Techniques. In: *Langmuir* 32 (2016), dec, Nr. 51, S. 13716–13727. http://dx.doi.org/10.1021/acs.langmuir.6b03644. – DOI 10.1021/acs.langmuir.6b03644. – ISSN 15205827

[101] PORTET, David ; DENIZOT, Benoît ; RUMP, Elmar ; LEJEUNE, Jean J. ; JALLET, Pierre: Non-polymeric coatings of iron oxide colloids for biological use as magnetic resonance imaging contrast agents. In: *Journal of Colloid and Interface Science* 238 (2001), jul, Nr. 1, S. 37–42. http://dx.doi.org/10.1006/jcis.2001.7500. – DOI 10.1006/jcis.2001.7500. – ISSN 00219797

[102] BENYETTOU, F ; MILOSEVIC, I ; OLSEN, JC ; MOTTE, L ; TRABOLSI, A: Ultra-Small Superparamagnetic Iron Oxide Nanoparticles Made to Order. In: *J Bioanal Biomed* (2012), S. 5. http://dx.doi.org/10.4172/1948-593X.S5-006. – DOI 10.4172/1948–593X.S5–006

[103] ISLAM, Monsur ; NATU, Rucha ; MARTINEZ-DUARTE, Rodrigo: A study on the limits and advantages of using a desktop cutter plotter to fabricate microfluidic networks. In: *Microfluidics and Nanofluidics* 19 (2015), oct, Nr. 4, S. 973–985. http://dx.doi.org/10.1007/s10404-015-1626-9. – DOI 10.1007/s10404–015–1626–9. – ISSN 16134990

[104] MAHMOUDI, Morteza ; SIMCHI, Abdolreza ; IMANI, Mohammad ; HAFELI, Urs O.: Superparamagnetic iron oxide nanoparticles with rigid cross-linked polyethylene glycol fumarate coating for application in imaging and drug delivery. In: *Journal of Physical Chemistry C* 113 (2009), may, Nr. 19, S. 8124–8131. http://dx.doi.org/10.1021/jp900798r. – DOI 10.1021/jp900798r. – ISSN 19327447

[105] SMOLKOVA, I. S. ; KAZANTSEVA, N. E. ; VITKOVA, L. ; BABAYAN, V. ; VILCAKOVA, J. ; SMOLKA, P.: Size dependent heating efficiency of multicore iron oxide particles in low-power alternating magnetic fields. In: *Acta Physica Polonica A* Bd. 131, Polish Academy of Sciences, apr 2017. – ISSN 1898794X, S. 663–665

[106] ROTH, Hans C. ; SCHWAMINGER, Sebastian P. ; SCHINDLER, Michael ; WAGNER, Friedrich E. ; BERENSMEIER, Sonja: Influencing factors in the CO-precipitation process of superparamagnetic iron oxide nano particles: A model based study. In: *Journal of Magnetism and Magnetic Materials* 377 (2015), mar, S. 81–89. http://dx.doi.org/10.1016/j.jmmm.2014.10.074. – DOI 10.1016/j.jmmm.2014.10.074. – ISSN 03048853

[107] VAYSSIÈRES, Lionel ; CHANÉAC, Corinne ; TRONC, Elisabeth ; JOLIVET, Jean P.: Size tailoring of magnetite particles formed by aqueous precipitation: An example of thermodynamic stability of nanometric oxide particles. In: *Journal of Colloid and Interface Science* 205 (1998), sep, Nr. 2, S. 205–212. http://dx.doi.org/10.1006/jcis.1998.5614. – DOI 10.1006/jcis.1998.5614. – ISSN 00219797

[108] CARROLL, Matthew R J. ; WOODWARD, Robert C. ; HOUSE, Michael J. ; TEOH, Wey Y. ; AMAL, Rose ; HANLEY, Tracey L. ; ST PIERRE, Timothy G.: Experimental validation of proton transverse relaxivity models for superparamagnetic nanoparticle MRI contrast agents. In: *Nanotechnology* 21 (2010), jan, Nr. 3, 035103. http://dx.doi.org/10.1088/0957-4484/21/3/035103. – DOI 10.1088/0957–4484/21/3/035103. – ISSN 1361–6528

[109] FRENZ, Lucas ; EL HARRAK, Abdeslam ; PAULY, Matthias ; BÉGIN-COLIN, Sylvie ; GRIFFITHS, Andrew D. ; BARET, Jean C.: Droplet-based microreactors for the synthesis of magnetic iron oxide nanoparticles. In: *Angewandte Chemie - International Edition* 47 (2008), aug, Nr. 36, 6817–6820. http://dx.doi.org/10.1002/anie.200801360. – DOI 10.1002/anie.200801360. – ISSN 14337851

[110] YOON, Tae-Jong ; LEE, Hakho ; SHAO, Huilin ; HILDERBRAND, Scott A. ; WEISSLEDER, Ralph: Multicore Assemblies Potentiate Magnetic Properties of Biomagnetic Nanoparticles. In: *Advanced Materials* 23 (2011), nov, Nr. 41, 4793–4797. http://dx.doi.org/10.1002/adma.201102948. – DOI 10.1002/adma.201102948. – ISSN 09359648

[111] MASCOLO, Maria C. ; PEI, Yongbing ; RING, Terry A.: Room Temperature Co-Precipitation Synthesis of Magnetite Nanoparticles in a Large ph Window with Different Bases. In: *Materials* 6 (2013), nov, Nr. 12, 5549–5567. http://dx.doi.org/10.3390/ma6125549. – DOI 10.3390/ma6125549. – ISSN 19961944

[112] RAMADAN, Wegdan ; KAREEM, Marwa ; HANNOYER, Béatrice ; SAHA, Shanta: Effect of pH on the structural and magnetic properties of magnetite nanoparticles synthesised by co-precipitation. In: *Advanced Materials Research* 324 (2011), Nr. November 2014, S. 129–

132. http://dx.doi.org/10.4028/www.scientific.net/AMR.324.129. – DOI 10.4028/www.scientific.net/AMR.324.129. – ISBN 9783037852293

[113] REISER, Maximilian ; SEMMLER, Wolfhard: *Magnetresonanztomographie*. Springer-Verlag Berlin Heidelberg, 2002

[114] AUE, W. P. ; BARTHOLDI, E. ; ERNST, R. R.: Two-dimensional spectroscopy. Application to nuclear magnetic resonance. In: *The Journal of Chemical Physics* 64 (1976), mar, Nr. 5, 2229–2246. http://dx.doi.org/10.1063/1.432450. – DOI 10.1063/1.432450. – ISSN 00219606

[115] POUZARD, G. ; SUKUMAR, S. ; HALL, L. D.: High Resolution, Zero Quantum Transition (Two-Dimensional) Nuclear Magnetic Resonance Spectroscopy: Spectral Analysis. In: *Journal of the American Chemical Society* 103 (1981), Nr. 14, S. 4209–4215. http://dx.doi.org/10.1021/ja00404a039. – DOI 10.1021/ja00404a039. – ISSN 15205126

[116] HESSE, Manfred ; MEIER, Herbert ; ZEEH, Bernhard: *Spektroskopische Methoden in der organischen Chemie*. Thieme, 2002

[117] WISHART, David S. ; FEUNANG, Yannick D. ; MARCU, Ana ; GUO, An C. ; LIANG, Kevin ; VÁZQUEZ-FRESNO, Rosa ; SAJED, Tanvir ; JOHNSON, Daniel ; LI, Carin ; KARU, Naama ; SAYEEDA, Zinat ; LO, Elvis ; ASSEMPOUR, Nazanin ; BERJANSKII, Mark ; SINGHAL, Sandeep ; ARNDT, David ; LIANG, Yonjie ; BADRAN, Hasan ; GRANT, Jason ; SERRA-CAYUELA, Arnau ; LIU, Yifeng ; MANDAL, Rupa ; NEVEU, Vanessa ; PON, Allison ; KNOX, Craig ; WILSON, Michael ; MANACH, Claudine ; SCALBERT, Augustin: HMDB 4.0: The human metabolome database for 2018. In: *Nucleic Acids Research* 46 (2018), jan, Nr. D1, S. D608–D617. http://dx.doi.org/10.1093/nar/gkx1089. – DOI 10.1093/nar/gkx1089. – ISSN 13624962

[118] ANTIC, Dean: *Lesson Plan: Regioisomers of Butanol, pS45*. www.thermoscientific.com

[119] MÜLLER, Luciano: Mapping of spin-spin coupling via zero-quantum coherence. In: *Journal of Magnetic Resonance (1969)* 59 (1984), Nr. 2, S. 326–331. http://dx.doi.org/10.1016/0022-2364(84)90177-X. – DOI 10.1016/0022–2364(84)90177–X. – ISSN 00222364

[120] JEENER, J. ; BROEKAERT, P.: Nuclear magnetic resonance in solids: Thermodynamic effects of a pair of rf pulses. In: *Physical Review* 157 (1967), Nr. 2, S. 232–240. http://dx.doi.org/10.1103/PhysRev.157.232. – DOI 10.1103/PhysRev.157.232. – ISSN 0031899X

[121] MARECI, Thomas H. ; FREEMAN, Ray: Mapping proton-proton coupling via double-quantum coherence. In: *Journal of Magnetic Resonance (1969)* 51 (1983), feb, Nr. 3, S. 531–535. http://dx.doi.org/10.1016/0022-2364(83)90305-0. – DOI 10.1016/0022–2364(83)90305–0. – ISSN 00222364

[122] BRAUNSCHWEILER, Lukas ; BODENHAUSEN, Geoffrey ; ERNST, R. R.: Analysis of networks of coupled spins by multiple quantum N.M.R. In: *Molecular Physics* 48 (1983), Nr. 3, S. 535–560. http://dx.doi.org/10.1080/00268978300100381. – DOI 10.1080/00268978300100381. – ISSN 13623028

[123] WOKAUN, A. ; ERNST, R. R.: Selective detection of multiple quantum transitions in NMR by two-dimensional spectroscopy. In: *Chemical Physics Letters* 52 (1977), dec, Nr. 3, S. 407–412. http://dx.doi.org/10.1016/0009-2614(77)80476-4. – DOI 10.1016/0009–2614(77)80476–4. – ISSN 00092614

[124] MCMURRY, John.: Amino Acids, the Henderson-Hasselbalch Equation, and Isoelectric Points. Version: 2011. https://books.google.com.tr/books/about/Organic{_}Chemistry.html?id=oVv4Az7VJRYC{&}redir{_}esc=y. In: *Organic Chemistry*. Brooks/Cole, Cengage Learning, 2011. – ISBN 084005453X, Kapitel 26.2

[125] GAINARU, C. ; MEIER, R. ; SCHILDMANN, S. ; LEDERLE, C. ; HILLER, W. ; RÖSSLER, E. A. ; BÖHMER, R.: Nuclear-magnetic-resonance measurements reveal the origin of the debye process in monohydroxy alcohols. In: *Physical Review Letters* 105 (2010), dec, Nr. 25, 258303. http://dx.doi.org/10.1103/PhysRevLett.105.258303. – DOI 10.1103/PhysRevLett.105.258303. – ISSN 00319007

[126] STERK, H. ; KALCHER, J.: Zur beeinflussung der relaxationszeit T1 von carbonylgruppen durch lanthaniden-shiftreagenzien. In: *Advances in Molecular Relaxation and Interaction Processes* 16 (1980), Nr. 1, S. 53–62. http://dx.doi.org/10.1016/0378-4487(80)80006-9. – DOI 10.1016/0378–4487(80)80006–9. – ISSN 03784487

[127] VAISH, S K. ; SINGH, A K. ; SINGH, Anupam: NMR spin lattice relaxation investigation of some molecular systems and its correlation with dielectric relaxation. 2003. – Forschungsbericht. – 858–862 S.

[128] SRINIVASA RAO, A. ; ARULMOZHI, V. ; RAJALAKSHMI, S.: Mutal interactions between hydrogen bonds in alcohols - nuclear magnetic relaxation study. In: *Bulletin des Sociétés Chimiques Belges* 102 (1993), sep, Nr. 11-12, 693–698. http://dx.doi.org/10.1002/bscb.19931021103. – DOI 10.1002/bscb.19931021103. – ISSN 00379646

[129] DOLPH, C. L.: A Current Distribution for Broadside Arrays Which Optimizes the Relationship Between Beam Width and Side-Lobe Level. In: *Proceedings of the IRE* 34 (1946), Nr. 6, S. 335–348. http://dx.doi.org/10.1109/JRPROC.1946.225956. – DOI 10.1109/JRPROC.1946.225956. – ISSN 00968390

[130] BLOEMBERGEN, N. ; POUND, R. V.: Radiation damping in magnetic resonance experiments. In: *Physical Review* 95 (1954), jul, Nr. 1, S. 8–12. http://dx.doi.org/10.1103/PhysRev.95.8. – DOI 10.1103/PhysRev.95.8. – ISSN 0031899X

[131] JEENER, J.: Equivalence between the "classical" and the "Warren" approaches for the effects of long range dipolar couplings in liquid nuclear magnetic resonance. In: *Journal of Chemical Physics* 112 (2000), mar, Nr. 11, S. 5091–5094. http://dx.doi.org/10.1063/1.481063. – DOI 10.1063/1.481063. – ISSN 00219606

[132] MCCOY, M. A. ; WARREN, W. S.: Three-quantum nuclear magnetic resonance spectroscopy of liquid water: Intermolecular multiple-quantum coherence generated by spin-cavity coupling. In: *The Journal of Chemical Physics* 93 (1990), jul, Nr. 1, 858–860. http://dx.doi.org/10.1063/1.459457. – DOI 10.1063/1.459457. – ISSN 00219606

[133] HE, Qiuhong ; RICHTER, Wolfgang ; VATHYAM, Sujatha ; WARREN, Warren S.: Intermolecular multiple-quantum coherences and cross correlations in solution nuclear magnetic resonance. In: *The Journal of Chemical Physics* 98 (1993), may, Nr. 9, 6779–6800. http://dx.doi.org/10.1063/1.464770. – DOI 10.1063/1.464770. – ISSN 00219606

[134] AHN, Sangdoo ; WARREN, Warren S. ; LEE, Sanghyuk: Quantum Treatment of Intermolecular Multiple-Quantum Coherences with Intramolecular J Coupling in Solution NMR. In: *Journal of Magnetic Resonance* 128 (1997), oct, Nr. 2, 114–129. http://dx.doi.org/10.1006/jmre.1997.1226. – DOI 10.1006/jmre.1997.1226. – ISSN 10907807

[135] JEENER, J. ; VLASSENBROEK, A. ; BROEKAERT, P.: Unified derivation of the dipolar field and relaxation terms in the Bloch-Redfield equations of liquid NMR. In: *The Journal of Chemical Physics* 103 (1995), jul, Nr. 4, 1309–1332. http://dx.doi.org/10.1063/1.469808. – DOI 10.1063/1.469808. – ISSN 00219606

[136] GARRETT-ROE, Sean ; WARREN, Warren S.: Numerical Studies of Intermolecular Multiple Quantum Coherences: High-Resolution NMR in Inhomogeneous Fields and Contrast Enhancement in MRI. In: *Journal of Magnetic Resonance* 146 (2000), sep, Nr. 1, 1–13. http://dx.doi.org/10.1006/jmre.2000.2096. – DOI 10.1006/jmre.2000.2096. – ISSN 10907807

[137] CHEN, Zhong ; HOU, Ting ; CHEN, Zhi W. ; HWANG, Dennis W. ; HWANG, Lian P.: Selective intermolecular zero-quantum coherence in high-resolution NMR under inhomogeneous fields. In: *Chemical Physics Letters* 386 (2004), mar, Nr. 1-3, S. 200–205. http://dx.doi.org/10.1016/j.cplett.2004.01.055. – DOI 10.1016/j.cplett.2004.01.055. – ISSN 00092614

[138] AHN, Sangdoo ; LISITZA, Natalia ; WARREN, Warren S.: Intermolecular Zero-Quantum Coherences of Multi-component Spin Systems in Solution NMR. In: *Journal of Magnetic Resonance* 133 (1998), aug, Nr. 2, S. 266–272. http://dx.doi.org/10.1006/jmre.1998.1461. – DOI 10.1006/jmre.1998.1461. – ISSN 10907807

[139] SØRENSEN, O. W. ; LEVITT, Malcolm H. ; ERNST, R. R.: Uniform excitation of multiple-quantum coherence: Application to multiple quantum filtering. In: *Journal of Magnetic Resonance (1969)* 55 (1983), Nr. 1, S. 104–113. http://dx.doi.org/10.1016/0022-2364(83)90280-9. – DOI 10.1016/0022–2364(83)90280–9. – ISSN 00222364

[140] SCHRITTWIESER, Stefan ; PELAZ, Beatriz ; PARAK, Wolfgang J. ; LENTIJO-MOZO, Sergio ; SOULANTICA, Katerina ; DIECKHOFF, Jan ; LUDWIG, Frank ; GUENTHER, Annegret ; TSCHÖPE, Andreas ; SCHOTTER, Joerg: Homogeneous biosensing based on magnetic particle labels. In: *Sensors (Switzerland)* 16 (2016), jun, Nr. 6. http://dx.doi.org/10.3390/s16060828. – DOI 10.3390/s16060828. – ISSN 14248220

[141] WEGEMANN, Andreas ; STAAT, Christoph ; RAPP, Jonathan ; HEIDSIECK, Alexandra ; HAASE, Axel ; GLEICH, Bernhard: A Portable NMR Spectrometer with a Probe Head Combining RF and DC Capabilities to Generate Pulsed Field Gradients. In: *IEEE Transactions on Instrumentation and Measurement* (2020), may, S. 1–1. http://dx.doi.org/10.1109/tim.2020.2993981. – DOI 10.1109/tim.2020.2993981. – ISSN 0018–9456

List of Publications

Peer-Reviewed First-Author Publications

- BEMETZ, Jonas ; WEGEMANN, Andreas ; SAATCHI, Katayoun ; HAASE, Axel ; HÄFELI, Urs O. ; NIESSNER, Reinhard ; GLEICH, Bernhard ; SEIDEL, Michael: Microfluidic-Based Synthesis of Magnetic Nanoparticles Coupled with Miniaturized NMR for Online Relaxation Studies. In: *Analytical Chemistry* 90 (2018), Nr. 16, S. 9975–9982. http://dx.doi.org/10.1021/acs.analchem.8b02374. – DOI 10.1021/acs.analchem.8b02374. – ISSN 15206882

- WEGEMANN, Andreas ; STAAT, Christoph ; RAPP, Jonathan ; HEIDSIECK, Alexandra ; HAASE, Axel ; GLEICH, Bernhard: A Portable NMR Spectrometer with a Probe Head Combining RF and DC Capabilities to Generate Pulsed Field Gradients. In: *IEEE Transactions on Instrumentation and Measurement* (2020), may, S. 1–1. http://dx.doi.org/10.1109/tim.2020.2993981. – DOI 10.1109/tim.2020.2993981. – ISSN 0018–9456

Peer-Reviewed Co-Author Publications

- Jouha, Min; Taehwang, Son; Andreas, Wegemann; Ralph, Weissleder; Hakho, Lee; Hyungsoon, Im; Plasmon-enhanced biosensing for multiplexed profiling of extracellular vesicles; Submitted to Advanced Biosystems in 01/2020

Conference Contributions

- Andreas, Wegemann; Jonas, Bemetz; Reinhard, Nießner; Michael Seidel; Bernhard Gleich; Breitbandiges NMR-Relaxometer zur on-line Bestimmung von Relaxationszeiten unter Flussbedingungen; 13. Dresdner Sensor-Symposium; Dresden, 2017

- Andreas, Wegemann; Jonas, Bemetz; Reinhard, Nießner; Michael, Seidel; Bernhard, Gleich; Automated Synthesis of Magnetic Nanoparticles and Process Monitoring by Nuclear Magnetic Relaxation; Magmeet 2018, Copenhagen, 2018

Acknowledgement

At this point, I would like to thank everybody who supported and encouraged me in completing this dissertation.
To my supervisor, Bernhard Gleich, I would like to express my sincere gratitude for his patient guidance and his continual support. Insightful comments and diverse suggestions throughout countless coffee breaks substantially helped me in completing this thesis.
A special thanks is also to Axel Haase and Werner Hemmert for sharing their extensive knowledge as well as the acceptance to supervise this thesis. I am very thankful for your support and your sympathetic ear for issues that arose throughout my research.
I also want to thank my colleagues and former colleagues, especially Christine Rümenapp, Alexandra Heidsieck, Christoph Staat, Jonathan Rapp, Bojan Sandurkov and Stephan Huber for their constant support and their cooperation. I enjoyed the talks during lunch at the Mensa as well as the outstanding darts and kicker sessions.
I really appreciated the fruitful cooperation with my partners from the Institute of Hydrochemistry, TUM. Therefore, I owe particular thanks to Michael Seidel, Angelika Nistler and Jonas Bemetz. Jonas, it was a pleasure to work with you!
For their hospitality and supervision throughout my research abroad, I want to thank Ralph Weissleder, Hakho Lee, Hyungsoon Im and Jouha Min from the CSB, Harvard Medical School, Boston.
Furthermore, I want to thank the IGSSE for funding and supporting my scientific work.
A very special thanks is to my girlfriend Corinna and my little daughter Hannah who spent numerous hours in proofreading and gave me all the motivation I required to finish this thesis.
Finally, I would like to thank my whole family for their sincere support throughout my academic studies.